Data Mining in Civil Engineering

Lead Guest Editor: Chongchong Qi
Guest Editors: Qiusong Chen, Binh Thai Pham, Zhong-Qiang Liu, and Raghvendra Kumar

Data Mining in Civil Engineering

Data Mining in Civil Engineering

Lead Guest Editor: Chongchong Qi
Guest Editors: Qiusong Chen, Binh Thai Pham,
Zhong-Qiang Liu, and Raghvendra Kumar

Chief Editor

Cumaraswamy Vipulanandan, USA

Chayut Ngamkhanong (iD), Thailand
Trung Ngo, Australia
Tengfei Nian, China
Mehdi Nikoo (iD), Canada
Youjun Ning (iD), China
Olugbenga Timo Oladinrin (iD), United Kingdom
Oladimeji Benedict Olalusi, South Africa
Timothy O. Olawumi (iD), Hong Kong
Alejandro Orfila (iD), Spain
Maurizio Orlando (iD), Italy
Siti Aminah Osman, Malaysia
Walid Oueslati (iD), Tunisia
SUVASH PAUL (iD), Bangladesh
John-Paris Pantouvakis (iD), Greece
Fabrizio Paolacci (iD), Italy
Giuseppina Pappalardo (iD), Italy
Fulvio Parisi (iD), Italy
Dimitrios G. Pavlou (iD), Norway
Daniele Pellegrini (iD), Italy
Gatheeshgar Perampalam (iD), United Kingdom
Daniele Perrone (iD), Italy
Giuseppe Piccardo (iD), Italy
Vagelis Plevris (iD), Qatar
Andrea Pranno (iD), Italy
Adolfo Preciado (iD), Mexico
Chongchong Qi (iD), China
Yu Qian, USA
Ying Qin (iD), China
Giuseppe Quaranta (iD), Italy
Krishanu ROY (iD), New Zealand
Vlastimir Radonjanin, Serbia
Carlo Rainieri (iD), Italy
Rahul V. Ralegaonkar, India
Raizal Saifulnaz Muhammad Rashid, Malaysia
Alessandro Rasulo (iD), Italy
Chonghong Ren (iD), China
Qing-Xin Ren, China
Dimitris Rizos (iD), USA
Geoffrey W. Rodgers (iD), New Zealand
Pier Paolo Rossi, Italy
Nicola Ruggieri (iD), Italy
JUNLONG SHANG, Singapore

Nikhil Saboo, India
Anna Saetta, Italy
Juan Sagaseta (iD), United Kingdom
Timo Saksala, Finland
Mostafa Salari, Canada
Ginevra Salerno (iD), Italy
Evangelos J. Sapountzakis (iD), Greece
Vassilis Sarhosis (iD), United Kingdom
Navaratnarajah Sathiparan (iD), Sri Lanka
Fabrizio Scozzese (iD), Italy
Halil Sezen (iD), USA
Payam Shafigh (iD), Malaysia
M. Shahria Alam, Canada
Yi Shan, China
Hussein Sharaf, Iraq
Mostafa Sharifzadeh, Australia
Sanjay Kumar Shukla, Australia
Amir Si Larbi (iD), France
Okan Sirin (iD), Qatar
Piotr Smarzewski (iD), Poland
Francesca Sollecito (iD), Italy
Rui Song (iD), China
Tian-Yi Song, Australia
Flavio Stochino (iD), Italy
Mayank Sukhija (iD), USA
Piti Sukontasukkul (iD), Thailand
Jianping Sun, Singapore
Xiao Sun (iD), China
T. Tafsirojjaman (iD), Australia
Fujiao Tang (iD), China
Patrick W.C. Tang (iD), Australia
Zhi Cheng Tang (iD), China
Weerachart Tangchirapat (iD), Thailand
Xiaxin Tao, China
Piergiorgio Tataranni (iD), Italy
Elisabete Teixeira (iD), Portugal
Jorge Iván Tobón (iD), Colombia
Jing-Zhong Tong, China
Francesco Trentadue (iD), Italy
Antonello Troncone, Italy
Majbah Uddin (iD), USA
Tariq Umar (iD), United Kingdom
Muahmmad Usman, United Kingdom
Muhammad Usman (iD), Pakistan
Mucteba Uysal (iD), Turkey

Ilaria Venanzi, Italy
Castorina S. Vieira, Portugal
Valeria Vignali, Italy
Claudia Vitone, Italy
Liwei WEN, China
Chunfeng Wan, China
Hua-Ping Wan, China
Roman Wan-Wendner, Austria
Chaohui Wang, China
Hao Wang, USA
Shiming Wang, China
Wayne Yu Wang, United Kingdom
Wen-Da Wang, China
Xing Wang, China
Xiuling Wang, China
Zhenjun Wang, China
Xin-Jiang Wei, China
Tao Wen, China
Weiping Wen, China
Lei Weng, China
Chao Wu, United Kingdom
Jiangyu Wu, China
Wangjie Wu, China
Wenbing Wu, China
Zhixing Xiao, China
Gang Xu, China
Jian Xu, China
Panpan, China
Rongchao Xu, China
HE YONGLIANG, China
Michael Yam, Hong Kong
Hailu Yang, China
Xu-Xu Yang, China
Hui Yao, China
Xinyu Ye, China
Zhoujing Ye, China
Gürol Yildirim, Turkey
Dawei Yin, China
Doo-Yeol Yoo, Republic of Korea
Zhanping You, USA
Afshar A. Yousefi, Iran
Xinbao Yu, USA
Dongdong Yuan, China
Geun Y. Yun, Republic of Korea

Hyun-Do Yun, Republic of Korea
Cemal YİĞİT, Turkey
Paolo Zampieri, Italy
Giulio Zani, Italy
Mariano Angelo Zanini, Italy
Zhixiong Zeng, Hong Kong
Mustafa Zeybek, Turkey
Henglong Zhang, China
Jiupeng Zhang, China
Tingting Zhang, China
Zengping Zhang, China
Zetian Zhang, China
Zhigang Zhang, China
Zhipeng Zhao, Japan
Jun Zhao, China
Annan Zhou, Australia
Jia-wen Zhou, China
Hai-Tao Zhu, China
Peng Zhu, China
QuanJie Zhu, China
Wenjun Zhu, China
Marco Zucca, Italy
Haoran Zuo, Australia
Junqing Zuo, China
Robert Černý, Czech Republic
Süleyman İpek, Turkey

Contents

Prediction of the Strength of Rubberized Concrete by an Evolved Random Forest Model

Yuantian Sun Ⓘ, Guichen Li Ⓘ, Junfei Zhang Ⓘ, and Deyu Qian Ⓘ

Research Article

Stability of a Roadway below a Coal Seam under Dynamic Pressure: A Case Study of the 11123 Floor Gas Drainage Roadway of a Mine in Huainan, China

Pingsong Zhang,[1,2] **Yuanchao Ou** ,[1,2] **Chang Liu,**[1,2] **Binyang Sun,**[1,2] **and Chong Xu**[3]

[1]*State Key Laboratory of Mining Response and Disaster Prevention and Control in Deep Coal Mines, Anhui University of Science and Technology, Huainan 232001, China*
[2]*School of Earth and Environment, Anhui University of Science and Technology, Huainan 232001, China*
[3]*Ping'an Coal Mining Institute of Engineering Technology Co., Ltd., Huainan 232001, China*

Correspondence should be addressed to Yuanchao Ou; ycou623@163.com

Coal and gas outburst is an important risk faced by coal seam mining in the Huainan region of China. In order to control gas outburst, the gas is predrained by digging a floor gas drainage roadway. To study deformation due to dynamic pressure, the failure characteristics of the floor, and their effect on the stability of the floor gas drainage roadway, a comprehensive monitoring method combining Brillouin optical time-domain reflectometry- (BOTDR-) distributed fiber optics and self-potential exploration was adopted. Dynamic data monitoring of the rock strata between the 11123 working face floor and the floor gas drainage roadway of a mine in Huainan was carried out. The field data obtained showed that, when stabilized by rock bolts and other fixed components in the surrounding rock mass of the floor gas drainage roadway, under the influence of mining, the area of concentrated stress appeared at a depth of 20.7 m, when cracks eventually formed, but the overall structural stability of the surrounding rock mass remained good. The stress distribution and crack evolution of the bottom plate under the influence of dynamic pressure showed spatiotemporal characteristics. Of these, the effect of the lead support stress was 107.48 m, and the range of effect of the hysteresis stress was 34.42 m. When the working face mining position arrives and is far from the monitoring station, the failure depth of floor rock stratum shows the following rule: unchanged in the early stage, deepened continuously in the middle stage, and finally remained stable. It takes about eight days for the dynamic adjustment of this process to finally stabilize. The results of this study can provide guidance for devising suitable procedures for carrying out intelligent green safety mining and for warning about the hazards of roadway damage.

1. Introduction

In coal and gas outburst mining areas [1], such as those surrounding the city of Huainan, in north-central Anhui Province, China, it is often necessary to design suitable floor gas drainage roadways [2] in advance, at a certain depth below the working face, and to carry out safety work related to equipment system layouts, such as coal seam gas extraction and ventilation. In the later stages of mining operations, once the working face has been mined, the original state of stress balance of the surrounding rock will be altered. The transfer of mining stress to the floor rock mass will eventually lead to the deformation and destruction of rock strata within a certain depth of the floor. At that time, if the floor gas drainage roadway is located in the affected area and the on-site support conditions are insufficient, this will inevitably lead to the instability of the surrounding rock and of the floor gas drainage roadway and even render the operation of the roadway equipment system unsafe [3–5]. For these reasons, we chose to study and determine the characteristics of floor failure under the influence of dynamic pressure and the effect on the stability of the rock surrounding the floor gas drainage roadway. The results obtained in this study will be of great practical importance

for safe and stable mining and for the support of roadways under coal seam working faces in areas such as Huainan and other high gas-rich mining areas.

In recent years, researchers in China and abroad have carried out numerous studies of the damage and characteristics of the floor under the influence of mining [6–12]. Song et al. [13] set up a mechanics calculation model of the floor along the inclination of the working face against the background of confined water mining in the 41503 working face of a mine and derived, theoretically, the stress distribution and failure characteristics of the floor. Zhang et al. [14] used seismic computed tomography (CT) detection technology to dynamically monitor the deformation and failure of a floor during coal mining. Zhang et al. [15] used the mutual verification method involving the field strain test as well as numerical simulations to comprehensively study the damage depth of a thick mined coal seam. By sorting and analyzing a large quantity of field-measured data, Zhu et al. [16] explored the different deformations and failure characteristics of different lithologies and composite floor structures under the influence of dynamic pressure.

There are also abundant research results relating to the deformation and failure characteristics of rock structures surrounding roadways [17–24]. Li et al. [25] used a numerical simulation method to study the mechanism of roadway failure caused by repeated caving in the Huaibei mining area and proposed a new supporting scheme. Chen et al. [26] used the true triaxial analog simulation method to study the characteristics of strain evolution and fracture of the rock surrounding a mining roadway under the gradient loading of dynamic pressure. Hua and Yang [27] used a Brillouin optical time-domain analysis- (BOTDA-) distributed fiber optical sensor (DFOS) and close-range photographic technology to monitor the deformation of the roadway floor during the process of gob-side entry retaining (GSER) excavation, first mining, retaining lane, and secondary mining. The dynamic evolution characteristics of the deformation of the floor of the GSER with a large cross section in a deep mine were obtained. Li et al. [28] used a high-precision microseismic monitoring system and a roof dynamic monitoring instrument to delineate the floor failure depth of the 2200 working face and also studied the deformation and failure mechanism of the 4106 material roadway and transportation roadway below the working face.

Based on the above research results, this study took the 11123 working face and the 11123 floor gas drainage roadway of a mine in Huainan as an engineering case study. Using the integrated monitoring method that combines Brillouin optical time-domain reflectometry (BOTDR)-DFOS and self-potential exploration, whole-process dynamic data monitoring was conducted. The failure characteristics of the 11123 working face floor were determined, and the stability of the rock surrounding the 11123 floor gas drainage roadway under the influence of dynamic pressure was studied.

The main contributions of this paper include the following: (1) a comprehensive monitoring technology consisting of distributed strain fiber optics and spontaneous potential tests was used to monitor the stability of the surrounding rock under dynamic pressure, which overcame the problems of single-test means and the small quantity of measured data obtained in previous studies. The results obtained by comprehensive monitoring data are self-verifying, which improves the reliability of the data; (2) the response characteristics of the multiphysical field data and the changes in the stability of the surrounding rock under dynamic pressure were obtained, which will aid future studies on the stability of the rock surrounding a roadway; (3) it was found that the failure depth of floor strata lags behind the secondary deepening of the coal wall under the action of mining. According to the spatiotemporal evolution characteristics of floor fracture, the characteristics of and time required from the moment of dynamic adjustment to the formation of a stable stage were determined.

2. Engineering Geological Conditions

The 11123 working face of the mine is located in the Huainan region, and the working face elevation was, at the time of the study, in the range from −450 to −490 m (working face 11123 belongs to the #3 coal seam). The average buried depth of the working face was approximately 470 m, the mining strike length of the working face was approximately 1345 m, and the inclined length was 155 m. The average thickness of the coal seam was 5.5 m, and the average dip angle of the coal seam was 10°. The #3 and #1 coal seams were both gas outburst seams. The gas content of the #3 coal seam was 6.6–7.7 m³/t, the gas pressure was 1.76–2.44 MPa, the gas content of the #1 coal seam was 5.2–6.5 m³/t, and the gas pressure was 1.35–2.08 MPa. In the early stages of mining, gas pre-extraction treatment was carried out for the #3 and #1 coal seams at the same time. After the standard of gas extraction was reached, mining operations on the #3 coal seam were carried out. Roof management was strengthened during the initial caving stage, and gas management and ventilation were strengthened during the mining process to prevent gas from being trapped in the sandstone layer and causing the gas to exceed the standard safety limit.

The 11123 working face was mined to a thickness of approximately 5 m. There were no large faults or structures in the working face. The lithology and other related information of the #3 coal seam are shown in Figure 1. The 11123 floor gas drainage roadway was located in ⑧ fine sandstone and ⑨ sandy mudstone, with a width × height of 4600 mm × 3500 mm. The top and bottom rock layers consisted of hard and dense limestone. The roadway was used mainly for the placing and installation of safety equipment and systems for gas drainage and ventilation.

The support scheme of the 11123 floor gas drainage roadway adopts the support form of "bolt + anchor net + local anchor cable and grouting". Some fractured or weak surrounding rock sections are strengthened in advance. The anchor is a strong pretensioned anchor, the anchor is Φ20 ∗ 2500 mm, the spacing is 700 × 700 mm, the anchor cable is Φ21.8 ∗ 6500 mm, and the spacing is 1900 × 2000 mm. Three anchor cables are designed

Serial number	Strate thickness (m)	Columnar	Lithology name
①	5.5		3 Coal seam
②	1.5		Mudstone
③	3.5		1 coal seam
④	3.8		Sandy mudstone
⑤	4.2		Fine sanddtone
⑥	9.0		Mudstone
			Limestone
⑦	1.2		Fine sandstone
⑧	2.0		Sandy mudstone
⑨	1.5		
⑩	2.5		Limestone

FIGURE 1: Comprehensive column map of strata.

FIGURE 2: Cross-section design of the supporting scheme of 11123 floor gas drainage roadway.

symmetrically in each roadway section according to the central axis; the spray layer adopts C20 concrete with a thickness of 100 mm (Figure 2).

3. Integrated Monitoring Scheme

3.1. Distributed Fiber Optical Strain Monitoring Technology.
During the monitoring period, an AV6419-distributed optical fiber tester was used for on-site data acquisition. The instrument realizes single-end measurements without a double-end closed loop, which was very convenient and meets the complex conditions of underground construction, layout, and data acquisition.

When the fiber attached to the surface (or inside) of the target is stretched or squeezed due to the deformation and failure of the target, the frequency of the Brillouin backscattered light reflected by the fiber in the strain region will change. The distributed optical fiber tester will measure the received Brillouin backscattered light power

and then obtain the Brillouin frequency shift of each point on the optical fiber. Finally, according to the linear relationship between the Brillouin frequency shift and strain, the strain distribution of each part of the target body was obtained. When the temperature of the target body changes by only a small amount during the monitoring period, the strain value of each point along the optical fiber can be calculated by the following formula:

$$v_B(\varepsilon) = v_B(0) + \frac{dv_B(\varepsilon)}{d\varepsilon}\varepsilon, \tag{1}$$

where ε is the strain value, $v_B(\varepsilon)$ is the Brillouin optical frequency shift when the strain is ε, $v_B(0)$ is the Brillouin frequency shift in the original state, and $dv_B(\varepsilon)/d(\varepsilon)$ is the proportional coefficient, which is about 493 MHz.

Some scholars [29–32] in China have introduced this technology underground to study the deformation and damage of the roof and the surrounding rock in the mining process, and the test accuracy and data volume are better than the conventional testing methods.

3.2. Self-Potential Monitoring Technology.
The data of the geoelectric field during the monitoring period were tested dynamically by the network parallel electrical instrument [33], and the data of the self-potential change in the monitoring section during the mining process of the working face were obtained completely.

In the absence of an artificial power supply to the geological body, the potential difference between any two points can be observed by the instrument, indicating that there was a natural electric field (self-potential field) inside the geological body. However, the self-potential field in the geological body will change dynamically due to the influence of groundwater flow and rock mass deformation and damage. It is believed that these effects will change the

stability of the original charge structure inside the rock mass and its distribution in space, accompanied by the separation, movement, and aggregation of the charge at different positions of the rock mass and then form the dynamic change of the self-potential field [34, 35].

3.3. System Construction.

To understand the damage depth of the 11123 working face under the influence of dynamic pressure and its stability in relation to the lower floor gas drainage roadway, site drilling was designed in the middle of the ⑧ fine sandstone rock layers on the sidewall of the floor gas drainage roadway and inclined upwards to the initial mining position of the working face (Figure 3 and Table 1).

Additionally, after the fiber optic cable and electric cable were implanted into the hole to a predetermined depth by means of the auxiliary tools, layered grouting was carried out in the hole and allowed to set there for a period of time (Figure 4 and Table 2). Each cable was then allowed to fully couple and solidify in contact with the slurry and the surrounding rock mass, and, once the slurry had reached the desired strength, data acquisition began on-site.

4. Results and Analysis of Field Data

4.1. Field Data Collection.

On-site monitoring took place from October 31, 2018, to February 25, 2019. The field data were obtained during the entire monitoring period for a total of 57 times and were of good quality.

According to the information provided by the mine during the monitoring period and the observations of the on-site personnel, there were no water leakages in the working face and floor gas drainage roadway during the entire monitoring period. We consider that the data collected at the site were not disturbed by any seepage field, such as groundwater. Because of the working shift of the coal mining team and the interference due to the industrial electric field, we chose to collect the field data at 2 p.m. each day.

4.2. Characteristics of Floor Failure and Stability of the Surrounding Rock in the Floor Gas Drainage Roadway

4.2.1. DFOS Monitoring Results.

We selected 12 groups of fiber optic strain data for processing during the monitoring period and obtained the corresponding relationship between the fiber optic strain distribution and the stratum (Table 3 and Figure 5). The cloud diagram of the fiber optical strain distribution during monitoring is shown in Figure 6. Figure 7 shows the cross section of the corresponding relationship between the support structure of the floor gas drainage roadway and the stratum.

On October 31, 2018, the working face was still in the nonmining stage, and at this time, the original stress state of the surrounding rock had not changed. On November 12, 2018, the fiber optic data changed for the first time, and the corresponding strain values were +416 and +347 $\mu\varepsilon$ (areas I and II). From the analysis of the stable composite rock beam structure formed by the action of the anchor bolts and the

other fixed components in the surrounding rock of the floor gas drainage roadway, it is considered that the stress distribution of the floor gas drainage roadway and its surrounding rock mass under the mining position was changed by the mining process on the working face. But, because the floor gas drainage roadway and its surrounding rock mass were strongly supported by anchoring, etc., they assumed a combination of high-strength and damage-resistant characteristics, which made the rock mass surrounding the floor gas drainage roadway better able to transmit stress than the other layers, over a greater distance, and with a greater bearing capacity. On November 21, 2018, the tensile strain values reached +3306 and +1003 $\mu\varepsilon$ (areas I and II), indicating that an area of concentrated stress had been formed in the rock mass beyond the control range of the anchor bolts above the floor gas drainage roadway. At the same time, the internal stress of the ④ sandy mudstone layer (area III) changed for the first time, and the tensile strain reached +517 $\mu\varepsilon$. This analysis shows that the mining lead stress of the working face was transmitted to the monitoring area through the ④ sandy mudstone layer under the mining position.

As the working face advanced continuously and gradually came closer to the monitoring section, the change in stress of the bottom slate layer affected by mining gradually increased. On December 12, 2018, the maximum strain values reached +8149 and +2574 $\mu\varepsilon$ (areas I and II) and the strain value of the ④ sandy mudstone layer increased to +1823 $\mu\varepsilon$ (area III). The internal stress of ⑤ fine sandstone changed rapidly to +1005 $\mu\varepsilon$ (area IV). According to the analysis, the effect of the leading stress of the working face mining position on the rock mass in the monitoring area increased, and microcracks gradually emerged in the rock mass. On December 22, 2018, the working face mining position had just crossed the top of the monitoring hole at 5.9 m. During this process, the changes in strain of areas V and IV were the most obvious, increasing by 1173 and 1755 $\mu\varepsilon$, respectively, which showed that the evolution of the floor crack under the influence of dynamic pressure had spatiotemporal effects. The tensile expansion of the floor in the goaf was obvious. The microcracks in areas III, V, and IV expanded further and joined together to produce macroscopic fractures. At the same time, the bottom drum expansion of the working surface was obvious. The rock mass in area I, with a significant concentration of stress, produced a separation crack, which was developed in the upper part of the control area of the anchor member (Figure 6). Although the degree of strain in area II of the surrounding rock of the roadway was large, it remained stable under the control of the bolt member and no damage occurred. Further analysis is carried out below in conjunction with the natural potential and electrode current data.

Between December 22, 2018, and January 12, 2019, the overlying rock mass of the goaf collapsed, and crushed and squeezed the floor rock mass. Areas III and V rapidly decreased and stabilized at +601 $\mu\varepsilon$; the strain value of area IV then decreased to +1304 $\mu\varepsilon$ and remained stable. From January 12, 2019, to February 25, 2019, the tensile strain in the mudstone layer in area I gradually decreased and finally
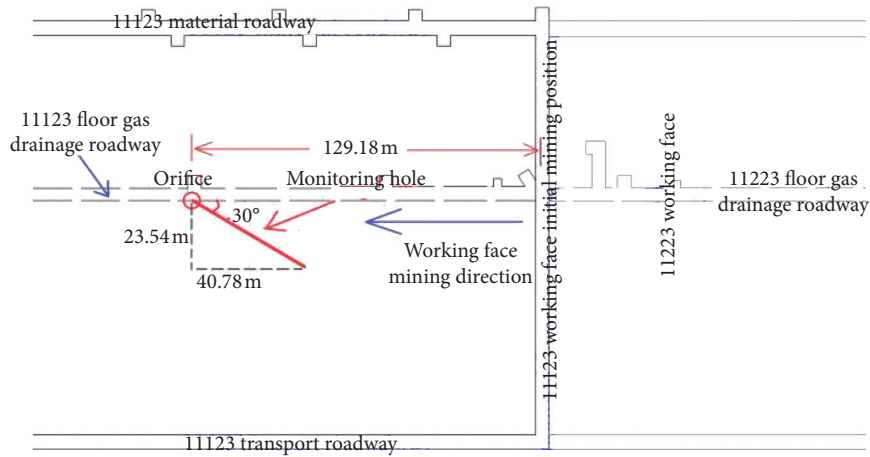
Figure 3: Plane layout sketch of the 11223 working face.

Table 1: Design parameters of the monitoring hole in the 11123 floor gas drainage roadway.

Technical parameter	Monitoring hole	Technical parameter	Monitoring hole
Angle with the roadway (°)	30	Drilling elevation angle (°)	20
Distance between orifice and initial mining position (m)	129.18	Angle between borehole and inclined stratum (°)	24
Actual hole length (m)	46.2	Control vertical height (m)	18.79
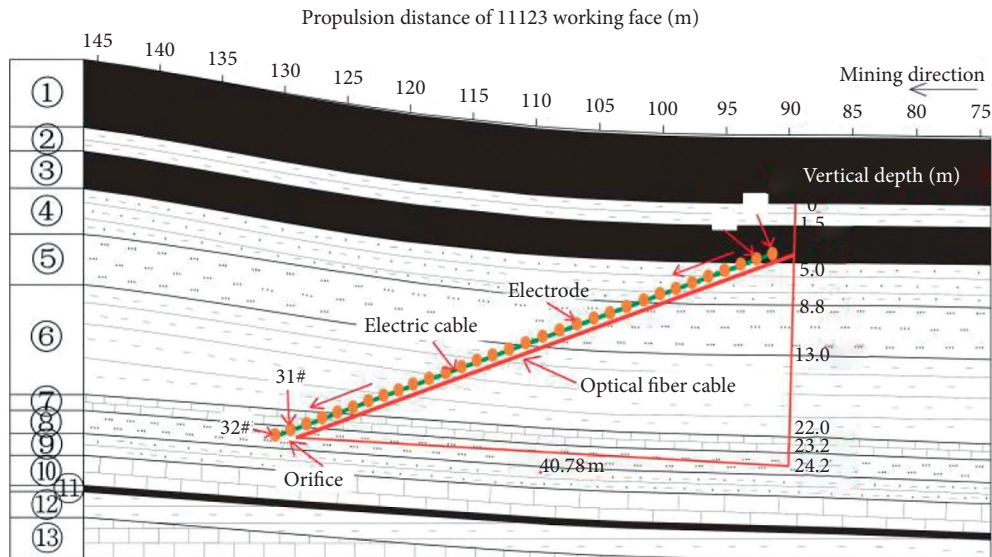
Figure 4: Schematic diagram of cable arrangement for the integrated monitoring system.

Table 2: Technical parameters of the integrated monitoring system.

Distributed optical fiber monitoring system		Self-potential monitoring system	
Diameter of fiber optic cable (mm)	5	Number of electrodes	32
Strain coefficient (MHz/%)	499.8	Electrode space (m)	1.5
Maximum break force (N)	2350	Effective length (m)	46.2
Strain fiber optic cable type	High-strength metal-based fiber optic cable	Control vertical height (m)	18.79
Effective length (m)	46.2	—	—
Control vertical height (m)	18.79	—	—

Electrode #32, which should be placed outside the monitoring orifice, was also fixed inside the orifice.

TABLE 3: Working face propulsion data record table.

Date of collection	Working face mining length (m)	Distance between mining location and orifice (m)
2018-10-31	0	129.18
11–12	18.9	110.28
11–21	38.3	90.88
12–02	54.9	74.28
12–12	78.7	50.48
12–22	94.3	34.88
2019-1-02	110.4	18.78
1–12	122.1	7.08
1–21	140.9	−11.72
1–29	153.8	−24.62
2–18	163.6	−34.42
2–25	178.1	−48.92
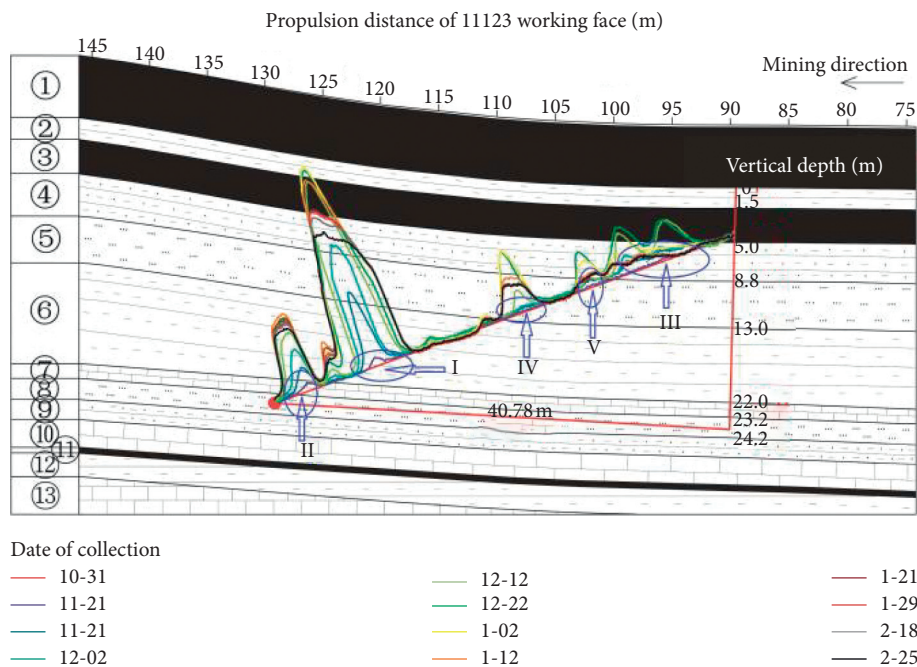
FIGURE 5: Corresponding relationship between strain distribution of the optical fibers and the stratum.
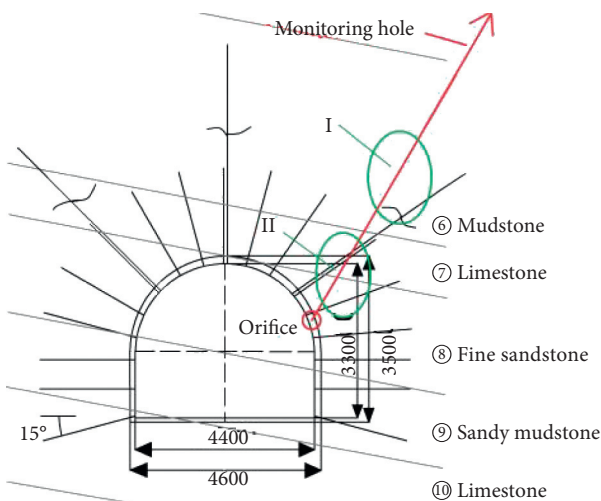
FIGURE 6: Sectional view of the corresponding relationship between the supporting structure of floor gas drainage roadway and the stratum.

stabilized at $+5923\,\mu\varepsilon$. In this process, the internal strain in the rock layer controlled by the anchor rod changed little and remained at $+2844\,\mu\varepsilon$. During this period, the stress in the rock mass under the influence of mining continued to adjust dynamically and finally formed a new stress equilibrium state.

Next, we analyzed the process of deformation and failure during the entire monitoring period through the fiber optic strain nephogram (Figure 7). From this, it can be seen that the strain value of area I (the vertical depth was 19.5–20.5 m) was larger than that of the other vertical depth positions. From an analysis of Figures 5 and 6, area 1 was found to be located in the ⑥ mudstone layer. Due to the low elastic modulus of mudstone, which was not in the actual control range of the anchor bolts, this position was controlled only by part of the anchor cable. Therefore, the rock mass in this area was affected not only by the mining of the working face but also by the surrounding rock support of the roadway, which first caused the stress to change in this area and then
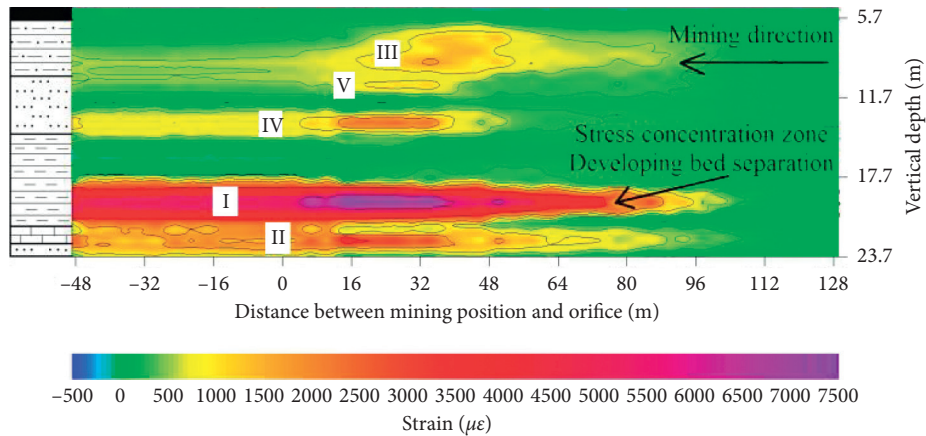
FIGURE 7: Fiber optic strain distribution nephogram during the monitoring period.

formed an area of concentrated stress. When the stress in the mudstone exceeded its bearing strength, the deformation and failure of the rock mass in this area could not be controlled and restrained effectively by the anchor cable. Finally, it ruptured, producing stratified cracks. In area II, however, which was also affected by many other factors, due to effective control by the anchor bolts, even though the internal strain in the surrounding rock that had a high elastic modulus changed substantially, it still did not cause structural failure of the rock mass, and the surrounding rock structure of the roadway as a whole remained relatively stable [36, 37]. Areas III, V, and IV were only affected by mining, and so, the strain amplitude of the rock mass was relatively small.

4.2.2. Self-Potential Monitoring. Comparative analysis of Figures 8(a) and 8(b) shows that the self-potential varied considerably, both within and outside the range over which damage occurred. The current through each electrode in the destruction zone decreased slowly as mining of the working face continued during the monitoring period. When the propulsion distance of the working face exceeded 58.9 m, the self-potential rose briefly and then dropped sharply, indicating that microcracks had sprouted in the rock mass. This was followed by a large fluctuation in the continuous steep rise and drop, with a maximum fluctuation of 600 mA (Figure 8(a)). When the rock mass was in a state of continuous damage, the development, penetration, and rupture of the microcracks alternated and coexisted and the self-potential signal generally decreased and fluctuated in a pulse-like manner. Until the working surface advanced by a distance of approximately 163.6 m, that is, until it exceeded the orifice of 34.42 m, the whole structure was in a stable state. In this process, the overall trend of each electrode was clear and highly consistent. From Figure 8(b), it can be seen that there was no obvious fluctuation due to the absence of severe deformation and damage in the internal structure of the rock mass, and the data in this range were less consistent than the data shown in Figure 8(a). The above results are also consistent with the findings of researchers such as Liu et al.

[38] and Hao et al. [39]. These authors believed that the amplitude of the self-potential field anomaly caused by the crack tip discharge during rock rupture was much larger than that caused by rock deformation. Judging from the self-potential measured by the electrodes at different depths in the borehole, the damage to the bottom plate was 0–20.7 m (electrodes #1–26 were inside the destruction zone). The self-potential data were basically consistent with the depth of damage data, as measured by the fiber optics.

To further verify the above analysis, the electrode current data obtained during monitoring were processed into a cloud map (Figure 9). From this map, it can be seen that as mining neared the monitoring hole, the electrode current at the bottom plate at a depth of 0–20.5 m decreased overall, indicating that the rock mass in this range was deformed due to the difference in rock lithology. Therefore, there were differences in how much the electrode currents decreased in the various rock formations, and stratification was obvious. By comparison with Figure 7, it can be seen that the electrode currents in areas I, III, IV, and V begin to decrease, and the corresponding fiber optic strain values begin to increase, which indicates that the rock mass in this area was damaged by stress and cracks; the strain value increased after the fiber optic was pulled, and the electrode current decreased because of the poor contact between the electrode and the rock mass. With the mining of the working face exceeding the orifice, the vertical depth of the floor was 0–20.5 m in the failure area, the electrode current increased, and the corresponding strain decreased due to the collapse of the overlying rock mass and the compression of the floor crack. In the process of mining, the electrode current in area I showed the largest decrease and the most obvious change in the value of strain, which was caused by the concentration of stress and the formation of separated layer cracks. Compared with the electrode current data gathered during the entire monitoring period, the electrode current in the upper part of the floor gas drainage roadway was increasing (area II). Although there was a certain amount of stress in the surrounding rock of the bottom extraction roadway, due to the anchoring effect of the anchor bolts, a
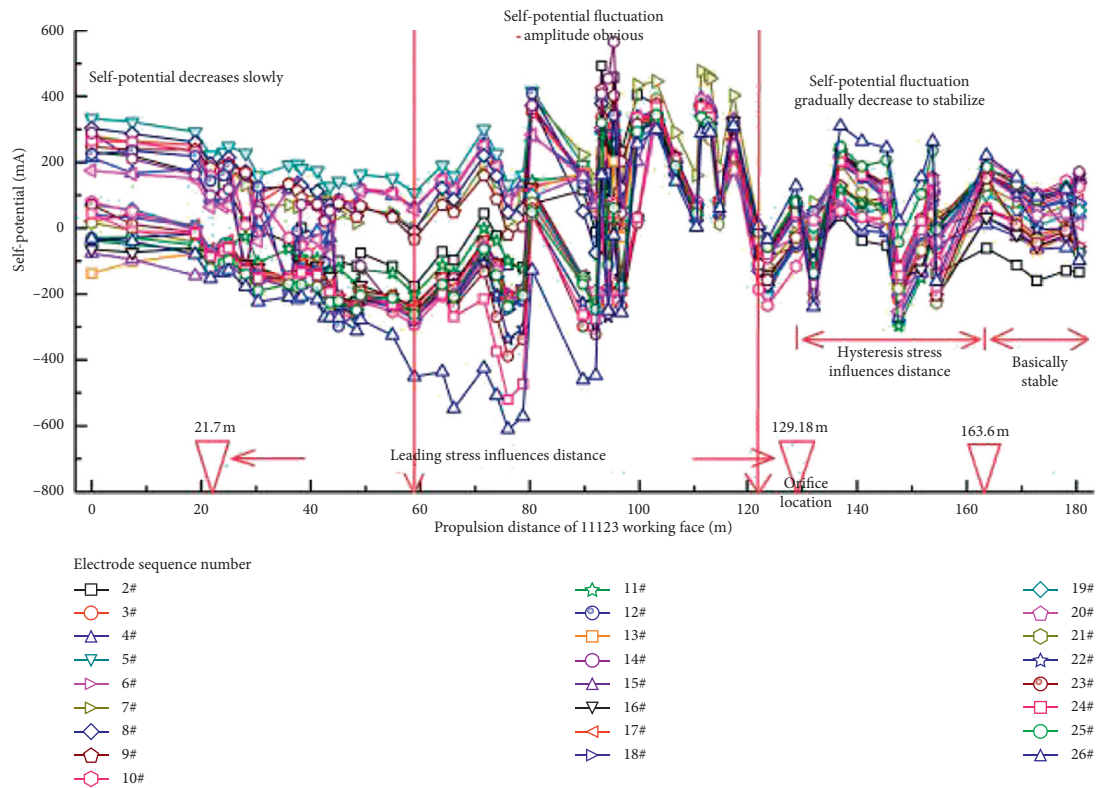
(a)
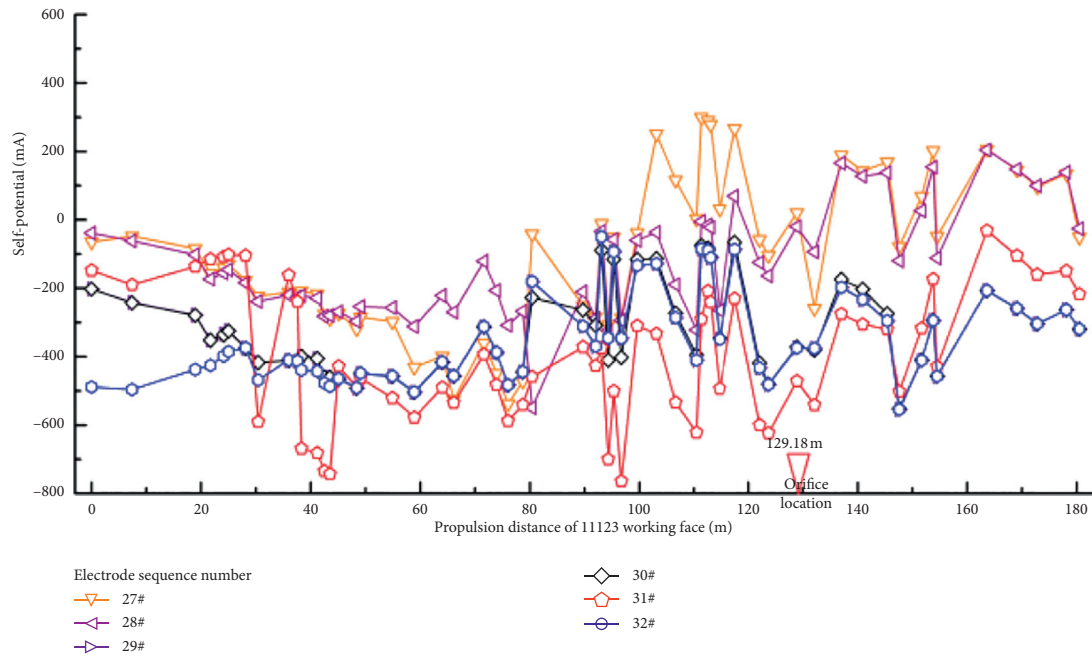
(b)

FIGURE 8: Self-potential curves at different depths.

composite rock beam with enhanced damage resistance and bearing capacity was formed, which was pulled on by the deep anchoring end of the surrounding rock of the roadway [40, 41]. By limiting its degree of deformation and failure, the electrode current and strain in that region increased at the same time.

According to the monitoring data and the actual observations of field personnel, there were no fracture and collapse of the surrounding rock of the floor gas drainage roadway under the strong supports, and the entire floor gas drainage roadway remained relatively stable under dynamic pressure.
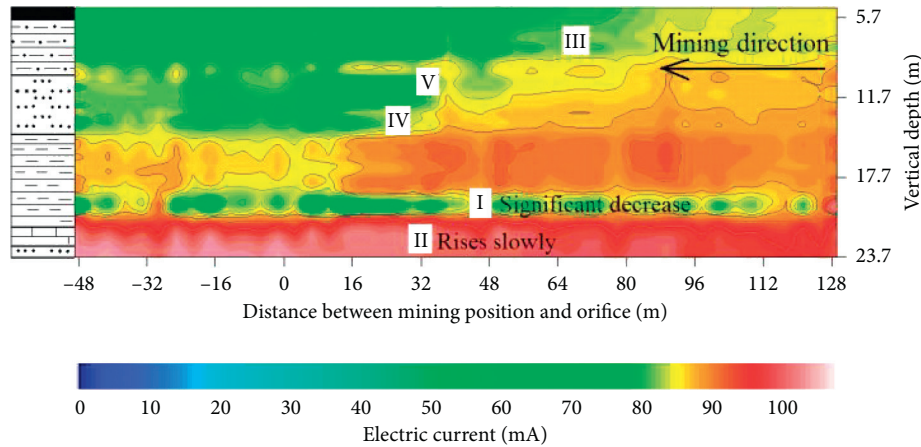
FIGURE 9: Nephogram of the changes in electrode current during monitoring.

4.2.3. Range of Effects of "Leading" and "Lagging" Stresses of the Working Face. Measurement points were selected at the fiber optic positions corresponding to the electrode positions on the cable in order to extract and process the data, which were combined with the natural potential and strain data in order to analyze the range of effects of the "leading" and "lagging" stresses of the working face (Figures 8 and 10).

By using natural potential exploration technology and BOTDR-distributed fiber optic testing technology, we were able to accurately measure and verify the deformation and failure characteristics as well as the evolution trend of the floor rock mass during the mining process of the 11123 working face. Our analysis shows that the mining distance of the 11123 working face of 21.7 m did no effect on the rock strata in the monitoring section. Until the mining distance was more than 21.7 m, the leading stress did not affect the surrounding rock mass of the floor gas drainage roadway in the monitoring area and gradually formed the area of concentrated stress. The distance of the mining working face was within 58.9 m, and there was no obvious fracture in or other damage to the rock floor. When the propulsion distance exceeded 58.9 m, the self-potential of the rock mass in the failure zone of the floor plate had a cyclical fluctuating pattern of a steep rise followed by a steep drop, while the strain value increased rapidly at the same time. During this process, the floor rock mass produced cracks and rapidly developed into the deep. Until the mining face exceeded the orifice, the overlying rock mass collapsed to fill the goaf and transferred the stress to the floor rock mass, causing the expansion crack generated by the original tension to gradually shrink. When the working face mining distance exceeded 163.6 m, the fluctuations in the self-potential and the strain data tended to be stable, indicating that the crack in the rock mass in the monitoring section shrank to reach its final degree of stability during this process.

According to this comprehensive analysis, we consider that the effect of the lead stress on the 11123 working face was 107.48 m, and the range of effect of the lagging stress was 34.42 m.

4.3. Variation in Multiparameter Data at Different Measurement Point Depths. By analyzing the strain, self-potential, and electrode current data, the failure of the floor under the influence of dynamic pressure and the stability of the surrounding rock mass of the floor gas drainage roadway are discussed. The floor failure depth of the 11123 working face was 0–20.7 m (electrodes #1–26 were located in it), and the surrounding rock structure of the floor gas drainage roadway was relatively stable (electrodes #27–32 were located in it). Further analysis of the variation in and relationship of the multiparameter data at different depths under the influence of dynamic pressure reveals the differences in dynamic evolution and the mechanism of changes in the rock mass of the destruction zone and the floor gas drainage roadway during the mining process. We selected six groups of data from different measurement point depths for analysis (Figure 11).

The changes in data at each measurement point located within the damage range of the floor (Figures 11(a)–11(d)) were observed. In the early stage of coal mining, the values of the self-potential data obtained at each measurement point gradually decreased by approximately 250 mV. The overall decrease in amplitude of the electrode current was not obvious and was approximately 3 mA only. However, the strain at each measuring point increased, but the range of values was different because of the different rock lithologies.

When the mining distance of the working face exceeded 58.9 m, the data collected from different measurement point depths changed gradually and by a significant amount. The self-potential fluctuated considerably, with a maximum amplitude of 400 mV, and then the fluctuation weakened before it finally stabilized. The electrode current, in contrast, showed a rapid decrease. This process continued until the working surface mining distance reached 118 m, and the electrode current value dropped by 18 mA. By this stage, the mining position had crossed the measuring point by approximately 26 m. Subsequently, the current value climbed quickly to 73 mA until the late monitoring period, while the current value slowly decreased and eventually stabilized at 68 mA. The strain value rose rapidly and then slowly decreased (Figure 11(a)).
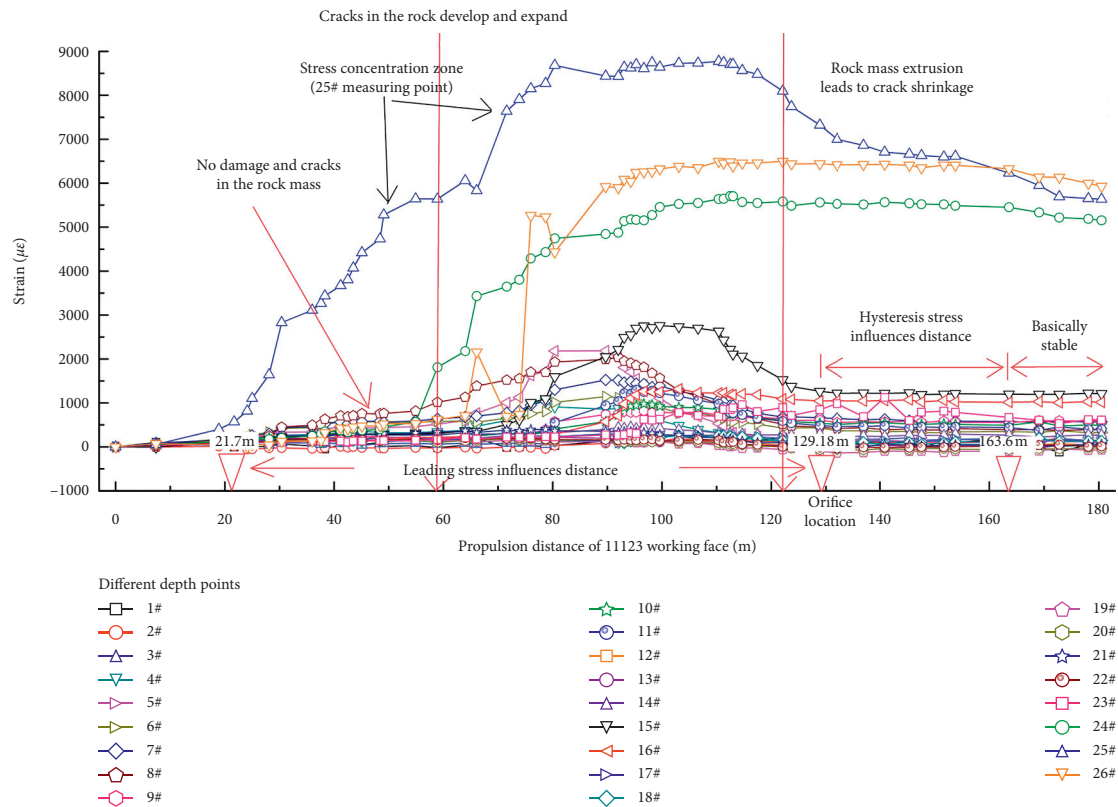
(a)
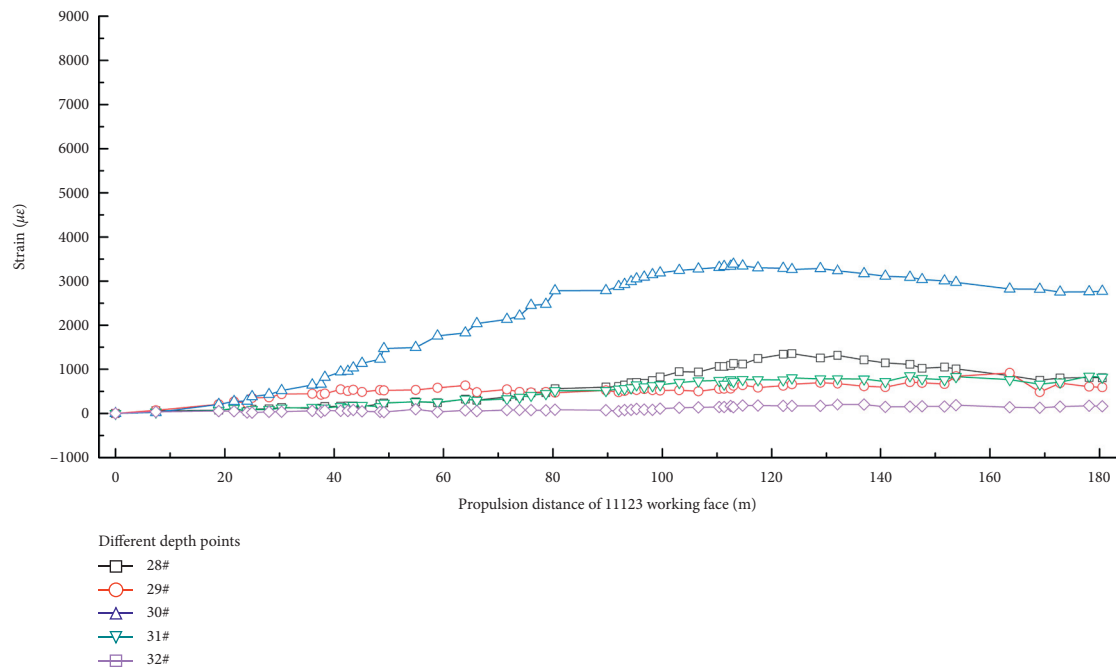
(b)

FIGURE 10: Variation of strain with advancing distance.

The values obtained for the measurement points at depths of 9.18 and 13.45 m were similar. Affected by mining, the self-potential in the rock also showed large fluctuations, and the maximum fluctuation was approximately 550 mV.

The decrease in electrode current in this depth range was small, at approximately 10 mA. Subsequently, there was only a small increase before a steady state was reached. The strain value rose rapidly and then fell (Figures 11(b) and 11(c)).
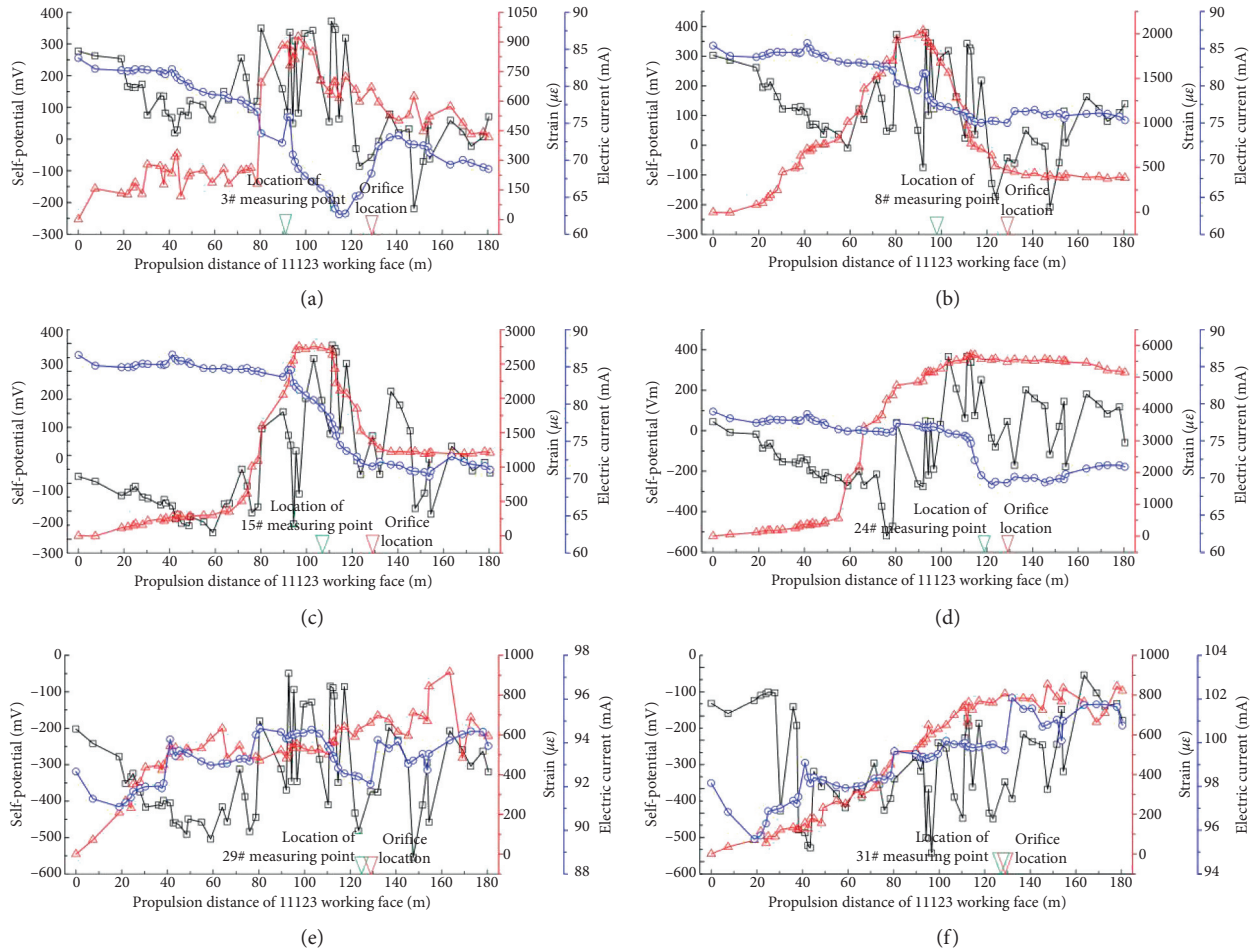
FIGURE 11: Multiparameter variation in the data obtained at different measuring point depths: (a) 6.13 m; (b) 9.18 m; (c) 13.45 m; (d) 18.94 m; (e) 22.6 m; (f) 23.21 m.

The #24 measurement point was located in the stress concentration area under the base plate, and the maximum value was 5800 $\mu\varepsilon$. The strain value decreased only slightly and finally stabilized at 5100 $\mu\varepsilon$ (Figure 11(d)). The change in amplitude of the same parameter at different measurement point depths was different, which was affected mainly by the differences in the rock lithology and the depth from the floor.

Under the influence of dynamic pressure, the deformation and failure of the rock mass in the range of floor failure were violent and obvious, and the dynamic changes in the self-potential, electrode current, and strain value were captured effectively at each measurement point depth. It should be noted that there were significant differences between the electrode currents obtained at the #3 measuring points close to the bottom plate and those obtained at the other positions. It is believed that the cracks in the rock mass were still developing and penetrating as the mining position exceeded the upper part of the measuring point. During this period, the compressive stress induced by the collapse of the overlying rock mass was not transmitted to the bottom slate layer, so that the electrode current was significantly reduced. When the mining distance of the working face exceeded

118 m, the electrode current stopped falling and then rose rapidly. This phenomenon shows that the stress in the overlying rock mass could be transferred effectively to the bottom plate when this happened, and this process took eight days to complete. From this, we infer that, after mining, there is a process of secondary failure and deepening in the floor rock mass. After a period of time, the downward stress of the overlying collapsed rock mass can be completely transferred to the floor, making the cracks in the shallow rock mass of the floor squeeze or close until the floor is finally stable, and this process can last for eight days or potentially longer. Therefore, attention should not only be paid to the deformation and failure of the floor rock mass in front of the mining but the failure of the floor rock mass behind the mining should also continue to be monitored.

Finally, we observed the changes in the parameters captured at two measuring points near the surrounding rock mass of the floor gas drainage roadway and then analyzed and determined the stability of the surrounding rock mass (Figures 11(e) and 11(f)). In contrast to the above four data plots, there were significant differences in the data presented in Figures 11(e) and 11(f). It is clear that the electrode currents obtained from these two measuring points do not

show a slow decrease, then a significant decrease, followed by an increase. In contrast, the electrode current shows a step-by-step rising phenomenon. It should be noted that each increase in electrode current is followed by a small decrease. We believe this to be a dynamic self-adjustment process of concentration and release of the stress in the surrounding rock under the joint action of working face mining and the roadway support structure. The existence of this process is an important indicator of the stability of the surrounding rock structure of the floor gas drainage roadway. In addition, the strain value during the entire monitoring period showed a slow rising trend, which finally stabilized, and this process was basically controlled within $1000\,\mu\varepsilon$. Combined with the natural potential data, it can be shown that the whole process fluctuated continuously within a certain range, which was different from the changes in the previous four measurement points.

5. Discussions

Based on the method using comprehensive monitoring of BOTDR-distributed fiber optics and spontaneous potential exploration, the floor failure characteristics and bottom extraction roadway stability of the 11123 working face of a coal mine in Huainan, Anhui Province, China were studied. The variations in the multiparameter data obtained at different depth measurement points were analyzed.

In summary, we find that the changes in the various parameters of rock formation under the influence of dynamic pressure are obvious and can reflect the deformation and failure process of the rock mass at different depths of the bottom plate. There are still some differences between the different depth measurement points in the failure range due to the different lithologies of the rock strata and their location relative to the floor. In the wake of coal mining, there is a process of secondary failure and deepening of the floor rock mass in the goaf. After a period of time, the downward stress of the overlying collapsed rock mass can be fully transmitted to the floor, making the cracks in the shallow rock mass of the floor squeeze or close until the floor is finally stable, and this process lasts approximately for eight days. The electrode current in the surrounding rock of the floor gas drainage roadway showed a step-by-step rising phenomenon. It should be noted that each increase in electrode current was followed by a small decrease. We believe that this is a dynamic self-adjustment process of the concentration and release of the stress in the surrounding rock under the joint action of working face mining and the roadway support structure. The existence of this process is an important indicator of the stability of the surrounding rock structure of the floor gas drainage roadway.

Under the influence of dynamic pressure, the rock mass will be deformed or even damaged macroscopically. Before the macroscopic change, the microcosmic complex dynamic process of physical and chemical fields will be formed in the rock mass. It is difficult to effectively capture the information in this stage by conventional testing methods (pressure gauge, displacement gauge, borehole TV, etc.) [5, 42]. The comprehensive monitoring technology adopted in this study can capture the change information of physical and chemical fields of rock mass at macro- and microlevels [8, 12, 29, 30, 34, 38]. Coal mining changes the original stress field distribution in the rock body:

(1) In the stage of rock elastic deformation, the change of stress field in rock mass is not obvious, but the distributed strain sensing optical fiber can capture the strain change greater than $25\,\mu\varepsilon$ and can reflect the compression or tension stress of rock mass [12, 30, 31]. In addition, there are a large number of primary microcracks in the deep rock mass under the natural state. The increase and decrease of the stress change rate in the rock mass will cause the change of the distance between the microcharges and then cause the change of the density of the polarization charge in the rock mass, forming the polarization current, resulting in the movement of the free charge and the change of the natural potential [34, 35, 38].

(2) With the increase of mining stress field, the rock mass will have obvious deformation, the rock porosity will also change, and the primary or secondary microcracks will increase and expand. The distributed strain sensing optical fiber and spontaneous potential exploration can capture the macroscopic and microscopic structural change characteristics of rock mass in the whole process of stress [12, 30, 38]. Once the load of rock mass exceeds its bearing limit, microcracks will connect with each other and produce macro cracks, that is, rock mass fracture and instability. In this process, a large number of free electrons leave the fracture area of rock mass instantaneously, resulting in electrical property mutation. When the rock mass is in a continuous damage state, the spontaneous potential will form a pulse-like fluctuation. During this period, the deformation and failure state of the rock mass can also be captured by distributed strain sensing optical fiber [35, 38, 39]. In addition, if there is fracture water flow in the rock mass, the distribution range and flow situation of the water body can be mastered by means of electrical prospecting technology such as spontaneous potential [43].

The multifield monitoring method has the following advantages compared with the conventional testing methods: (1) the conventional test methods usually use a single-test method, usually from the macromeasurement of the movement and deformation of rock mass, the development and fracture of rock mass, etc. Our research can capture the response characteristics and change rules of multifield data caused by deformation and damage of rock mass in the process of mining from macro- and microperspectives. Also, different sensors have their own advantages. The results obtained by comparative analysis of various data are more reliable. (2) The conventional test methods are mostly point acquisition, with less measurement data and shorter sensor survival time, so it is difficult to continuously obtain the data after the working face mining exceeds the measurement point. In this study, the sensor has

the advantages of strong anti-interference, high survivability, more data points, and large amount of data. It can completely capture the multifield data information of rock mass damage change in each stage of mining.

In this study, multiphysical field monitoring technology is applied to monitor the stability of roadway surrounding rock. In addition, this set of multifield monitoring system can also be applied to the monitoring of roof and floor rock deformation failure, protection of coal pillar stability, and other related monitoring.

6. Conclusions

(1) The extent of damage to the working face was concentrated mainly in the upper mudstone layer of the top anchor of the floor gas drainage roadway, and the depth of damage was approximately 20.7 m. The overall stability of the surrounding rock mass structure of the floor gas drainage roadway was good.

(2) The influence of mining pressure on the bottom plate had the characteristics of "advance" and "lag" continuation over long distances. Of these, the range of effect of the leading support stress of the 11123 working face was 107.48 m and that of the lagging stress was 34.42 m.

(3) Under the influence of dynamic pressure, the evolution of floor cracks showed spatiotemporal characteristics. In the wake of coal mining, there is a process of secondary failure and deepening of the floor rock mass in the goaf. After a period of time, the downward stress of the overlying collapsed rock mass can be fully transmitted to the floor, making the cracks in the shallow rock mass of the floor squeeze or close until the floor is finally stable, and this process lasts approximately for eight days.

(4) By installing a fiber optic cable and an electric cable monitoring system in the monitoring hole, the process of damage to the bottom plate was completely captured. A comprehensive technical evaluation system with multiple physical fields and parameters was designed and implemented. The results of this study can provide guidance for devising suitable procedures, for carrying out intelligent green safety mining, and for warning about the hazards of roadway damage.

The limitations of this study and the future direction of this work are as follows: (1) only one monitoring hole is designed on-site, and the data obtained can only objectively reflect the actual situation of the area. Therefore, in the later research work, it is necessary to design multiple monitoring boreholes in different directions in the surrounding rock of roadway, so as to obtain comprehensive and multiangle deformation and failure of surrounding rock; (2) in the study, the monitoring method of multiple physical fields is used to obtain a large number of reliable data, but it still needs to be compared with some traditional verification methods. In the later research, we need to further strengthen

the relevant verification and comparison work; and (3) at present, the field monitoring work generally relies on the underground data collection of researchers, and the degree of intelligent collection is not high. In the future, the underground sensor monitoring system needs to be connected to the ground remote automatic monitoring and early warning platform through 5G network technology to realize unmanned, automatic, intelligent and integrated data acquisition, processing and analysis, forecasting, and early warning.

Data Availability

The data used to support the findings of this study are available from the corresponding author upon request.

Conflicts of Interest

The authors declare that there are no conflicts of interest regarding the publication of this paper.

Acknowledgments

References

[1] L. Yuan, "Scientific problem and countermeasure for precision mining of coal and associated resources," *Journal of China Coal Society*, vol. 44, no. 1, pp. 1–9, 2019.

[2] Y. G. Li, N. J. Ma, J. Ma, H. Zhang, and Z. Gao, "Surrounding rock's failure characteristic and rational location of floor gas drainage roadway above deep confined water," *Journal of China Coal Society*, vol. 43, no. 9, pp. 2491–2500, 2018.

[3] S. Mo, P. Sheffield, and P. Corbett, "A numerical investigation into floor buckling mechanisms in underground coal mine roadways," *Tunnelling and Underground Space Technology*, vol. 103, Article ID 103497, 2020.

[4] J. B. Wei, S. M. Wang, Z. Zhao, D. L. Li, and L. P. Guo, "Numerical study of damage to rock surrounding an underground coal roadway excavation," *Advances in Civil Engineering*, vol. 2020, Article ID 8863289, 16 pages, 2020.

[5] Y. Yuan, W. J. Wang, S. Q. Li, and Y. J. Zhu, "Failure mechanism for surrounding rock of deep circular roadway in coal mine based on mining-induced plastic zone," *Advances in Civil Engineering*, vol. 2018, Article ID 1835381, 14 pages, 2018.

[6] L. Q. Shi and J. Han, "Theory and practice of dividing coal mining area floor into four-zone," *Journal of China University of Mining and Technology*, vol. 34, no. 1, pp. 17–23, 2005.

[7] M. G. Qian, X. X. Miao, and L. J. Li, "MeChalism for the fracture behaviours of main floor in longwall mining," *Chinese Jounral of Goetechnical Engineering*, vol. 17, no. 6, pp. 55–62, 1995.

[8] Y. Ou, P. Zhang, and W. Wang, "Study on the evolution rule of land damage based on electrical resistivity imaging

technology in mining face," *Geotechnical and Geological Engineering*, vol. 37, no. 5, pp. 4259–4268, 2019.

[9] M. C. He, H. P. Xie, S. P. Peng, and Y. D. Jiang, "Study on rock mechanics in deep mining engineering," *Chinese Journal of Rock Mechanics and Engineering*, vol. 24, no. 16, pp. 2803–2813, 2005.

[10] Q. Wu, B. Li, S. Q. Liu, and Y. F. Zeng, "Vulnerability assessment of coal floor groundwater bursting based on zoning variable weight model: a case study in the typical mining region of Kailuan," *Journal of China Coal Society*, vol. 38, no. 9, pp. 1516–1521, 2013.

[11] P. L. Su and Z. F. Wei, "Depth of floor failure of stope with medium-thickness coal seam," *Geotechnical and Geological Engineering*, vol. 36, no. 2, pp. 1341–1347, 2018.

[12] P. Zhang, Y. Ou, B. Sun, and C. Liu, "A case study of floor failure characteristics under fully mechanised caving mining conditions in extra-thick coal seams," *Journal of Geophysics and Engineering*, vol. 17, no. 5, pp. 813–826, 2020.

[13] W. C. Song, Z. Z. Liang, and C. B. Zhao, "Mechanical failure characteristics of mining floor along working face inclination above confined water," *Chinese Journal of Rock Mechanics and Engineering*, vol. 37, no. 9, pp. 144–156, 2018.

[14] P. S. Zhang, J. W. Wu, and S. D. Liu, "Study on dynamic observation of coal seam floor failure law," *Chinese Journal of Rock Mechanics and Engineering*, vol. 25, no. s1, pp. 3009–3013, 2006.

[15] R. Zhang, Z. Q. Jiang, Z. C. Yue, L. T. Zhao, and X. L. Yu, "In-Situ dynamic observation and numerical analysis of thick coal seam floor's failure law under the mining," *Journal of Mining & Safety Engineering*, vol. 29, no. 5, pp. 625–630, 2012.

[16] S. Y. Zhu, D. T. Cao, H. Y. Zhou, C. W. Yang, and J. G. Liu, "Restrictive function of lithology and its composite structure on deformation and failure depth of mining coal seam floor," *Journal of Mining & Safety Engineering*, vol. 31, no. 1, pp. 90–96, 2014.

[17] H. P. Kang, G. F. Wang, P. F. Jiang et al., "Conception for strata control and intelligent mining technology in deep coal mines with depth more than 1000 m," *Journal of China Coal Society*, vol. 43, no. 7, pp. 1789–1800, 2018.

[18] X. Y. Wu, J. Y. Wang, W. C. Wang, C. Tian, Q. W. Bu, and L. Wu, "Study on the stage failure mechanism and stability control of surrounding rock of repeated mining roadway," *Advances in Civil Engineering*, vol. 2020, Article ID 8866559, 16 pages, 2020.

[19] X. L. Zhang, H. A. Nguyen, X. N. Bui et al., "Evaluating and predicting the stability of roadways in tunnelling and underground space using artificial neural network-based particle swarm optimization," *Tunnelling and Underground Space Technology*, vol. 103, Article ID 103517, 2020.

[20] J. Wang, Z. Guo, Y. Yan, J. Pang, and S. Zhao, "Floor heave in the west wing track haulage roadway of the Tingnan coal mine: mechanism and control," *International Journal of Mining Science and Technology*, vol. 22, no. 3, pp. 295–299, 2012.

[21] M. G. Qian, P. W. Shi, and J. L. Xu, *Mine Pressure and Rock Formation Control*, China University of Mining and Technology Press, Xuzhou, China, 2010.

[22] C. J. Hou, "Effective approach for surrounding rock control in deep roadway," *Journal of China University of Mining & Technology*, vol. 46, no. 3, pp. 467–473, 2017.

[23] H. Yavuz, "An estimation method for cover pressure re-establishment distance and pressure distribution in the goaf of longwall coal mines," *International Journal of Rock Mechanics and Mining Sciences*, vol. 41, no. 2, pp. 193–205, 2004.

[24] B. Duan, H. Xia, and X. Yang, "Impacts of bench blasting vibration on the stability of the surrounding rock masses of roadways," *Tunnelling and Underground Space Technology*, vol. 71, pp. 605–622, 2018.

[25] G. C. Li, Z. Q. Ma, N. Zhang, P. P. Wang, and R. Ma, "Research on failure characteristics and control measures of roadways affected by multiple overhead mining in Huaibei mining area," *Journal of Mining & Safety Engineering*, vol. 30, no. 2, pp. 181–187, 2013.

[26] D. H. Chen, X. Z. Hua, Y. W. Duan, and S. X. Cheng, "Simulation of zonal tensile and compressive deformation and failure of surrounding rock in deep large deformation mining gateway," *Rock and Soil Mechanics*, vol. 37, no. 9, pp. 2654–2662, 2016.

[27] X. Z. Hua and P. Yang, "Floor deformation dynamic evolution of gobside entry retaining with large section in deep mine," *Journal of China University of Mining & Technology*, vol. 47, no. 3, pp. 39–46, 2018.

[28] S. C. Li, L. Wang, B. Jiang, Q. Wang, H. J. Zhang, and B. H. Liu, "Microseismic characteristic and failure mechanism of roadway below coal pillar under dynamic pressure," *Journal of China University of Mining & Technology*, vol. 48, no. 2, pp. 247–257, 2019.

[29] D. Zhang, P. S. Zhang, B. Shi, H. X. Wang, and C. S. Li, "Monitoring and analysis of overburden deformation and failure using distributed fiber optic sensing," *Chinese Journal of Geotechnical Engineering*, vol. 37, no. 5, pp. 952–957, 2015.

[30] S. A. Xu, S. M. Wang, P. S. Zhang, D. X. Yang, and B. Y. Sun, "Study on strain characterization and failure location of rock fracture process using distributed optical fiber under uniaxial compression," *Sensors*, vol. 20, no. 14, p. 3853, 2020.

[31] J. Chai, Z. W. Xue, R. Guo, D. D. Zhang, Q. Yuan, and Y. Li, "Experimental study of overlying mine strata collapse and its evolution by a distributed optical fiber system," *Journal of China University of Mining & Technology*, vol. 47, no. 6, pp. 32–39, 2018.

[32] P. S. Zhang and S. A. Xu, "Development and application of mine fiber testing technology," *Progress in Geophysics*, vol. 31, no. 3, pp. 1381–1389, 2016.

[33] S. D. Liu and P. S. Zhang, "Distributed parallel intelligent electrode potential difference signal acquisition method and system," Chinese Invention Patent: ZL200410014020.0, 2005.

[34] E. Y. Wang, Z. H. Li, Z. T. Liu, Y. N. Li, and X. Y. Song, "Expermental study on surface potential effect of coal under load," *Chinese Journal of Geophysics*, vol. 52, no. 5, pp. 1318–1325, 2009.

[35] X. Y. Song, Z. H. Li, and E. Y. Wang, "Charging characteristics of the crack propagation of rock under load," *Journal of China Coal Society*, vol. 41, no. 8, pp. 1941–1945, 2016.

[36] H. P. Kang, J. Lin, and M. J. Fan, "Investigation on support pattern of a coal mine roadway within soft rocks—a case study," *International Journal of Coal Geology*, vol. 140, pp. 31–40, 2015.

[37] J. C. Chang, D. Li, T. F. Xie, W. B. Shi, and K. He, "Deformation and failure characteristics and control technology of roadway surrounding rock in deep coal mines," *Geofluids*, vol. 2020, Article ID 8834347, 15 pages, 2020.

[38] J. Liu, S. D. Liu, and Y. Cao, "Self-potential characteristics in deep rock mass damage based on point discharge mechanism," *Chinese Journal of Geophysics*, vol. 61, no. 1, pp. 323–330, 2018.

[39] J.-Q. Hao, L.-Q. Liu, H.-L. Long et al., "New result of the experiment on self-potential change of rocks under biaxial

compression," *Chinese Journal of Geophysics*, vol. 47, no. 3, pp. 539–547, 2004.

[40] P. H. S. W. Kulatilake, Q. Wu, Z. Yu, and F. Jiang, "Investigation of stability of a tunnel in a deep coal mine in China," *International Journal of Mining Science and Technology*, vol. 23, no. 4, pp. 579–589, 2013.

[41] Z. L. Su, W. B. Xie, S. G. Jing, X. K. Wang, and Q. T. Tang, "Fracturing of the soft rock surrounding a roadway subjected to mining at kouzidong coal mine," *Advances in Civil Engineering*, vol. 2020, Article ID 6858643, 17 pages, 2020.

[42] H. S. Jia, K. Pan, S. W. Liu, B. Peng, and K. Fan, "Evaluation of the mechanical instability of mining roadway overburden: research and applications," *Energies*, vol. 12, no. 22, p. 4265, 2019.

[43] S. D. Liu, J. Liu, J. Qi, Y. Cao, and R. Q. Lv, "Applied technologies and new advances of parallel electrical method in mining geophysics," *Journal of China Coal Society*, vol. 44, no. 8, pp. 2336–2345, 2019.

Research Article

Bayesian Estimation of Resistance Factor for Bored Piles Based on Load Test Database

Zhijun Xu [ID], Ranran Zhang, Liang Fan, Xing Han, Fang Yuan, and Mingfang Du

College of Civil Engineering, Henan University of Technology, Zhengzhou 450001, China

Correspondence should be addressed to Zhijun Xu; zj.xu_hust@qq.com

The quality of in situ data is key to calculating resistance factor of bored piles. However, it is difficult to summarize accuracy data due to various uncertainties in engineering. This paper employs the Bayesian method and mathematical statistics theory to put forward an estimation method for updating in situ data. A testing database (33 tests in noncohesive soils and 53 tests in cohesive soils) of bored piles is summarized. The model factor of bored piles is quantified as the ratio of the measured capacity to the calculated capacity. The proposed method is used to classify summarized data into three categories, which are "good data," "general data," and "bad data." The "bad data" are discarded because of bad contribution to calculation, and Bayesian theory is incorporated into updating the model factor statistics. Three methods are used to calculate the reliability index and resistance factor of bored piles, and the results show that the reliability index and resistance factor are sensitive to the quality of data. Finally, the available values of resistance factors are proposed based on resistance factor design for bridge design specification, which can offer references to revision relevant specifications. The proposed method can be used to update other geotechnical data.

1. Introduction

Bored piles, especially large-diameter piles, are commonly employed to support high-rise buildings and bridges in China and other countries because of their ability to sustain large load [1–5]. The safety of bored pile foundation is significantly important. Due to various uncertainties, the design parameters should have random variances. However, design parameters are described as constants by allowable stress design (ASD) philosophy, which is unreasonable and unscientific. To overcome the deficiencies, load resistance factor design (LRFD) method is mandated by American Association of State Highway and Transportation Officials [6]. Therefore, resistance factor calculation of bored piles is of engineering significance.

The resistance factor is calculated incorporating in reliability analysis methods based on pile load test data [7, 8]. Enough-accuracy in situ data are necessary to calculate resistance factor of bored piles. However, it is difficult to collect accuracy in situ data to calculate reliability index and resistance factor because of various uncertainties, for

example, parameter uncertainty, calculation model uncertainty, testing random error, and systematic error. A large number of investigations are carried out to calibrate resistance factor of driven piles [7–16], and significant achievements have been developed. However, few investigations about resistance factor of bored piles have been reported.

Parameter uncertainty and model uncertainty are two troubles for pile foundation designers. Numerous investigations are conducted to study parameter uncertainty, which shows that parameter uncertainty contains random error of monitor, system error, statistical uncertainty, and so on. Model uncertainty is mainly caused by simplified calculation model. European design specification of geotechnical engineering (EN997-1) clearly suggests that a model revised factor should be incorporated when the pile capacity is calculated using the simplification model [17]. However, this specification does not specify revised factor values and only suggests that different countries should adopt different values. Jones et al. [18], Kulhawy and Trutmann [19], Lacsse and Nadim [20], Meyerhof [21], and Phoon and Kulhawy

[22, 23] study model uncertainty based on lots of in situ data of pile capacity, which shows that enough-accuracy data are necessary to solve model uncertainty problem. However, it is difficult to get enough-accuracy data due to various uncertainties. In addition, the quality of collected data is not all perfect, and some of them are considered as "bad data" or "data outliers." It is necessary that data optimization is incorporated into calculating resistance factor of bored piles.

This paper puts forward a Bayesian estimation method to update the in situ data of bored piles, and three reliability index calculation methods are incorporated into calculating the reliability index of pile capacity using the processing data. Then American LRFD for Bridge Design Specification is used to estimate the resistance factor of bored piles.

2. Bayesian Optimization Method

Bayesian principle is a tool to update the probability distribution using new information. Assuming that the prior distribution of a random variable (X) is $f'_X(X)$, its posterior distribution can be written as [24]

$$f''_X(X) = K \cdot L(X) \cdot f'_X(X), \tag{1}$$

where $f''_X(X)$ is posterior distribution of X; K is a normalization constant; and $L(X)$ is likelihood function. Normal distribution and log-normal distribution are frequently employed to fit probability distribution of pile capacity [25].

Assume that n values of X are collected from engineering, which are described as $X = (X_1, X_2, \ldots, X_n)$. The mean (μ_p) and standard variance (σ_p) are

$$\mu_P = \frac{1}{n} \sum_{i=1}^{n} X_i,$$

$$\sigma_p = \sqrt{\frac{1}{n-1} \sum_{i=1}^{n} (x_i - \mu_x)^2}. \tag{2}$$

Assume that μ_K and σ_K are considered as the mean and standard variance of likelihood function. If X obeys normal distribution, the posterior mean (μ_U) and variance (σ_U) are

$$\mu_U = \frac{\mu_P \sigma_K + \mu_K \sigma_P^2}{\sigma_P^2 + \sigma_K^2}, \tag{3}$$

$$\sigma_U^2 = \frac{\sigma_P^2 \sigma_K^2}{\sigma_P^2 + \sigma_K^2}. \tag{4}$$

If X obeys log-normal distribution, it can be translated into normal random variable through dealing X with natural logarithm, which is described as $\ln X$. The mean $(\mu_{\ln X})$ and standard variance $(\sigma_{\ln X})$ of $\ln X$ are

$$\mu_{\ln X} = \exp\left(\mu_U + 0.5\sigma_U^2\right), \tag{5}$$

$$\sigma_{\ln X}^2 = \mu_{\ln X}\left[\exp\left(\sigma_U^2\right) - 1\right]. \tag{6}$$

The model factor is frequently represented as the ratio of the measured capacity to calculated capacity [1, 7, 8]:

$$\lambda = \frac{Q_m}{Q_p}, \tag{7}$$

where λ is model factor of pile capacity; Q_m is the measured pile capacity; and Q_p is the calculated pile capacity. Numerous investigations show that model factor is a random variable and obeys log-normal distribution [1, 2, 7, 10, 13, 14].

To improve accuracy of collected data from engineering, this paper employs the biased factor of λ, which is shown in the following equation [26]:

$$\zeta_i = \frac{|\lambda_i - \lambda_R|}{\lambda_R}, \quad 1 \le i \le n, \tag{8}$$

where λ_i is the ith model factor; ζ_i is ith biased factor of λ; and λ_R is the mean of λ.

Based on equation (8), the data are classified as follows [26]:

(1) If $\zeta_i < 0.25$, the data are defined as "good data" because it is near to the fact data.

(2) If $0.25 \le \zeta_i < 0.5$, the data are defined as "general data."

(3) If $\zeta_i \ge 0.5$, the data are defined as "bad data." "Bad data" are identified as extreme values, which should be discarded.

"Good data" are considered to be more reliable and should be treated as the prior information in estimation of the population statistics. However, the sample size of the "good data" is not sufficient to represent the total. This paper employs Bayesian updating technique to evaluate the probability characteristics of the resistance bias factor for bored piles. The "general data" are treated as prior information, and the "good data" are treated as likelihood information. Then, the updating model factor statistics can be obtained using equations (3)–(6).

3. Resistance Factor Estimation

This paper summarizes various bored pile capacity data shown in Tables 1 and 2 [1]. The data are divided into two groups, which are the data in noncohesive soil (D-NC) and the data in cohesive soil (D-C).

Dithinde et al. [1] use load-displacement curves (shown in Figure 1) to improve the quality of collected data. The characteristic of Case Numbers 25 curve is far away from other curves; it falsely needs to be discarded. In addition, Dithinde et al. [1] employ Box-Plots Method to detect that Case Number 24 and Case Number 26 are outliers. Therefore, Case Numbers 24, 25, and 26 should be discarded. Figure 2 shows the scatter diagram of the remaining data, which indicates that there are no data deviating markedly from other data. However, it does not mean that the remaining data are absolutely reliable. This paper will use the proposed method to update remaining data.

TABLE 1: Load testing data of pile capacity in noncohesive soil.

Case number	D_s (mm)	D_B (mm)	L (m)	s (mm)	Q_p (kN)	Q_m (kN)	a	b
1	430	430	8	0.42	1321	1375	0.06	0.99
2	600	750	9	0.76	3783	4600	0.74	0.94
3	750	600	11	1.2	2705	3000	0.40	0.97
4	360	350	7.8	35	1084	1050	7.98	0.61
5	400	400	9.5	5.6	1202	1357	1.40	0.89
6	400	400	9.5	10.1	1202	1380	1.45	0.92
7	400	400	8	6	1131	1050	0.80	0.92
8	400	400	9.5	5	1202	1225	1.97	0.84
9	400	400	3	11	1178	840	3.70	0.72
10	520	520	16.5	12.7	6754	5600	3.91	0.86
11	430	430	11.5	3.41	1287	1250	0.75	0.94
12	450	450	9	0.97	1145	1500	2.08	0.80
13	400	400	10	50	940	970	3.88	0.74
14	400	400	7	70	679	540	2.89	0.73
15	500	500	7.8	75	1226	600	10.93	0.46
16	500	500	10	77	1583	1175	5.29	0.59
17	400	400	11	41	605	800	5.92	0.72
18	400	400	9.2	57	472	480	7.87	0.58
19	500	500	9.5	60	793	625	8.13	0.44
20	500	500	11.8	62	1060	1025	10.46	0.51
21	500	500	12.3	60	916	1160	4.29	0.70
22	500	500	14.5	80	1132	1500	3.90	0.75
23	305	305	13	40.3	2028	2010	8.44	0.50
24	305	305	13	6.4	3051	6000	4.80	0.60
25	305	305	13	97	2028	1200	1.30	0.53
26	305	305	13	18.3	3051	4650	1.13	0.97
27	520	760	12.2	50	2563	1690	2.97	0.83
28	520	760	12.2	93	2478	1620	3.36	0.84
29	520	760	12	26.5	2111	1650	5.36	0.80
30	520	760	12	35	2451	2100	4.60	0.70
31	520	760	15	23.3	2974	2680	8.80	0.85
32	520	760	6	3.5	3644	3650	0.06	0.99
33	520	760	8	5	3739	5600	0.74	0.94

The classified results are shown in Tables 3 and 4. There are 21 and 38 pieces of data, of which bias factor is less than 0.25 in noncohesive soil and cohesive soil, respectively. The in situ uncertainties have little contribution to these data classified as "good data." There are 8 and 12 pieces of data, of which bias factor is larger than 0.25 but less than 0.50 in noncohesive soil and cohesive soil, respectively, considered as "general data." However, the bias factors of Case Number 15 in noncohesive soil and Cases Numbers 37, 68, and 69 in cohesive soil are 0.5187, 0.5271, 0.7315, and 0.5203, respectively. These data are classified as "bad data." These data can cause insecurity to engineering and should be discarded.

Log-normal distribution is used as the distribution of model factor, and the model factor statistics are presented in terms of the mean and coefficient of variation (COV). Based on equations (5) and (6), the updating model factors statistics are obtained in Table 5 for reliability analysis and

resistance factor calculation. The coefficient of variation of updating data is minimum. The coefficient of variation for " general data" is maximum. In summary, the updating model factors are reliable enough to calculate the reliability index and resistance factor of bored piles.

According to reliability theory, the limit state equation of bored pile capacity is [16]:

$$g\left(R, Q_D, Q_L\right) = R - Q_D - Q_L, \tag{9}$$

where R is vertical pile capacity (kN); Q_D is dead load (kN); and Q_L is live load (kN). Three methods are employed to calculate the reliability index.

3.1. First-Order Reliability Method.
If the three parameters in equation (9) obey log-normal distribution, the calculation formula of reliability index can be written as [6]

$$\beta = \frac{\ln\left(\left(\left(\lambda_R \text{FOS}\left(\left(Q_D/Q_L\right) + 1\right)\right)/\left(\lambda_{QD}\left(Q_D/Q_L\right) + \lambda_{QL}\right)\right)\sqrt{\left(\left(1 + \text{COV}_{QD}^2 + \text{COV}_{QL}^2\right)/\left(1 + \text{COV}_R^2\right)\right)}\right)}{\sqrt{\ln\left(1 + \text{COV}_R^2\right)\left(1 + \text{COV}_{Q_D}^2 + \text{COV}_{QL}^2\right)}}, \tag{10}$$

TABLE 2: Load testing data of pile capacity in cohesive soil.

Case number	D_s (mm)	D_B (mm)	L (m)	s (mm)	Q_p (kN)	Q_m (kN)	a	b
34	600	600	9	0.59	4807	4800	0.48	0.96
35	600	600	11.5	2.7	6447	4100	2.87	0.82
36	750	750	21.8	2.34	6521	7100	3.55	0.71
37	350	350	17.3	0.18	1398	760	0.05	0.99
38	610	610	6.5	21.19	2062	2300	3.40	0.80
39	600	600	6.5	13.5	3280	3100	4.96	0.84
40	600	800	24	12	2545	3360	12.43	0.64
41	610	610	9	22.9	3040	2650	5.30	0.72
42	610	610	7	1.65	2235	1800	1.08	0.90
43	750	750	13	37	4179	3700	3.05	0.80
44	450	450	9	1.79	3658	2930	1.76	0.88
45	350	350	5	1.7	1196	1700	2.55	0.76
46	500	500	6	1.7	2333	1900	2.85	0.76
47	600	600	6	85.3	707	520	2.65	0.62
48	450	450	6	20.3	1225	1175	0.82	0.94
49	300	300	6	14.1	975	1080	1.19	0.86
50	600	600	9.6	4.4	3223	3500	2.92	0.80
51	400	400	8.7	2.9	1221	1240	0.82	0.93
52	350	350	8.7	9	834	825	1.76	0.84
53	410	410	11	0.95	1444	1450	1.45	0.87
54	615	615	12	36	2375	3000	4.83	0.75
55	615	615	12	35	1948	2450	3.92	0.74
56	610	610	7	25.4	1184	1400	2.43	0.72
57	610	610	1.5	17.8	462	510	1.00	0.93
58	500	500	7.8	5.58	2392	3600	2.67	0.84
59	430	430	6.5	4.49	907	1150	3.36	0.74
60	450	600	15.5	4.19	1818	2310	2.98	0.82
61	750	750	10.2	1.89	5869	8500	3.94	0.79
62	450	450	8	45.53	1292	1230	8.40	0.50
63	450	450	8	22.7	1292	1820	1.66	0.85
64	450	450	8	3.93	2110	2580	1.52	0.89
65	450	450	8	4.83	2110	2670	2.14	0.86
66	450	450	8	4.0	2110	2790	2.39	0.84
67	450	450	8	3.35	2110	2900	2.20	0.85
68	450	450	8	2.85	2110	4200	3.86	0.76
69	450	450	8	3.2	1602	2800	1.74	0.87
70	450	750	4.5	2.96	8906	9600	4.22	0.76
71	430	430	7	1.19	1156	1660	1.67	0.86
72	550	550	6	6.57	2916	4800	1.46	0.90
73	910	910	12	1.3	5088	7050	1.07	0.92
74	910	910	9	1.8	5088	5900	0.99	0.93
75	910	910	9	1.16	7648	9700	4.58	0.72
76	910	910	9	0.68	4721	7000	1.78	0.86
77	530	430	8	3.38	1955	1880	3.63	0.75
78	600	600	14.9	2.13	4230	5430	3.48	0.79
79	600	600	14.6	3.26	4196	3000	1.31	0.92
80	750	750	15.4	2.35	6153	6250	1.93	0.89
81	600	600	14.7	1.74	4207	4450	1.95	0.87
82	750	750	15.7	1.95	10172	13000	5.37	0.75
83	500	500	7.2	2.2	3294	3300	1.64	0.87
84	750	750	7.2	1.6	6266	4810	0.88	0.93
85	500	500	7.2	9.5	1901	2200	2.79	0.81
86	750	750	7.2	7.2	3515	5300	4.03	0.77

Note. D_s is the pile shaft diameter; D_B is the pile bottom diameter; L is the pile length; s is the final settlement of load tests; a and b are two hyperbolic curve-fitting parameters.

where FOS is the factor of safety according to allowable stress design method; λ_{QD} and λ_{QL} are the partial factors of dead load and live load, respectively; COV_{QD} and COV_{QL} are the coefficients of variation of dead load and live load, respectively;

Table 5 gives the means and coefficients of variation for "updating data," "good data," and "general data," and the specifications give the load statistics; then the reliability index can be calculated using equation (10), which is described as β_{MvF}.
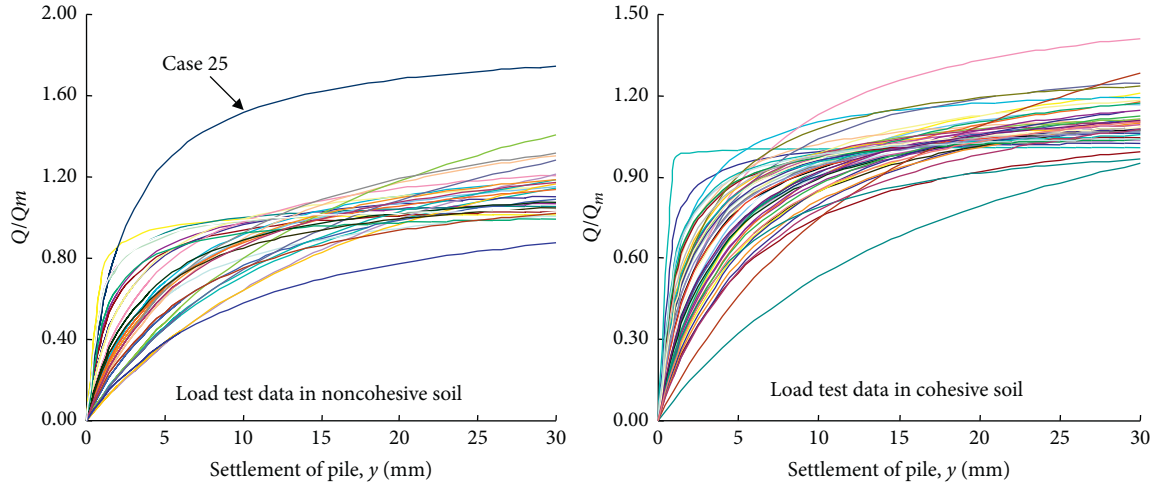
Figure 1: Normalized load-settlement curves of load test data.
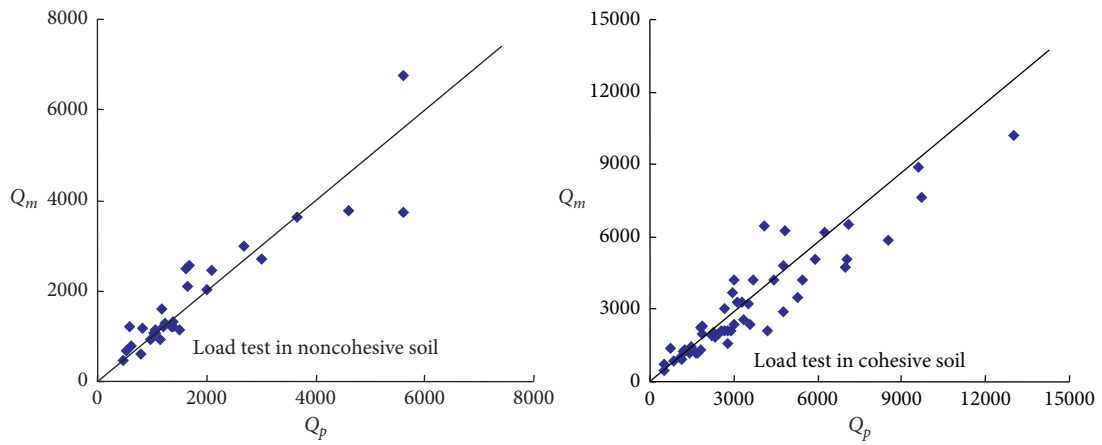
Figure 2: The scatter diagram of testing pile capacity and calculation pile capacity.

Table 3: Classified results of load test data in noncohesive soil.

	Good data					General data		
Case number	λ_R	ζ_i	Case number	λ_R	ζ_i	Case number	λ_R	ζ_i
1	1.04	0.02	14	0.80	0.22	9	0.71	0.30
2	1.22	0.20	18	1.02	0.00	12	1.31	0.29
3	1.11	0.09	19	0.79	0.22	16	0.74	0.27
4	0.97	0.05	20	0.97	0.05	17	1.32	0.30
5	1.13	0.11	21	1.27	0.24	22	1.33	0.30
6	1.15	0.13	23	0.99	0.03	27	0.66	0.35
7	0.93	0.09	29	0.78	0.23	28	0.65	0.36
8	1.02	0.00	30	0.86	0.16	33	1.50	0.47
10	0.83	0.18	31	0.90	0.11	—	—	—
11	0.97	0.04	32	1.00	0.00	—	—	—
13	1.03	0.01	—	—	—	—	—	—

3.2. Design Point Method. The limit-state function is linear at a point on the failure surface; its performance function is [6]

$$g = \ln\left(\frac{\text{FOS}\,\lambda_R\left((Q_D/Q_L) + 1\right)}{\lambda_{\text{QD}}\left(Q_D/Q_L\right) + \lambda_{\text{QL}}}\right). \tag{11}$$

All the parameters in equation (11) have the same meanings as equation (10). The calculation can be carried out using MATLAB software, which is described as β_{AF}.

3.3. Monte Carlo Simulation Method. Monte Carlo simulation method is an accuracy method to calculate reliability index, which is employed for comparison with the

TABLE 4: Classified results of load test data in cohesive soil.

	Good data					General data		
Case number	λ_R	ζ_i	Case number	λ_R	ζ_i	Case number	λ_R	ζ_i
34	1.00	0.13	60	1.27	0.11	35	0.64	0.45
36	1.09	0.05	62	0.95	0.17	42	0.81	0.30
38	1.12	0.03	63	1.41	0.23	44	0.80	0.30
39	0.95	0.18	64	1.22	0.06	46	0.81	0.29
40	1.32	0.15	65	1.27	0.10	47	0.74	0.36
41	0.87	0.24	66	1.32	0.15	58	1.51	0.31
43	0.89	0.23	67	1.37	0.20	61	1.45	0.26
45	1.42	0.24	70	1.08	0.06	72	1.65	0.43
48	0.96	0.17	71	1.44	0.25	76	1.48	0.29
49	1.11	0.04	73	1.39	0.21	79	0.71	0.38
50	1.09	0.06	74	1.16	0.01	84	0.77	0.33
51	1.02	0.12	75	1.27	0.10	86	1.51	0.31
52	0.99	0.14	77	0.96	0.16	—	—	—
53	1.00	0.13	78	1.28	0.12	—	—	—
54	1.26	0.10	80	1.02	0.12	—	—	—
55	1.26	0.09	81	1.06	0.08	—	—	—
56	1.18	0.03	82	1.29	0.11	—	—	—
57	1.10	0.04	83	1.00	0.13	—	—	—
59	1.27	0.10	85	1.16	0.01	—	—	—

TABLE 5: The updating model factor for pile capacity.

	Model factor							
Soil type	All data		Good data		General data		Updating data	
	Mean	COV	Mean	COV	Mean	COV	Mean	COV
Noncohesive soil	1.000	0.217	0.990	0.138	1.028	0.357	0.987	0.129
Cohesive soil	1.134	0.210	1.153	0.140	1.073	0. 372	1.134	0.132

accuracy of other calculation methods. Its performance function is

$$g = \text{FOS}\, \lambda_R \left(\frac{Q_D}{Q_L} + 1 \right) - \left(\lambda_{QD} \frac{Q_D}{Q_L} + \lambda_{QL} \right). \quad (12)$$

The calculation can be carried out using MATLAB software; the times of simulation are 10 million, described as β_{MCS}.

The values of λ_{QD}, λ_{QL}, COV_{QD}, and COV_{QL} can be obtained according to LRFD for Bridge Design Specification. 3.69 is selected as the value of (Q_D/Q_L) [27].

Figures 3 and 4 show the calculation results of reliability index. The results indicate that the deviation of reliability index for "good data" and "general data" is larger than 1.0, which is caused by the quality of data. However, the

reliability index of "good data" is near to the reliability index of "updating data." In addition, reliability index is sensitive to soil type. Reliability index in cohesive soil is larger than that in noncohesive soil.

The formula of load and resistance factor design method is [6]

$$\phi R_n \geq \eta \sum \gamma_i Q_i, \quad (13)$$

where R_n is standard value of resistance (kN); Q_i is standard value of load (kN); ϕ is the resistance factor; and γ_i is load factor.

Reliability analysis is the bias of resistance factor calculation. Load and resistance factor design method proposes the calculation formula shown in equation (14) based on first-order reliability method [6]:

$$\phi = \frac{\lambda_R \left(\gamma_{QD} (Q_D/Q_L) + \gamma_{QL} \right) \sqrt{\left(\left(1 + COV_{QD}^2 + COV_{QL}^2 \right) / \left(1 + COV_R^2 \right) \right)}}{\left(\lambda_{QD} (Q_D/Q_L) + \lambda_{QL} \right) \exp\left(\beta_T \sqrt{\left(\left(1 + COV_{QD}^2 + COV_{QL}^2 \right) / \left(1 + COV_R^2 \right) \right)} \right)}, \quad (14)$$

where β_T is target reliability index of piles. 1.75 and 1.08 are selected as the values of γ_{Q_L} and γ_{Q_D} according to LRFD for

Bridge Design Specification. The resistance factor is described as ϕ_{MvF} according to equation (14).
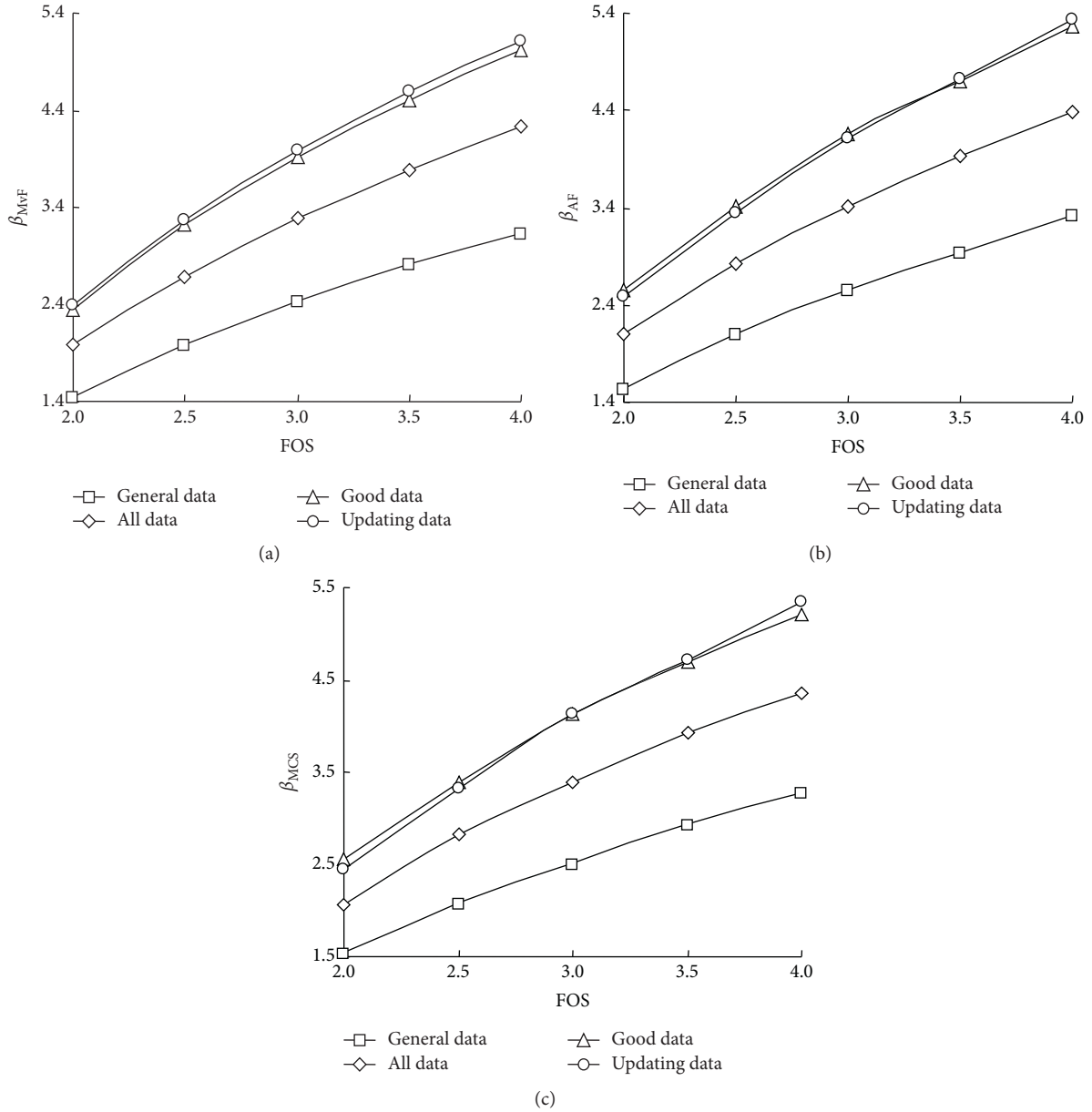
Figure 3: Reliability index in noncohesive soil. (a) First-order reliability method. (b) Design point method. (c) Monte Carlo simulation method.

If the reliability index is calculated using equation 11), the limit state equation for resistance factor calculation is

$$g_\varphi = \ln\left(\frac{\lambda_R\left(\gamma_{QD}\left(Q_D/Q_L\right) + \gamma_{QL}\right)}{\phi\left(\lambda_{QD}\left(Q_D/Q_L\right) + \lambda_{QL}\right)}\right) = 0. \qquad (15)$$

The resistance factor is described as ϕ_{AF} according to equation (15).

If the reliability index is calculated using equation (12), the limit state equation for resistance factor calculation is

$$g = \left(\frac{\lambda_R}{\phi}\right)\left(\gamma_{QD}\frac{Q_D}{Q_L} + \gamma_{QL}\right) - \left(\lambda_{QD}\frac{Q_D}{Q_L} + \lambda_{QL}\right) = 0. \qquad (16)$$

The resistance factor is described as ϕ_{MCS} according to equation (16).

2.0, 2.5, and 3.0 are selected as the target reliability index. Based on equations (14)–(16), the calculation results of resistance factor are shown in Table 6.

The quality of data has distinct contribution to resistance factor of bored piles. The accuracies of design point method and Monte Carlo simulation method are satisfactory, which can be considered as the criterion to verify the accuracy of proposed method. The results based on two methods are larger than the results based on first-order reliability method, and the difference are 6.9% and 18.3%, respectively. Meanwhile, the difference between the two methods is near 0. The accuracies based on "good data" and "updating data" are better than the accuracies based on "general data" and "all data."

In summary, Table 7 shows the recommended values of resistance factors. However, the reliability theory of pile

(a)

(b)

(c)
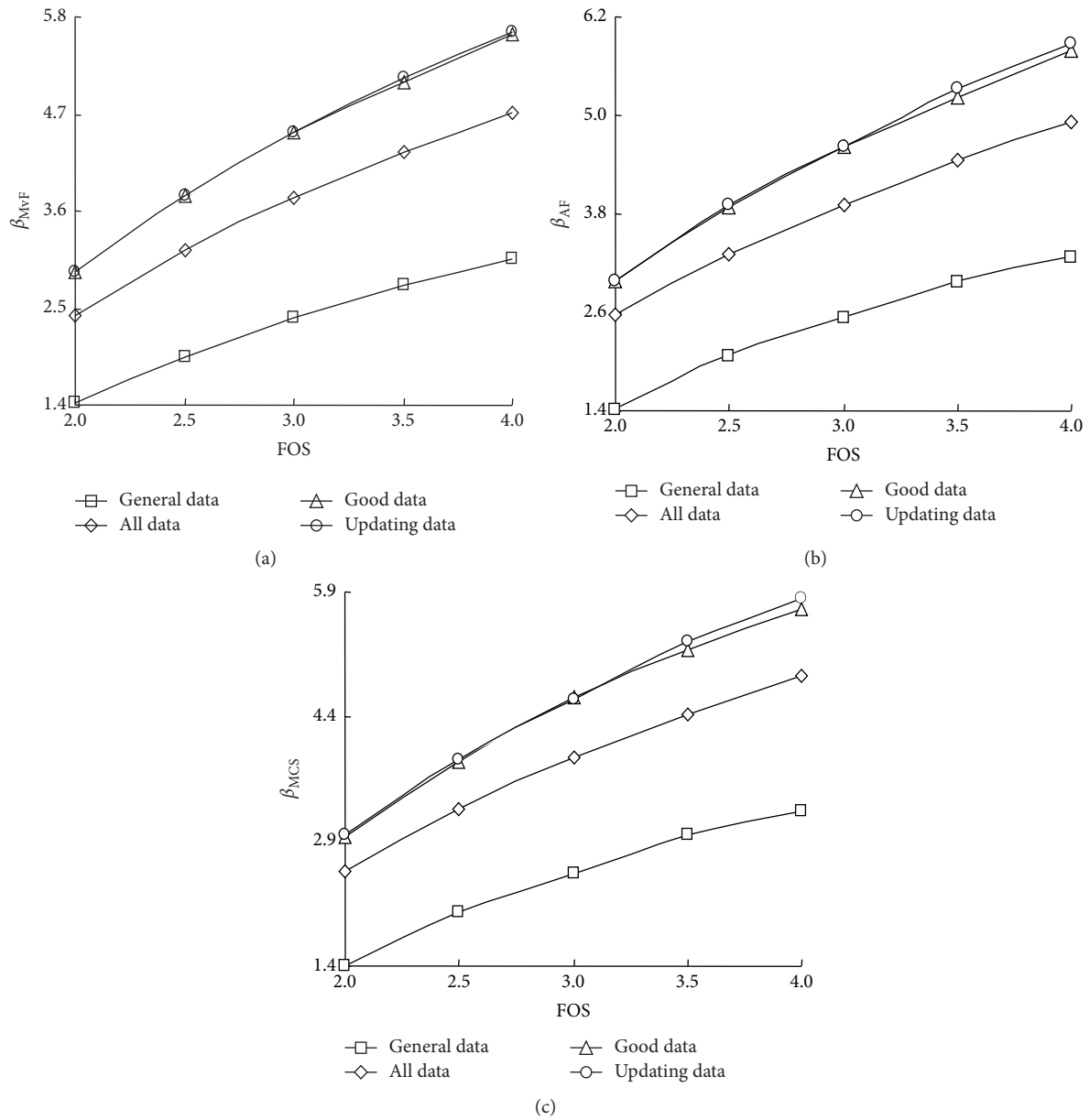
FIGURE 4: Reliability index in cohesive soil. (a) First-order reliability method. (b) Design point method. (c) Monte Carlo simulation method.

TABLE 6: Calculation results of resistance factor.

Target reliability, β_T	Noncohesive soil			Cohesive soil		
	ϕ_{MvF}	ϕ_{AF}	ϕ_{MCS}	ϕ_{MvF}	ϕ_{AF}	ϕ_{MCS}
All data						
2.0	0.440	0.452	0.450	0.461	0.476	0.475
2.5	0.375	0.389	0.389	0.387	0.396	0.394
3.0	0.336	0.354	0.353	0.344	0.362	0.360
General data						
2.0	0.437	0.446	0.445	0.443	0.450	0.450
2.5	0.371	0.382	0.380	0.375	0.385	0.384
3.0	0.333	0.350	0.350	0.335	0.347	0.345
Good data						
2.0	0.440	0.446	0.445	0.467	0.475	0.474
2.5	0.376	0.385	0.385	0.391	0.399	0.399
3.0	0.337	0.348	0.347	0.346	0.356	0.354

TABLE 6: Continued.

Target reliability, β_T	Noncohesive soil			Cohesive soil		
	ϕ_{MvF}	ϕ_{AF}	ϕ_{MCS}	ϕ_{MvF}	ϕ_{AF}	ϕ_{MCS}
Updating data						
2.0	0.440	0.449	0.448	0.463	0.472	0.471
2.5	0.376	0.385	0.384	0.390	0.400	0.400
3.0	0.337	0.348	0.348	0.345	0.358	0.356

TABLE 7: Recommended values of resistance factors.

β_T	Noncohesive soil	Cohesive soil
2.0	0.456	0.473
2.5	0.386	0.400
3.0	0.347	0.356

foundation is not perfect enough to be applied in engineering fact. The recommended values are proposed only according to the calculation results and American LRFD for Bridge Design Specification. Its application in engineering field needs to be further studied.

4. Conclusions

From this study, some conclusions are presented:

(1) The proposed method incorporating probability theory and Bayesian method can not only classify the in situ data but also overcome the deficiency caused by small sample for accuracy data.

(2) Data classification has significant contribution to reliability index and resistance factor. The results according to "good data" and "updating data" are larger than the results according to "general data" and "all data." Meanwhile the difference of results using two types of data is near 0. Therefore, "good data" and "updating data" can be used as the basis of resistance factor calculation.

(3) Reliability index and resistance factor are sensitive to the type of soil, and the calculation results in cohesive soil are larger than the results in noncohesive soil.

(4) The recommended values are proposed only according to the calculation results and American LRFD for Bridge Design Specification. Its application in engineering fact needs to be further studied. However, the proposed method can be used to update other geotechnical data.

Data Availability

The data used to support the findings of this study are available from the corresponding author upon request.

Conflicts of Interest

The authors declare that there are no conflicts of interest regarding the publication of this paper.

Acknowledgments

References

[1] M. Dithinde, K. K. Phoon, D. M. Wet, and J. V. Retief, "Characterization of model uncertainty in the static pile design formula," *Journal of Geotechnical and Geoenvironmental Engineering*, vol. 137, no. 1, pp. 70–85, 2010.

[2] L. M. Zhang, D. Q. Li, and W. H. Tang, "Reliability of bored pile foundations considering bias in failure criteria," *Canadian Geotechnical Journal*, vol. 42, no. 4, pp. 1086–1093, 2005.

[3] W. Y. Lam, "Reliability of bored piles with defects," Final Year Report, Hong Kong University of Science and Technology, Hong Kong, 2004.

[4] N. F. Ismael, "Axial load tests on bored piles and pile groups in cemented sands," *Journal of Geotechnical and Geoenvirmental Engineering*, vol. 127, no. 9, pp. 766–773, 2001.

[5] D. Q. Li, W. H. Tang, and L. M. Zhang, "Updating occurrence probability and size of defect for bored piles," *Structural Safety*, vol. 30, no. 2, pp. 130–143, 2008.

[6] AASHTO, *LRFD for Bridge Design Specifications*, American Association of State Highway and Transportation Officials, Washington, WA, USA, 8th edition, 2017.

[7] C. Tang and K. K. Phoon, "Characterization of model uncertainty in predicting axial resistance of piles driven into clay," *Canadian Geotechnical Journal*, vol. 56, no. 8, pp. 1098–1118, 2019.

[8] C. Tang and K. K. Phoon, "Evaluation of model uncertainties in reliability based design of steel H-piles in axial compression," *Canadian Geotechnical Journal*, vol. 55, no. 11, pp. 1513–1532, 2018.

[9] D. Kim and J. Lee, "Resistance factor contour plot analyses of load and resistance factor design of axially-loaded driven piles in clays," *Computers and Geotechnics*, vol. 44, pp. 9–19, 2012.

[10] K. N. Flynn and B. A. Mccabe, "Shaft resistance of driven cast-in-situ piles in sand," *Canadian Geotechnical Journal*, vol. 53, no. 1, pp. 49–59, 2016.

[11] W. Gong, C. H. Juang, S. Khoshnevisan, and K.-K. Phoon, "R-LRFD: load and resistance factor design considering robustness," *Computers and Geotechnics*, vol. 74, pp. 74–87, 2016.

[12] K. Kwak, K. J. Kim, J. Huh, J. H. Lee, and J. H. Parka, "Reliability-based calibration of resistance factors for static bearing capacity of driven steel pipe piles," *Canadian Geotechnical Journal, Forum*, vol. 47, no. 5, pp. 528–538, 2010.

[13] J. H. Park, J. Huh, K. J. Kim et al., "Resistance factors calibration and its application using static load test data for driven

steel pipe piles," *KSCE Journal of Civil Engineering*, vol. 17, no. 5, pp. 929–938, 2013.

[14] D. W. Kim, M. Y. Chung, and K. Kwak, "Resistance factor calculations for LRFD of axially loaded driven piles in sands," *KSCEJournal of Civil Engineering*, vol. 15, no. 7, pp. 1185–1196, 2011.

[15] K. W. Ng and S. Sritharan, "A procedure for incorporating setup into load and resistance factor design of driven piles," *Acta Geotechnica*, vol. 11, no. 2, pp. 347–358, 2016.

[16] J. J. Zheng, Z. J. Xu, Y. Liu, and X. Y. Bian, "Bayesian optimization for resistance factor of piles," *Chinese Journal of Geotechnical Engineering*, vol. 34, no. 5, pp. 1716–1721, 2012.

[17] CEN EN 1997-1., *Geotechnical Design-Part 1: General Rules*, European Committee for Standardization (CEN), Brussels, Belgium, 2004.

[18] A. L. Jones, S. L. Keamer, and P. Arduino, "Estimation of uncertainty in geotechnical properties for performance earthquake engineering," PEER Report 2002/16, University of California, Berkeley, CA, USA, 2002.

[19] F. K. Kulhawy and C. H. Trutmann, "Estimation of in-situ test uncertainty," *Geotechnical Special Publication*, vol. 58, pp. 269–286, ACSE, Reston, VA, USA, 1996.

[20] S. Lacsse and F. Nadim, "Model uncertainty in pile axial capacity calculations," in *Proceeding of 28th Offshore Technology Annual Conference*, Houston, TX, USA, 1996.

[21] G. G. Meyerhof, "Bearing capacity and settlement of pile foundations," *Journal of the Geotechnical Engineering Division*, vol. 102, no. 3, pp. 197–228, 1976.

[22] K. K. Phoon and F. H. Kulhawy, "Characterization of geotechnical variability," *Canadian Geotechnical Journal*, vol. 36, no. 4, pp. 612–624, 1999.

[23] K. K. Phoon, *Reliability-Based Design in Geotechnical Engineering: Computations and Applications*, Taylor & Francis, London, UK, 2008.

[24] M. William, *Introduction to Bayesian Statistics*, Wiley & Sons, New York, NY, USA, 2nd edition, 2007.

[25] K. K. Phoon, *Reliability-based design of foundations for transmission line structures*, Ph.D. dissertation, Cornell University, New York, NY, USA, 1995.

[26] A. H. S. Ang and W. H. Tang, *Probability Concepts in Engineering: Emphasis on Applications to Civil and Environmental Engineering*, John Wiley & Sons, New York, NY, USA, 2nd edition, 2006.

[27] R. M. Barker, J. M. Duncan, K. B. Rojiani, P. S. K. Ooi, C. K. Tan, and S. G. Kim, "Load factor design criteria for highway structure foundations," Final Report NCHRP Project 24-4, Virginia Polytechnic Institute and State University, Blacksburg, VA, USA, 1991.

Research Article

A Novel Prediction Method of Dynamic Wall Pressure for Silos Based on Support Vector Machine

Hanhua Yu,[1,2] **Zhijun Xu** [iD],[1,2] **Tingting Liu,**[1,2] **and Fang Yuan**[1,2]

[1]*College of Civil Engineering, Henan University of Technology, Zhengzhou 450001, China*
[2]*China National Engineering Laboratory for Grain Storage and Transportation, Zhengzhou 450001, China*

Correspondence should be addressed to Zhijun Xu; zj.xu_hust@qq.com

The physical properties and mechanical characteristics of storage materials are significantly different from those of ordinary solids and liquids. The distribution of dynamic wall pressure during silo discharge is quite complicated. Considering the nonlinear relationship between the factors which affect the dynamic lateral pressure of silos, a prediction method of dynamic wall pressure for silos based on support vector machine (SVM) is proposed here, and furthermore, the modified grid search method (GSM) is incorporated in obtaining the optimal support vector machine parameters to improve the accuracy of the prediction. Comparing the results of the proposed prediction model with the results of experiment methods and simulation methods, it can be found that the SVM prediction model shows high accuracy and high generalization ability, and the prediction results of the model fit well with the results of experiment and simulation methods. The proposed method can provide reference for the prediction of the dynamic wall pressure of silos.

1. Introduction

Silos are widely used to store coals, grains, and gravels because of their small footprint, large capacity, and low cost. The dynamic wall pressure during silo discharge is the main factor that causes silo damage [1]. The investigations about static wall pressure of silos have been relatively perfect [2, 3]. However, there is no widely accepted theory and calculation method of dynamic wall pressure for silos. Smith and Lohnes proposed the theory of lateral grain expansion [4]. Su proposed the theory of instantaneous arching for grains [5]. Janssen proposed the Janssen theory based on the continuous medium model [6]. These investigations present the theoretical basis for the dynamic wall pressure of silos. Liu and Hao [7] proposed a method for the calculation of dynamic lateral pressure of silos based on the overall flow of stored materials. Yuan et al. [8] proposed a method for the calculation of lateral pressure on squat silo wall by considering the influence of silo diameter ratio, and the methods are mainly used to solve the calculation of lateral

pressure of large shallow silos. Based on the unified strength theory and by considering the common influence of three principal stresses, Sun et al. [9] proposed a lateral pressure coefficient which is applied to both the deep and shallow silos. The dynamic lateral pressure of silos is affected by various factors, and the relationships between the influencing factors are nonlinear and complex. Traditional research methods (such as Jassen formula) only consider one or a few factors [10], and it is not conducive to the analysis and research of dynamic lateral pressure. In this way, it is necessary to establish an efficient and simple dynamic lateral pressure prediction method which takes the various factors into consideration. Recently, with the development of artificial intelligence, machine learning has been widely applied in many research fields. As one of the methods of machine learning, support vector machine (SVM) has good generalization performance and is one of the present investigation focus of artificial intelligent algorithms [11]. The SVM is widely used for classification and regression analysis, it is quite efficient in solving the problems about which the characteristics are nonlinear,

uncertain, small sample, and also, it has been widely applied in civil engineering and shows its efficiency and reliability in such problems. For example, Dai et al. [12] proposed a support vector density-based importance sampling for reliability assessment and showed its efficiency. Also, the least squares support vector machine (LSSVM) technology is applied to the reliability analysis of soft clay foundation settlement in [13]. Wang et al. [14] proposed a support vector machine basing model to predicate the stability coefficient of slope, and the grid search method is used to optimize the parameters.

Thus, considering the efficiency of the support vector machine in solving the problems of complex, nonlinear, multifactor, small sample problems and its advantage in the aspect of prediction, here, the support vector machine method is employed to help the prediction of the dynamic wall pressure for silos. First, the relevant factors affecting the dynamic lateral pressure of silos are set as the input variables, and the dynamic lateral pressure is set as the output value; second, the penalty parameters and kernel function parameters are optimized, respectively, under the help of grid search method, and the prediction model of dynamic lateral pressure of silos is established. Compared with other methods, the proposed model shows its prediction ability in the measurement of dynamic lateral pressure of silos. It provides a new method and basis for calculation and silo design.

2. Support Vector Machine Principle and Parameter Optimization

Support vector machine algorithm is based on statistical theory. The advantage of this method is that it adopts the principle of minimizing structural risk. Its model is [10, 15]

$$f(x) = \omega \cdot \varphi(x) + b f(x),$$ (1)

where x is the input feature vector; $f(x)$ is the output value; $\varphi(x)$ is the nonlinear function mapped to high-dimensional feature space; ω is the weighted vector of the hyperplane; and b is the bias vector.

The solution of nonlinear regression is the key point to support vector machine, and it can be solved by using the optimal solution of the following equation:

$$\min_{w,b} \frac{1}{2}\|w\|^2 + c\sum_{i=1}^{l}(\xi_i + \xi_*).$$ (2)

Equation (2) satisfies the following constraints:

$$\text{s.t.} = \begin{cases} (\omega \cdot x_i) + b - y_i \leq \varepsilon + \xi_i, & i = 1,\ldots,l, \\ y_i - (\omega \cdot x_i) - b \leq \varepsilon + \xi_i^*, & i = 1,\ldots,l, \\ \xi_i, \xi_i^* \geq 0, & i = 1,\ldots,l. \end{cases}$$ (3)

where c is the penalty parameter; ε is the insensitive loss parameter; and ξ_i and ξ_i^* are the slack variables.

The Lagrange formula and Karush–Kuhn–Tucker condition are employed to solve the optimal solution shown in the following equation:

$$\min_{a,a^*} \frac{1}{2}\sum_{i,j=1}^{l}(\alpha_i^* + \alpha_i)(\alpha_j^* - \alpha_j)(x_i \cdot x_i) + \varepsilon\sum_{i=1}^{l}(\alpha_i^* - \alpha_i).$$ (4)

Equation (4) satisfies the following constraints:

$$\text{s.t.} \begin{cases} \sum_{i=1}^{l}(\alpha_i^* - \alpha_i) = 0, \\ 0 \leq \alpha_i, \alpha_i^* \leq c, i = 1,\ldots,l. \end{cases}$$ (5)

where α_i and α_i^* are the Lagrange multipliers.

Kernel function described as $K(x_i, y_i)$ is incorporated to solve high-dimensional equations according to support vector machine algorithm. The radial basis function is used as the kernel function due to its satisfactory prediction accuracy, which is shown in the following equation:

$$K(x_i, y_j) = \exp\left(-\frac{\|x_{i-}y_j\|^2}{2\sigma^2}\right).$$ (6)

According to equations (1) and (4)–(6), the regression fitting function of support vector machine can be obtained:

$$f(x) = \sum_{i=1}^{nsv}(\alpha_i - \alpha_i^*)K(x_i, y_j) + b.$$ (7)

Here, the LIBSVN toolbox is employed to help implement the prediction based on support vector machine [16].

The working principle of the grid search method is to search all parameters to obtain the optimal parameters. However, this algorithm is simple to implement but it seems to be time consuming. This paper employs an improved grid search method to evaluate the performance of each parameter [17]. In detail, a coarse search is performed in a large range, and a fine search is performed in a small range. Then, all possible parameters are found out and the optimal SVM parameters will be chosen then. The calculation model is shown in Figure 1.

3. Prediction of Dynamic Wall Pressure for Silos

The geometric sizes of silos and the physical parameters of storage materials have significant impacts on the dynamic wall pressure of silos. In addition, during silo discharge, the dynamic wall pressure is also different at different locations. Usually, the scale model, numerical simulation, and theoretical analysis are often combined to study the dynamic lateral pressure of silos, and it shows that results of the three methods fit well and can be used as the basis for silo design and dynamic lateral pressure research. Here, to verify the efficiency of the proposed support vector machine-based model on the prediction of the dynamic side pressure prediction model of silos, a database of 505 dynamic side pressures during silo central discharge is collected [18–23]. Some relevant parameters are presented in Table 1.

This paper takes the depth of silos, inner diameter, height-diameter ratio, discharge opening width, dip angle of funnel, internal friction coefficient, external friction coefficient, gravity density, and measurement point position as
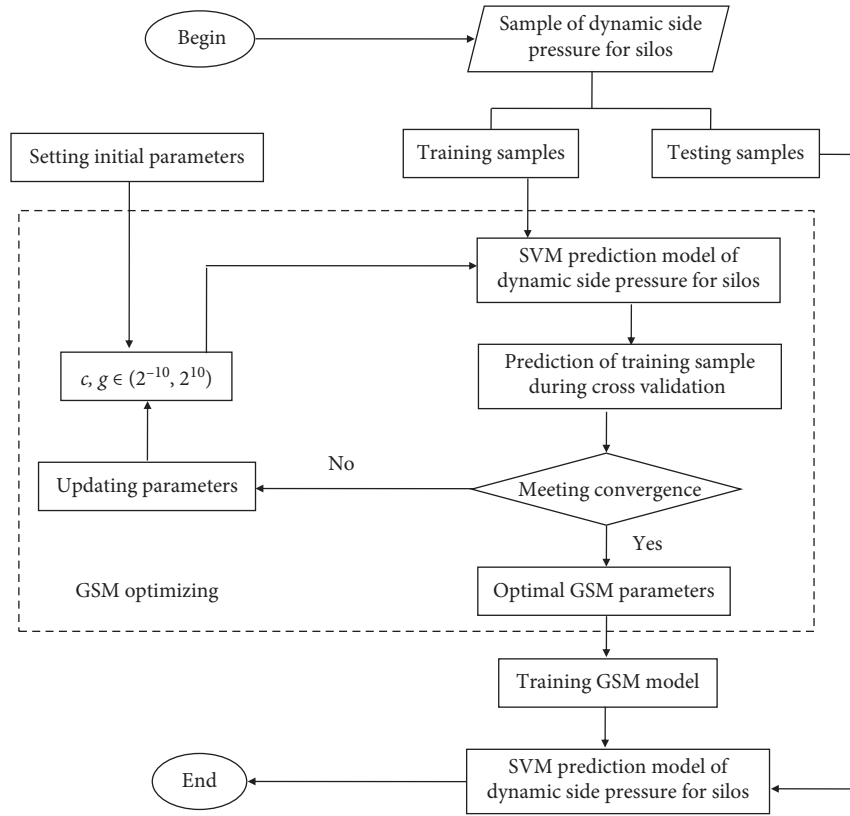
Figure 1: SVM prediction model of dynamic wall pressure for silos.

Table 1: Relevant parameters.

Sources	Depth of silos (m)	Inner diameter (m)	Height-diameter ratio	Dip angle of funnel (°)	Width of discharge opening (m)	Internal friction coefficient	External friction coefficient	Gravity density (kg/m³)
Zhao [18]	1.2	0.7	1.71	50	0.1	0.3	0.3	1000
				55	0.18	0.4	0.4	
				60	0.26	0.5	0.5	
Ding [19]	1.2	0.7	1.71	55	0.12	0.25	0.35	2000
				60	0.18	0.3	0.45	
				60	0.24	0.35	0.55	
Yuan and Liu [20]	5	1.5	2.9	50	0.3	0.58	0.4	816
		2	2.2		0.4			
		2.5	1.76		0.5			
		3	1.47		0.6			
		3.5	1.28		0.7			
		4	1.1		0.8			
Li [21]	5	1.5	3.3		0.3	0.5	0.4	800
	3.5	1	3.5	50	0.2			
	1.7	0.5	0.49		0.03			
Wang et al. [22]	1	0.5	2	0	0.1	0.6	0	970
Chen and Liang [23]	3.6	1.5	2.4	60	0.3	0.53	0.4	800
						0.64	0.53	
						0.75	0.64	

Best c = 5.278 g =3.0314 CVmse = 0.00066176

Best c = 5.278 g =3.0314 CVmse = 0.00066176

(a)

(b)
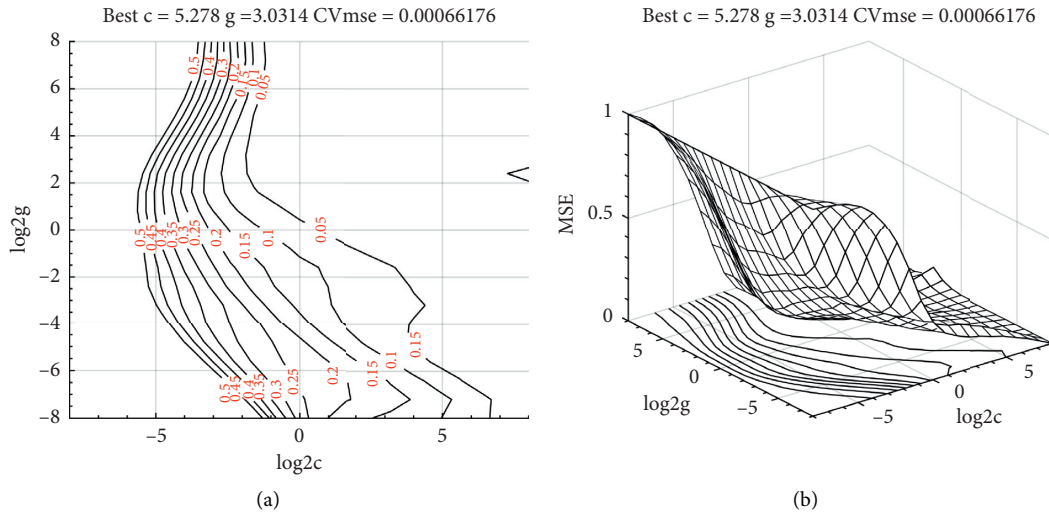
Figure 2: (a) Fine choosing results of c and g (contour diagram). (b) Fine choosing results of c and g (3D diagram).

-⊖- PFC simulation values
-☐- SVM prediction values
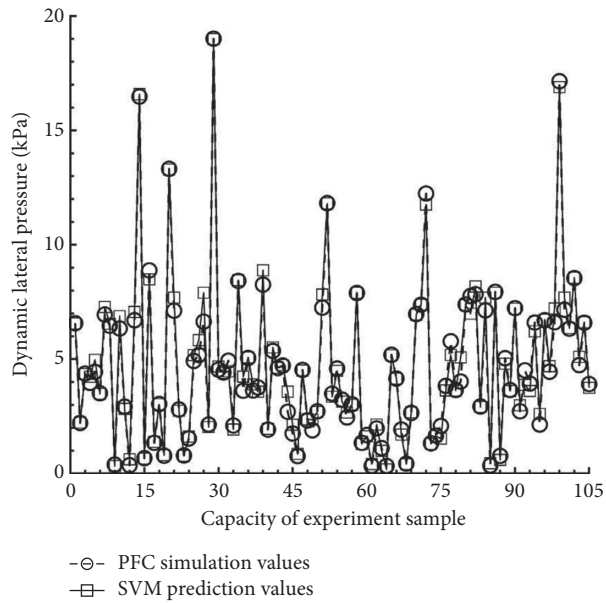
Figure 3: Prediction results of testing samples.
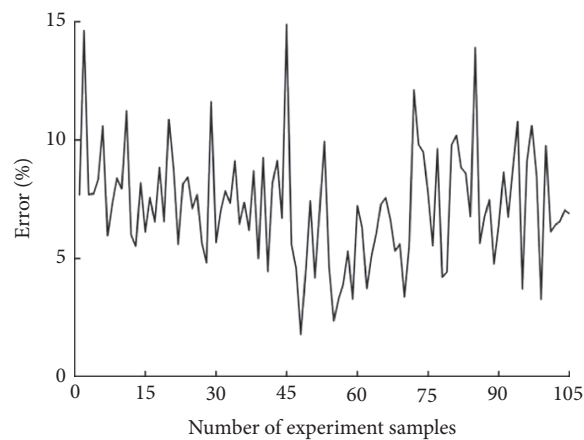
Figure 4: Error values.

TABLE 2: Comparison of the SVM model and BP neural network.

	MSE	R^2
BP neural network	0.0016884	0.95141
SVM method	0.00041866	0.98381
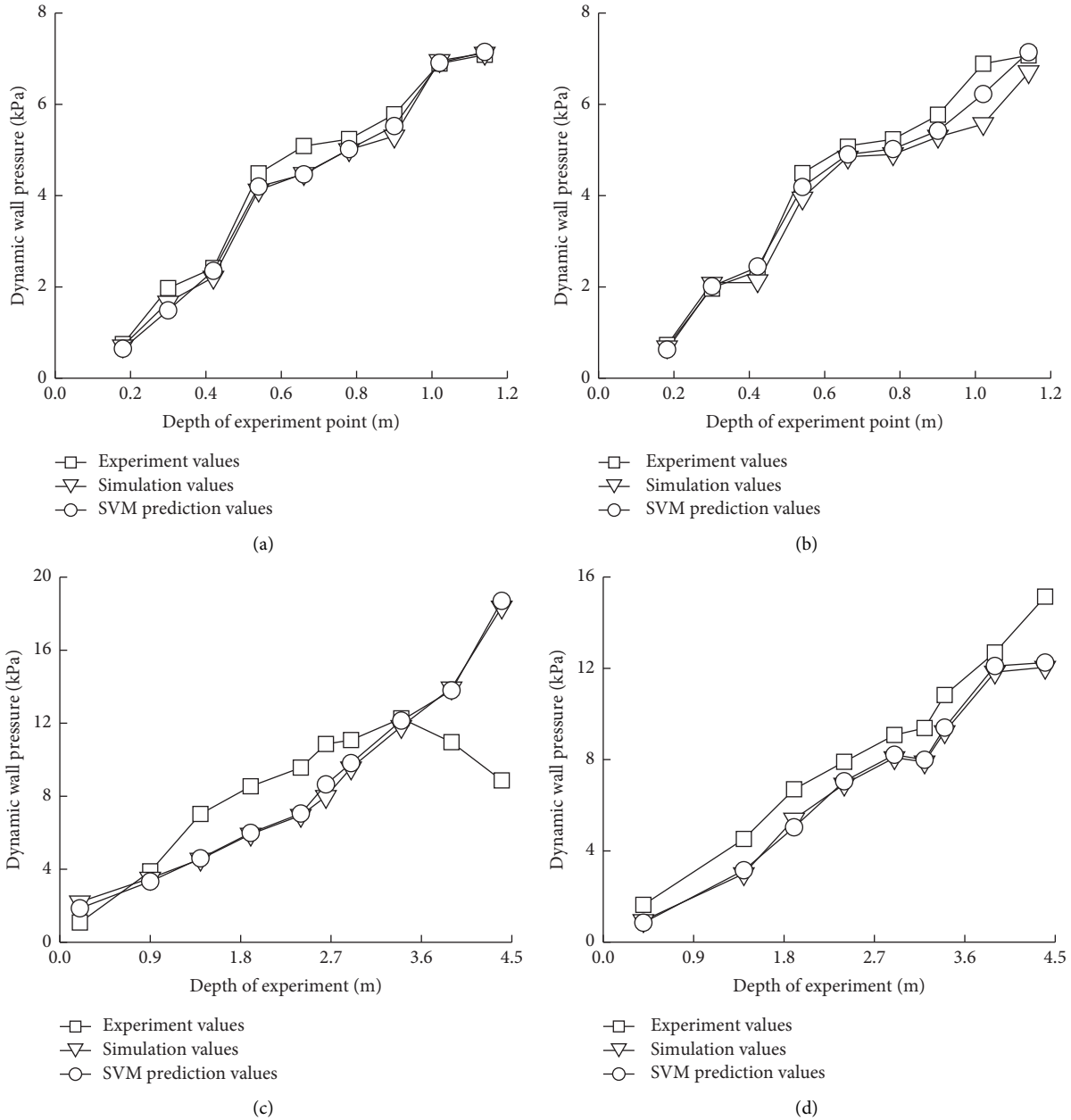
FIGURE 5: Comparisons with experiment values, simulation values, and prediction values. (a) For literature [18]. (b) For literature [19]. (c) For literature [20]. (d) For literature [21].

input variables and the dynamic wall pressure of silos as the output value. 400 data are randomly selected from the database as training samples, and the remaining 105 data are used as testing samples. The data are described in the form of a matrix, and each row is a set of data, and each column corresponds to a variable. In order to ensure the accuracy and reliability of the prediction model, the original data are normalized as shown in the following equation:

$$x_{ij} = \frac{x_{ij} - \min_{k}(x_{kj})}{\max_{k}(x_{kj}) - \min_{k}(x_{kj})}, \tag{8}$$

where $\max(x_{kj})$ and $\min(x_{kj})$ are the maximum and minimum data, respectively.

The prediction accuracy of the support vector machine (SVM) model is sensitive to the penalty parameter c and kernel parameter g. At present, for the support vector machine (SVM) method, the relevant parameters are mainly based on experiences and there is no unified mode. This paper uses the improved grid search method to determine the optimal values of c and g [24, 25]. The grid optimization program is written by MATLAB program. The parameter optimization process is as follows:

> Step 1: the range and step size of c and g are first initialized.
>
> Step 2: c and g are cursorily chosen. The range of c and g is set as $[2^{-10}, 2^{10}]$. The default values are set as the step sizes of c and g, and the default values are also set as the number of cross validations and the step size of the optimal mean square error.
>
> Step 3: c and g are precisely chosen. The range of c and g is set as $[2^{-8}, 2^8]$. 0.8 is set as the step size of c and g. 3.0 is set as the number of the cross validations. 0.05 is set as the step size of the optimal mean square error. The fine choosing results are shown in Figure 2.

According to the fine choosing results, 5.278 and 3.0314 are the optimal c and g values, respectively. The optimal c and g values are substituted into the SVM prediction model shown in Figure 1. The mean square error (MSE) and correlation coefficient (R^2) are employed as the evaluating indicators. The prediction results of 105 testing samples are shown in Figure 3. From Figure 3, MSE is 0.00041866 and R^2 is 0.98381, which indicate that the testing sample curve basically matches the predicted curve. The errors are shown in Figure 4. The minimum and maximum errors are 1.1% and 14.88%, and the average relative error is 7.21%.

In order to verify the applicability of the SVM prediction model, the prediction result is compared with BP neural network using the same data, and the results are shown in Table 2. The results show that the support vector machine method can describe well the complex nonlinear relationship between the dynamic side pressure of silos and its influencing factors.

In summary, the proposed SVM prediction model has higher accuracy and can effectively predict the dynamic wall pressure of silos.

4. Application Analysis

Relevant parameters in the literature are selected and substituted into the proposed SVM prediction model [18–21]. The results are shown in Figure 5.

It can be seen that the simulated values are slightly larger than the predicted values in the early stage of silo discharge and slightly smaller than the predicted values in the late stage of silo discharge. The prediction accuracy is higher. The testing values are higher than the predicted values. However, with the increment of the depth for measurement points, the dynamic wall pressures are roughly the same. The main

reason is that the training samples of the SVM prediction model are from simulated values; therefore, the predicted values are closer to the simulated values. Compared with the PFC program, the proposed method not only improves the calculation efficiency but also can provide a reference for the investigation on dynamic wall pressure when the PFC program cannot calculate the dynamic wall pressure of large silos.

5. Conclusions

From this study, some conclusions are presented:

(1) An improved grid search method is used to optimize the punish parameters (c) and kernel function (g) of SVM. The optimal c and g are 5.278 and 3.0314, respectively. The proposed method can avoid the subjective view of relevant parameters based on experiences.

(2) The mean square error (MSE) and the correlation coefficient (R^2) of the SVM prediction model are close to 0 and 1.0, respectively, which indicates that the accuracy of SVM prediction model is satisfied.

(3) The proposed prediction model can effectively solve the nonlinear relationship between the dynamic side pressure of silos and its influencing factors and provide a novel method for the study of the dynamic wall pressure of silos.

Data Availability

The data used to support the findings of this study are available from the corresponding author upon request.

Conflicts of Interest

The authors declare that there are no conflicts of interest regarding the publication of this paper.

Acknowledgments

References

[1] T. Jacek, *Confined Granular Flow in Silos, Experimental and Numerical Investigations*, Springer, Berlin, China, 2013.

[2] G. Blight, *Assessing Loads on Silos and Other Bulk Storage Structures*, Taylor & Francis, New York, NY, USA, 2006.

[3] C. J. Brown and J. Nielsen, *Silos: Fundamentals of Theory, Behaviour and Design*, E & FN Spon, London, UK, 1998.

[4] D. L. O. Smith and R. A. Lohnes, *Grain Bin Overpres-sures Induced by Dilatancy Upon Unloading, ASAE Paper No.80-3013*, American Society of Agricultural Engineers, St.Joseph, MI, USA, 1980.

[5] L. X. Su, "The elastic deformation and its effect on the wall pressure caused by dischargeing arch in silo," *Journal of Zhengzhou Grain College*, vol. 18, no. 4, pp. 59–63, 1997.

[6] H. A. Janssen, "Versucheùber getreidedruck in silozellen," *Zeitschriff des Vereines Deutscher Ingenieure*, vol. 39, pp. 1045–1049, 1895.

[7] D. H. Liu and J. P. Hao, "Research on lateral pressure upon wall of reinforced concrete silo," *Journal of Buliding Structure*, vol. 16, no. 5, pp. 57–63, 1995.

[8] F. Yuan, X. Shao, L. M. Wang et al., "A method for calculation lateral pressures on squat silo walls," *Engineering Mechanics*, vol. 21, no. 3, pp. 96–100, 2004.

[9] S. S. Sun, J. H. Zhao, and C. G. Zhang, "New solution for lateral pressure of silos and bunkers," *Journal of Guangxi University (Natural Science Edition)*, vol. 43, no. 1, pp. 168–177, 2018.

[10] J. Zhou, Z. Zhang, M. F. Du et al., "Mesoscopic study on the influence of funnel form changing on silo pressure," *Special Sructure*, vol. 23, no. 4, pp. 14–16, 2006.

[11] A. Christmann and I. Steinwart, *Support Vector Machines*, Springer, Berlin, Germany, 2008.

[12] H. Dai, H. Zhang, and W. Wang, "A support vector density-based importance sampling for reliability assessment," *Reliability Engineering & System Safety*, vol. 106, pp. 86–93, 2012.

[13] Y. Wang, X. Zhao, and B. Wang, "LS-SVM and Monte Carlo methods based reliability analysis for settlement of soft clayey foundation," *Journal of Rock Mechanics and Geotechnical Engineering*, vol. 5, no. 4, pp. 312–317, 2013.

[14] J. W. Wang, Y. S. Xu, and J. X. Li, "Prediction of slope stability coeff icient based on grid search support vector machine," *Railway Engineering*, vol. 59, no. 5, pp. 312–317, 2019.

[15] S. Weerasinghe, S. Erfani, T. Alpcan et al., "Support vector machines resilient against training data integrity attacks," *Pattern Recognition*, vol. 96, no. 12, 2019.

[16] C. C. Chang and C. J. Lin, "A library for support vector machines," *ACM Transactions on Intelligent Systems and Technology*, vol. 2, no. 3, pp. 389–396, 2011.

[17] H. A. Fayed and A. F. Atiya, "Speed up grid-search for parameter selection of support vector machines," *Applied Soft Computing*, vol. 80, no. 7, pp. 202–210, 2019.

[18] S. Zhao, *Analysis and Application of Silo Storage pressure,Doctoral Dissertation*, Wuhan University of Technology, Wuhan, China, 2013.

[19] S. W. Ding, "Discrete element analysis of storage side pressure of silo based on PFC3D", M.S. thesis, Wuhan University of Technology, Wuhan, China, 2014.

[20] F. Yuan and H. L. Liu, "Numerical simulation of unloading pressure in deep and shallow warehouses using discrete element method," *Journal of Henan University of Technology (Natural Science Edition)*, vol. 41, no. 1, pp. 68–74, 2020.

[21] J. W. Li, "Study on the numerical simulation of the discharge pressure of the silo considering the influence of the warehouse diameter", M.S. thesis, Henan University of Technology, Zhegnzhou, China, 2018.

[22] S. H. Wang, Z. R. Xiao, and K. J. Liu, "Study on the meso-scopic mechanism of the influence of storage particle size on the unloading flow state and silo wall pressure of silos," *Journal of Henan University of Technology(Natural Science Edition)*, vol. 38, no. 6, pp. 86–90, 2017.

[23] C. B. Chen and X. P. Liang, "Discrete element simulation analysis of silo unloading process," *Oils and Food Science and Technology*, vol. 16, no. 1, pp. 11–13, 2008.

[24] S. Kostić, N. Vasović, and D. Sunarić, "A new approach to grid search method in slope stability analysis using Box–Behnken statistical design," *Applied Mathematics and Computation*, vol. 256, no. 4, pp. 425–437, 2015.

[25] C. C. Qi and A. Fourie, "Cemented paste backfill for mineral tailings management: review and future perspectives," *Minerals Engineering*, vol. 144, no. 12, pp. 1–21, 2019.

Research Article

A New Reliability Rock Mass Classification Method Based on Least Squares Support Vector Machine Optimized by Bacterial Foraging Optimization Algorithm

S. Zheng,[1] A. N. Jiang ⬤,[1] X. R. Yang,[1] and G. C. Luo[2]

[1]*Highway and Bridge Research Institute, College of Transportation Engineering, Dalian Maritime University, Dalian, China*
[2]*China Railway Construction Bridge Engineering Bureau Group Co., Ltd., Tianjin, China*

Correspondence should be addressed to A. N. Jiang; jiangannan@163.com

Classification of the surrounding rock is the basis of tunnel design and construction. However, conventional classification methods do not allow dynamic tunnel construction adjustments because they are time-consuming and do not consider the randomness of rock mass. This paper presents a new reliability rock mass classification method based on a least squares support vector machine (LSSVM) optimized by a bacterial foraging optimization algorithm (BFOA). The LSSVM is adopted to express the implicit relationship between classification indicators and rock mass grades, which is a response surface function for reliability evaluation. LSSVM parameters were optimized by the BFOA to form a hybrid BFOA-LSSVM algorithm. Using geological prediction and rock strength resilience results as classification indicators, samples were developed to train the LSSVM model using the hybrid algorithm. The Monte Carlo sampling method of reliability classification was implemented and applied to the Suqiao tunnel at the Puyan highway in the Fujian province of China; the influence of parameters on the performance of the algorithm is discussed. The results indicate that the new method is feasible for tunnel engineering; it can improve the classification accuracy of surrounding rock exhibiting randomness, to provide an effective means of classifying surrounding rock in the dynamic design of tunnel construction.

1. Introduction

Classification of surrounding rock is the basis of tunnel design and construction; a complete classification system should include two parts: a preconstruction survey classification and a modification classification during construction [1]. Limited by environmental conditions and technical means, rock classification in the survey stage produces only a relatively rough result. Thus, it is essential to conduct a more detailed and accurate classification through statistical processing of rock mass disclosure information in the construction process [2–4].

To date, researchers have proposed a variety of rock mass classification methods, such as those of Wickham [5], Barton et al. [6], Hoek et al. [7], and Palmström [8, 9]. Among these classification methods, the most widely used method is the rock mass rating (RMR) method, which was first proposed

by Bieniawski [10–12] and has been continuously improved and applied since then [13–16]. The basic quality (BQ) method was proposed and widely applied in China [17–20]. These conventional rock classification methods are mostly used in the preconstruction survey stage and are unable to meet tunnel construction requirements because the classification indicators cannot be easily and rapidly obtained in the construction process [21]. For most classification methods, the mapping relationship between the indicators and rock mass grades is not clear, and the randomness of indicator distribution is not considered.

Much research has been conducted in the last few decades to solve these problems. Geological advanced prediction information is considered to reflect the properties of rock masses, and prediction results are used as classification indicators for the evaluation of rock mass grade [22–24]. To find the optimal parameters of machine learning models,

intelligent algorithms such as convolutional neural networks [25] and support vector machines [26] can be used, or other methods such as the PCA-ideal point method [27] and rough set theory [28]. These studies analyzed the advanced geological prediction characteristics and established a nonlinear mapping relationship between indicators and rock grade, partly solving the problem of acquiring indicators in the rock mass classification process.

Among the intelligent algorithms used in these studies, SVM has been widely used in geotechnical engineering in recent years, owing to its excellent small-sample-learning ability, including blasting vibration control [29], blasting risk prediction [30], new material development [31], and tunneling machine control [32]. The LSSVM [33] adopted in this study is a type of SVM using the least squares linear system as the loss function to replace the traditional quadratic programming method of the support vector machine, which has a more concise model group and higher computational efficiency. However, the regression effect of the LSSVM is significantly affected by the values of its key parameters. To obtain better calculation accuracy, we adopted a bacterial foraging optimization algorithm (BFOA) [34] with good global optimization ability to optimize the key parameters of the LSSVM, forming a BFOA-LSSVM hybrid algorithm.

However, the randomness of spatial distribution still exists in rock indicators. Thus, the deterministic classification method can lead to inaccurate calculation results. A reliability algorithm can solve the problem [35] and is a powerful method of obtaining a reliability classification result. However, reliability theory based on conventional indicators can only be evaluated after the excavation of the target location, which produces a certain hysteresis and cannot meet the needs of dynamic design for tunnel engineering.

Research on surrounding rock classification has produced significant results, but there are still some problems to be solved: (1) Conventional classification uses traditional methods to obtain the classification indicators, which is time-consuming and slows down construction progress. (2) Conventional classification methods do not consider the randomness of a rock mass; there has been little research on rock mass classification using advanced prediction indicators. (3) Machine learning algorithms have been used in surrounding rock classification. However, human limitations in the selection of the learning machine parameters affect calculation accuracy.

Difficulty in quickly obtaining a grading evaluation index and definitive grading result information makes the current grading evaluation method of surrounding rock insufficient and unpopular in the construction process. Some tunnel construction still uses the artificial experience method to determine the state of surrounding rock. In this study, a method of surrounding rock classification is established based on advanced geological prediction. The classification indicators using this method are easy to obtain, the operation difficulty is low, and it is convenient in engineering applications. Reliability theory is introduced to evaluate the classification results, and the uncertainty of surrounding rock properties is fully considered, to provide a more comprehensive data reference for project builders.

In this study, we established a reliability classification method for surrounding rock based on reliability theory, using an LSSVM optimized by the BFOA as the response surface function. Samples were produced for LSSVM machine learning, including geological prediction and rock strength resilience results as classification indicators. The Monte Carlo sampling method was used for calculation. To verify its feasibility, the new reliability classification method was applied to the Suqiao tunnel of the Puyan expressway in Fujian province, China.

2. A New Reliability Classification Method of Surrounding Rock

2.1. Reliability Classification Method. In the classification of rock masses in tunnel engineering, the obtained classification indicators are discrete and random due to instrument operation, data statistics, and human error. Rock masses surrounding the tunnel have certain variability, such as a local broken zone or a weak layer, which leads to a large variation in classification indicators and misjudgment of the rock mass grade. There is a reliability issue in the rock mass classification process; the probability of success or failure of the final classification result is regarded as a two-category classification problem. The probability expression of the classification result, the rock mass classification reliability [35], is expressed by reliability theory to avoid prediction error caused by the randomness of the classification indicators.

The surrounding rock is generally categorized into grades I–V. As an example to introduce the reliability classification method, rock mass grade IV is examined. To evaluate the reliability of classification results belonging to this grade, classification boundaries must be defined. The reliability function is shown as follows:

$$\left.\begin{array}{l} Z_{IV}^L = F_i(x_i) - [N_u]_{IV}^L \\ Z_{IV}^R = F_i(x_i) - [N_u]_{IV}^R \end{array}\right\}, \tag{1}$$

where $F_i(\cdot)$ is the response surface function that expresses the mapping relationship between the evaluation value of the rock mass and the classification indicators, x_i is the rock mass classification indicator group, $x_i = [x_1, x_2, ..., x_n]$, and $[N_u]_{IV}^L$ and $[N_u]_{IV}^R$ are the limit values of grade IV.

The reliable probability calculation method for the classification results relative to the two bounds of formula (1) is shown as follows:

$$\left.\begin{array}{l} P_{IV^L}^s = P(Z_{IV}^L \geq 0) = \int\int_{Z_{IV}^L > 0} \cdots \int h(x_i) dx_1 dx_2 \ldots dx_n \\ P_{IV^R}^s = P(Z_{IV}^R \geq 0) = \int\int_{Z_{IV}^R > 0} \cdots \int h(x_i) dx_1 dx_2 \ldots dx_n \end{array}\right\}, \tag{2}$$

where $h(x_i)$ is the joint probability density of the classification indicator group.

The reliability classification evaluation result of a rock mass of grade IV is expressed as

$$P_{IV}^s = P_{IV^L}^s - P_{IV^R}^s. \tag{3}$$

In solving formula (2), it is difficult to integrate the joint probability density $h(x_i)$. The Monte Carlo sampling method is used to solve the problem, with the number of samples set at 10^5 [36]. Similarly, classification reliability evaluation results for other rock mass grades can be obtained.

2.2. BFOA-LSSVM Hybrid Algorithm

2.2.1. LSSVM Regression Model.
In view of the shortcomings of traditional evaluation methods such as RMR and BQ that cannot meet the demands of dynamic construction, the geological prediction index has been used in surrounding rock grading evaluation in recent years [22–24]. The mapping relationship between the new indicators and the surrounding rock grade is complex and nonlinear. In this study, the least squares support vector machine (LSSVM) is used to express this implicit model, as shown in Figure 1, and is used as the response surface function $F_i(\cdot)$ in formula (1).

The LSSVM is another form of SVM regression [37]; it abstracts the nonlinear mapping into a process of fitting known data by hyperplane [38]. Neural network training easily falls into local optimization and the complexity of BP network modeling. Quadratic programming problems requiring training samples in SVM are avoided, which greatly improves computational efficiency.

For a given N training samples $\{x_i, y_i\}_{i=1...N}$, $x_i \in R^n$ is the six-dimensional sample input of the grading indicator group, and $y_i \in R^1$ is the one-dimensional sample output of the rock mass evaluation value. The LSSVM regression model is shown as follows:

$$y(x) = \sum_{k=1}^{N} \alpha_k K(x, x_k) + b, \tag{4}$$

where $K(x, x_k)$ is the radial basis kernel function, $K(x, x_k) = \exp\{(-\|x - x_k\|^2/\sigma^2)\}$, σ^2 is the square bandwidth representing the influence degree of a single sample vector, α_k is the Lagrange operator, and b is the error term, solved by

$$\begin{bmatrix} 0 & L^T \\ L & \Omega + \gamma^{-1}I \end{bmatrix} \begin{bmatrix} b \\ \alpha \end{bmatrix} = \begin{bmatrix} 0 \\ y \end{bmatrix}, \tag{5}$$

where $y = [y_1, y_2, ..., y_N]$, L is an n-dimensional array, $\mathbf{L} = [1, 1, ..., 1]$, $\alpha = [\alpha_1, \alpha_2, ..., \alpha_N]$, $\Omega = \varphi(x_k)^T \varphi(x_l) = K(x_k, x_l)$, $k, l = 1, 2, ..., N$, $\mathbf{I}$ is the unit vector, and γ is the canonical parameter that represents the fitting degree within the interval.

The computation speed improvement of the LSSVM is due to the least square value function and equality constraint, which reduces the complexity of the solution process. However, the sample training result is highly dependent on the regular parameter γ and the square
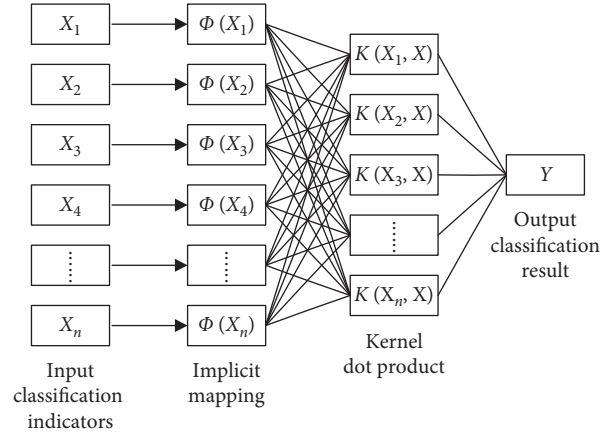
FIGURE 1: Implicit mapping model expressed by LSSVM.

bandwidth σ^2 of the kernel function. LSSVM theory does not provide effective selection methods; parameter determination is somewhat arbitrary. This study uses the BFOA to optimize the parameters.

2.2.2. BFOA Optimizes LSSVM.
The bacterial foraging optimization algorithm (BFOA) is a computational method that simulates human *Escherichia coli* foraging behavior and searches for the optimal parameters through iterative calculation [39–41]. It is a random search algorithm with good overall performance; the search results do not easily result in a local optimal solution. During the calculation, S bacterial individuals were randomly generated within the value range of the parameters to be optimized, and each individual contained a group of numerical combinations of the parameters:

$$\theta_i = \left[\theta_i^1, \theta_i^2, \ldots, \theta_i^D\right], \tag{6}$$

where θ_i is the individual bacteria and $i = 1, 2, ..., S$. θ_i^D represents the target parameter to be optimized.

All bacteria underwent N_c consecutive trending operations with a trend step size of $C(i)$ and performed self-replication optimization under the condition that the minimum fitness value of the population did not meet the expected value. After repeating the replication operation N_{re} times, population migration was conducted with P_{ed} as the control probability, and the maximum migration was limited to N_{ed}. The iterative information of individual bacteria is expressed as

$$\theta(i, g+1, n, m) = \theta(i, g, n, m) + C(i)\frac{\Delta(i)}{\sqrt{\Delta^T(i)\Delta(i)}}, \tag{7}$$

where g, n, and m represent the current executed trend, replication, and migration times, respectively. Δ represents a random unit random vector on $[-1, 1]$.

The adaptive value refers to the error between the predicted result and the actual result using the parameters represented by certain bacteria to calculate the test sample. Many methods can be used to evaluate this error; the root

mean square error evaluation method is adopted in this study:

$$Fv_e = \frac{\sqrt{\left[\sum_{t=1}^{S_0} (y_t - y_t')^2\right]}}{S_0}, \tag{8}$$

where y_t and y_t' represent the predicted and true values of the test sample t, respectively, and S_0 is the number of test samples.

The implementation process is shown in Figure 2.

For the LSSVM regression model, the BFOA is used to optimize the parameters γ and σ^2; the optimization process is as follows:

Step 1: In a certain optimization interval, the initial population is randomly generated. In this study, the number of optimal targets is two; the population is in a two-dimensional space, and the dimensional coordinates of each bacterial individual represent γ and σ^2, respectively.

Step 2: The current position information of the individual is substituted into the LSSVM model, and the sample group is tested for the trial calculation to obtain the adaptive value of the current bacteria according to formula (8). Comparing the global minimum adaption value $Fv_{\min}$ with the expected adaption value Fv_e, if $Fv_{\min} \leq Fv_e$, then proceed to Step (7); otherwise, proceed to Step (3). In this study, $Fv_e = 10^{-2}$.

Step 3: Perform the bacterial trending operation. Within the length of the [−1, 1] interval, random vectors are generated to adjust the position of each individual bacterium, and the adaptive values before and after adjustment are compared. A smaller adaptive value is chosen to maintain the position of the bacterium. A total of N_c tendency operations are performed. In this study, $N_c = 10$.

Step 4: Perform the bacterial replication operation. The total number of bacteria was recorded as $2S_r$, arranged from large to small in accordance with the adaptive value; S_r individuals with larger adaptive values were deleted, and the remaining individuals were duplicated. Return to Step (2) and record the number of replicates $N_{re} = N_{re} + 1$.

Step 5: Perform the bacterial migration operation. When the number of replication operations reaches the maximum ($N_{re\,max} = 15$ in this study), all bacteria in the current region are destroyed, and other regions are randomly selected to reexecute Step (1). This operation effectively avoids the local optimal solution and gives the BFOA a good global property.

Step 6: When the migration operation reaches the expected limit, the iteration is stopped, and the minimum fitness of the current population is recorded. In this study, the limited value of migration operation is set as $N_{ed\,max} = 5$.

Step 7: Output the optimal parameters represented by the bacteria dimension coordinate with the minimum fitness, and use it as the LSSVM parameter to establish the optimal regression model.
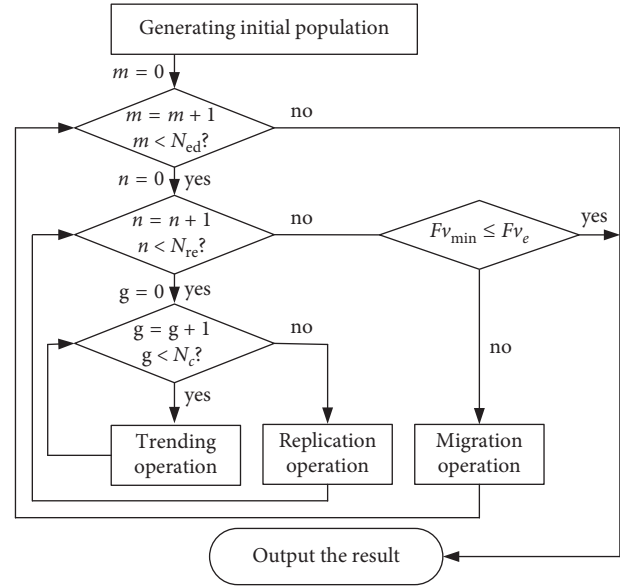
Figure 2: BFOA optimization process.

2.3. Learning Samples for BFOA-LSSVM

2.3.1. Classification Indicators. TSP203 is a geological prediction system for tunnel engineering that can obtain rock mass properties before excavation according to the principle of echo measurement. The propagation speed, waveform, frequency, strength, and direction of the reflected wave signal of the TSP203 geological prediction system are closely related to the corresponding properties and distribution of the weak geological body [22–24]. The resilience value of the rock mass can characterize its strength and supplement the lack of advanced geological prediction results. Considering the feasibility and accuracy of data acquisition in the process of tunnel construction, combined with BQ and RMR classification standards, six indicators were selected as evaluation factors, including rock mass integrity coefficient, reflector distribution coefficient, Poisson's ratio, Young's modulus, groundwater development state, and strength resilience of the rock mass. The classification indicator group established in this study is faster and easier to obtain than traditional classification indicators and more comprehensively reflects the properties of the rock mass.

These six indexes can be obtained by geological advance prediction using TSP203 and measurement of strength resilience of the rock mass. The strength resilience of the rock mass is measured by a springback instrument; the testing time of a single sample point is approximately 30 s, which is convenient. Geological prediction is a necessary link in the tunnel construction process and is completed by a professional survey team. Through analysis and processing of the predicted results data, the classification index information can be obtained.

Considering construction efficiency and the accuracy of prediction results, in the Suqiao tunnel project of the Puyan expressway in Fujian province, China, the consistency interval of the rock mass was verified through continuous

rebound measurement. In this study, the unit distance of sample selection and prediction calculation was determined to be 30 m. The specific calculation method of each index is described as follows.

(1) Integrity coefficient of rock mass

The two-dimensional interpretation results of the advanced geological prediction of a tunnel are shown in Figure 3.

The integrity coefficient of the rock mass is calculated as formula (9).

$$K_r = \left(\frac{V_p}{V_r}\right)^2, \tag{9}$$

where V_p is the P wave velocity of the rock mass, obtained from the interpretation results of geological prediction. V_r is the rock block longitudinal wave velocity, derived from field measurement.

(2) Reflector distribution coefficient

The lower part of Figure 3 shows the negative reflection of seismic waves in the advanced geological prediction forecast. The position of negative reflection symbolizes the weak structural surface in the rock mass; its strength is proportional to the weakening degree of the rock mass. At present, there is no clear evaluation method for the value of the distribution coefficient of the reflection layer, and quantitative evaluation is performed mostly in the form of experience summary [42]. Quantitative criteria for evaluation indicators are shown in Table 1.

(3) Poisson's ratio

In the two-dimensional interpretation results of geological advance prediction, the equivalent Poisson's ratio of the tunnel axial rock mass can be obtained.

(4) Young's modulus

Similar to the Poisson's ratio, the Young's modulus can be obtained from the two-dimensional interpretation of geological advance prediction.

(5) Groundwater development state

TSP prediction results can qualitatively reflect the development state of groundwater to a certain extent and can be quantified, as shown in Table 2. P and S represent the transverse and longitudinal wave intensities of geological prediction, respectively.

(6) Strength resilience of rock mass

The strength resilience value represents the compressive strength property of a material [1]. On the working face in tunnel engineering, the rebound strength of each section of the vault, spandrel, arch waist, arch feet, and the intersection of each position was measured to form a measurement group, and the data distribution law was statistically obtained.

2.3.2. Learning Sample Establishment. In the sampling area, the mean values of the classification indicators were calculated as the sample input before tunnel excavation. After excavation at the same location, the grading value of surrounding rock is calculated by the BQ method and used as the sample output:

$$BQ = 90 + 3R_c + 250K_v - 100\left(K_1 + K_2 + K_3\right), \tag{10}$$

where R_c, K_v, K_1, K_2, and K_3 represent rock hardness, rock mass integrity, groundwater development coefficient, occurrence of main weak structure surface, and initial stress state, respectively. These parameters can be obtained through experiments or field observation after tunnel excavation, and the measurement method is referred to in the literature [1, 17, 29].

This process is repeated $N + t$ times to establish learning samples, including N training samples and t-test samples. The classification of rock mass in this study is subject to the subclassification standard [43], as shown in Table 3.

2.4. Calculation Process of the Reliability Rock Mass Classification. Based on the learning samples, an implicit mapping model was established and used as a response surface function for the surrounding rock reliability grading calculation. The calculation process is shown in Figure 4; the specific steps are as follows.

Step 1: Establish learning samples. Refer to Section 2.3 for sample types and acquisition methods.

Step 2: Establish a nonlinear regression model between classification indicators and rock mass grade using the LSSVM, and select the optimal model parameters through the BFOA.

Step 3: Based on the LSSVM regression model optimized by the BFOA, establish a classification reliability function and calculate using the Monte Carlo method.

Step 4: According to the geological prediction results of the region to be classified, the classification indicators (1)-(5) are read at an interval of 0.5 m, and indicator (6) is measured continuously. Obtain the probability density function for each indicator using the distribution characteristics statistics of the results. Classify the rock mass by the reliability classification method established in this study, and make corresponding construction adjustments based on the classification result.

3. Engineering Applications

3.1. Description of the Study Project. The YA15 section of Puyan expressway connects the town of Zhongxian in Youxi county with the town of Xinkou town in Sanyuan county and the city of Sanming in Fujian province, China, as shown in Figure 5. The section is 9.55 km in length, including five tunnels: Jishan tunnel, Suqiao tunnel, Wugongshan tunnel, Mingxi tunnel, and Leshanting tunnel. The Suqiao tunnel is used as an example to verify the applicability of the rock mass classification method. Suqiao tunnel is a double-hole separated tunnel with a total length of 724 m. It is located in a rock mass
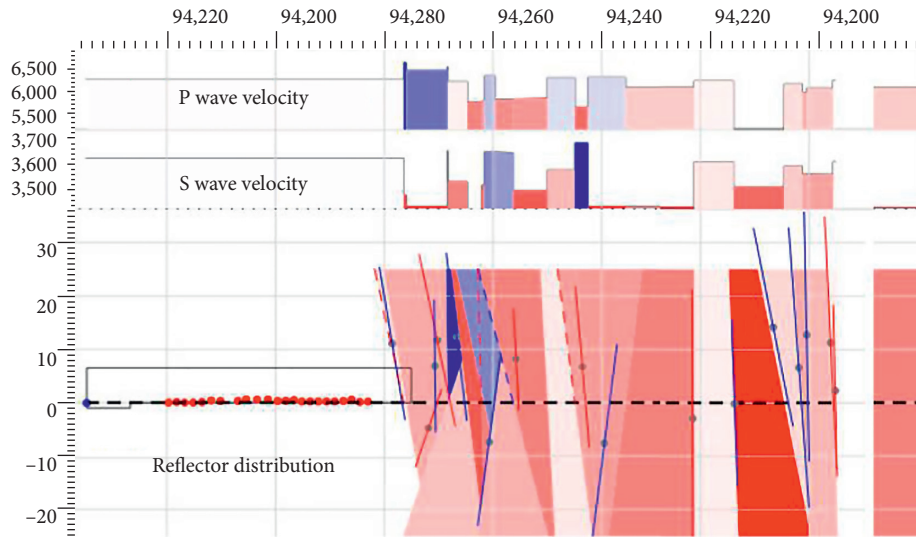
FIGURE 3: Two-dimensional results map of advanced geological prediction.

TABLE 1: Selection rule of reflection surface coefficient.

Reflector distribution	Not obvious	Visible	Obvious	Strong	Extremely obvious
Evaluation value	$0 \sim 0.2$	$0.2 \sim 0.4$	$0.4 \sim 0.6$	$0.6 \sim 0.8$	$0.8 \sim 1.0$

TABLE 2: Selection rule of groundwater development state.

Reflected wave strength case	$S < P$	$S \geq P$	$S >> P$	$S >> P$ and Vp/Vs increases suddenly	$S >> P$ and Vp/Vs increases sharply
Evaluation value	$0 \sim 0.2$	$0.2 \sim 0.4$	$0.4 \sim 0.6$	$0.6 \sim 0.8$	$0.8 \sim 1.0$

TABLE 3: Subclassification criteria of rock mass around tunnels.

Rock classification	I	II	III_1	III_2	IV_1	IV_2	IV_3	V_1	V_2
BQ interval	≥ 551	$550 \sim 451$	$450 \sim 401$	$400 \sim 351$	$350 \sim 316$	$315 \sim 285$	$284 \sim 251$	$250 \sim 211$	$210 \sim 150$
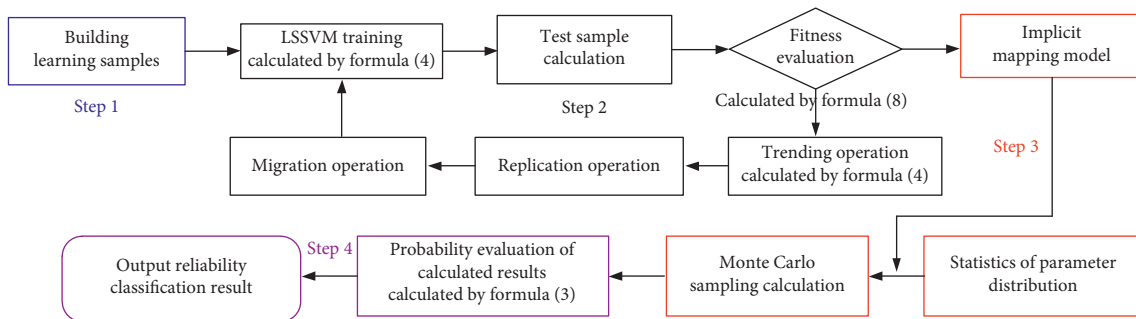
FIGURE 4: Calculation flow chart.

with relatively developed joints in surrounding rock and abundant underground water. The complexity of the construction environment presents high construction difficulty, and dynamic design is necessary in the construction process.

3.2. Sample Construction and LSSVM Machine Learning.
Using the method in Section 2.3, 80 learning samples were established during the construction of the tunnels along the

Puyan expressway; partial learning samples are shown in Table 4. Ten randomly selected samples marked with "*" in the table were used as test samples; the others were used as training samples.

In the mapping relationship obtained through machine learning, the key parameters of the LSSVM obtained through the BFOA are $\gamma = 0.51$ and $\sigma^2 = 1.8$. An additional ten samples were used to test the predictive effect of the model.
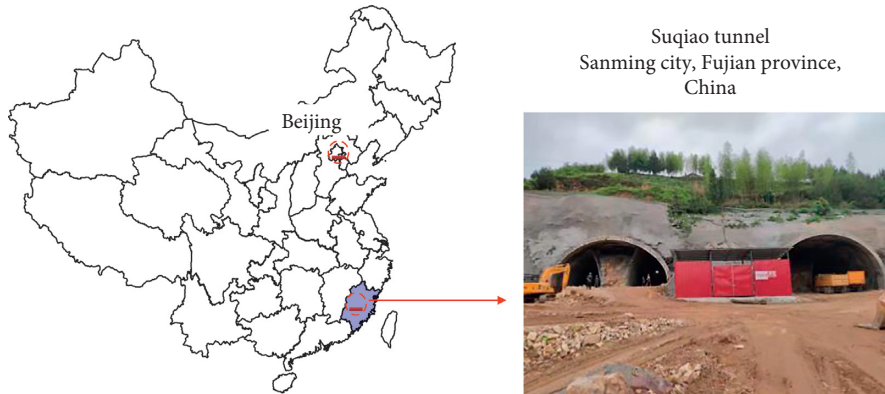
Figure 5: Geographical location of the project.

The calculation results are verified, as shown in Table 5; the adaptive value (root mean square error, calculated by formula (7)) is 3.85. It is observed that the predicted result is consistent with the real value; the maximum relative error is −3.26%, indicating that the parameter optimization is effective.

3.3. Reliability Classification Result Analysis.
According to the method in Section 2.4, parameters are measured for several typical sections; partial statistical results are shown in Figure 6. The bar chart shows the statistical measurement results of the parameters. According to its characteristics, Poisson's ratio conforms to the exponential distribution law, and the strength resilience conforms to the normal distribution law. The probability density function curve of parameter distribution is obtained through data fitting.

Combined with the LSSVM training results in Section 3.2, the reliability classification of surrounding rock was calculated according to the method in Section 2.1. The reliability distribution of the evaluation results in each section is shown in Figure 7.

The reliability classification results provide more complete information than traditional methods. Figure 7(a) shows that the surrounding rocks in the K94 + 653 ~ 683 tunnel area belong to grade V_1, and the subordinate probability of this level is far greater than that of other levels. Therefore, it is believed that the probability results of the other levels are caused by measurement errors or geological variations in small regions, and the engineering construction can be conducted according to grade V_1. In Figure 7(c), the surrounding rocks in the K94 + 743 ~ 773 tunnel area are of similar probability in grade III_2 and grade IV_1, indicating that some of the rock masses in this area have poor properties or weak zones. Therefore, when the tunnel is constructed according to grade III_2, the construction plan should be conservative.

It is observed from the data statistics and comparison in Table 6 that there is a difference between geological survey results before construction and evaluation results after excavation. The reliability classification method proposed in this study can obtain a grade of rock mass around tunnels that is closer to actual conditions, achieve the dependent probability of each grade, and meet the requirements of rock mass quality evaluation during the construction process, providing a basis for the dynamic adjustment of the construction scheme.

The probability density in the calculation results in Table 6 is generally near 50%, which is not high from a statistical perspective. The reliability evaluation of the surrounding rock is calculated according to the distribution statistics of a series of indicators, such as rock mass strength, joints and cracks, and groundwater. In this study, the distribution characteristics of these parameters generally exhibit exponential or normal distribution, and the parameter values tend to be scattered. Therefore, multiple probabilities that are subordinate to different levels of the surrounding rocks often appear in the calculation results, which is the main reason for the generally low probability density, as shown in Figure 7. Another reason for this phenomenon is that the subclass classification standard is adopted in this paper, and the surrounding rock is divided into 9 classes, so the probability of reaching a certain class is not very high. In some areas, the probability densities of two grades of the surrounding rock are close to each other, as shown in Figures 7(c) and 7(d), indicating that the overall nature of the surrounding rock in this area falls between two grades. This result demonstrates that the proposed method can fully reflect the actual state of surrounding rock and provide more abundant data reference for tunnel construction.

4. Discussion

To further clarify the influence law of the relevant parameters in the classification method established in this study, the parameters of the LSSVM model, calculation conditions of the BFOA, and Monte Carlo sampling times are discussed.

4.1. Influence of LSSVM Parameters on Regression Accuracy.
The LSSVM is trained based on the data in Table 4. Adjusting the values of the square root bandwidth σ^2 and the regularization parameter γ, the relative error between the predicted results and the real results under different parameter combinations was calculated, as shown in Figure 8.

TABLE 4: Partial learning samples.

| Serial number | Input parameters | | | | | | Output parameter |
	Integrity coefficient	Reflector distribution coefficient	Poisson's ratio	Young's modulus (N/m^2)	Groundwater development state	Strength resilience (MPa)	BQ evaluation after excavation
1	0.33	0.3	0.38	1.7	0.7	43.6	223
*2	0.61	0.4	0.31	3.4	0.4	62.8	326
3	0.42	0.6	0.41	1.9	0.8	41.5	192
4	0.65	0.4	0.33	2.8	0.4	47.2	262
5	0.5	0.2	0.36	1.8	0.5	44.7	231
*6	0.75	0.3	0.27	7.4	0.2	67.9	384
7	0.7	0.2	0.30	6.6	0.3	60.5	323
8	0.45	0.4	0.35	2.1	0.5	42.3	247
9	0.26	0.5	0.37	1.3	0.8	39.6	208
10	0.45	0.3	0.33	2.8	0.4	46.7	275
.	.	.	.	.	.	.	.
.	.	.	.	.	.	.	.
.	.	.	.	.	.	.	.
*31	0.55	0.1	0.27	8.4	0.2	59.1	368
32	0.4	0.5	0.43	2.1	0.6	44.8	183
*33	0.44	0.3	0.37	2.6	0.4	47.2	282
34	0.57	0.3	0.33	3.5	0.4	52.5	312
35	0.23	0.2	0.45	1.4	0.2	41.2	169
36	0.43	0.4	0.37	2.2	0.4	41.8	232
37	0.35	0.2	0.33	3.1	0.4	50.6	292
38	0.55	0.1	0.26	7.6	0.2	59.9	378
*39	0.23	0.5	0.36	1.7	0.4	42.5	224
40	0.54	0.4	0.34	2.7	0.3	48.5	268
.	.	.	.	.	.	.	.
.	.	.	.	.	.	.	.
.	.	.	.	.	.	.	.
76	0.40	0.3	0.35	2.8	0.4	46.5	282
77	0.41	0.4	0.33	2.2	0.3	47.3	272
*78	0.31	0.3	0.42	1.5	0.5	39.5	194
79	0.20	0.5	0.35	1.9	0.4	41.8	240
80	0.77	0.3	0.31	7.2	0.2	69.4	392

TABLE 5: Verification of hybrid algorithm regression effect.

Serial number	Predicted result	BQ evaluation after excavation	Relative error (%)
1	303.36	308	−1.51
2	169.03	164	3.07
3	298.10	295	1.05
4	371.29	371	0.08
5	230.11	234	−1.66
6	266.06	264	0.78
7	176.39	177	−0.35
8	189.61	196	−3.26
9	296.33	299	−0.89
10	182.88	178	2.74

It is observed in Figure 8 that the accuracy of the regression results is affected by the parameters, and the error distribution is an irregular surface, indicating that it is difficult to determine the values of LSSVM parameters in the training process. Thus, the BFOA is necessary to find the optimal parameters.

4.2. Influence of BFOA Parameters on Convergence Speed. The learning process of samples in Table 4 is repeated, adjusting the value of BFOA parameters to explore the influence of the approach length $C(i)$ and the probability of migration P_{ed} on the convergence result. According to the sample characteristics, the population spatial dimension of the BFOA is six, represented by the six classification parameters in Table 4. The population size is 200, and the upper limit of trend, copy, and migration are all set to 10.

Based on experience, P_{ed} is fixed as 0.3; the convergence curves under different $C(i)$ are calculated as shown in Figure 9. The value of $C(i)$ is the percentage of the total
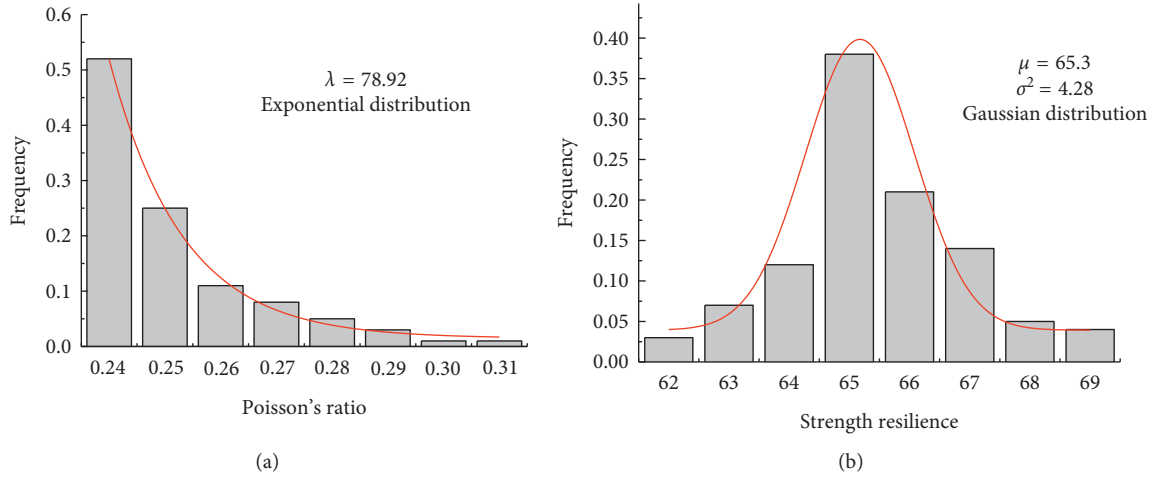
FIGURE 6: Statistics of partial classification indicators of K94 + 713 ~ 743.
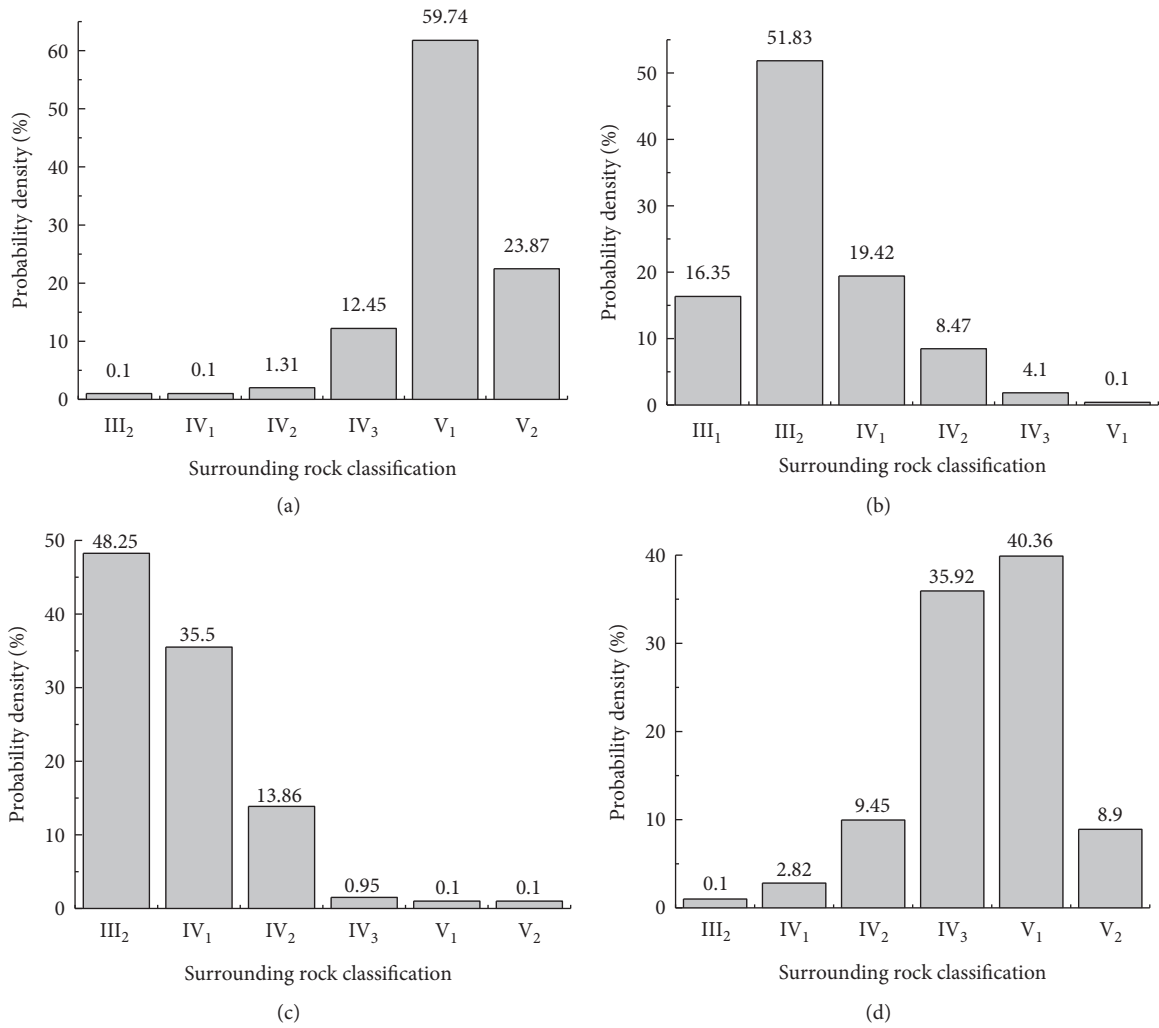
FIGURE 7: Probability classification results of surrounding rock. (a) K94 + 653 ~ 683. (b) K94 + 713 ~ 743. (c) K94 + 743 ~ 773. (d) K94 + 816 ~ 846.

TABLE 6: Classification results verification of Suqiao tunnel.

Group number	Tunnel mileage (YK)	Survey results before excavation	Forecast results		BQ evaluation after excavation
			Classification	Probability (%)	
1	K94 + 653 ~ K94 + 683	V_1	V_1	59.74	V_1
2	K94 + 713 ~ K94 + 743	IV_1	III_2	51.83	III_2
3	K94 + 743 ~ K94 + 773	IV_1	III_2	48.25	III_2
4	K94 + 816 ~ K94 + 846	IV_3	V_1	40.36	V_1
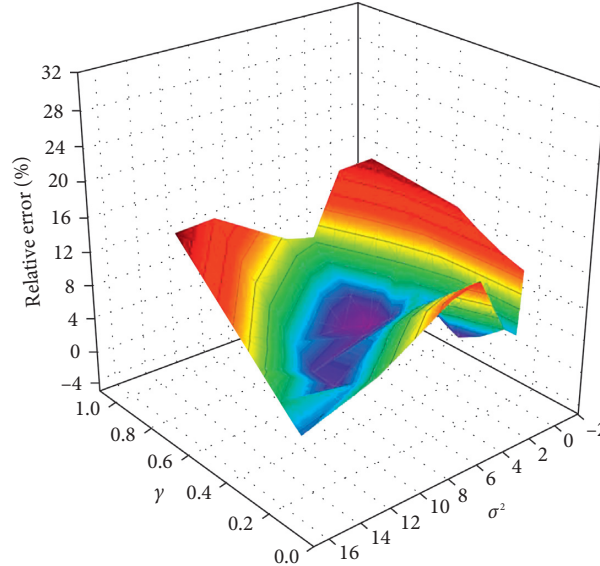
FIGURE 8: The influence law of LSSVM parameters on regression accuracy.

length of the interval. It is observed that the convergence of the algorithm is best when $C(i) = 0.1\%$.

$C(i)$ is fixed as 0.1%, and the convergence curve under different P_{ed} is calculated, as shown in Figure 9. The results show that, in this study, the best value of P_{ed} is 0.25; the convergence effect is weakened if P_{ed} is too large or too small.

4.3. Influence of Monte Carlo Sampling Times on the Stability of Evaluation Results. On the basis of BFOA parameters, the probability evaluation of rock mass grade is conducted for Group 4 in Table 6 under different Monte Carlo sample numbers. Calculations are repeated 20 times for each sampling number; the root mean square error (RMSE) of the calculated results is shown in Figure 10. It is observed that, with increasing sample number, the calculated results gradually become stable. To obtain effective evaluation results, the sample number should not be set less than 10^5.

4.4. Computing Ability Evaluation of BFOA-LSSVM. The samples in Table 5 were calculated by SVM, LSSVM, and BFOA-LSSVM. The error was calculated using formula (11); error analysis of the results is shown in Figure 11.

$$e = \frac{BQ_P - BQ_R}{BQ_R} \times 100\%, \quad (11)$$

where e is the relative error, BQ_P is the predicted value, and BQ_R is the measured value.

It is observed that SVM and LSSVM essentially have the same computing power in terms of classification; the computing accuracy of the LSSVM optimized by the BFOA is effectively improved, demonstrating that the hybrid algorithm established in this study can be effectively applied to the grading evaluation of surrounding rock.

4.5. Application Scope of This Study. The reliability classification method of tunnel surrounding rock established in this study adopted the BQ standard as an example; the BQ value after tunnel excavation is considered to evaluate the rock mass state. In the process of reliability evaluation in Section 2.1, reliability formula (1) uses the BQ value as the classification boundary and the rock grade as the output of LSSVM samples. Similarly, the method is also applicable to other evaluation criteria (such as RMR). It would be necessary to change Table 3 to the RMR criteria and modify the boundary value of formula (1) accordingly. The reliability classification indicators established in Section 2.3 are limited to the research results with current technological means. With the development of geological prediction technology, when more information can be obtained before tunnel excavation, this indicator group can be reasonably improved.

(a)

(b)
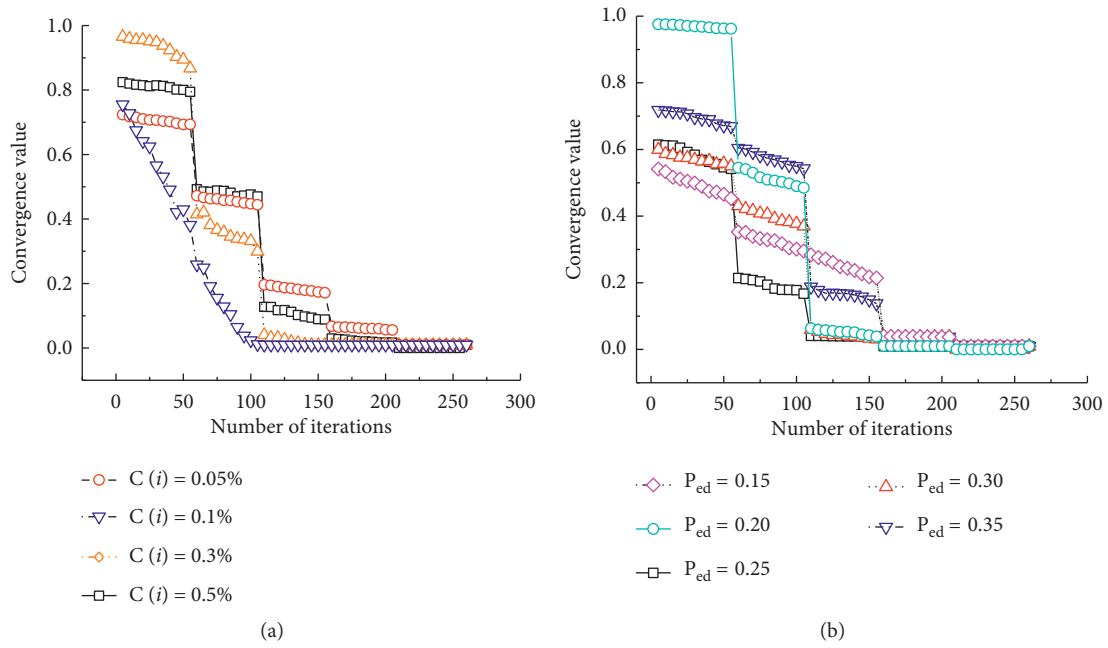
FIGURE 9: The influence law of BFOA parameters on convergence speed.
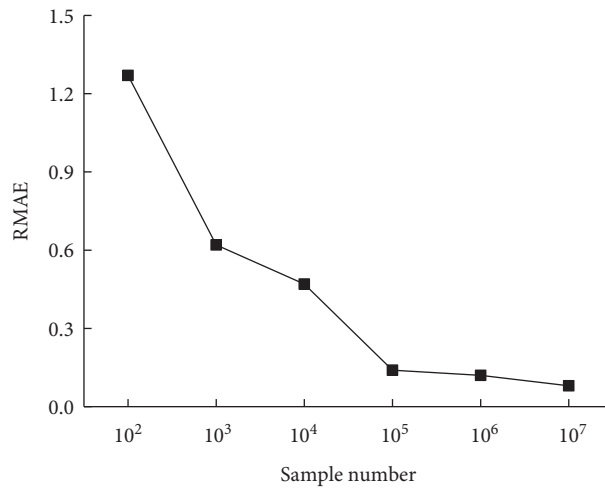
FIGURE 10: The influence law of Monte Carlo sample number.
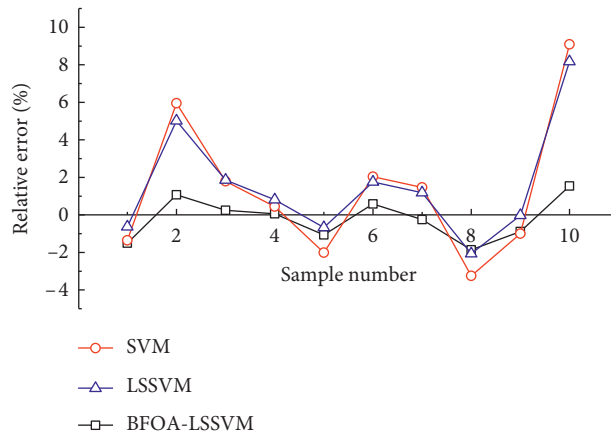
FIGURE 11: Model computing ability verification.

5. Conclusions

We proposed a new reliability classification method based on a hybrid algorithm BFOA-LSSVM, and it is applied to the construction process of the Suqiao tunnel. The following conclusions are drawn from the study.

(1) The new reliability classification method established in this study uses the BFOA-LSSVM as the response surface function, considers geological prediction and rock strength resilience as classification indicators in machine learning samples, and uses the Monte Carlo sampling method to implement the calculation. The results show that this reliability classification method has easy access to parameters and calculation accuracy and can accurately determine the rock mass grade in situ.

(2) The calculation results of the classification method are affected by the setting of relevant parameters. The key parameters of the LSSVM have significant influence on the accuracy of the regression model; and the optimal values obtained from the BFOA are $\gamma = 0.51$ and $\sigma^2 = 1.8$. In the optimization process, the parameters of the BFOA are recommended as $C(i) = 0.1\%$ and $P_{ed} = 0.25$. To ensure the accuracy of the reliability evaluation results, it is suggested that the number of Monte Carlo samples should not be less than 10^5.

(3) As a small-sample learning machine, the LSSVM algorithm was introduced to establish the implicit mapping relationship between classification indicators and rock mass grade. Further, the BFOA was used to automatically search for the best LSSVM model parameters during the sample training process, thereby effectively improving the generalization performance of the LSSVM algorithm.

(4) For the randomness of the classification indicators, the probability evaluation of rock mass classification results was conducted based on reliability theory. This evaluation method effectively avoids the impact of randomness of the classification indicators on the classification results and provides more comprehensive reference for the project.

The classification indicators and related methods of this study are implemented in accordance with the specific engineering background. It should be further optimized and improved according to specific characteristics when applied to different engineering projects. If conditions permit, the number of learning samples should be further expanded, and as many distribution statistical samples of grading indicators as possible should be obtained.

Data Availability

Due to the space limitation, only parts of the learning samples are given in Table 4. The complete sample data can be obtained by sending e-mail to 534821326@qq.com.

Conflicts of Interest

The authors declare that there are no conflicts of interest regarding the publication of this paper.

Acknowledgments

References

[1] K. Liu, B. Liu, and Y. Fang, "An intelligent model based on statistical learning theory for engineering rock mass classification," *Bulletin of Engineering Geology and the Environment*, vol. 78, no. 6, pp. 4533–4548, 2019.

[2] J. Y. Ko and S. S. Jeong, "A study on rock mass classifications and tunnel support systems in unconsolidated sedimentary rock," *Sustainability*, vol. 9, no. 4, p. 573, 2017.

[3] C.-S. Chen and Y.-C. Liu, "A methodology for evaluation and classification of rock mass quality on tunnel engineering," *Tunnelling and Underground Space Technology*, vol. 22, no. 4, pp. 377–387, 2007.

[4] R. Gholami, V. Rasouli, and A. Alimoradi, "Improved RMR rock mass classification using artificial intelligence algorithms," *Rock Mechanics and Rock Engineering*, vol. 46, no. 5, pp. 1199–1209, 2013.

[5] G. E. Wickham, H. R. Tiedman, and E. H. Skinner, "Support determination based on geologic predictions," in *Proceedings of the Process Rapid Excavator Tunneling Conference*, AIME, New York, USA, pp. 43–64, January 1972.

[6] N. Barton, R. Lien, and J. Lunde, "Engineering classification of rock masses for the design of tunnel support," *Rock Mechanics Felsmechanik Mecanique Des Roches*, vol. 6, no. 4, pp. 189–236, 1974.

[7] E. Hoek, P. Marinos, and M. Benissi, "Applicability of the geological strength index (GSI) classification for very weak and sheared rock masses. the case of the Athens Schist formation," *Bulletin of Engineering Geology and the Environment*, vol. 57, no. 2, pp. 151–160, 1998.

[8] A. Palmström, "RMi: a rock mass classification system for rock engineering purposes," Ph. D. thesis, The University of Oslo, Oslo, Norway, 1995.

[9] PalmströmA, "Recent development in rock support estimates by the RMi," *Journal of Rock Mechanical in Tunnel Technology*, vol. 6, no. 1, pp. 1–19, 2000.

[10] Z. T. Bieniawski, "Engineering classification of jointed rock masses," *Siviele Ingenieurswese Civil Engineering*, vol. 15, no. 12, pp. 335–344, 1973.

[11] Z. T. Bieniawski, "Rock mass classification in rock engineering," in *Proceedings International Symposium. Explode for Rock Engineering Johannesburg*, Balkema, Johannesburg, South Africa, pp. 97–106, November 1976.

[12] Z. T. Bieniawski, *Engineering Rock Mass Classification*, Wiley, New York, USA, 1989.

[13] E. N. Ali, "Engineering geology assessment of El-Rabweh landslide, south-east of Amman City, Jordan," *Bulletin of Engineering Geology and the Environment*, vol. 60, no. 2, pp. 109–116, 2001.

[14] K. S. Fukui, "Some attempts for estimating rock strength and rock mass classification from cutting force and investigation of optimum operation of tunnel boring machines," *Rock Mechanics and Rock Engineering*, vol. 39, no. 1, pp. 25–44, 2006.

[15] M. Hashemi, S. Moghaddas, and R. Ajalloeian, "Application of rock mass characterization for determining the mechanical properties of rock mass: a comparative study," *Rock Mechanics and Rock Engineering*, vol. 43, no. 3, pp. 305–320, 2010.

[16] M. Mohammad, F. H. Mohammad, and B. Heydar, "Rock bolt supporting factor: rock bolting capability of rock mass," *Bulletin of Engineering Geology and the Environment*, vol. 76, no. 1, pp. 231–239, 2017.

[17] The National Standards Compilation Group of People's Republic of China, *GB 50218-94 Standard for Engineering Classification of Rock Masses*, China Planning Press, Beijing, China, 1995, in Chinese.

[18] Y. Sun, J. P. Chen, M. Liu, P. Wu, D. Song, and Z. You, "Classification of deep buried long tunnel surrounding rock in karst fracture belt areas," *Electronic Journal of Geotechnical Engineering*, vol. 19, pp. 4765–4776, 2014.

[19] Q. Liu, J. Liu, Y. Pan, X. Kong, and K. Hong, "A case study of TBM performance prediction using a Chinese rock mass classification system-hydropower classification (HC) method," *Tunnelling and Underground Space Technology*, vol. 65, pp. 140–154, 2017.

[20] H. T. Xie, "Bayesian network based expert system for tunnel surrounding rock mass classification," *Applied Mechanics and Materials*, vol. 482, pp. 248–251, 2013.

[21] R. Huang, J. Huang, N. Ju, and Y. Li, "Automated tunnel rock classification using rock engineering systems," *Engineering Geology*, vol. 156, pp. 20–27, 2013.

[22] A. Alimoradi, "A comparison between RMR values of TSP-203 and the real values," M.Sc. thesis in Mine Exploration Engineering, Shahrood University of Technology, Shahrud, Iran, 2006.

[23] A. Alimoradi, A. Moradzadeh, R. Naderi, M. Z. Salehi, and A. Etemadi, "Prediction of geological hazardous zones in front of a tunnel face using TSP-203 and artificial neural networks," *Tunnelling and Underground Space Technology*, vol. 23, no. 6, pp. 711–717, 2008.

[24] S.-S. Salehi, S.-C. Li, L.-P. Li, Z.-Q. Zhou, and J. Wang, "Advance optimized classification and application of surrounding rock based on fuzzy analytic hierarchy process and Tunnel Seismic Prediction," *Automation in Construction*, vol. 37, pp. 217–222, 2014.

[25] A. Zhou, I. Sutskever, and G. E. Hinton, "ImageNet classification with deep convolutional neural networks," *Communications of the ACM*, vol. 60, no. 6, pp. 84–90, 2017.

[26] S. Chatterjee, "Vision-based rock-type classification of limestone using multi-class support vector machine," *Applied Intelligence*, vol. 39, no. 1, pp. 14–27, 2013.

[27] Y. Xue, Z. Li, D. L. Qiu, Y. Zhao, X. Zhang, and B. Zhou, "Classification model for surrounding rock based on the PCA-ideal point method: an engineering application," *Bulletin of Engineering Geology and the Environment*, vol. 78, no. 5, pp. 3627–3635, 2019.

[28] C. F. Zhang, S. G. Tian, Q. Li, and J. Huang, "Evaluation of rock quality of tunnel wall rock based on rough set theory and unascertained measurement theory," *Mathematical Problems in Engineering*, vol. 2018, Article ID 3571028, 10 pages, 2018.

[29] M. Hasanipanah, M. Monjezi, A. Shahnazar, D. Jahed Armaghani, and A. Farazmand, "Feasibility of indirect determination of blast induced ground vibration based on support vector machine," *Measurement*, vol. 75, pp. 289–297, 2015.

[30] H. Guo, H. Nguyen, X. Bui, and D. Jahed Armaghani, "A new technique to predict fly-rock in bench blasting based on an ensemble of support vector regression and GLMNET," *Engineering with Computers*, 2019.

[31] E. Li, J. Zhou, X. Shi et al., "Developing a hybrid model of salp swarm algorithm-based support vector machine to predict the strength of fiber-reinforced cemented paste backfill," *Engineering with Computers*, 2020.

[32] H. Xu, J. Zhou, P. Asteris, D. Jahed Armaghani, and M. M. Tahir, "Supervised machine learning techniques to the prediction of tunnel boring machine penetration rate," *Applied Sciences*, vol. 9, no. 18, p. 3715, 2019.

[33] T. Wen, H. Tang, Y. Wang, C. Lin, and C. Xiong, "Landslide displacement prediction using the GA-LSSVM model and time series analysis: a case study of three Gorges Reservoir, China," *Natural Hazards and Earth System Sciences*, vol. 17, no. 12, pp. 2181–2198, 2017.

[34] Z. G. Zeng, L. H. Guan, and W. Q. Zhu, "Face recognition based on SVM optimized by the improved bacterial foraging optimization algorithm," *International Journal of Pattern Recognition and Artificial Intelligence*, vol. 33, no. 7, Article ID 1956007, 2019.

[35] S. C. Li, P. He, L. P. Li et al., "Reliability analysis method of sub-classification of tunnel rock mass and its engineering application," *Rock and Soil Mechanics*, vol. 39, no. 3, pp. 967–976, 2018, in Chinese.

[36] P. Wei, C. Tang, and Y. Yang, "Structural reliability and reliability sensitivity analysis of extremely rare failure events by combining sampling and surrogate model methods," *Proceedings of the Institution of Mechanical Engineers, Part O: Journal of Risk and Reliability*, vol. 233, no. 6, pp. 943–957, 2019.

[37] S. Rannar, F. Lindgren, P. Geladi, and S. Wold, "A PLS kernel algorithm for data sets with many variables and fewer objects, part 1: theory algorithm," *Chemometrics and Intelligent Laboratory Systems*, vol. 8, no. 4, pp. 111–125, 1994.

[38] B. Sholkopf, K. K. Sung, C. J. C. Burges et al., *Comparing Support Vector Machines with Gaussian Kernels to Radial Basis Function Classificrs*, MIT Press, Cambridge, MA, USA, 1996.

[39] K. M. Passino, "Biomimicry of bacterial foraging for distributed op-timization and control," *IEEE Control System Magazine*, vol. 22, no. 3, pp. 52–67, 2002.

[40] Z. Lu and J. G. Shen, "Bacterial foraging optimization algorithm of improvement," *Computer Systems & Applications*, vol. 23, no. 5, pp. 182–187, 2014.

[41] N. Li and X. J. Lei, "Research on bacterial foraging optimization algorithm," *Computer Technology and Development*, vol. 24, no. 8, pp. 39–44, 2014.

[42] D. H. Qiu, S. Li, W. L. Zhang, and Y. Xue, "Prediction of surrounding rock classification based on TSP203 system and GA-SVM," *Chinese Journal of Rock Mechanical and Engineering*, vol. 29, no. S1, pp. 3221–3226, 2010.

[43] The National Standards Compilation Group of People's Republic of China, *JTG/T D70-2010 Guidelines for Design of Highway Tunnel*, China Communicatons Press, Beijing, China, 2010, in Chinese.

Research Article

A Novel Approach for Automatic Detection of Concrete Surface Voids Using Image Texture Analysis and History-Based Adaptive Differential Evolution Optimized Support Vector Machine

Nhat-Duc Hoang [1,2] and Quoc-Lam Nguyen[2]

[1]*Institute of Research and Development, Duy Tan University, Da Nang 550000, Vietnam*
[2]*Faculty of Civil Engineering, Duy Tan University, Da Nang 550000, Vietnam*

Correspondence should be addressed to Nhat-Duc Hoang; hoangnhatduc@dtu.edu.vn

To inspect the quality of concrete structures, surface voids or bugholes existing on a concrete surface after the casting process needs to be detected. To improve the productivity of the inspection work, this study develops a hybrid intelligence approach that combines image texture analysis, machine learning, and metaheuristic optimization. Image texture computations employ the Gabor filter and gray-level run lengths to characterize the condition of a concrete surface. Based on features of image texture, Support Vector Machines (SVM) establish a decision boundary that separates collected image samples into two categories of no surface void (negative class) and surface void (positive class). Furthermore, to assist the SVM model training phase, the state-of-the-art history-based adaptive differential evolution with linear population size reduction (L-SHADE) is utilized. The hybrid intelligence approach, named as L-SHADE-SVM-SVD, has been developed and complied in Visual C#.NET framework. Experiments with 1000 image samples show that the L-SHADE-SVM-SVD can obtain a high prediction accuracy of roughly 93%. Therefore, the newly developed model can be a promising alternative for construction inspectors in concrete quality assessment.

1. Research Background

The construction industry is widely known as a highly competitive environment within which product quality is a crucial element for a contractor's survival [1]. In addition to the project cost and schedule, quality is a key factor that determines customer satisfaction [2]. Typically, for high-rise concrete buildings, architects and project owners impose strict specifications on the condition of the concrete surface. These requirements often involve the delivery of high-quality concrete surface with minimum presence of surface voids or bugholes [3]. It is because the phenomenon of excessive bugholes is one of the most serious and widely encountered defects on a formed concrete surface [4] and is often a subject of dispute between project owners, architects, and construction contractors [3].

Surface voids (see Figure 1) generally refer to small pits and craters on the concrete surface observed after the process of formwork removal [5]. These defects are brought about by the migration of an entrapped air bubble to the interface between fresh concrete and formwork [6]. The diameter of these voids typically ranges from several millimeters to 15 millimeters and even 25 millimeters in some cases [4]. For more details on the factors leading to the excessive presence of bugholes, readers are guided to the technical paper compiled by ACI [4]. In addition, bugholes are often distributed scatteredly on the concrete surface [7].

A high density of surface voids can result in several harmful effects on the performance of concrete structures:

  (i) Bugholes obviously reduce the aesthetics of concrete structures

  (ii) These voids reduce the protective depth of concrete structures and make the reinforcements inside them more vulnerable to corrosion [6]
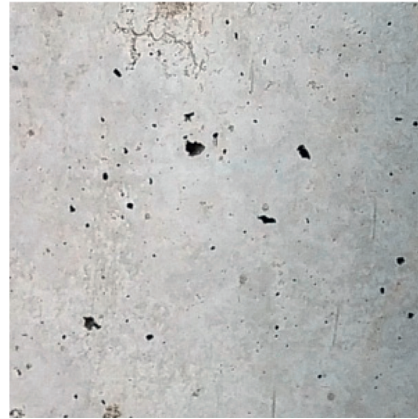
(a)

(b)
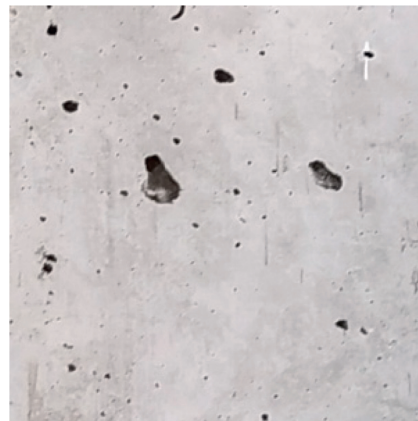
(c)

FIGURE 1: Concrete surface voids.

(iii) For structures retrofitted by fiber-reinforced plastic (FRP) material, excessive voids reduce the adhesion properties of the FRP material applied to the structure surface [8]

(iv) Recent works have pointed out that salt accumulated in surface voids can lead to premature degradation of reinforced concrete structures [6, 9]

(v) Existence of bugholes does increase the cost and time of painting and finishing activities because additional corrections must be performed to achieve a flat concrete surface [5]

Consequently, project owners and architects demand that the number of surface voids on concrete surfaces should be limited to ensure the aesthetic appearance and durability of concrete structures. Currently, in Vietnam, as well as many other countries, inspection works on uncoated concrete surface are manually performed by human technicians. These procedures rely heavily on domain knowledge and the

experience of inspectors with very limiting assistances of intelligent tools [4, 10–12]. Therefore, the current structure condition assessment process is notoriously time-consuming, laborious, and costly [7, 13–18]. It is due to the sheer volume of surface area needed to be inspected, labeled, and reported. Moreover, as pointed out by Perez et al. [19], the manual procedure also brings safety threat to human inspectors since certain concrete surfaces cannot be reached with ease, especially for those which are located at high/roof levels and narrow space. The current practice is also problematic due to the unavoidable inconsistency in inspecting outcomes. The reason is that the assessment process is dependent of subjective judgment of human technicians [2, 3].

Therefore, project owners are increasingly seeking for fast, effective, and consistent tools to better structure condition assessment [19–24]. The assessment outcomes can also enhance communication between various stakeholders regarding the condition of the buildings. Image processing and machine learning with their fast pace of improvement provide feasible means to achieve such goals. Processed digital images and machine intelligence are capable of automating the concrete surface condition assessment, especially the task of detecting surface voids.

Hence, in the recent years, various state-of-the-art methods relying on these two aforementioned techniques have been proposed to tackle the problem of interest. Zhu and Brilakis [25] put forward an image processing approach employing image segmentation and merging/splitting of pixels to detect air pockets on the concrete surfaces. Santos and Julio [26] presented an approach relying on the digital image processing and laser scanning techniques to analyze the roughness of the substrate surface. Fekri-Ershad and Tajeripour [27] put forward a robust approach based on a one-dimensional local binary pattern for recognizing surface defect. da Silva and Štemberk [28] also employed image processing (i.e., image binarization and morphological analyses) and fuzzy logic to inspect the surface quality of self-consolidating concrete for precast members with a focus on the presence of bugholes. Tajeripour and Fekri-Ershad [29] proposed novel one-dimensional local binary patterns used for recognizing abnormalities in stone textures.

Kwasny et al. [30] investigated the influence of rheology on the quality of surface finish of cement-based mortars; the surface voids existing on concrete were then analyzed and quantified via digital image processing. Sadowski and Mathia [31] pointed out the needs of a more useful method for characterizing properties of a heterogeneous concrete surface; the authors also reviewed various image analyzing tools including image filtering and transformation. The effectiveness of wavelet transform and Gaussian image filtering in detecting surface defects were studied by Goïc et al. [32]. Liu and Yang [33] extracted the features of bugholes on a concrete surface via the utilization of the Otsu image binarization method. A texture classification model that incorporates of gray-level run-length matrix and robust illumination normalization techniques has been constructed by Dash and Senapati [34]. Khan et al. [35] relied on ground

penetrating radar to detect water inside the cavities of concrete hollow core slabs.

Yoshitake et al. [36] relied on binary image and color image analyses to detect bugholes distributed on sidewalls and tunnel-lining concrete. Perez et al. [19] utilized the state-of-the-art deep convolutional neural networks (DCNN) for detecting and categorizing building surface defects. A novel instance-level recognition and quantification for concrete surface bughole based on the deep neural network has been recently developed by Wei et al. [18]; this study demonstrates a great capability of machine learning in identifying concrete void surfaces accurately. Nevertheless, the implementation of deep learning models often requires a large number of training samples and a capable computing capability.

As can be seen in the current literature, previous works have mainly relied on image thresholding methods for detecting concrete surface voids. These methods require substantial fine-tuning to adapt to variable characteristics of heterogeneous concrete surface [31]. Due to the complexity of concrete surface background and varying lighting conditions, the accuracy and applicability of image thresholding methods are generally limited. Therefore, image processing techniques should be integrated with advanced machine learning methods to deal with such issues. Hybrid image processing and machine learning tools have demonstrated their outstanding performances in detecting concrete surfaces in previous studies [15, 37–39]. However, too few studies have dedicated to investigating hybrid image processing—machine learning models for the problem of concrete surface void detection. Therefore, the current work is an attempt to fill this gap in the current literature.

In this study, image processing techniques including the Gabor filtering and gray-level run lengths are employed to compute image texture of a concrete surface with and without voids. The texture information is, then, employed by the Support Vector Machines (SVM) to discriminate these two groups of concrete surface. Furthermore, since the training phase of the SVM-based bughole detection model requires a proper setting of the hyperparameters including the penalty coefficient and the kernel function parameter, the history-based adaptive differential evolution with linear population size reduction (L-SHADE) [40, 41] is used to optimize the model training phase. It is because these two hyperparameters strongly influence the learning and predicting performances of the SVM model. If the penalty coefficient and the kernel function parameter are not determined appropriately, the SVM-based surface void detection model cannot deliver the desired due to either overfitting or underfitting phenomena [42, 43].

The subsequent parts of the study are organized in the following order: The second section reviews the research methodology including the employed image processing and computational tools, followed by the third section of the collected image samples; the fourth section presents the proposed hybrid model used for automatic detection of concrete surface voids. The fifth section reports experimental results and concluding remarks of this research are stated in the final section.

2. The Employed Image Processing and Computational Intelligence Methods

Since the surface of a concrete structure contains a diverse form of texture (e.g., intact surface, cracks, bugholes, and stains), texture information of an image region needs to be analyzed to support the surface void detection process. Accordingly, a large image is separated into a number of disjoint image samples of 20×20 pixels via image cropping operations. Subsequently, numerical features are extracted from these samples to construct the machine learning-based surface void recognition model. In this study, the Gabor filter and gray-level run-length methods are used for feature extraction. A novel method combining the SVM and L-SHADE is employed for data classification.

2.1. Gabor Filter (GF). Gabor filters have been widely used for texture segmentation and feature extraction [44, 45]. Due to the capability of optimal joint localization in both spatial and spatial-frequency domains, Gabor filtering is an effective method for recognizing abnormal regions regular textured surfaces [46]. Various successful implementations of this texture discrimination approach have been reported in the literature [45–50]. Basically, a two-dimensional GF is a complex sinusoidal wave modulated by a Gaussian envelope [51]. This filter carries out a localized and oriented frequency analysis of a two-dimensional signal. Mathematically, the response of a GF can be given by the following equation [52]:

$$h(x, y)\exp\left\{-\frac{1}{2}\left[\frac{x^2}{\sigma_x^2} + \frac{y^2}{\sigma_y^2}\right]\right\}\cos(2\pi u_0 x), \qquad (1)$$

where u_0 denotes the frequency of a sinusoidal plane wave along the x-axis. σ_x and σ_y represent the space constants of the Gaussian envelope along the x- and y-axis, respectively.

Notably, Gabor filters with different orientations can be attained via a rigid rotation of the x-y coordinate system [46]. The Fourier transform of the Gabor function described in equation (1) can be expressed as follows [52]:

$$H(u, v) = A\left(\exp\left\{-\frac{1}{2}\left[\frac{(u-u_0)^2}{\sigma_u^2} + \frac{v^2}{\sigma_v^2}\right]\right\} + \exp\left\{-\frac{1}{2}\left[\frac{(u+u_0)^2}{\sigma_u^2} + \frac{v^2}{\sigma_v^2}\right]\right\}\right), \qquad (2)$$

where $\sigma_u = (1/2)\pi\sigma_x$, $\sigma_v = (1/2)\pi\sigma_y$, and $A = 2\pi\sigma_x\sigma_y$. It is noted that this Fourier transform of the Gabor function determines the amount of each frequency component of the original image that is altered by a GF [50].

Notably, to construct Gabor filters used for texture computation, their tuning parameters including the orientation angles and the radial frequency must be specified. As suggested in the previous work of Jain and Farrokhnia [52], $0°$, $45°$, $90°$, and $135°$ orientations can be used. Moreover, given an image with a width of N_w pixels and N_w is a power of 2, the commonly used radial frequency u_0 are as follows: $1\sqrt{2}, 2\sqrt{2}, 4\sqrt{2}, \ldots, (N_w/4)\sqrt{2}$. Based on the response of the GF operations, statistical measurements can be calculated and employed as features for texture discrimination [53].

2.2. Gray-Level Run Lengths. In this study, the task of concrete surface voids is formulated as image texture discrimination. Therefore, information regarding a set of connected image pixels with their distinctive pattern needs to be analyzed. Due to the complex nature of concrete surface, automatic texture discrimination is by no means an easy task. To deal with such challenge, statistical texture analysis models can be employed. Among the statistical models, the gray-level run lengths (GLRL) [54] are very effective to extract information of an image sample based on sizes of homogeneous runs for each gray level [34].

The GLRL was first proposed by Galloway [54] to distill discriminative features from terrain images. This method was, then, applied and improved by various scholars for classifying texture and other tasks in computer vision [34, 55]. This texture computation method relies on the fact that image texture can be considered as a pattern of gray intensity pixel in a particular direction from a reference point [34]. Based on the analysis of second-order statistical information, the GLRL computes the number of gray-level runs which is a collection of linearly adjacent pixels with similar gray intensities.

Given an image sample and a certain direction, a run-length matrix $p(i, j)$ stores the information regarding the number of times that the sample contains a run length j of gray level i [54]. Based on $p(i, j)$ with different orientations (e.g. $0°, 45°, 90°, 135°$), a variety of texture information can be obtained [56].

Based on a constructed run-length matrix, the Short Run Emphasis (SRE), Long Run Emphasis (LRE), Gray-Level Nonuniformity (GLN), Run-Length Nonuniformity (RLN), and Run Percentage (RP) are computed according to the following equations [54, 57, 58]:

$$\text{SRE} = \frac{1}{N_r}\sum_{i=1}^{M}\sum_{j=1}^{N}\frac{p(i, j)}{j^2},$$

$$\text{LRE} = \frac{1}{N_r}\sum_{i=1}^{M}\sum_{j=1}^{N} p(i, j) \times j^2,$$

$$\text{GLN} = \frac{1}{N_r}\sum_{i=1}^{M}\left(\sum_{j=1}^{N} p(i, j)\right)^2, \qquad (3)$$

$$\text{RLN} = \frac{1}{N_r}\sum_{j=1}^{N}\left(\sum_{i=1}^{M} p(i, j)\right)^2,$$

$$\text{RP} = \frac{N_r}{N_p},$$

where M and N are the number of gray levels and the maximum run length. N_r is the total number of runs, and N_p denotes the number of pixels in the image.

Furthermore, Chu et al. [55] extended the original GLRL's measurement with the indices of Low Gray-Level Run Emphasis (LGRE) and High Gray-Level Run Emphasis (HGRE):

$$\text{LGRE} = \frac{1}{N_r} \sum_{j=1}^{N} \sum_{i=1}^{M} \frac{p(i,j)}{i^2},$$

$$\text{HGRE} = \frac{1}{N_r} \sum_{j=1}^{N} \sum_{i=1}^{M} p(i,j) \times i^2. \tag{4}$$

Additionally, Short Run Low Gray-Level Emphasis (SRLGE), Short Run High Gray-Level Emphasis (SRHGE), Long Run Low Gray-Level Emphasis (LRLGE), and Long Run High Gray-Level Emphasis (LRHGE) are put forward by Dasarathy and Holder [59]:

$$\text{SRLGE} = \frac{1}{N_r} \sum_{j=1}^{N} \sum_{i=1}^{M} \frac{p(i,j)}{i^2 \times j^2},$$

$$\text{SRHGE} = \frac{1}{N_r} \sum_{j=1}^{N} \sum_{i=1}^{M} \frac{p(i,j) \times i^2}{j^2},$$

$$\text{LRLGE} = \frac{1}{N_r} \sum_{j=1}^{N} \sum_{i=1}^{M} \frac{p(i,j) \times j^2}{i^2},$$

$$\text{LRHGE} = \frac{1}{N_r} \sum_{j=1}^{N} \sum_{i=1}^{M} p(i,j) \times i^2 \times j^2. \tag{5}$$

2.3. The History-Based Adaptive Differential Evolution with Linear Population Size Reduction.

Differential Evolution (DE) [60, 61] is unquestionably a powerful stochastic search for solving numerical optimization. This stochastic search engine relies on a novel integrated mutation-crossover operation to explore and exploit the search space. During the last decade, various enhancements of the standard DE have been put forward to improve its searching performance [62–65].

Among these enhanced DE variants, the history-based adaptive differential evolution with linear population size reduction (L-SHADE) [40, 41] stands out to be a highly successful version with competitive outcomes reported in various comparative studies [66–69]. Therefore, this improved version of the DE is selected in this study to optimize the performance of the machine learning and image processing-based concrete void detection model.

The L-SHADE algorithm, proposed by Tanabe and Fukunaga [41], improves the original DE algorithm via several aspects. First, the mutation scale (F) and the crossover probability (CR) are fine-tuned adaptively during the optimization process instead of being fixed. Second, an effective mutation strategy called DE/current-to-pbest/1 is implemented to better explore the search space. Third, a population size shrinking strategy is used to both enhance the convergence rate and reduce computational expense.

The operational flow of the L-SHADE algorithm is tersely presented in Figure 2. Since the L-SHADE inherits the main characteristics of the standard DE, its searching process can also be divided into four steps of population initialization, mutation, crossover, and selection. In the first step, based on the prespecified searched domain (lower and upper boundaries), the number of decision variable (N_{DV}), and an initial number of members (N_{M}), a population of N_{M} vectors is randomly created and expected to be distributed evenly throughout the searched space. In the second step, a new candidate solution called a mutated vector is generated via the DE/current-to-pbest/1 strategy. The DE/current-to-pbest/1 strategy used for generating a new candidate solution is given by [40]

$$v_{i,g+1} = x_{i,g} + F_i\left(x_{r1,g} - x_{r2,g}\right) + F_i\left(x_{\text{pbest},g} - x_{i,g}\right). \tag{6}$$

In the third step, the crossover operation is used to combine the information of the newly created candidate and its parent according to the following manner [60]:

$$u_{j,i,g+1} = \begin{cases} v_{j,i,g+1}, & \text{if } \text{rand}_j \leq \text{Cr or } j = rnb(i), \\ x_{j,i,g}, & \text{if } \text{rand}_j > \text{Cr and } j \neq rnb(i). \end{cases} \tag{7}$$

In the last step, a greedy selection which compares the fitness of the candidate solution and its parent is carried out. It is noted that the L-SHADE employs archives of MF and MCR which are vectors of a fixed length H; these two archives store the mean values of the mutation scale and the crossover probability. Moreover, the two sets of SF and SCR store all CR and F values that helped to yield child solutions better than the parents. After each generation, the current population size reduces via the removal of inferior solutions [41].

2.4. Support Vector Machine.

Support Vector Machines (SVM), constructed on the basis of the statistical learning theory, are a robust method for establishing pattern classification models. Introduced by Vapnik [70], the SVM have gained popularity in the research community via various works which reported their successful implementations [71–73]. It is because this machine learning method features significant advantages including resilience to noisy data via a framework of maximum margin construction and capability of handling nonlinearly separable data by means of kernel tricks. Furthermore, the learning phase of the SVM is bolt down to solving a convex optimization problem; this guarantees a global convergence and avoids being trapped in local optima [74].

The concept of the SVM used for concrete surface void detection is demonstrated in Figure 3. The model deals with nonlinearly separable data by mapping the data from the original input space to a high-dimensional feature space; in such high-dimensional feature space, linear separability can become feasible.

Given a training dataset $\{x_k, y_k\}_{k=1}^{N}$ with a numerical feature $x_k \in R^n$ and corresponding class categories $y_k \in \{-1, +1\}$, an SVM model establishes a classification boundary to distinguish data from a positive class +1 (surface void) and a negative class −1 (nonsurface void). It is noted that a numerical feature x_k is actually texture information extracted from an image sample using the Gabor filter and the GLRL. To establish such classification
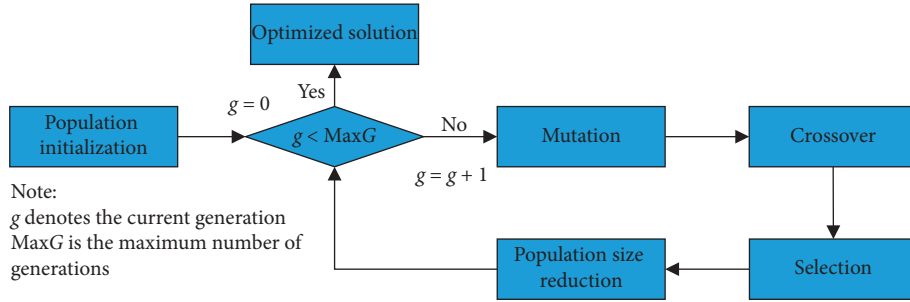
FIGURE 2: The operational flow of the L-SHADE algorithm.

- ● Nonsurface void
- ■ Surface void

- --- Nonlinear decision boundary
- — Hyperplane used for data classification
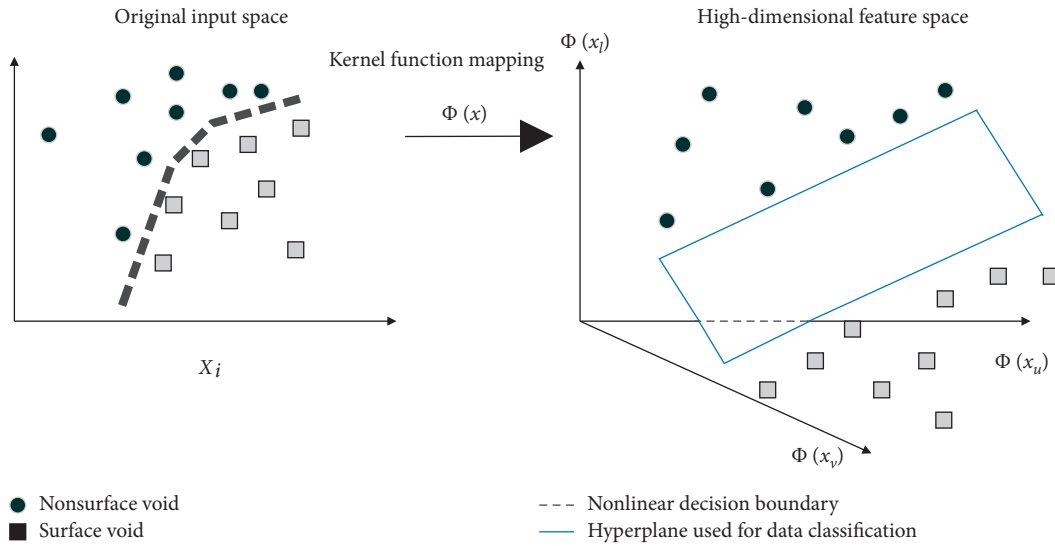
FIGURE 3: Demonstration of an SVM model.

boundary, it is required to solve the following nonlinear programming problem [43]:

$$\text{Minimize} \quad J_p(w, e) = \frac{1}{2}w^T w + c\frac{1}{2}\sum_{k=1}^{N} e_k^2$$

$$\text{Subjected to} \quad y_k\left(w^T \varphi(x_k) + b\right) \geq 1 - e_k, \quad k = 1, \ldots, N, e_k \geq 0, \tag{8}$$

where $w \in R^n$ is a normal vector to the classification hyperplane and $b \in R$ represents the model bias; $e_k > 0$ is slack variables; c represents a penalty constant; and $\varphi(x)$ denotes the nonlinear data mapping used for dealing with nonlinear separable data.

It is noted that the SVM does not necessitate an explicit expression of the data mapping function $\varphi(x)$. The quantity of interest is the product of $\varphi(x)$ in the input space which is defined as a Kernel function:

$$K(x_k, x_l) = \varphi(x_k)^T \varphi(x_l). \tag{9}$$

The Radial Basis Function Kernel (RBFK) is often employed and it is shown as follows:

$$K(x_k, x_l) = \exp\left(-\frac{\|x_k - x_l\|^2}{2\sigma^2}\right), \tag{10}$$

where σ represents a tuning parameter of the RBFK.

After solving the aforementioned nonlinear programming, the SVM model used for data classification can be tersely presented in the following equation:

$$y(x_l) = \text{sign}\left(\sum_{k=1}^{SV} \alpha_k y_k K(x_k, x_l) + b\right), \tag{11}$$

where α_k denotes the solution of the dual form of the aforementioned nonlinear programming. SV represents the number of support vectors (the number of $\alpha_k > 0$).

3. The Image Samples of the Concrete Surface

To construct the SVM machine learning model used for concrete surface void recognition, the set of image samples capturing the texture of concrete structures must be prepared. This image set includes samples which contain concrete bugholes and samples without such defect. Accordingly, a set of 1000 image samples with assigned ground

truth categories has been manually collected via field trip to several construction sites in Danang city (Vietnam). To guarantee a balanced dataset, the numbers of the negative (without surface voids) and positive (having surface voids) samples are both 500. The categories of image samples have been determined by human inspectors. Herein, the label = -1 means the negative class and the label = 1 denotes a positive class. It is noted that the collected images in this study have been taken by using the Cannon EOS M10 (CMOS 18.0 MP) and Nikon D5100 (CMOS 16.2 MP). To enhance the speed of the texture computation phase and to ensure the consistency of an image region, the image size has been set to be 20x20 pixels. The image samples are illustrated in Figure 4. Additionally, to better cope with the diversity of the concrete surface, the negative class of nonsurface void deliberately includes samples of sound concrete surface, cracks, and stains.

4. The Proposed Hybridization of Image Processing, Machine Learning, and Metaheuristic for Detecting Concrete Surface Voids

The proposed hybridization of image processing, machine learning, and metaheuristic optimization used for detection of concrete surface voids is presented in this section of the study. The integrated model is denoted as L-SHADE-SVM-SVD. The overall model structure is graphically summarized in Figure 5. The L-SHADE-SVM-SVD model is developed in the Visual C#.NET environment (Framework 4.6.2) and run in ASUS FX705GE—EW165T (Core i7 8750H, 8 GB Ram, 256 GB solid-state drive).

The L-SHADE-SVM-SVD operation can be divided into three steps:

(i) Image texture computation: the step computes texture information of concrete surface obtained from image samples stored in training and testing subsets. The first subset includes 90% of the collected samples and is used for model construction. The second set occupies 10% of the collected samples and is reserved for validating the model predictive capability. Image texture including the Gabor filter and GLRL is computed and used as the numerical feature.

(ii) The L-SHADE metaheuristic optimization: as mentioned earlier, the model training and pattern classification phases of the SVM require appropriate values of the penalty coefficient (c) and the kernel function parameter (σ). The former hyperparameter dictates how the loss function of the SVM increases due to misclassified data points. The latter hyperparameter affects the smoothness of the decision boundary. Therefore, these hyperparameters strongly influence the learning and predictive performance of the SVM-based bughole detection model. The selection of the penalty coefficient (c) and the kernel function parameter (σ) can be

formulated as an optimization task within which metaheuristic algorithms can be employed. Based on the previous comparative works [41, 67, 68, 75], this study employs the L-SHADE metaheuristic algorithm for conducting the SVR model optimization. This DE variant first generates an initial population of hyperparameters in a random manner. In each generation, the optimization algorithm explores and exploits the search space to gradually guide the population to a better solution representing SVM models with good predictive capability.

(iii) The SVM-based pattern classification: based on the optimized solution of the model hyperparameters, the SVM model is employed to construct a decision surface that is capable of distinguish concrete surface with and without voids. Notably, the SVM model is constructed via a built-in function supported by the Accord.NET Framework [76].

It is also noted that, to optimize the SVM model performance, a K-fold cross validation (with $K = 5$) is used. Using this cross validation, the whole dataset is separated into 5 mutual exclusive subsets. In each of the five runs, one subset is used for model testing and the other subsets are employed for model training. The average predictive performance is used to quantify the model generalization capability. Accordingly, the following cost function is used by the L-SHADE-SVM-SVD:

$$\mathrm{CF} = \frac{\sum_{k=1}^{K}\left(FNR_k + FPR_k\right)}{K}, \tag{12}$$

where FNR_k and FPR_k denote the false negative rate (FNR) and the false positive rate (FPR) obtained from kth run, respectively.

The FNR and FPR indices are computed as follows:

$$\mathrm{FNR} = \frac{\mathrm{FN}}{\mathrm{FN} + \mathrm{TP}},$$
$$\mathrm{FPR} = \frac{\mathrm{FP}}{\mathrm{FP} + \mathrm{TN}}, \tag{13}$$

where FN, FP, TP, and TN are false negative, false positive, true positive, and true negative data samples, respectively.

Moreover, it is noted that, to compute the Gabor filter, it is necessary to convert the original image to grayscale ones. Based on the recommendations of Jain and Farrokhnia [52], four values of orientations (0°, 45°, 90°, and 135°) and four values of radial frequency ($1\sqrt{2}, 2\sqrt{2}, 4\sqrt{2}, 8\sqrt{2}$) have been employed to calculate the Gabor filtering features. In this study, the Gabor filters are implemented with the assistance of built-in functions provided by the Accord.NET Framework [76]. Based on the filtered image, the following statistical indices can be measured to characterize image texture:

(i) The mean of the Gabor filter response:

(a)

(b)
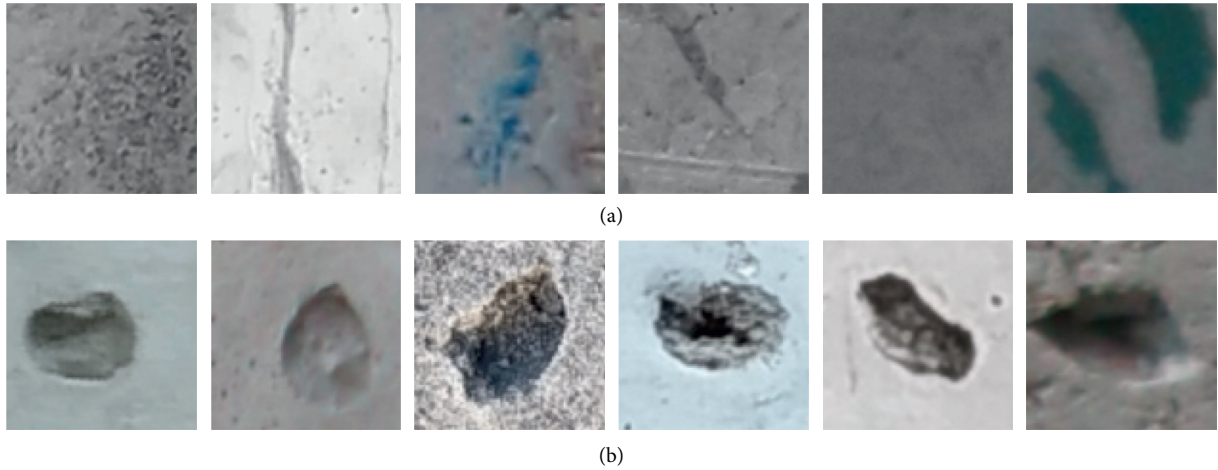
FIGURE 4: The collected image samples: (a) nonsurface void and (b) surface void.
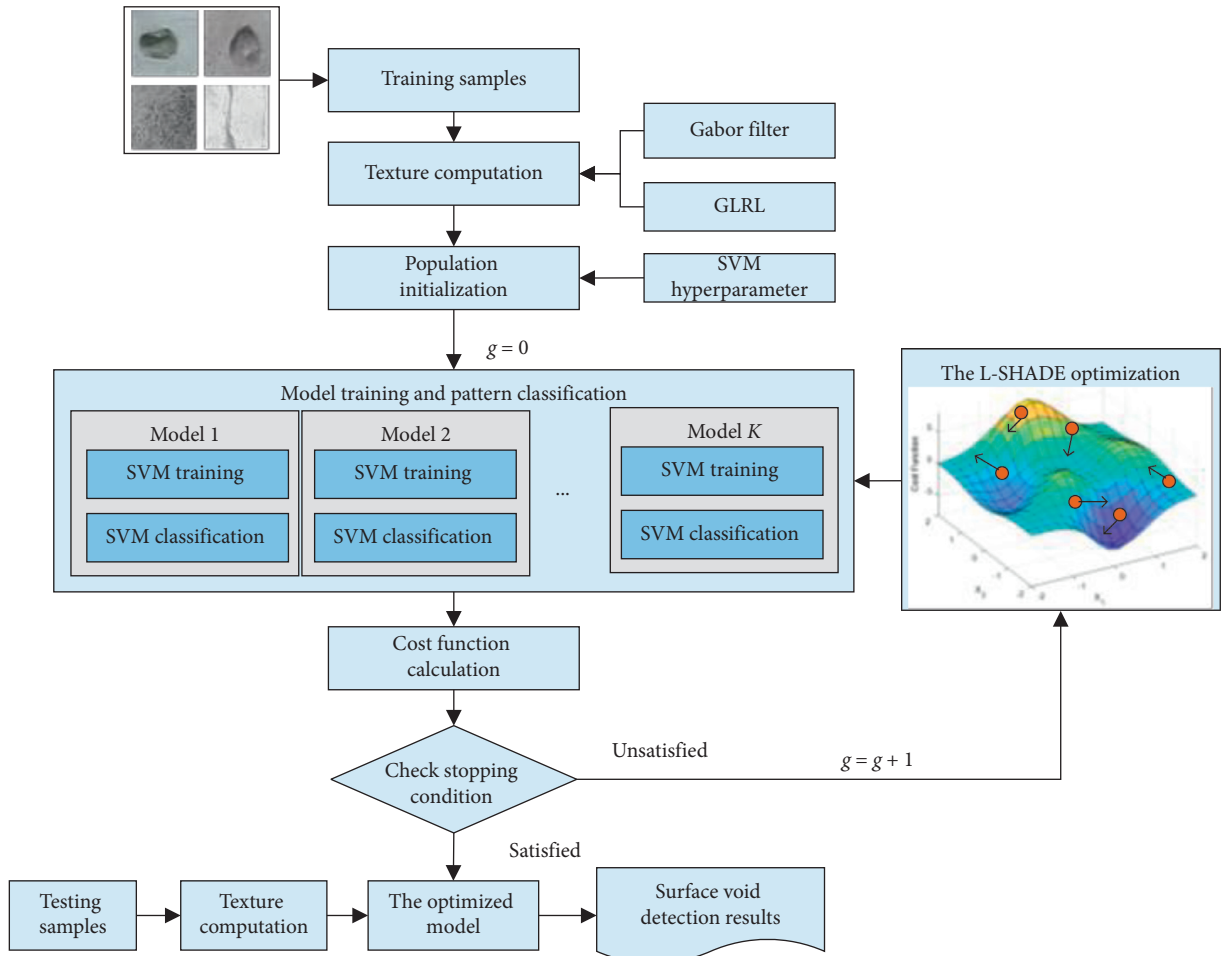
FIGURE 5: The proposed L-SHADE-SVM-SVD used for automatic detection of concrete surface voids.

$$\text{Mean}_{\text{GaborFilter}} = \frac{\sum_{i=0}^{H_{\text{IM}}-1} \sum_{j=0}^{W_{\text{IM}}-1} \text{GFR}(i, j)}{W_{\text{IM}} \times H_{\text{IM}}}, \quad (14)$$

where H_{IM} and W_{IM} are the width and height of an image sample, respectively. $\text{GFR}(i, j)$ denotes the Gabor filter response at a pixel (i, j).

(ii) The standard deviation of the Gabor filter response:

$$\text{STD}_{\text{GaborFilter}} = \frac{\sum_{i=0}^{H_{\text{IM}}-1} \sum_{j=0}^{W_{\text{IM}}-1} \left[\text{GFR}(i,j) - \text{Mean}_{\text{GaborFilter}} \right]^2}{W_{\text{IM}} \times H_{\text{IM}}}.$$

$$(15)$$

(iii) The skewness of the Gabor filter response [77]:

$$\text{Skewness}_{\text{GaborFilter}} = \frac{\left(1/(W_{\text{IM}} \times H_{\text{IM}})\right) \sum_{i=0}^{H_{\text{IM}}-1} \sum_{j=0}^{W_{\text{IM}}-1} \left[\text{GFR}(i,j) - \text{Mean}_{\text{GaborFilter}} \right]^3}{\left[\left(1/(W_{\text{IM}} \times H_{\text{IM}} - 1)\right) \sum_{i=0}^{H-1} \sum_{j=0}^{W-1} \left\{ \text{GFR}(i,j) - \text{Mean}_{\text{GaborFilter}} \right\}^2 \right]^{3/2}}. \quad (16)$$

(iv) The entropy of the Gabor filter response:

$$\text{Entropy}_{\text{GaborFilter}} = -\sum_{i=0}^{\text{NDV}-1} \text{FOH}_{\text{Filter}} \times \log_2 \left[P_{\text{Filter}} \right], \quad (17)$$

where $\text{FOH}_{\text{Filter}}$ represents the first-order histogram of the Gabor filter response. Moreover, $\text{NDV} = 256$ denotes the number of discrete gray intensity values for an 8 bit grayscale image.

Because 16 Gabor filters are employed for computing image texture and each filter has four statistical indices (the mean, standard deviation, skewness, and entropy), the number of Gabor filtering features is 64. Moreover, since there are four orientations $(0°, 45°, 90°, \text{ and } 135°)$ used for GLRL matrix construction and each GLRL matrix has 11 features, the number of GLRL features is 44 [57]. Accordingly, the total number of features used for the SVM pattern classification is $64 + 44 = 108$.

Additionally, to facilitate the data classification based on the SVM, the established dataset has been normalized by the Z-score equation given by

$$X_{ZN} = \frac{X_o - m_X}{s_X}, \quad (18)$$

where X_o and X_{ZN} represent the original and the standardized input feature, respectively. m_X and s_X denote the mean and the standard deviation of the original input feature, respectively.

5. Experimental Result and Comparison

As mentioned earlier, to train and validate the hybrid model used for concrete surface void detection, the collected dataset has been divided into two packages of training and testing datasets. The training dataset (90% of the original dataset) is used for model construction, and the testing dataset is reserved for evaluating the model performance when predicting novel image samples. Moreover, to diminish the effect of randomness in data sampling and to reliably assess the predictive capability of the newly developed method, the training/testing data sampling has been performed 20 times. In each time of running, 10% of the original dataset is randomly drawn out to form the testing dataset; the rest of the original dataset is used for model construction. The datasets used for time of model running are illustrated in Table 1. Herein, the column of sample index expresses the number of data samples employed in the training and testing datasets.

In addition, to quantify the predictive capability of the proposed L-SHADE-SVM-SVD, the classification accuracy rate (CAR), precision, recall, negative predictive value (NPV), and F1 score are computed from the four basic results of TP, TN, FP, and FN. These performance indicators are presented as follows [78]:

$$\begin{aligned} \text{CAR} &= \frac{\text{TP} + \text{TN}}{\text{TP} + \text{TN} + \text{FP} + \text{FN}} \times 100\%, \\ \text{Precision} &= \frac{\text{TP}}{\text{TP} + \text{FP}}, \\ \text{Recall} &= \frac{\text{TP}}{\text{TP} + \text{FN}}, \\ \text{NPV} &= \frac{\text{TN}}{\text{TN} + \text{FN}}, \\ \text{F1 Score} &= \frac{2\text{TP}}{2\text{TP} + \text{FP} + \text{FN}}. \end{aligned} \quad (19)$$

The L-SHADE with an initial population size of 30 and a maximum number of searching generations of 100 was utilized to seek for the most appropriate set of the SVM model's hyperparameters. The searching progress of the L-SHADE metaheuristic is graphically presented in Figure 6. The optimization process yields the penalty parameter $(c) = 3.712$ and the kernel function parameter $(\sigma) = 6.031$. In addition, the statistical outcomes of the L-SHADE-SVM-SVD (mean and standard deviation) using the hyperparameters found by the L-SHADE metaheuristic are reported in Table 2. The averaging values of the CAR, precision, recall, NPV, and F1 score are 92.600%, 0.911, 0.942, 0.940, and 0.926, respectively. In addition, the average runtime of the proposed approach is roughly 13.30 seconds. Since there are 100 data samples in the testing set, the computational time used for classifying one testing data sample is approximately 0.13 seconds.

Furthermore, to demonstrate the predictive ability of the newly developed L-SHADE-SVM-SVD model used for concrete surface void recognition, the model performance has been compared to those of Deep Convolution Neural

TABLE 1: The training and testing datasets.

Datasets	Sample index	Features							Class label
		F1	F2	F3	...	F106	F107	F108	
Training	1	108.115	33.580	−15.236	...	6866.946	11.141	658.625	−1
	2	109.645	33.763	−18.768	...	5026.965	11.007	381.245	−1
	...	...	...	...	...	...	...	...	...
	899	106.063	32.555	−14.066	...	32167.854	10.600	640.701	1
	900	108.305	33.135	−13.449	...	31379.524	10.674	1039.198	1
Testing	1	108.435	32.954	−16.630	...	9425.744	11.802	2016.670	−1
	2	105.565	30.844	−16.665	...	8383.504	11.505	1440.862	−1
	...	...	...	...	...	...	...	...	...
	99	107.228	32.628	−12.087	...	30558.259	10.551	631.624	1
	100	107.223	32.418	−13.006	...	30292.417	10.575	514.372	1
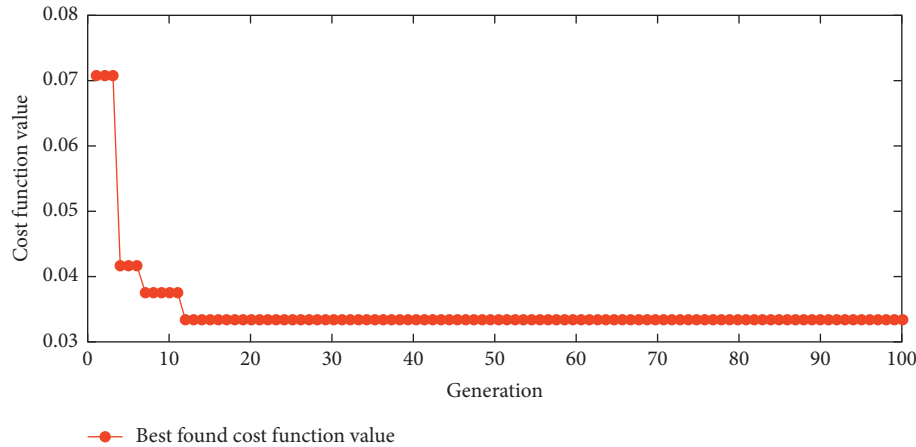
FIGURE 6: The L-SHADE optimization process.

TABLE 2: Prediction performance of the L-SHADE-SVM-SVD.

Phases	Indices	CAR (%)	TP	TN	FP	FN	Precision	Recall	NPV	F1 score
Training	Mean	97.417	437.200	439.550	9.550	13.700	0.979	0.970	0.970	0.974
	Std.	0.222	4.938	5.753	1.605	1.302	0.004	0.003	0.003	0.002
Testing	Mean	92.600	46.200	46.400	4.500	2.900	0.911	0.942	0.940	0.926
	Std.	2.761	4.873	5.305	1.878	2.125	0.037	0.040	0.044	0.027

Network (DCNN) models [79–81] with stochastic gradient descent with momentum (Sgdm) [82], Adaptive Moment Estimation (Adam) [83], and root mean square propagation (Rmsprop) [84]. The three DCNN models are denoted as DCNN-Sgdm, DCNN-Adam, and DCNN-Rmsprop and are implemented via the MATLAB deep learning toolbox [85]. Via a trial-and-error process, appropriate configurations of the DCCN model are selected and shown in Table 3.

Moreover, the minibatch Backpropagation Neural Network (MB-BPNN) [86, 87] is also employed as a benchmark method. The MB-BPNN model has been developed in Visual C#.NET by the authors and trained with the minibatch mode [87, 88]; the batch-size is selected to be 32. and the number of neurons in the hidden layer is set to be $(2/3)D_X + C_N$, as suggested by Heaton [89]; D_X and C_N denote the numbers of features and outputs, respectively. The MB-BPNN model is, then, trained with the sigmoidal

TABLE 3: Configurations of the DCNN models.

CNN layers	Convolution layers		Pooling layers
	Filter number	Filter size	Filter size
1	36	10	2
2	36	8	2
3	36	4	2
4	36	2	2

activation function with the maximum number of epochs = 1000 epochs and the learning rate = 0.01.

The prediction results of the proposed L-SHADE-SVM-SVD model, as well as the benchmark models, are summarized in Table 4 and graphically presented as box plots in Figure 7. As can be seen from the prediction results, the performance of the L-SHADE-SVM-SVD (CAR = 92.600%, Precision = 0.911, Recall = 0.942, NPV = 0.940, and F1 score = 0.926) is better than that of the DCNN-Rmsprop

TABLE 4: Prediction result comparison.

Phase	Indices	L-SHADE-SVM-SVD		DCNN-Rmsprop		DCNN-Adam		DCNN-Sgdm		MB-BPNN	
		Mean	Std.	Mean	Std.	Mean	Std.	Mean	Std.	Mean	Std.
Training	CAR (%)	97.417	0.222	87.922	2.585	89.211	1.937	87.756	6.165	86.763	6.889
	TP	437.200	4.938	369.000	25.984	390.250	17.693	375.650	40.359	333.900	63.570
	TN	439.550	5.753	422.300	20.683	412.650	21.755	414.150	21.866	360.200	9.540
	FP	9.550	1.605	27.700	20.683	37.350	21.755	35.850	21.866	66.100	63.570
	FN	13.700	1.302	81.000	25.984	59.750	17.693	74.350	40.359	39.800	9.540
	Precision	0.979	0.004	0.934	0.044	0.916	0.042	0.912	0.064	0.835	0.159
	Recall	0.970	0.003	0.820	0.058	0.867	0.039	0.835	0.090	0.895	0.012
	NPV	0.970	0.003	0.842	0.041	0.875	0.029	0.851	0.065	0.901	0.024
	F1 score	0.974	0.002	0.871	0.030	0.889	0.019	0.870	0.075	0.852	0.132
Testing	CAR (%)	92.600	2.761	88.350	3.133	86.900	4.204	86.800	6.178	85.700	7.248
	TP	46.200	4.873	41.700	3.246	42.200	3.792	40.900	4.767	40.900	8.130
	TN	46.400	5.305	46.650	2.323	44.700	3.326	45.900	2.674	44.800	2.587
	FP	4.500	1.878	3.350	2.323	5.300	3.326	4.100	2.674	9.100	8.130
	FN	2.900	2.125	8.300	3.246	7.800	3.792	9.100	4.767	5.200	2.587
	Precision	0.911	0.037	0.929	0.045	0.893	0.057	0.909	0.065	0.818	0.163
	Recall	0.942	0.040	0.834	0.065	0.844	0.076	0.818	0.095	0.890	0.042
	NPV	0.940	0.044	0.852	0.049	0.856	0.059	0.839	0.067	0.896	0.052
	F1 score	0.926	0.027	0.877	0.036	0.865	0.044	0.859	0.076	0.839	0.137
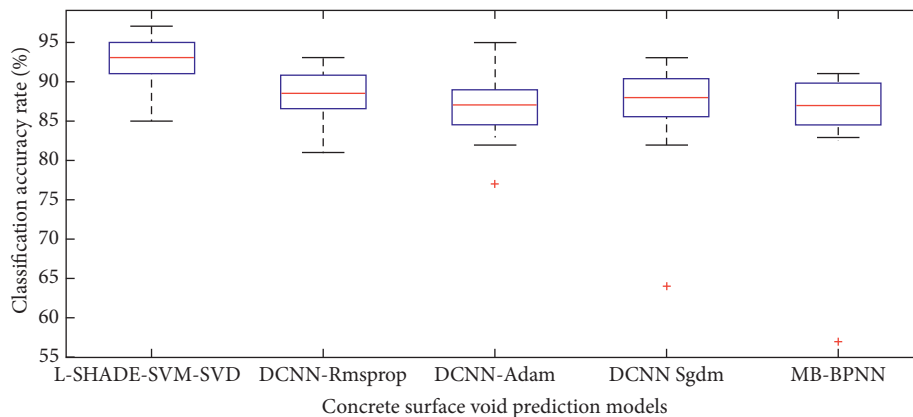
FIGURE 7: Box plots of model performances.

(CAR = 88.350%, Precision = 0.929, Recall = 0.834, NPV = 0.852, and F1 score = 0.877), DCNN-Adam (CAR = 86.900%, Precision = 0.893, Recall = 0.844, NPV = 0.856, and F1 score = 0.865), DCNN-Sgdm (CAR = 86.800%, Precision = 0.909, Recall = 0.818, NPV = 0.839, and F1 score = 0.859), and MB-BPNN (CAR = 85.700%, Precision = 0.818, Recall = 0.890, NPV = 0.896, and F1 score = 0.839).

In addition, the two-sample t-test [90] is utilized in this study to better confirm the statistical significance of the model predictive capabilities. This statistical test is often employed to inspect the null hypothesis that the model prediction performances of two machine learning models may be drawn from normal distributions with equal means. Herein, the significant level (p value) of the test is set to be 0.05, and the results of the t-test are reported in Table 5. As can be observed from this table, the p values <0.05 reliably reject the null hypothesis. This fact confirms that the proposed L-SHADE-SVM-SVD is best suited for the task of detecting concrete surface bugholes.

TABLE 5: The t-test outcomes of pairwise model comparisons.

Model comparison	Test outcome	p value
L-SHADE-SVM-SVD vs. DBNN-Rmsprop	Significant	0.00005
L-SHADE-SVM-SVD vs. DBNN-Adam	Significant	0.00001
L-SHADE-SVM-SVD vs. DBNN-Sgdm	Significant	0.00046
L-SHADE-SVM-SVD vs. MB-BPNN	Significant	0.00030

6. Conclusions

Detection of a concrete surface is crucial for inspecting quality of cast-in-place concrete elements. To enhance the productivity and eliminate subjective judgment of concrete quality inspection works, this research proposes an intelligent method that hybridizes state-of-the-art image processing, machine learning, and metaheuristic methods. Image texture is used as the input feature that characterizes the states of a concrete surface. Gabor filter and GLRL-based texture information is computed and employed by the SVM

to construct a decision boundary that divides the input into two categories of no surface void (negative class) and surface void (positive class).

In addition, to optimize the SVM model training phase, the L-SHADE metaheuristic is used. This metaheuristic algorithm autonomously searched for the most appropriate set of the SVM model's hyperparameters including the penalty coefficient and the kernel function parameter. The integrated model, named as L-SHADE-SVM-SVD, has been developed and compiled in the Visual C#.NET framework to ease its implementation. The experimental outcome using 1000 image samples and a repeated data sampling with 20 runs demonstrate that the newly developed L-SHADE-SVM-SVD is able to attain good predictive performances (CAR = 92.600%, Precision = 0.911, Recall = 0.942, NPV = 0.940, and F1 score = 0.926). Thus, the L-SHADE-SVM-SVD can be a helpful tool to assist construction inspectors in assessing concrete surface quality.

Nevertheless, since the current L-SHADE-SVM-SVD model aims at recognizing the status of no surface void and surface void, the task of localizing surface voids on a concrete surface image can be performed in a future study. In addition, other future directions of the current works may include the extension of the collected image dataset to enhance the generalization of the developed machine learning model, investigation of other advanced metaheuristic algorithms to improve the surface void detection performance, and employment of other performance measurements such as model runtime [91].

Data Availability

The image dataset and the compiled L-SHADE-SVM-SVD program used to support the findings of this study have been deposited in the repository of github (https://github.com/NhatDucHoang/L-SHADE-SVM-SVD).

Conflicts of Interest

The authors confirm that there are no conflicts of interest.

Acknowledgments

References

[1] D. W. Halpin and B. A. Senior, *Construction Management*, Wiley, Hoboken, NJ, USA, 4th edition, 2010.

[2] C. Laofor and V. Peansupap, "Defect detection and quantification system to support subjective visual quality inspection via a digital image processing: a tiling work case study," *Automation in Construction*, vol. 24, pp. 160–174, 2012.

[3] G. Lemaire, G. Escadeillas, and E. Ringot, "Evaluating concrete surfaces using an image analysis process," *Construction and Building Materials*, vol. 19, no. 8, pp. 604–611, 2005.

[4] ACI, *Identification and Control of Visible Effects of Consolidation on Formed Concrete Surfaces American Concrete*, ACI, Naples, FL, USA, 2003, https://wwwconcreteorg/publications/internationalconcreteabstractsportal/m/details/id/5145.

[5] T. Ozkul and I. Kucuk, "Design and optimization of an instrument for measuring bughole rating of concrete surfaces," *Journal of the Franklin Institute*, vol. 348, no. 7, pp. 1377–1392, 2011.

[6] B. Liu, T. Yang, and Y. Xie, "Factors influencing bugholes on concrete surface analyzed by image processing technology," *Construction and Building Materials*, vol. 153, pp. 897–907, 2017.

[7] G. Yao, F. Wei, Y. Yang, and Y. Sun, "Deep-learning-based bughole detection for concrete surface image," *Advances in Civil Engineering*, vol. 2019, Article ID 8582963, 12 pages, 2019.

[8] A. S. Kalayci, B. Yalim, and A. Mirmiran, "Effect of untreated surface disbonds on performance of FRP-retrofitted concrete beams," *Journal of Composites for Construction*, vol. 13, no. 6, pp. 476–485, 2009.

[9] F. Benito Saorin, I. Miñano Belmonte, C. Parra Costa, C. Rodriguez Lopez, and M. Valcuende Paya, "QSI methods for determining the quality of the surface finish of concrete," *Sustainability*, vol. 10, no. 4, p. 931, 2018.

[10] ACI, *ACI Manual of Concrete Inspection ACI Committee 311, SP-2(07)*, American Concrete Institute, Detroit, MI, USA, 2007.

[11] CIB, *Report N. 24: Tolerances on Blemishes of Concrete Concrete International Board-Comission W29*, CIB, Cairo, Egypt, 1973, https://wwwirbnetde/daten/iconda/06059000983pdf.

[12] M. S. Thompson, "Blowholes in concrete surface concrete," 1970, https://wwwconcreteconstructionnet/products/decorative-concrete-surfaces/blowholes-in-concrete-surfaces_o.

[13] M. Gao, X. Wang, S. Zhu, and P. Guan, "Detection and segmentation of cement concrete pavement pothole based on image processing technology," *Mathematical Problems in Engineering*, vol. 2020, Article ID 1360832, 13 pages, 2020.

[14] N.-D. Hoang, "Image processing-based recognition of wall defects using machine learning approaches and steerable filters," *Computational Intelligence and Neuroscience*, vol. 2018, Article ID 7913952, 18 pages, 2018.

[15] H. Kim, E. Ahn, M. Shin, and S.-H. Sim, "Crack and noncrack classification from concrete surface images using machine learning," *Structural Health Monitoring*, vol. 18, no. 3, pp. 725–738, 2018.

[16] S. Li and X. Zhao, "Image-based concrete crack detection using convolutional neural network and exhaustive search technique," *Advances in Civil Engineering*, vol. 2019, Article ID 6520620, 12 pages, 2019.

[17] T. Qingguo, L. Qijun, B. Ge, and Y. Li, "A methodology framework for retrieval of concrete surface crack's image properties based on hybrid model," *Optik*, vol. 180, pp. 199–214, 2019.

[18] F. Wei, G. Yao, Y. Yang, and Y. Sun, "Instance-level recognition and quantification for concrete surface bughole based on deep learning," *Automation in Construction*, vol. 107, Article ID 102920, 2019.

[19] H. Perez, J. H. M. Tah, and A. Mosavi, "Deep learning for detecting building defects using convolutional neural networks," *Sensors*, vol. 19, no. 16, Article ID 3556, 2019.

[20] P. Asadi, M. Gindy, and M. Alvarez, "A machine learning based approach for automatic rebar detection and quantification of deterioration in concrete bridge deck ground

penetrating radar B-scan images," *KSCE Journal of Civil Engineering*, vol. 23, no. 6, pp. 2618–2627, 2019.

[21] P. C. Fonseca and G. W. Scherer, "An image analysis procedure to quantify the air void system of mortar and concrete," *Materials and Structures*, vol. 48, no. 10, pp. 3087–3098, 2015.

[22] Y. Huang, X. He, Q. Wang, and J. Xiao, "Deformation field and crack analyses of concrete using digital image correlation method," *Frontiers of Structural and Civil Engineering*, vol. 13, no. 5, pp. 1183–1199, 2019.

[23] W. Song, G. Jia, H. Zhu, D. Jia, and L. Gao, "Automated pavement crack damage detection using deep multiscale convolutional features," *Journal of Advanced Transportation*, vol. 2020, Article ID 6412562, 11 pages, 2020.

[24] I. Venanzi, R. Castellani, L. Ierimonti, and F. Ubertini, "An automated procedure for assessing local reliability index and life-cycle cost of alternative girder bridge design solutions," *Advances in Civil Engineering*, vol. 2019, Article ID 5152031, 17 pages, 2019.

[25] Z. Zhu and I. Brilakis, "Machine vision-based concrete surface quality assessment," *Journal of Construction Engineering and Management*, vol. 136, no. 2, pp. 210–218, 2010.

[26] P. M. D. Santos and E. N. B. S. Julio, "Comparison of methods for texture assessment of concrete surfaces," *ACI Materials Journal*, vol. 107, no. 5, 2010.

[27] S. Fekri-Ershad and F. Tajeripour, "A robust approach for surface defect detection based on one dimensional local binary patterns," *Indian Journal of Science and Technology*, vol. 5, no. 8, pp. 1–7, 2012.

[28] W. R. L. da Silva and P. Štemberk, "Expert system applied for classifying self-compacting concrete surface finish," *Advances in Engineering Software*, vol. 64, pp. 47–61, 2013.

[29] F. Tajeripour and S. Fekri-Ershad, "Developing a novel approach for stone porosity computing using modified local binary patterns and single scale retinex," *Arabian Journal for Science and Engineering*, vol. 39, no. 2, pp. 875–889, 2014.

[30] J. Kwasny, M. Sonebi, J. Plasse, and S. Amziane, "Influence of rheology on the quality of surface finish of cement-based mortars," *Construction and Building Materials*, vol. 89, pp. 102–109, 2015.

[31] Ł. Sadowski and T. G. Mathia, "Multi-scale metrology of concrete surface morphology: fundamentals and specificity," *Construction and Building Materials*, vol. 113, pp. 613–621, 2016.

[32] G. L. Goïc, M. Bigerelle, S. Samper, H. Favrelière, and M. Pillet, "Multiscale roughness analysis of engineering surfaces: a comparison of methods for the investigation of functional correlations," *Mechanical Systems and Signal Processing*, vol. 66-67, pp. 437–457, 2016.

[33] B. Liu and T. Yang, "Image analysis for detection of bugholes on concrete surface," *Construction and Building Materials*, vol. 137, pp. 432–440, 2017.

[34] S. Dash and M. R. Senapati, "Gray level run length matrix based on various illumination normalization techniques for texture classification," *Evolutionary Intelligence*, 2018.

[35] M. A. Khan, R. Vehmas, and A. Visa, "Automatic detection of water inside concrete slabs using ground penetrating radar," in *Proceedings of the 2019 IEEE Radar Conference (Radar-Conf)*, pp. 1–5, Boston, MA, USA, April 2019.

[36] I. Yoshitake, T. Maeda, and M. Hieda, "Image analysis for the detection and quantification of concrete bugholes in a tunnel lining," *Case Studies in Construction Materials*, vol. 8, pp. 116–130, 2018.

[37] G. K. Choudhary and S. Dey, "Crack detection in concrete surfaces using image processing, fuzzy logic, and neural networks," in *Proceedings of the 2012 IEEE Fifth International Conference on Advanced Computational Intelligence (ICACI)*, pp. 404–411, Nanjing, China, October 2012.

[38] N.-D. Hoang and Q.-L. Nguyen, "Metaheuristic optimized edge detection for recognition of concrete wall cracks: a comparative study on the performances of Roberts, Prewitt, Canny, and Sobel algorithms," *Advances in Civil Engineering*, vol. 2018, Article ID 7163580, 16 pages, 2018.

[39] C. Koch, S. G. Paal, A. Rashidi, Z. Zhu, M. König, and I. Brilakis, "Achievements and challenges in machine vision-based inspection of large concrete structures," *Advances in Structural Engineering*, vol. 17, no. 3, pp. 303–318, 2014.

[40] R. Tanabe and A. Fukunaga, "Success-history based parameter adaptation for differential evolution," in *Proceedings of the 2013 IEEE Congress on Evolutionary Computation*, pp. 71–78, Beijing, China, June 2013.

[41] R. Tanabe and A. S. Fukunaga, "Improving the search performance of SHADE using linear population size reduction," in *Proceedings of the 2014 IEEE Congress on Evolutionary Computation (CEC)*, pp. 1658–1665, Beijing, China, July 2014.

[42] C. Bishop, *Pattern Recognition and Machine Learning*, Springer Science+Business Media, Singapore, 2006.

[43] N.-D. Hoang, Q.-L. Nguyen, and D. T. Bui, "Image processing-based classification of asphalt pavement cracks using support vector machine optimized by artificial bee colony," *Journal of Computing in Civil Engineering*, vol. 32, no. 5, Article ID 04018037, 2018.

[44] D. Dunn and W. E. Higgins, "Optimal Gabor filters for texture segmentation," *IEEE Transactions on Image Processing*, vol. 4, no. 7, pp. 947–964, 1995.

[45] N. N. Kachouie, J. Alirezaie, and P. Fieguth, "A hybrid algorithm using discrete cosine transform and Gabor filter bank for texture segmentation," in *Proceedings of the Canadian Conference on Electrical and Computer Engineering 2004 (IEEE Cat. No. 04CH37513)*, vol. 1803, pp. 1805–1808, Waterloo, Canada, May 2004.

[46] Z. Eduardo, G. G. B. Jaime, M. Roberto, and L. José, "Road crack detection using visual features extracted by Gabor filters," *Computer-Aided Civil and Infrastructure Engineering*, vol. 29, no. 5, pp. 342–358, 2014.

[47] N. C. Kim and H. J. So, "Directional statistical Gabor features for texture classification," *Pattern Recognition Letters*, vol. 112, pp. 18–26, 2018.

[48] R. Medina, F. Gayubo, L. M. González-Rodrigo et al., "Automated visual classification of frequent defects in flat steel coils," *The International Journal of Advanced Manufacturing Technology*, vol. 57, no. 9–12, pp. 1087–1097, 2011.

[49] S. Zehang, G. Bebis, and R. Miller, "Improving the performance of on-road vehicle detection by combining Gabor and wavelet features," in *Proceedings of the IEEE 5th International Conference on Intelligent Transportation Systems*, pp. 130–135, San Sebastián, Spain, September 2002.

[50] S. Zehang, G. Bebis, and R. Miller, "On-road vehicle detection using evolutionary Gabor filter optimization," *IEEE Transactions on Intelligent Transportation Systems*, vol. 6, no. 2, pp. 125–137, 2005.

[51] K. Hammouda, "Texture segmentation using Gabor filters," Technical Report, University of Waterloo, Waterloo, Canada, 2000, http://wwwpamiuwaterlooca/pub/hammouda/sd775-paperpdf.

[52] A. K. Jain and F. Farrokhnia, "Unsupervised texture segmentation using Gabor filters," *Pattern Recognition*, vol. 24, no. 12, pp. 1167–1186, 1991.

[53] J. Jo and Z. Jadidi, "A high precision crack classification system using multi-layered image processing and deep belief learning," *Structure and Infrastructure Engineering*, vol. 16, no. 2, pp. 297–305, 2019.

[54] M. M. Galloway, "Texture analysis using gray level run lengths," *Computer Graphics and Image Processing*, vol. 4, no. 2, pp. 172–179, 1975.

[55] A. Chu, C. M. Sehgal, and J. F. Greenleaf, "Use of gray value distribution of run lengths for texture analysis," *Pattern Recognition Letters*, vol. 11, no. 6, pp. 415–419, 1990.

[56] N.-D. Hoang and V.-D. Tran, "Image processing-based detection of pipe corrosion using texture analysis and metaheuristic-optimized machine learning approach," *Computational Intelligence and Neuroscience*, vol. 2019, Article ID 8097213, 13 pages, 2019.

[57] N.-D. Hoang, Q.-L. Nguyen, and X.-L. Tran, "Automatic detection of concrete spalling using piecewise linear stochastic gradient descent logistic regression and image texture analysis," *Complexity*, vol. 2019, Article ID 5910625, 14 pages, 2019.

[58] T. Xiaoou, "Texture information in run-length matrices," *IEEE Transactions on Image Processing*, vol. 7, no. 11, pp. 1602–1609, 1998.

[59] B. V. Dasarathy and E. B. Holder, "Image characterizations based on joint gray level-run length distributions," *Pattern Recognition Letters*, vol. 12, no. 8, pp. 497–502, 1991.

[60] K. Price, R. M. Storn, and J. A. Lampinen, *Differential Evolution—A Practical Approach to Global Optimization*, Springer-Verlag, Berlin, Germany, 2005.

[61] R. Storn and K. Price, "Differential evolution—a simple and efficient heuristic for global optimization over continuous spaces," *Journal of Global Optimization*, vol. 11, no. 4, pp. 341–359, 1997.

[62] S. Das, S. S. Mullick, and P. N. Suganthan, "Recent advances in differential evolution—an updated survey," *Swarm and Evolutionary Computation*, vol. 27, pp. 1–30, 2016.

[63] A. P. Piotrowski, "Review of differential evolution population size," *Swarm and Evolutionary Computation*, vol. 32, pp. 1–24, 2017.

[64] X. Shen, D. Zou, X. Zhang, Q. Zhang, and P. Xiao, "A phase-based adaptive differential evolution algorithm for the economic load dispatch considering valve-point effects and transmission losses," *Mathematical Problems in Engineering*, vol. 2018, Article ID 4585403, 24 pages, 2018.

[65] A. Viktorin, R. Senkerik, M. Pluhacek, T. Kadavy, and A. Zamuda, "Distance based parameter adaptation for success-history based differential evolution," *Swarm and Evolutionary Computation*, vol. 50, Article ID 100462, 2019.

[66] P. Biswas, P. Suganthan, and G. Amaratunga, "Optimal power flow solutions using algorithm success history based adaptive differential evolution with linear population reduction," in *Proceedings of the 2018 IEEE International Conference on Systems, Man, and Cybernetics (SMC)*, pp. 249–254, Miyazaki, Japan, October 2018.

[67] A. P. Piotrowski, "L-SHADE optimization algorithms with population-wide inertia," *Information Sciences*, vol. 468, pp. 117–141, 2018.

[68] A. P. Piotrowski and J. J. Napiorkowski, "Step-by-step improvement of JADE and SHADE-based algorithms: success or failure?" *Swarm and Evolutionary Computation*, vol. 43, pp. 88–108, 2018.

[69] A. Zamuda, "Adaptive constraint handling and success history differential evolution for CEC 2017 constrained real-parameter optimization," in *Proceedings of the 2017 IEEE Congress on Evolutionary Computation (CEC)*, pp. 2443–2450, June 2017.

[70] V. N. Vapnik, *Statistical Learning Theory*, John Wiley & Sons, Inc., Hoboken, NJ, USA, 1998.

[71] S. Deng, X. Wang, Y. Zhu, F. Lv, and J. Wang, "Hybrid grey wolf optimization algorithm based support vector machine for groutability prediction of fractured rock," *Mass Journal of Computing in Civil Engineering*, vol. 33, no. 2, Article ID 04018065, 2019.

[72] B. T. Pham, A. Jaafari, I. Prakash, and D. T. Bui, "A novel hybrid intelligent model of support vector machines and the MultiBoost ensemble for landslide susceptibility modeling," *Bulletin of Engineering Geology and the Environment*, vol. 78, no. 4, pp. 2865–2886, 2018.

[73] H. Wei, M. Wang, B. Song, X. Wang, and D. Chen, "Study on the magnitude of reservoir-triggered earthquake based on support vector machines," *Complexity*, vol. 2018, Article ID 2830690, 10 pages, 2018.

[74] C. M. Bishop, *Pattern Recognition and Machine Learning (Information Science and Statistics)*, Springer, Berlin, Germany, 2011.

[75] S. Guo, J. S. Tsai, C. Yang, and P. Hsu, "A self-optimization approach for L-SHADE incorporated with eigenvector-based crossover and successful-parent-selecting framework on CEC 2015 benchmark set," in *Proceedings of the 2015 IEEE Congress on Evolutionary Computation (CEC)*, pp. 1003–1010, Sendai, Japan, May 2015.

[76] Accord, *Accord.NET Framework*, http://accord-frameworknet/, 2019.

[77] D. N. Joanes and C. A. Gill, "Comparing measures of sample skewness and kurtosis," *Journal of the Royal Statistical Society: Series D (The Statistician)*, vol. 47, no. 1, pp. 183–189, 1998.

[78] D. Tien Bui, N.-D. Hoang, H. Nguyen, and X.-L. Tran, "Spatial prediction of shallow landslide using bat algorithm optimized machine learning approach: a case study in Lang Son Province, Vietnam," *Advanced Engineering Informatics*, vol. 42, Article ID 100978, 2019.

[79] I. Goodfellow, Y. Bengio, and A. Courville, *Deep Learning (Adaptive Computation and Machine Learning Series)*, The MIT Press, Cambridge, MA, USA, 2016.

[80] P. Kim, *MatLab Deep Learning with Machine Learning, Neural Networks and Artificial Intelligence*, Apress, New York, NY, USA, 2017.

[81] Y. LeCun, Y. Bengio, and G. Hinton, "Deep learning," *Nature*, vol. 521, no. 7553, pp. 436–444, 2015.

[82] N. Qian, "On the momentum term in gradient descent learning algorithms," *Neural Networks*, vol. 12, no. 1, pp. 145–151, 1999.

[83] D. P. Kingma and J. Ba, "Adam: a method for stochastic optimization," in *Proceedings of the 3rd International Conference on Learning Representations (ICLR)*, San Diego, CA, USA, May 2015.

[84] T. Tieleman and G. Hinton, "Lecture 6.5—RMSProp COURSERA: neural networks for machine learning," Technical Report, University of Toronto, Toronto, Canada, 2012.

[85] Matwork, "Deep learning toolbox," 2018, https://wwwmathworkscom/help/deeplearning/indexhtml.

[86] M. T. Hagan, H. B. Demuth, M. H. Beale, and O. D. Jesús, *Neural Network Design*, University of Colorado Bookstore, Boulder, CO, USA, 2nd edition, 2014.

[87] G. Montavon, G. Orr, and K.-R. Müller, "Neural networks: tricks of the trade," in *Lecture Notes in Computer Science*, Springer-Verlag, Berlin, Germany, 2012.

[88] S. Skansi, *Introduction to Deep Learning—from Logical Calculus to Artificial Intelligence*, Springer International Publishing, New York, NY, USA, 2018.

[89] J. Heaton, *Artificial Intelligence for Humans, Volume 3 Deep Learning and Neural Networks*, Heaton Research, Inc., St. Louis, MO, USA, 2015.

[90] G. W. Snedecor and W. G. Cochran, *Statistical Methods*, Iowa State University Press, Iowa City, IA, USA, 8th edition, 1989.

[91] S. Fekri-Ershad and F. Tajeripour, "Impulse-noise resistant color-texture classification approach using hybrid color local binary patterns and Kullback-Leibler divergence," *The Computer Journal*, vol. 60, no. 11, pp. 1633–1648, 2017.

Research Article

Assessment of Waterlogging Risk in the Deep Foundation Pit Projects Based on Projection Pursuit Model

Han Wu [iD] **and Junwu Wang** [iD]

School of Civil Engineering and Architecture, Wuhan University of Technology, Wuhan 430070, China

Correspondence should be addressed to Junwu Wang; junwuwang@163.com

As a result of global climate change and urbanization, waterlogging disasters have occurred frequently around the world, and deep foundation pit projects with lower terrain suffer even more. This study puts forward a method for the waterlogging risk assessment of deep foundation pit projects via the combination of a projection pursuit model, particle swarm optimization, and an interpolation algorithm. First, through a comprehensive analysis of the water circulation process in waterlogging and the characteristics of deep foundation pit projects, a risk index system with 11 indicators is identified and constructed. Then, a projection pursuit model optimized by particle swarm optimization is leveraged to determine the weights of the indicators and the best projection values of evaluation objects, and the mathematical function between the best projection values and the risk levels is constructed by an interpolation algorithm. Finally, three deep foundation pit projects of the Chengdu Metro Line 11 in China are selected as case studies. The results demonstrate that the frequency of storms, intensity of rainfall, preparation of emergency rescue plans, and proportion of older workers have the greatest impacts on waterlogging risk in deep foundation pits. The risk ranking of the case studies is found to be consistent with the actual situations, which proves the objectivity and effectiveness of the proposed method.

1. Introduction

In recent years, under the coupled effects of global climate change and urbanization, urban rainstorms and floods have frequently occurred and pose tremendous threats to public safety [1, 2]. In July 2016, Wuhan, the capital city of Hubei Province in China, suffered a serious waterlogging disaster. This catastrophe caused a direct economic loss of 351 million RMB, and transport and traffic were paralyzed [3]. In January 2020, heavy rain and floods in Jakarta, the capital of Indonesia, resulted in the death of 16 people and the evacuation of 35,600 people. The construction sites of deep foundation pit projects are extremely low; rainwater therefore naturally converges into these pits, making them more vulnerable to waterlogging disasters. Thus, conducting the waterlogging risk assessment of deep foundation pit projects will alleviate the injuries and property losses caused by waterlogging. This is of the highest guiding significance

for disaster prevention, mitigation, and preparedness work in the project management of deep foundation pit engineering.

The assessment manner of waterlogging risk is to rate the level of risk via an established mathematical model and evaluation index. According to the key influencing factors of waterlogging disaster risk and different risk levels, project managers are able to implement different measures of waterlogging prevention, mitigation, and preparedness. Scholars have carried out substantial research on urban waterlogging risk assessment. Hou [4] constructed a stormwater management model by combining geographic information system (GIS) and remote sensing (RS) technologies. This model was used to simulate the changes of the inundation range and accumulated water depth with the increase of rainfall intensity in the large-scale area of Jinfeng District, Yinchuan City, China. From the perspective of the discipline of disaster science, Jia et al. [5] studied the risk

level of waterlogging in prefecture-level cities in Henan, China. The results showed that the ability to prevent and reduce disasters had a critical impact on rainfall and waterlogging risk. Wu et al. [6] investigated the vulnerability of Zhengzhou City to flood disasters from the perspective of government management. Yu et al. [7] used an optimal weighting method and fuzzy comprehensive evaluation method to study waterlogging risk assessment in the construction and operation of subway stations; however, this indicator system was too simple and was unable both to consider the water circulation process during waterlogging and to effectively reflect the characteristics of subway stations. In addition, this study did not incorporate high-dimensional data that could be obtained before evaluation, which reduces the application and popularization values of the proposed model. In summary, existing related research has been primarily focused on large-scale areas such as cities and provinces, rather than small-scale areas such as projects under construction. To the best of the authors' knowledge, research on the assessment of the waterlogging risk in deep foundation pits has not yet been reported.

Currently, soft computing techniques are widely used in risk assessment and have achieved excellent research results. Mikael et al. [8] used the harmony search algorithm to effectively evaluate the geological disasters of railway tunnels. Bui et al. [9] studied the flood forecasting by the multivariate adaptive regression splits and PSO. This paper pointed out that PSO had better reliability and accuracy than other artificial intelligence algorithms. Artificial bee colony algorithm was also used to evaluate the risks of tunnel projects [10].

There are numerous factors that affect the waterlogging risk of deep foundation pits, and waterlogging risk assessment data is therefore high-dimensional. Determining how to effectively deal with this high-dimensional data is the key for improving the objectivity and effectiveness of waterlogging risk assessment. The projection pursuit model (PPM) projects high-dimensional data into low-dimensional space for analysis. In recent years, it has been used increasingly more in the field of risk evaluation [11] and decision-making [12] to effectively evaluate high-dimensional data.

To effectively analyse complex indexes in the research of gas outburst prediction, Liang [13] established a prediction model by using a PPM optimized by a genetic algorithm (GA). In this model, the one-dimensional projection values calculated by the GA were used to indicate the potential gas outburst risk, and the PPM was confirmed to be objective and effective. Liu et al. [14] proposed a PPM improved by the Ameliorative Moth-Flame Optimization (AMFO) algorithm for high-dimensional data for the evaluation and spatial change rule of surface water quality. The empirical analysis results showed that the proposed AMFO-PPE was stable and reliable. To effectively evaluate the sustainability of prefabricated parts, Jiang et al. [15] used a PPM optimized by the Real-code Accelerated Genetic Algorithm (RAGA), based on which a customer satisfaction evaluation algorithm for an e-commerce platform was constructed [16]. According to the previous research results, the key step in the processing of high-dimensional data by a PPM is to

determine the optimum projection direction, which is a complex nonlinear optimization problem [17]. At present, most researchers adopt the GA to solve this problem, though it is characterized by some shortcomings including the dependence on the initial population selection, a slow convergence speed, and too many parameter settings [18, 19]. Compared with a GA and ant colony optimization, particle swarm optimization (PSO), which is also a typical metaheuristic algorithm, is characterized by fast convergence and fewer parameter settings [20]. Although PSO does not require tedious mathematical operations, it has been proven to better solve most optimizations. Dormishi et al. [21] used a variety of metaheuristic algorithms to comprehensively evaluate cutting machine performance in the mineral processing field, and the research results demonstrated that the PSO exhibited advantages over a differential evolution algorithm. Hasanipanah et al. [22] used the PSO model and the other methods to, respectively, predict the ground vibration caused by an explosion; the results also revealed that the PSO model performed better than the other methods.

According to the preceding analysis, the present paper proposes a method of waterlogging risk assessment using the combination of a PPM and PSO. The main contributions of this paper are as follows. (1) From the perspectives of the fields of environmental science and civil engineering, a rainstorm waterlogging disaster risk index system that can reflect the characteristics of small-scale areas in deep foundation pit engineering and construction project management is constructed for the first time. (2) The PPM is used to effectively deal with the problem of the high-dimensional data of rainstorm waterlogging disaster risk, and PSO is used to determine the optimum projection direction of the PPM. (3) This paper, for the first time, reveals that the frequency of storms, intensity of rainfall, preparation of emergency rescue plans, and proportion of older workers have the greatest impacts on the waterlogging risk of deep foundation pits and are the key factors in project management. The series of research in this paper provides a scientific basis for the prevention, mitigation, and preparedness of waterlogging disasters in deep foundation pit engineering.

The remainder of this paper is organized as follows. Section 2 details the research materials and methods, including index selection and the risk assessment method. The process of the case analysis and discussion of the results are presented in Section 3, and the research conclusions are presented in Section 4.

2. Materials and Methods

2.1. The Index System of Waterlogging Risk in Deep Foundation Pits

2.1.1. Determination of Risk Factors of Waterlogging Risk in Deep Foundation Pits. The risk assessment of waterlogging in deep foundation pits is a complicated and interdisciplinary issue. In the field of environmental science, waterlogging disasters are always provincial; thus, waterlogging risk factors should be considered from the perspective of the

water cycle process of waterlogging disasters in both deep foundation pits and their surrounding areas [23]. The factors associated with the surrounding area reflect the characteristics of waterlogging disasters in large-scale urban areas, while the factors associated with deep foundation pits reflect the detailed process of waterlogging disasters. The factors that clearly indicate the characteristics of deep foundation pit engineering should then be selected from the perspective of civil engineering; these factors should naturally reflect both structural characteristics and project management characteristics. Finally, the factors related to the capacity of disaster prevention and mitigation should be chosen from the perspective of scientific fields such as disaster management.

In the project management practice of deep foundation pit engineering, many construction and management measures are used to resist waterlogging. For example, a retaining wall along the foundation pit is usually put in place to prevent waterlogging; the higher the height of the retaining wall is, the harder the floods to enter the construction site are, and the less risk of waterlogging there is. Water pumps are also often stored and utilized for draining in deep foundation pits; the more the pumps there are, the faster the water is pumped out and less the risk of waterlogging there is. In addition, the waterlogging risk in deep foundation pit projects is related to the population structure [24]; the public emergency capacity of citizens over 50, namely, the elderly, is significantly hindered; thus, these populations are more vulnerable when faced with emergencies. In other words, the greater the proportion of construction workers over the age of 50, the greater the vulnerability the society has to waterlogging disasters [25] and the higher the risk of waterlogging in deep foundation pit projects.

Referring to previous research results [26, 27], the risk factors associated with disaster prevention and mitigation are the preparation of an emergency rescue plan, efficiency of emergency rescue, proportion of relief workers, and reserve of emergency rescue materials. An emergency rescue plan is the foundation for emergency management when disasters and emergencies occur; the more fully prepared the emergency plan, the stronger the disaster prevention and mitigation capability. The factors related to disaster reduction are divided into two categories, namely, emergency rescue support factors and emergency rescue organization factors. Copious professional rescue personnel and sufficient relief materials are the foundations of successful emergency response work. When natural disasters such as waterlogging occur, the more complete the emergency rescue organization, the faster the information communication, and the higher the efficiency of emergency rescue.

2.1.2. Construction of Evaluation Index System.
Taking fully into account objectivity, systematism, availability, and independence, risk indicators that are representative of all risk factors identified in Section 2.1.1 were chosen in this study. An evaluation index system including 11 risk indicators was constructed, as presented in Table 1.

In Table 1, X1, X2, X3, X5, X6, X7, and X10 are quantitative indicators, and their data was obtained by field

research and the review of local water resources announcements, local yearbooks, etc. Considering the unavailability of partial data in current engineering practice, X4, X8, X9, and X11 are all qualitative indexes without measurement units, and their scores were obtained by a questionnaire survey. X1, X2, X3, and X7 are benefit-based indicators; the greater the numerical values of these indicators, the greater the level of waterlogging risk. The remaining indicators are cost-based; the smaller the numerical values, the greater the level of waterlogging risk.

2.1.3. Assessment Standard of Waterlogging Risk.
Currently, there are no uniform standards for the assessment of waterlogging risk [28, 29]. To meet the needs of deep foundation pit project management practice, the risk assessment levels in this study were classified by the different risk response measures that should be taken. Four levels of waterlogging risk, namely, low risk (I), moderate risk (II), high risk (III), and extreme risk (IV), were identified. The low risk (I) category denotes that there is no need to take further measures, only to check how existing measures are implemented. Moderate risk (II) indicates that additional measures should be developed to deal with the risk of waterlogging. High risk (III) implies that there is no need to stop the construction operation, but further measures must be immediately formulated to reduce the level of waterlogging risk as soon as possible. Extreme risk (IV) signifies that the construction task must be suspended immediately and that project managers are obliged to promptly take measures to decrease the waterlogging risk level.

As indicated in Table 1, the standards of different evaluation levels for the 11 indicators were established by combining the expert experience of project managers and previous research results [30, 31]. The risk level descriptions of the four qualitative indicators, X4, X8, X9, and X11, are divided into 2 components, namely, the qualitative language description and corresponding quantitative score range. For example, the low risk (I) level of X8 is "fully sufficient [90, 100];" "fully sufficient" is a qualitative language description, and "90–100" is the corresponding quantitative score range. If an expert judged from experience that the situation of the X8 index to be evaluated was fully sufficient, it would have been scored to be between 90 and 100 in the questionnaire.

It must be pointed out that, to the best of the authors' knowledge, there has been no study on the upper limit values of X1, X2, X3, X5, and X6. To better generalize the index system, the upper limits of these indexes are "+∞" in Table 1. When this index system was used to carry out case studies, their upper limit values would have been reasonably selected in combination with deep foundation pit engineering practice, rather than being considered to be +∞.

2.2. Risk Assessment Method of Waterlogging Risk in the Deep Foundation Pits

2.2.1. Projection Pursuit Model.
The PPM is a statistical method for processing and analysing high-dimensional data. The method was originally coined by Friedman and Tukey

TABLE 1: The index system of waterlogging risk in the deep foundation pit projects.

Indicator level	Unit	I	II	III	IV
Intensity of rainfall X1	mm/24 h	[0, 50)	[50, 100)	[100, 250)	[250, +∞)
Frequency of storms X2	times/year	[0, 1)	[1, 3)	[3, 6)	[6, +∞)
Distance to urban drains X3	m	[0, 50)	[50, 200)	[200, 500)	[500, +∞)
Surrounding environment X4	—	No [90, 100]	Few [75, 90)	Moderate [60, 75)	Many [0, 60)
Height of retaining wall X5	m	[1.2, +∞)	[0.6, 1.2)	[0.3, 0.6)	[0, 0.3)
Number of pumps X6	/100 m²	[0.5, +∞)	[0.2, 0.5)	[0.1, 0.2)	[0, 0.1)
Proportion of older workers X7	%	[0, 5)	[5, 10)	[10, 20)	[20, 100]
Preparation of emergency rescue plans X8	—	Fully sufficient [90, 100]	Sufficient [75, 90)	Basically insufficient [60, 75)	Insufficient [0, 60)
Efficiency of emergency rescue X9	—	Fully efficient [90, 100]	Efficient [75, 90)	Basically efficient [60, 75)	Inefficient [0, 60)
Proportion of relief workers X10	%	[30, 100]	[20, 30)	[10, 20)	[0, 10)
Situation of emergency relief supplies X11	—	Fully efficient [90, 100]	Efficient [75, 90)	Basically efficient [60, 75)	Inefficient [0, 60)

from Stanford University in 1974 [32]. The basic idea is tantamount for projecting high-dimensional data into a low-dimensional space. Therefore, this model can effectively eliminate variable interference that is not related to the data structure. Additionally, the objective weights of the indicators were computed directly from the characteristics of the sample data [33] in their application to system evaluation.

The general steps of the PPM used in the system evaluation are as follows.

(1) Standardization of Data

Let the indicator sequence be $[x_{ij}]_{m \times n}$, where m is equal to the number of samples and n is the number of indicators.

To eliminate the dimensional impact of the evaluation indicators and ensure the generalizability of the modelling, the extreme value normalization method was employed in this study to standardize the data.

The benefit-based indicators [34] are as follows:

$$x_{ij}^* = \frac{x_{ij} - \min(x_j)}{\max(x_j) - \min(x_j)}, \tag{1}$$

and the cost-based indicators [34] are as follows:

$$x_{ij}^* = \frac{\max(x_j) - x_{ij}}{\max(x_j) - \min(x_j)}, \tag{2}$$

where x_{ij}^* indicates the value of the evaluation index after standardization, $\max(x_j)$ represents the maximum value of indicator j, and $\max(x_j)$ represents the minimum value of indicator j.

(2) Construction of Projection Indicator Function

The core idea of the PPM is to project $[x_{ij}^*]_{m \times n}$ to obtain the projection value $z(i)$ according to projection indicators $= (a_1, a_2, \cdots, a_m)$ [35]. The projection indicator function is

$$\mathbf{Z}(i) = \sum_{j=1}^{m} a_j x_{ij}^*. \tag{3}$$

Optimizing $\mathbf{a}$ requires that the distribution characteristics of $\mathbf{Z}(i)$ are such that the projection points are locally as dense as possible and overall spread out as much as possible. Therefore, the best projection direction is determined by maximizing the product of the standard deviation and the local density. The optimal projection function [36] is

$$S_z = \sqrt{\frac{\sum_{i=1}^{n} (\mathbf{Z}(i) - E(z))^2}{n - 1}}, \tag{4}$$

where S_z is the standard deviation of $\mathbf{Z}(i)$ and $E(z)$ is the average of $\mathbf{Z}(i)$.

$$D_z = \sum_{i=1}^{n} \sum_{j=1}^{m} (R - r_{ij}) u(R - r_{ij}), \tag{5}$$

where D_z is the local density of $\mathbf{Z}(i)$, r_{ij} is the distance between samples, R is the window radius of the local density, and it is also the only parameter set in the PPM. Additionally, $u(R - r_{ij})$ is the unit step function. When $R - r_{ij} \geq 0$, $u(R - r_{ij}) = 1$; otherwise, $u(R - r_{ij}) = 0$.

(3) Optimizing the Projection Index Function

When the indicator sample set $[x_{ij}]_{m \times n}$ is determined, $\mathbf{Q}(a)$ only changes with the projection direction $\mathbf{a}$. If the projection direction is the best projection direction $\mathbf{a}^*$, $\mathbf{Q}(a)$ must be at the maximum value. The low-dimensional data obtained in the best projection direction $\mathbf{a}^*$ can be best explained by the characteristic structure of the original data [37].

Based on the preceding analysis, the method of finding the maximum value of the projection index function was employed to find the best projection direction.

The function to maximize the objective is [38]

$$\max \mathbf{Q}(a) = S_z |D_z|, \tag{6}$$

and the constraint is

$$\sum_{j=1}^{m} a_j^2 = 1, \quad 0 \le a_j \le 1. \tag{7}$$

(4) Solving the Optimum Projection Direction

Equations (6) and (7) are utilized to compute the optimal projection vector. Generally, most scholars would use GA [13, 15, 16] and other algorithms for the solution. However, the GA has drawbacks, including the computing result having certain dependence on the initial population selection, its slow convergence speed, and its excessive parameter settings [18, 19]. In contrast, PSO is characterized by advantages including a fast convergence speed and fewer parameter settings [20–22, 39]; thus, PSO was employed in the present study to find the best projection vector $\mathbf{a}^*$.

By substituting $\mathbf{a}^*$ into (3), the projection vector $\mathbf{Z}^*(i)$ can be solved.

2.2.2. Particle Swarm Optimization. PSO is a group-based random search algorithm that is designed by simulating the predation behaviour of bird swarms. Its basic idea is to start from a random solution, find the optimal solution through iteration, and then evaluate and determine the optimal solution through fitness.

In each iteration of PSO, a particle updates its own position by tracking the individual optimal solution and the group optimal solution, thereby constantly adjusting its position to approach the optimal position.

Let the population size of the particles be N; the velocity update formula of the particle b is as follows:

$$v_b(t+1) = \omega v_b(t) + c_1 r [q_b(t) - a_b(t)] + c_2 r [g(t) - a_b(t)]. \tag{8}$$

The velocity update formula is as follows:

$$a_b(t+1) = a_b(t) + v_b(t+1), \tag{9}$$

where ω is the inertia weight factor, c_1 and c_2 are the learning factors, r is a random number within the interval $[0, 1]$, q is the individual optimal value, and g is the global optimum value.

After reaching a certain condition in which the iteration terminates, the best projection vector $\mathbf{a}^*$ is obtained by the position of the particle swarm aggregation.

2.2.3. Risk Assessment Method Construction. The flow chart of this evaluation method is illustrated in Figure 1.

The specific steps of the construction of the risk assessment method based on the PPM are as follows.

Step 1. Preparing Data

(1) According to Table 1, the random sampling method is used to generate the standard sample set $[\mathbf{x}_{ij}]_{p \times n}$, where p is the number of standard samples obtained

by the random sampling method. Equation (1) or (2) is leveraged to normalize it to obtain $[\mathbf{x}_{ij}^*]_{p \times n}$. To ensure the accuracy and stability of subsequent interpolation function models, hundreds of standard sample sets are extracted, so $[\mathbf{x}_{ij}^*]_{p \times n}$ is always high-dimensional data. Because the standard sample set $[\mathbf{x}_{ij}]_{p \times n}$ is generated according to the random sampling method, the risk levels $\mathbf{Y}_1(i)$ are also known.

(2) Field research, theoretical computing, and questionnaires were used to obtain the evaluation indicator set of the research object $[\mathbf{x}_{ij}]_{m \times n}$. According to the characteristics of each indicator, (1) or (2) is adopted to standardize it and subsequently obtain $[\mathbf{x}_{ij}^*]_{m \times n}$.

Step 2. Calculating the Weights and Projection Values by the PPM and PSO

(1) $[\mathbf{x}_{ij}^*]_{p \times n}$ and $[\mathbf{x}_{ij}^*]_{m \times n}$ are combined into a computing set $[\mathbf{x}_{ij}^*]_{(m+p) \times n}$. The projection index function $\mathbf{Z}(i)$ is constructed according to (3).

(2) Equations (4) and (5) are used to find the maximum objective function $\mathbf{Q}(a)$, and PSO is utilized to solve the function $\mathbf{Q}(a)$.

(3) When the PSO reaches the convergence condition, the optimal projection direction $\mathbf{a}^*$ is obtained. $\mathbf{Z}(i)$ is then computed, where $i = 1, 2, 3, \cdots, m + p$. The projected value $\mathbf{Z}_1(i)$ of the standard sample set $[\mathbf{x}_{ij}^*]_{p \times n}$ and the projected value $\mathbf{Z}_2(i)$ of the evaluation indicator set $[\mathbf{x}_{ij}^*]_{m \times n}$ are both included in $\mathbf{Z}(i)$.

(4) Every element of $\mathbf{a}^*$ is squared to obtain the objective weight of each index [35].

Step 3. Obtaining Evaluation Levels by the Interpolation Algorithm

(1) According to the projection value of the standard sample set $\mathbf{Z}_1(i)$ and its default risk level $\mathbf{Y}_1(i)$, the interpolation method is used to construct the mathematical model of risk assessment as follows [40]:

$$\mathbf{Y} = f(\mathbf{Z}_1). \tag{10}$$

(2) By introducing the projection value of the evaluation sample set $\mathbf{Z}_2(i)$ into the mathematical model $\mathbf{Y} = f(\mathbf{Z}_1)$, the waterlogging risk level of each evaluation sample is computed.

From these steps, it is evident that this method is directly motivated by data. Compared with functional mode evaluation methods, such as fuzzy comprehensive evaluation, the proposed method effectively avoids the difficulty of constructing the functional relationship between the evaluation index set and evaluation level.

3. Results and Discussion

3.1. Engineering Background. The Chengdu Metro Line 11 project involves a total investment of about 16.5 billion yuan.
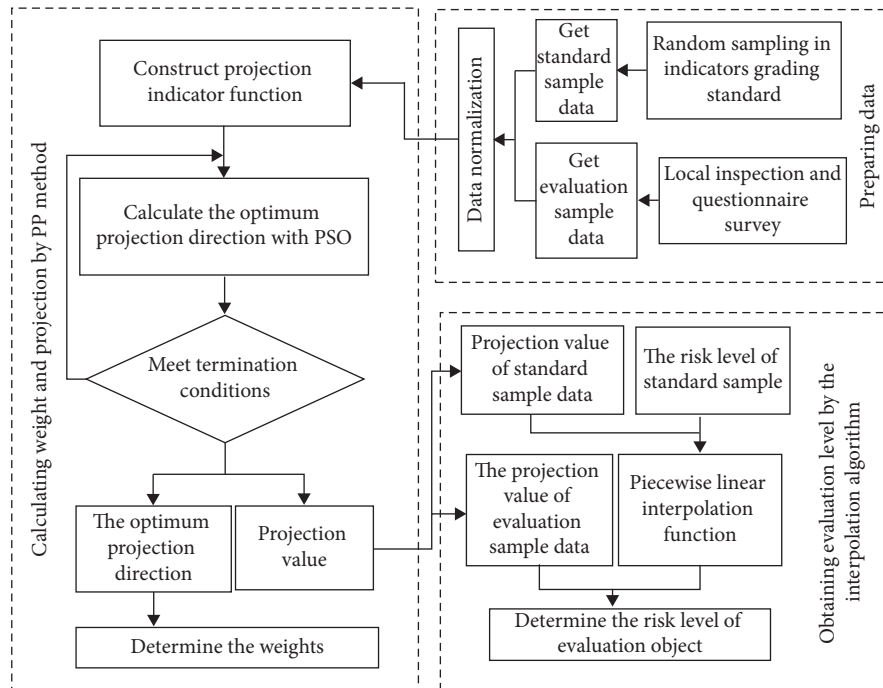
FIGURE 1: Flow chart of the waterlogging risk evaluation method based on the PPM.

It is about 22 km in length and comprises 22 station projects. This major project traverses the Chengdu Hi-tech Zone, Tianfu New District, and Shuangliu District. The landform features are mostly plains, platforms, or a small number of low hills. The average annual rainfall in Chengdu is 879.3 mm, and the maximum rainfall in 24 h is 167.6 mm. Waterlogging and droughts often occur in Chengdu.

The deep foundation pit projects of Diaoyuzui Station, Tianfu CBD North Station, and Xinchuan Science Park East Station were selected as a case study. The platforms of these three stations are two-story islands. The deep foundation pits were all constructed by the open-cut method, and there are no adverse geological effects or special geotechnical soil within their construction scopes. However, among all 22 station projects on Chengdu Metro Line 11, these three projects have the following differences.

(1) The construction company used for Diaoyuzui Station and Xinchuan Science Park East Station, China Construction Third Bureau Group Co., Ltd., has rich experience in subway construction; however, the construction company used for Tianfu CBD North Station is China Railway Investment and Construction Co., Ltd., which lacks experience in subway.

(2) Diaoyuzui Station, which is located in the suburban countryside, has almost no urban drains in its surrounding area, which is characterized by environmental elements that are prone to waterlogging, such as flood canals and high slopes. Tianfu CBD North Station is located in the CBD area that is under construction, where the municipal drains are well developed and there are no adverse environmental

elements. Xinchuan Science Park East Station is situated in the suburban development zone, in which there are fish ponds and a large number of gas pipelines.

(3) Diaoyuzui Station is the largest station on Chengdu Metro Line 11, with a total length of 340.40 m, a total width of 21.5 m, and an excavation depth of 16.9–27.3 m, all of which are the largest among the three case study stations. Xinchuan Science Park East Station is the smallest.

3.2. Sources of Data. Based on the hydrological and meteorological characteristics of Chengdu and the 22 deep foundation pit projects of Chengdu Metro Line 11, the upper limit values of X1, X2, X3, X5, and X6 were, respectively, determined to be 500, 12, 3000, 2.4, and 1.

The quantitative indicator scores of these three deep foundation pits were obtained by consulting the Chengdu Water Resources Announcement, the project management documents of the Chengdu Metro Line 11 project, and field surveys. Their scores are presented in Table 2. The scores of the quantitative indexes X4, X8, X9, and X11 were obtained from a questionnaire survey of ten experts.

Among the ten experts, three were from universities, two were from construction companies, and five were from subway construction units. Seven experts had the title of senior engineer or above, and the other three experts had titles of associate senior engineer or associate professor. Six experts were well aware of construction safety risks and have produced related research. Seven experts were familiar with the construction of Chengdu Metro Line 11 and participated in the construction of the project. SPSS 22 software was used

TABLE 2: Indicators' scores of three evaluation objects.

Indicator	Diaoyuzui Station	Tianfu CBD North Station	Xinchuan Science and Technology Park	Data sources
X1	167.6	167.6	167.6	Chengdu Water Resources Announcement
X2	3.125	3.125	3.125	Chengdu Water Resources Announcement
X3	2600	150	50	Field research
X4	13.5	31	92	Field research and questionnaire survey
X5	0.6	1	0.4	Field research
X6	0.11	0.11	0.17	Field research
X7	8.61	9.09	11.72	Field research
X8	87.5	33	46.5	Field research and questionnaire survey
X9	73	70.5	80	Field research and questionnaire survey
X10	19.95	10.87	19.01	Field research
X11	73	72.5	79.5	Field research and questionnaire survey

to test the reliability of this questionnaire. The value of Cronbach's α was found to be 0.743 and therefore met the reliability requirement of a questionnaire survey [41]; thus, the results of this questionnaire survey were reliable. The average of the scoring results of the 10 experts was the scores of these quantitative indicators.

3.3. Mathematical Risk Assessment Model with the Interpolation Algorithm.
According to Table 1 and Figure 1, 100 standard evaluation objects in each risk level were generated by the random sampling method [39]. Thus, there were 400 standard evaluation objects obtained for the establishment of a mathematical model of risk evaluation. The data of these 400 standard evaluation objects (the standard sample data in Figure 1) and the data of 3 units to be assessed (the evaluation sample data in Figure 1) were substituted into a self-programmed program based on MATLAB R2016a software. Referring to previous research results [42–45], the swarm size was 200, the personal learning coefficient and global learning coefficient were both 2, the inertia weights decreased linearly from 0.9 to 0.4, the minimum acceptance accuracy was 0.00001, and the maximum number of iterations was 1000. Although the minimum accuracy requirement was met when the iteration number reached about 200 in the case analysis, the population number and the maximum iteration number were set to be relatively large in this study to ensure that the model could calculate more complex problems. The convergence curve of the 1000 iterations is presented in Figure 2.

Following the optimization calculation process of PSO, the error between the 194th iteration and 195th iteration was greater than the minimum acceptance precision (0.00001), and the error between the 195th iteration and 196th iteration was less than that of the minimum acceptance precision stage. After that, the errors of the calculation results were all less than 0.00001. Based on the calculation termination conditions of the algorithm, the calculation was arrested at the 1000th iteration with a very small error. These findings indicate that the PSO algorithm found the best projection vector at the 196th iteration, which is illustrated by both Figure 2 and Table 3.
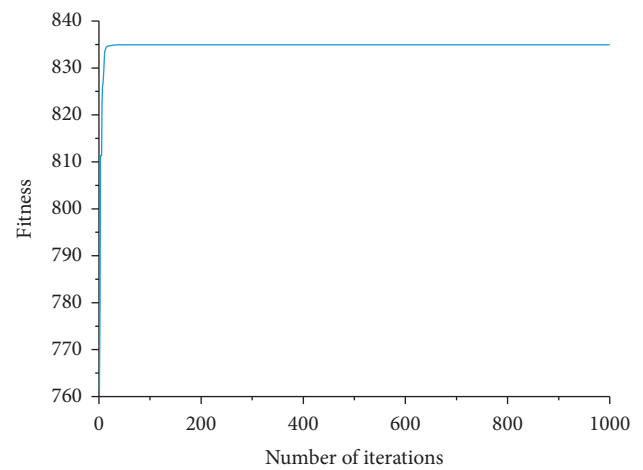
FIGURE 2: The convergence curve of the PPM optimized by PSO.

After calculation, the best projection direction $\mathbf{a}^*$ was found to be (0.3642, 0.3784, 0.3225, 0.3207, 0.1765, 0.1887, 0.3340, 0.3481, 0.31860, 0.1004, 0.3258). The scatter diagram of the projection values $\mathbf{Z}_1(i)$ of 400 standard evaluation objects and the corresponding risk level $\mathbf{Y}_1(i)$ is presented in Figure 3.

As exhibited in Figure 3, the scatter diagram of the best projection values and risk levels was a ladder-type and was characterized by an increasing curve; the larger the projection value, the greater the waterlogging risk. The projection values were aggregated rather than being continuously distributed. This graphic feature was determined by the basic idea of the PPM. Locally, the optimized projection points should be clustered as much as possible. On the whole, they should be spread as much as possible. This clustering phenomenon presented in Figure 3 was fairly consistent with the results of previous classical literature [46], and Figure 3 further demonstrates that the PPM utilized in this study had been optimized.

The maximum projection value in the low risk (I) level was 0.3818. The maximum projection value in the moderate risk (II) level was 0.8562, and the minimum projection value was 0.6079. The maximum projection value in the high risk

TABLE 3: Precision level and calculation termination in the 1000th iteration.

Iteration (n)	Fitness ($n-1$)	Fitness (n)	Fitness (n) – Fitness ($n-1$)	Result
194	834.956821	834.956821	0 < 0.00001	Continue
195	834.956821	834.956841	0.0000197 > 0.0001	Continue
196	834.956841	834.956841	0 < 0.0001	Continue
1000	834.956842	834.956842	0 < 0.0001	Stop
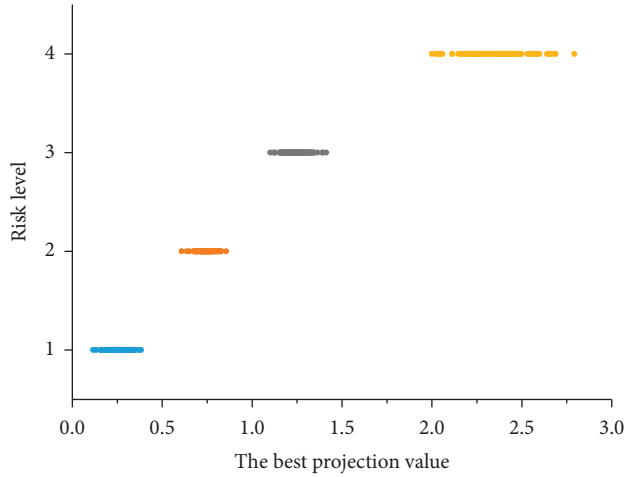
FIGURE 3: Scatter diagram of the standard evaluation object projection values and risk levels.

(III) level was 1.4125, and the minimum projection value was 1.1010. The minimum projection value in the extreme risk (IV) level was 1.9991. Using the piecewise linear interpolation method, a mathematical model for the waterlogging risk assessment of deep foundation pit engineering was established:

$$y(i) = \begin{cases} 1, & z^* \leq 0.3818, \\[2mm] 1 + \dfrac{z^* - 0.3818}{0.6079 - 0.3818}, & 0.3818 < z^* < 0.6079, \\[2mm] 2, & 0.6079 \leq z^* \leq 0.8562, \\[2mm] 2 + \dfrac{z^* - 0.8562}{1.1010 - 0.8562}, & 0.8562 < z^* < 1.1010, \\[2mm] 3, & 1.1010 \leq z^* \leq 1.4125, \\[2mm] 3 + \dfrac{z^* - 1.4125}{1.9991 - 1.4125}, & 1.4125 < z^* < 1.9991, \\[2mm] 4, & z^* \geq 1.9991. \end{cases}$$

(11)

3.4. Analysis and Discussion. This section analyses and discusses the calculation results of the weights and risk levels in detail. However, the waterlogging risk evaluation index system presented in this work was constructed from the perspectives of environmental science and civil engineering; if this research had been carried out from the perspectives of other disciplines, the index system and calculation results of the weights and risk levels would have been different. Due to the lack of academic research on the waterlogging risk assessment of deep foundation pit engineering, the calculation results are primarily compared and discussed with the actual disaster situation of Chengdu Metro Line 11 in the 2018 flood season. In addition, while the PSO was successfully employed to optimize the PPM in the present case study, many other optimization calculation methods could be applied for the optimization of the PPM. Depending on the results of the case analysis, this section also presents detailed measures suggested for addressing the waterlogging risk in deep foundation pit engineering.

3.4.1. Weight Analysis. After squaring each element in the calculated optimal projection direction [35], namely (0.3642, 0.3784, 0.3225, 0.3207, 0.1765, 0.1887, 0.3340, 0.3481, 0.31860, 0.1004, 0.3258), the objective weights of the 11 indicators were calculated and are presented in Table 4.

From Table 4, it is evident that X2 (frequency of storms) and X1 (intensity of rainfall) had the greatest impacts on the risk of waterlogging in deep foundation pit engineering. These results were similar to the calculation results of a previous study [47]. From the perspective of disaster science, X1 and X2 were found to be the greatest indicators, which demonstrates that disaster-causing factors have the greatest impacts on waterlogging risk.

The weight of X8 ranked third and was also the largest among the indicators related to disaster prevention and mitigation. This further demonstrates that emergency rescue plans form the basis of emergency management. The weight of X7 (proportion of older workers) ranked fourth and therefore also has a great influence on the waterlogging risk. It is worth noting that the superior weight of X7 might be closely related to the aging phenomenon of Chinese construction workers in the past decade.

The weight analysis results were found to be in agreement with the actual disaster situation of the deep foundation pit project of Diaoyuzui Station during the flood season of 2018. At the beginning of July 2018, a series of torrential rainstorms in Chengdu led to the inflow of water in the deep foundation pit of Diaoyuzui Station. When the waterlogging disaster occurred, the project managers prioritized saving lives, so the workers at the construction site and in the living area, especially the older workers, were first evacuated, resulting in a delay in the rescue of the site, thereby enlarging the disaster losses.

TABLE 4: Weights and rankings of all risk indicators.

Indicator	X1	X2	X3	X4	X5	X6	X7	X8	X9	X10	X11
Weight	0.1327	0.1432	0.1040	0.1029	0.0312	0.0356	0.1116	0.1212	0.1015	0.0101	0.1061
Ranking	2	1	6	7	10	9	4	3	8	11	5

Based on these results, some advice is provided for project managers regarding the carrying out of the risk management and decision-making related to waterlogging disasters in deep foundation pit projects; focus should be placed on X2 (frequency of storms), X1 (intensity of rainfall), X8 (preparation of emergency rescue plans), and X7 (proportion of older workers), while the investment of resources in factors X5, X6, and X10 should be of secondary concern.

3.4.2. Risk Level Analysis. The best projected values for the deep foundation pit projects of Diaoyuzui Station, Tianfu CBD North Station, and Xinchuan Science Park East Station were found to be 1.4524, 1.3275, and 1.0644, respectively. By substituting these values into (11), the respective risk levels were determined to be 3.0681, 3.0000, and 2.8505. The waterlogging risk level of the Diaoyuzui Station was between the high risk (III) and the extreme risk (IV) levels. The waterlogging risk in Tianfu CBD station was at the high risk (III) level and that of Xinchuan Science Park East Station was between the moderate risk (II) and high risk (III) levels. Thus, the waterlogging risks in these three deep foundation pits from greatest to least were found to be as follows: Diaoyuzui Station > Tianfu CBD North Station > Xinchuan Science Park East Station.

During the 2018 flood season in Chengdu, Diaoyuzui Station was the most severely damaged of all the 22 station projects. Tianfu CBD North Station was the second-most damaged, but Xinchuan Science Park East Station was hardly affected by this flood disaster. The actual disaster situations of the three deep foundation pit projects from greatest to least were therefore as follows: Diaoyuzui Station > Tianfu CBD North Station > Xinchuan Science Park East Station Project. This ranking obtained by the on-site investigation was consistent with the waterlogging risk results calculated by the method proposed in this study. The consistency proves that the proposed method is both objective and effective.

3.4.3. Measures to Address Waterlogging Risk in Deep Foundation Pit Projects

(1) To better ensure construction safety, the deep foundation pit project of Diaoyuzui Station should deal with risks in accordance with the extreme risk (IV) level. Project managers should immediately suspend construction tasks and take steps to reduce the risk level. The construction operations of Tianfu CBD North Station and Xinchuan Science Park East Station do not require termination, but their project management staff should immediately formulate further measures to address waterlogging risk and

decrease the level of waterlogging risk as soon as possible.

(2) In the design and planning of the construction organization of deep foundation pit projects, the local hydrometeorological data, especially the data of regional annual rainfall frequency and the largest rainfall intensity in history, should be fully investigated. During construction, project managers should consider future climate changes and adjust the measures for waterlogging risk according to the changes in weather.

(3) The managers of deep foundation pit projects should attach more importance to the preparation of emergency rescue plans. Before the flood season, they should conduct emergency rescue drills for waterlogging, strengthen the construction of rescue organizations, and improve the efficiency of emergency rescue.

(4) The proportion of older workers should be reduced to mitigate the vulnerability of the local population. However, in China, the aging of construction workers has become increasingly more severe in the past ten years, and it is a difficult task to reduce the proportion of older employees. Therefore, as an alternative measure, increasing emergency rescue training is recommended.

4. Conclusions

The intention of this study was to conduct an objective and effective evaluation of waterlogging risk in deep foundation pits based on the projection pursuit method. According to the process of water circulation and the characteristics of deep foundation pits, an evaluation index system with 11 indicators was constructed for the first time. Then, a combination of the projection pursuit method, particle swarm optimization, and the interpolation algorithm was used to construct a waterlogging risk assessment method. In this method, the projection pursuit method is used to handle the high-dimensional data of waterlogging risk assessment, and the optimal projection vector is solved by particle swarm optimization, which is characterized by relatively rapid and appropriate convergence. The mathematical function between the best projection values and the risk levels was constructed by an interpolation algorithm. Finally, three typical deep foundation pits of Chengdu Metro Line 11 were analysed, and some risk response strategies were provided based on the results of the case analysis. The results of the case study revealed that the frequency of storms, intensity of rainfall, preparation of emergency rescue plans, and proportion of older workers have the greatest impacts on the waterlogging risk in deep foundation pits. These four factors

were also the key factors in the waterlogging disaster of Diaoyuzui Station during the 2018 flood season, and project management personnel should place focus on them in future waterlogging risk management and decision-making. The waterlogging risk ranking results of the three typical deep foundation pits calculated by the proposed method were basically congruent with the disaster situation in the 2018 flood season. Consequently, it can be concluded that the proposed method based on the projection pursuit method is both objective and effective. Future research will concentrate on the establishment of a unified waterlogging risk evaluation index system and the use of more soft computing methods for waterlogging risk evaluation.

Data Availability

The MATLAB programs and case analysis data used to support the findings of this study are available from the corresponding author upon request.

Conflicts of Interest

The authors declare that there are no conflicts of interest regarding the publication of this paper.

Acknowledgments

References

[1] S. Tei, T. Morozumi, S. Nagai et al., "An extreme flood caused by a heavy snowfall over the Indigirka river basin in Northeastern Siberia," *Hydrological Processes*, vol. 34, no. 3, pp. 522–537, 2020.

[2] S. Liu, M. N. Lin, and C. L. Li, "Analysis of the effects of the river network structure and urbanization on waterlogging in high-density urban areas-a case study of the Pudong new area in Shanghai," *International Journal of Environmental Research and Public Health*, vol. 16, no. 18, Article ID 3306, 2019.

[3] H. Wu, "Research and discussion on urban waterlogging in Wuhan," *Water Supply and Sewerage*, vol. 53, no. 1, pp. 117–119, 2017.

[4] J. Hou and Y. Du, "Spatial simulation of rainstorm waterlogging based on a water accumulation diffusion algorithm," *Geomatics, Natural Hazards and Risk*, vol. 11, no. 1, pp. 71–87, 2020.

[5] J. X. Jia, X. Y. Wang, N. A. M. Hersi et al., "Flood-risk zoning based on analytic hierarchy process and fuzzy variable set theory," *Natural Hazards Review*, vol. 20, no. 3, Article ID 04019006, 2019.

[6] Z. N. Wu, Y. X. Shen, and H. L. Wang, "Assessing urban areas' vulnerability to flood disaster based on text data: a case study in Zhengzhou city," *Sustainability*, vol. 11, no. 17, Article ID 4548, 2019.

[7] H. Y. Yu, C. Liang, P. Li et al., "Evaluation of waterlogging risk in an urban subway station," *Advances in Civil Engineering*, Article ID 5393171, 2019.

[8] R. Mikaeil, S. Shaffiee Haghshenas, Y. Shirvand, M. Valizadeh Hasanluy, and V. Roshanaei, "Risk assessment of geological hazards in a tunneling project using harmony search algorithm (case study: Ardabil-Mianeh Railway tunnel)," *Civil Engineering Journal*, vol. 2, no. 10, pp. 546–554, 2016.

[9] D. T. Bui, N. D. Hoang, T. D. Pham et al., "A new intelligence approach based on GIS-based multivariate adaptive regression splines and metaheuristic optimization for predicting flash flood susceptible areas at high-frequency tropical typhoon area," *Journal of Hydrology*, vol. 575, pp. 314–326, 2019.

[10] R. Mikaeil, M. Beigmohammadi, E. Bakhtavar et al., "Assessment of risks of tunneling project in Iran using artificial bee colony algorithm," *SN Applied Sciences*, vol. 1, no. 12, Article ID 1711, 2019.

[11] P. Wei, F. Qiang, L. Dong et al., "Assessing agricultural drought vulnerability in the Sanjiang Plain based on an improved projection pursuit model," *Natural Hazards*, vol. 82, no. 1, pp. 683–701, 2016.

[12] Y. Sen and L. H. Wei, "An integrated model of water resources optimization allocation based on projection pursuit model-grey wolf optimization method in a transboundary river basin," *Journal of Hydrology*, vol. 559, pp. 156–165, 2018.

[13] Y. Liang, D. Guo, Z. Huang, and X. Jiang, "Prediction model for coal-gas outburst using the genetic projection pursuit method," *International Journal of Oil, Gas and Coal Technology*, vol. 16, no. 3, pp. 271–282, 2017.

[14] D. Liu, G. D. Zhang, and H. Li, "Projection pursuit evaluation model of a regional surface water environment based on an Ameliorative Moth-Flame Optimization algorithm," *Ecological Indicators*, vol. 107, no. 1, Article ID 105674, 2019.

[15] Y. S. Jiang, D. Zhao, D. D. Wang et al., "Sustainable performance of buildings through modular prefabrication in the construction phase: a comparative study," *Sustainability*, vol. 11, no. 20, Article ID 5658, 2019.

[16] S. Li, C. Jiang, and A. Li, "Research on Chinese well-known e-commerce enterprises' innovation ability based on real comment," *International Journal of Computing Science and Mathematics*, vol. 11, no. 1, pp. 54–62, 2020.

[17] W. J. Zhang, F. Wei, R. Zhou et al., "Risk assessment of cotton textile enterprise working environment based on projection pursuit model," *China Safety Science Journal*, vol. 28, no. 4, pp. 103–108, 2018.

[18] A. Kukker and R. Sharma, "Genetic algorithm-optimized fuzzy lyapunov reinforcement learning for nonlinear systems," *Arabian Journal for Science and Engineering*, vol. 45, no. 3, pp. 1629–1638, 2020.

[19] R. Bendaoud, H. Amiry, M. Benhmida et al., "New method for extracting physical parameters of PV generators combining an implemented genetic algorithm and the simulated annealing algorithm," *Solar Energy*, vol. 194, pp. 239–247, 2019.

[20] R. Mikaeil, S. Shaffiee Haghshenas, and Z. Sedaghati, "Geotechnical risk evaluation of tunneling projects using optimization techniques (case study: the second part of Emamzade Hashem tunnel)," *Natural Hazards*, vol. 97, no. 3, pp. 1099–1113, 2019.

[21] A. R. Dormishi, M. Ataei, R. K. Kakaie et al., "Performance evaluation of gang saw using hybrid ANFIS-DE and hybrid ANFIS-PSO algorithms," *Journal of Mining and Environment*, vol. 10, no. 2, pp. 543–557, 2019.

[22] M. Hasanipanah, R. Naderi, J. Kashir, S. A. Noorani, and A. Zeynali Aaq Qaleh, "Prediction of blast-produced ground vibration using particle swarm optimization," *Engineering with Computers*, vol. 33, no. 2, pp. 173–179, 2017.

[23] P. Ronco, V. Gallina, S. Torresan et al., "The KULTURisk regional risk assessment methodology for water-related natural hazards–part 1: physical-environmental assessment," *Hydrology and Earth System Sciences*, vol. 18, no. 12, pp. 5399–5414, 2014.

[24] P. Cui and D. Li, "Measuring the disaster resilience of an urban community using ANP-FCE method from the perspective of capitals," *Social Science Quarterly*, vol. 100, no. 6, pp. 2059–2077, 2019.

[25] Y. Zhou, N. Li, W. Wu, and J. Wu, "Assessment of provincial social vulnerability to natural disasters in China," *Natural Hazards*, vol. 71, no. 3, pp. 2165–2186, 2014.

[26] Y. Wei and O. Linet, "A dynamic logistics coordination model for evacuation and support in disaster response activities," *European Journal of Operational Research*, vol. 179, no. 3, pp. 1177–1193, 2007.

[27] M.-S. Chang, Y.-L. Tseng, and J.-W. Chen, "A scenario planning approach for the flood emergency logistics preparation problem under uncertainty," *Transportation Research Part E: Logistics and Transportation Review*, vol. 43, no. 6, pp. 737–754, 2007.

[28] E. L. Guo, J. Q. Zhang, Y. F. Wang et al., "Dynamic risk assessment of waterlogging disaster for maize based on CERES-Maize model in Midwest of Jilin province, China," *Natural Hazards*, vol. 83, no. 3, pp. 1747–1761, 2016.

[29] X. Liu and H. Chen, "Integrated assessment of ecological risk for multi-hazards in Guangdong province in southeastern China," *Geomatics, Natural Hazards and Risk*, vol. 10, no. 1, pp. 2069–2093, 2019.

[30] Y. L. Liang, Y. L. Wang, Y. J. Zhao et al., "Analysis and projection of flood hazards over China," *Water*, vol. 11, no. 5, Article ID 1022, 2019.

[31] M. Ma, H. Wang, P. Jia et al., "Investigation of inducements and defenses of flash floods and urban waterlogging in Fuzhou, China, from 1950 to 2010," *Natural Hazards*, vol. 91, no. 2, pp. 803–818, 2018.

[32] D. Liu, C. Liu, Q. Fu et al., "Projection pursuit evaluation model of regional surface water environment based on improved chicken swarm optimization algorithm," *Water Resources Management*, vol. 32, no. 4, pp. 1325–1342, 2018.

[33] J. Zhao, J. Jin, Q. Guo, L. Liu, Y. Chen, and M. Pan, "Dynamic risk assessment model for flood disaster on a projection pursuit cluster and its application," *Stochastic Environmental Research and Risk Assessment*, vol. 28, no. 8, pp. 2175–2183, 2014.

[34] S. Wang, X. Zhang, Z. Yang, J. Ding, and Z. Shen, "Projection pursuit cluster model based on genetic algorithm and its application in Karstic water pollution evaluation," *International Journal of Environment and Pollution*, vol. 28, no. 3/4, pp. 253–260, 2006.

[35] D. Liu, J. P. Feng, H. Li et al., "Spatiotemporal variation analysis of regional flood disaster resilience capability using an improved projection pursuit model based on the wind-driven optimization algorithm," *Journal of Cleaner Production*, vol. 241, Article ID 118406, 2019.

[36] X. Huang and H. Bai, "Risk prediction of rural public security environmental carrying capacity based on the risk entropy," *Natural Hazards*, vol. 90, no. 1, pp. 157–171, 2018.

[37] Z. Lan and M. Huang, "Safety assessment for seawall based on constrained maximum entropy projection pursuit model," *Natural Hazards*, vol. 91, no. 3, pp. 1165–1178, 2018.

[38] J. H. Yuan and C. B. Li, "Intuitionistic trapezoidal fuzzy group decision-making based on prospect choquet integral operator and grey projection pursuit dynamic cluster," *Mathematical Problems in Engineering*, vol. 2017, Article ID 2902506, 13 pages, 2017.

[39] C. Qi, A. Fourie, Q. Chen et al., "Neural network and particle swarm optimization for predicting the unconfined compressive strength of cemented paste backfill," *Construction and Building Materials*, vol. 159, pp. 473–478, 2018.

[40] X. H. Yang, Z. F. Yang, Z. Y. Shen et al., "Interpolation model for flood disaster assessment based on projection pursuit," *Disaster Science*, vol. 4, pp. 3–8, 2004.

[41] J. E. Ware, M. Kosinski, and S. D. Keller, "A 12-item short-form health survey," *Medical Care*, vol. 34, no. 3, pp. 220–233, 1996.

[42] J. J. Liang, A. K. Qin, P. N. Suganthan, and S. Baskar, "Comprehensive learning particle swarm optimizer for global optimization of multimodal functions," *IEEE Transactions on Evolutionary Computation*, vol. 10, no. 3, pp. 281–295, 2006.

[43] N. Lynn and P. N. Suganthan, "Heterogeneous comprehensive learning particle swarm optimization with enhanced exploration and exploitation," *Swarm and Evolutionary Computation*, vol. 24, pp. 11–24, 2015.

[44] Z. H. Zhan, J. Zhang, Y. Li, and H. S.-H. Chung, "Adaptive particle swarm optimization," *IEEE Transactions on Systems Man and Cybernetics Part B-Cybernetics*, vol. 39, no. 6, pp. 1362–1381, 2009.

[45] A. Berro, S. Larabi Marie-Sainte, and A. Ruiz-Gazen, "Genetic algorithms and particle swarm optimization for exploratory projection pursuit," *Annals of Mathematics and Artificial Intelligence*, vol. 60, no. 1-2, pp. 153–178, 2010.

[46] R. J. Bolton and W. J. Krzanowski, "Projection pursuit clustering for exploratory data analysis," *Journal of Computational and Graphical Statistics*, vol. 12, no. 1, pp. 121–142, 2003.

[47] A. I. Gorshkov, H. M. Hassan, and O. V. Novikova, "Seismogenic nodes (M ≥ 5.0) in northeast Egypt and implications for seismic hazard assessment," *Pure and Applied Geophysics*, vol. 176, no. 2, pp. 593–610, 2019.

Research Article

Strength and Microscopic Damage Mechanism of Yellow Sandstone with Holes under Freezing and Thawing

Huren Rong,[1,2,3] **Jingyu Gu,**[4] **Miren Rong** [ID],[5] **Hong Liu,**[1] **Jiayao Zhang,**[4] **and Hao Dong**[4]

[1]*Department of Civil Engineering Shanxi University, Taiyuan, Shanxi 030013, China*
[2]*Road College of Chang'an University, Shanxi, Xian 710064, China*
[3]*Qinghai Provincial Institute of Transportation Science, Xining, Qinghai 810016, China*
[4]*Hebei Institute of Architecture and Civil Engineering, Zhangjiakou, Hebei 075024, China*
[5]*Shijiazhuang Tiedao University, Shijiazhuang 050043, Hebei, China*

Correspondence should be addressed to Miren Rong; tdxyrong2004@163.com

Received 10 November 2019; Accepted 13 February 2020; Published 30 April 2020

Academic Editor: Jorge Branco

In order to study the damage characteristics of the yellow sandstone containing pores under the freeze-thaw cycle, the uniaxial compression test of saturated water-stained yellow sandstones with different freeze-thaw cycles was carried out by rock servo press, the microstructure was qualitatively analyzed by Zeiss 508 stereo microscope, and the microdamage mechanism was quantitatively studied by using specific surface area and pore size analyzer. The mechanism of weakening mechanical properties of single-hole yellow sandstone was expounded from the perspective of microstructure. The results show the following. (1) The number of freeze-thaw cycles and single-pore diameter have significant effects on the strength and elastic modulus of the yellow sandstone; the more the freeze-thaw cycles and the larger the pore size, the lower the strength of the yellow sandstone. (2) The damage modes of the yellow sandstone containing pores under the freeze-thaw cycle are divided into five types, and the yellow sandstone with pores is divided into two areas: the periphery of the hole and the distance from the hole; as the number of freeze-thaw cycles increases, different regions show different microscopic damage patterns. (3) The damage degree of yellow sandstone is different with freeze-thaw cycle and pore size. Freeze-thaw not only affects the mechanical properties of yellow sandstone but also accelerates the damage process of pores. (4) The damage of the yellow sandstone by freeze-thaw is logarithmic function, and the damage of the yellow sandstone is a power function. The damage equation of the yellow sandstone with pores under the freezing and thawing is a log-power function nonlinear change law and presents a good correlation.

1. Introduction

With the gradual implementation of the strategy of developing the western region, the cold area needs a lot of engineering construction [1] and more and more rocks and rock damage problems under the conditions of alternating low temperature and temperature; the rock itself is a relative water content. The higher materials, combined with the temperature difference between day and night, make the freeze-thaw cycle appear, accompanied by the generation and disappearance of the frost heaving force, which causes cumulative damage to the rock mass structure. Therefore, with the deepening of the development of the western region, it is of great theoretical and practical significance to study the mechanism of rock mechanical deterioration under the action of freeze-thaw cycles.

At present, scholars at home and abroad have made corresponding research on the performance of rocks under freeze-thaw cycles. Hall et al. [1, 2] studied the mechanical properties of rocks under freezing and thawing; Yamabe et al. [3–5] studied damage degradation of different types of rocks under freeze-thaw cycles; Yang et al. [6, 7] used CT scanning technique to study the mesoscopic damage propagation mechanism inside rocks with different freezing and thawing temperatures; DelRoa et al. [8] analyzed the damage degradation mechanism of different types of granite under the freeze-thaw cycle by ultrasonic wave monitoring technology through ultrasonic monitoring technology; using

CT scanning technology, CT image, scanning electron microscope by Wang et al. [9–11], the mechanical properties and internal damage of rocks with different saturated states under freeze-thaw cycles were studied. Zhang et al. [12–17] found that the mechanical properties of sandstone deteriorated under the combined action of freezing and thawing and load. The speed is accelerated; Huseyin [18] analyzed the deterioration of hardness, wave velocity, and compressive strength of andesite after freeze-thaw cycles; Li et al. [19], taking the rock mass under the action of freeze-thaw cycles as research object, based on the mesoscopic damage theory and macroscopic damage model, established a single-fracture sandstone damage model under freeze-thaw-load coupling. Zhou et al. [20] used NMR experiments to study the compressive strength of sandstone under freeze-thaw cycles. Reasons for the decrease are as follows: Tian and Xu [21], based on the pore characteristics inside the rock after freezing and thawing, established the relationship between the mechanical properties of the rock and the porosity during the freeze-thaw cycle.

Most scholars have studied the physical and microscopic properties of rocks after freezing and thawing. There are few studies on the properties of rock with pores and the apparent damage characteristics after freezing and thawing by microscope. This paper takes the construction of rock mass in cold area as the background. The saturated single-hole yellow sandstone with pores is studied. The mechanical properties of saturated yellow sandstone with pores under freezing and thawing are obtained by uniaxial compression test. The pores and yellows are described by stereo microscope and pore size analyzer. The microscopic damage mechanism of sandstone provides a reference for the construction of rock mass engineering in cold regions.

2. Test Overview

2.1. Sample Preparation and Working Conditions. The origin of the yellow sandstone in this experiment is Sichuan. The main mineral components of the sandstone are quartz, feldspar, muscovite, clay, and silty materials. The apparent crumbs are densely compacted and the cement is tightly connected. According to the rock test standards and specifications, a rectangular parallelepiped sample of 30 mm × 60 mm × 120 mm was prepared. The selected test conditions were as follows: single-hole yellow sandstone samples with pore diameters of 0 mm (control group), 6 mm, 8 mm, 10 mm, and 12 mm. The freeze-thaw cycle test was carried out at 0, 5, 10, 20, and 40 times. At the early stage, 5 samples were selected for each working condition. At the later stage, 2 samples with relatively high dispersion (mechanical properties were taken as the main reference) were removed, and 3 samples with relatively small dispersion were listed for analysis.

The list of compressive strength and average value of each sample was added, and samples close to the average value were listed for microscopic analysis in this paper.

2.2. Test Methods and Principles. Freeze-thaw cycle test method: using the freeze-thaw cycle test machine to simulate the cold-thaw environment of the cold zone, set the freeze-thaw cycle temperature to −20°C~20°C, the temperature from 20°C to −20°C, and then the constant temperature for 4 hours. After rising to 20°C, the temperature is kept constant for 4 hours. By default, this process is one cycle.

German Zeiss 508 stereo microscope principle: the microscope can clearly observe the surface and pore variation characteristics of yellow sandstone before and after freezing and thawing by high magnification amplification principle. One surface of yellow sandstone is selected as the observation surface, and the observation surface is divided into A and B. Two areas (B area is a square with a side length of 10 mm) and several points are uniformly selected in different areas for observation, as shown in Figure 1; in order to reduce the test error, two observations before and after the freeze-thaw test ensure that the room is in a dark environment, the only source of light is the instrument's own light, using the same light intensity, and the eyepieces use the same magnification, to ensure that the two test conditions are exactly the same.

The principle of specific surface area and pore size analyzer: its essence is nitrogen adsorption method, nitrogen has good reversible adsorption characteristics, and nitrogen molecules are used as measuring tools. Under constant temperature and pressure, the surface of the sample forms monomolecular nitrogen due to van der Waals force between molecules. In the adsorption layer, when the pressure of the adsorption gas is changed, the curve of the adsorption/desorption amount of the sample surface with the pressure can be obtained, and the specific surface area and the pore size distribution of the sample are calculated by the BET method and the BJH method.

The test is based on saturated yellow sandstone as follows: ① The prepared yellow sandstone is immersed in water for 48 hours and then dried and weighed. ② The saturated sample is placed in a German Zeiss 508 stereo microscope (as shown in Figure 2). The apparent particle and pore structure are observed under the microscope. ③ The saturated sample observed by the microscope is placed in the freeze-thaw cycle test machine in turn. ④ The frozen sample after freezing and thawing is taken out, weighed, placed under the microscope again and observed and compared with the apparent granules and pore structure of the unfrozen and thawed samples. ⑤ After the freeze-thaw test, take a small number of samples under different freeze-thaw cycles, using the specific surface area and pore size analyzer (Figure 3). The specific surface area and the change of the pore diameter are detected. ⑥ The sample after the freeze-thaw and the microscopic observation is subjected to uniaxial compression test to test the mechanical properties.

3. Mechanical Properties of Yellow Sandstone before and after Freezing and Thawing Cycles

3.1. Peak Strength of Different Diameter Yellow Sandstone after Freeze-Thaw Cycle. Tables 1 and 2 in Appendix are lists of
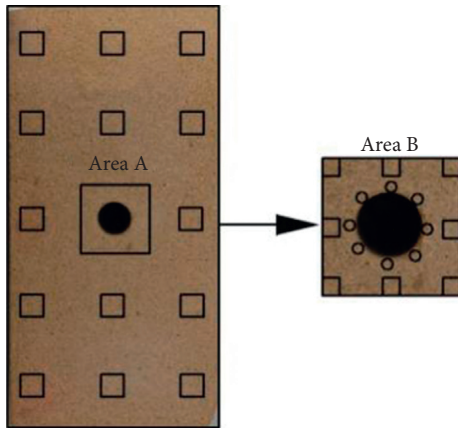
Figure 1: Single-hole yellow sandstone observation area.

Figure 2: German Zeiss 508 stereo microscope.

Figure 3: Specific surface area and pore size analyzer.

test samples for compressive strength and microscopic analysis. The average compressive strength is used for mechanical properties analysis below.

Figure 4 is a graph showing the compressive strength of different diameter yellow sandstones with the number of freeze-thaw cycles. It can be seen from the figure that as the number of freeze-thaw cycles increases, the compressive strength of five groups of different diameter yellow sandstones gradually decreases. When the freeze-thaw cycle is 0 times, the compressive strength of the yellow sandstone with different pore sizes is the largest. When the freeze-thaw cycle is 40 times, the compressive strength of the yellow sandstone with different pore sizes is the smallest. The case of the complete 12 mm yellow sandstone with different freeze-thaw cycles is taken as an example. Description: the compressive strength of intact yellow sandstone is 60.07 MPa when the freeze-thaw cycle is 0 times, and the compressive strength is 54.89 MPa, 51.38 MPa, 48.07 MPa, and 41.3 MPa when the freeze-thaw cycle is 5, 10, 20, and 40 times. Compared with freezing and thawing, the intensity decreased by 8.62%, 14.47%, 19.98%, and 31.25%, respectively. The compressive strength of the 12 mm yellow sandstone was 37.86 MPa when frozen and thawed, and the freeze-thaw cycle was 5, 10, 20, and 40 times. When the compressive strength is 37.59 MPa, 30.55 MPa, 27.07 MPa, and 19.05 MPa, respectively, the strength is reduced by 0.71%, 19.3%, 28.5%, and 49.68%, respectively.
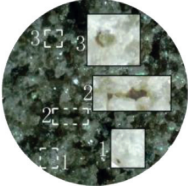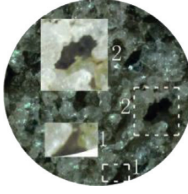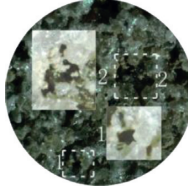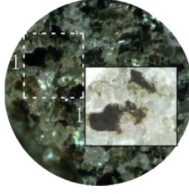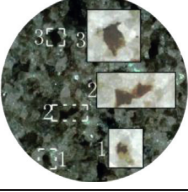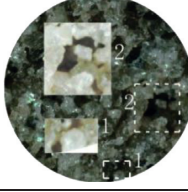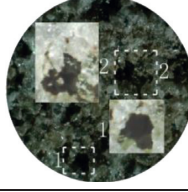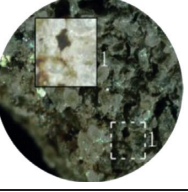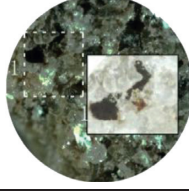
It is found that the compressive strength of the yellow sandstone with the same pore diameter increases with the increase of the number of freeze-thaw cycles, indicating that the freezing and thawing effect is an important factor affecting the compressive strength of the yellow sandstone.

In addition, the compressive strength of different diameter yellow sandstones also showed different changes under the same number of freeze-thaw cycles. When the freeze-thaw cycle was 0 times, the compressive strength of intact yellow sandstone was 60.07 MPa, and with the increase of the pore diameter, the strengths are 51.33 MPa, 49.95 MPa, 45.34 MPa, and 37.86 MPa, respectively. The strength is reduced compared with the intact yellow sandstone. When the freeze-thaw cycle is 40 times, the compressive strength of the intact yellow sandstone is 41.3 MPa. With the increase of the pore size, the compressive strengths are 38.64 MPa, 34.83 MPa, 29.79 MPa, and 19.05 MPa, respectively, and the strengths are reduced by 6.4%, 15.67%, 27.43%, and 53.87%, respectively, compared with the intact yellow sandstone, indicating that the pores reduce the compressive strength of the yellow sandstone. And the larger the aperture, the larger the reduction.

3.2. Elastic Modulus of Yellow Sandstone with Different Pore Sizes after Freeze-Thaw Cycles. The elastic modulus is the physical parameter that characterizes the yellow sandstone resisting the external elastic deformation. Figure 5 is the curve of the elastic modulus of the yellow sandstone with different pore sizes as a function of the number of freeze-thaw cycles. The elastic modulus of the yellow sandstone after different freeze-thaw cycles can be seen from the figure. Similar to the compressive strength, the overall trend is gradually decreasing. Under different freezing and thawing cycles, the elastic modulus of intact yellow sandstone is 9.653 GPa, 8.645 GPa, 8.31 GPa, 6.499 GPa, and 6.32 GPa, respectively, compared with freezing and thawing 0 times. The reductions are 10.44%, 13.91%, 32.67%, and 34.53%,

TABLE 1: Microdamage mode table.

Microscopic damage mode	(1) Particle flaking	(2) Pore is granules filling	(3) Pore expansion	(4) Pore shrinkage	(5) Pore connectivity
Microscopic under the microscope damage before					
Microscopic under the microscope damage after					

respectively. The elastic modulus of the 12 mm yellow sandstone is 8.16 GPa, 6.303 GPa, 5.975 GPa, 4.59 GPa, and 3.658 GPa, which is lower than that of freezing and thawing 0 times. They are 22.76%, 26.781%, 43.75%, and 55.17%, respectively; with the increase of the number of freeze-thaw cycles and the elastic modulus of yellow sandstone, the amount is decreasing and the decline is increasing. The elastic modulus of different diameter yellow sandstones with the same number of freeze-thaw cycles is analyzed. It can be seen that the elastic modulus of yellow sandstone with different pore sizes is the largest when the freeze-thaw cycle is 0 times, which are 9.653 GPa, 11.06 GPa, 7.581 GPa, 8.78 GPa, and 8.16 GPa, respectively. The elastic modulus of the 6 mm yellow sandstone is the largest under the number of freeze-thaw cycles, and the elastic modulus of the 8 mm yellow sandstone is the smallest, which indicates that the yellow sandstone has no significant change with the hole. However, as the number of freeze-thaw cycles increases, at the freeze-thaw cycle 5, 10, 20, and 40, the yellow sandstones with different pore sizes show that the elastic modulus decreases with the increase of the pores.

Comparing the mechanical properties of different diameter yellow sandstones under different freeze-thaw cycles, it is found that the damage of yellow sandstone caused by freezing and thawing will increase the damage of yellow sandstone.
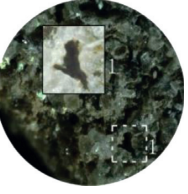
4. Microscopic Characteristics of Different Diameter Yellow Sandstones after Freeze-Thaw Cycles

4.1. Microscopic Damage Pattern Analysis. The microscopic pores and particle changes of different diameter yellow sandstones under different freeze-thaw cycles observed by microscope were summarized, and the five microscopic damage modes shown in Table 1 were summarized.

4.2. Microscopic Qualitative Analysis. In order to more clearly characterize the effects of freezing and thawing and pore action on the granules and pores of the yellow sandstone, the micropictures of the yellow sandstones with different freeze-thaw cycles and different pore sizes were pretreated, and the particles were separated from the pores. The treatment effect is shown in Figure 6, showing that the black areas represent pores and the white areas represent particles.

The freezing and thawing cycles cause different degrees of damage inside the yellow sandstone. The existence of the pores divides the damage of the yellow sandstone into the A and B regions as shown in Figure 1. With the increase of the diameter of the holes, the A and B regions of the yellow sandstone have the following characteristics. The range is different, but the damage mode remains unchanged. This paper focuses on the analysis of the difference of damage patterns in the A and B regions under different freeze-thaw cycles.

Combined with Figures 7 and 8 and microscope observations, the following has been found: ① When the freeze-thaw cycle is 5 times, the main damage mode of the yellow sandstone in the A region is pore shrinkage, the pores are filled by particles, and the main damage mode in the B region is pore expansion, the number of freeze-thaw cycles. Under the joint action of frost heaving force and hole effect, the B area is seriously damaged and the pores become large. The A area suffers from the frost heaving force on one hand, and the fine ice crystal particles fill the pores. On the other hand, the B area has different effects on the A area. The degree of extrusion causes the pores in zone A to become smaller. ② When the freeze-thaw cycle is 10 times, the main damage modes of the yellow sandstones in the A and B regions are particle spalling. Under this cycle, the surface of the yellow sandstone in the A and B regions falls off and is exposed. The internal particles and pores are more serious. ③ When the freeze-thaw cycle is 20 times, the main damage mode of the yellow sandstone in the A area is pore expansion, and the main damage mode in the B area is pore communication. Under the cycle number, the yellow sandstone particles are affected by the frost heaving force. The intergelation is reduced, the continuous damage in zone A leads to the increase of pores, the effect of pores in zone B accelerates the failure of the rock sample around the hole, and the surface of the yellow sandstone is

TABLE 2: List of test samples for compressive strength and microscopic analysis.

	Standard yellow sandstone		The hole diameter 6 mm		The hole diameter 8 mm		The hole diameter 10 mm		The hole diameter 12 mm	
	Compression strength (MPa)	Average value (MPa)	Compression strength (MPa)	Average value (MPa)	Compression strength (MPa)	Average value (MPa)	Compression strength (MPa)	Average value (MPa)	Compression strength (MPa)	Average value (MPa)
0 times	61.75		53.46		46.32		46.62		41.96	
0 times	60.20▲	60.07	51.13▲	51.33	48.62▲	49.95	46.19▲	45.34	36.38▲	37.86
0 times	58.26		49.32		54.92		43.23		35.23	
5 times	56.22		50.23		49.82		45.07		40.72	
5 times	55.73▲	54.89	48.62▲	48.60	47.06▲	47.48	42.87▲	43.20	36.17▲	37.59
5 times	52.73		46.96		45.56		41.65		35.88	
10 times	52.67		51.08		43.02		41.06		32.51	
10 times	50.89▲	51.38	46.62▲	47.68	41.16▲	41.46	39.37▲	38.90	31.12▲	30.55
10 times	50.59		45.33		40.21		36.23		28.03	
20 times	51.54		46.26		41.55		32.58		29.23	
20 times	46.56▲	48.07	45.27▲	44.88	39.01▲	39.26	31.29▲	31.03	27.86▲	27.07
20 times	46.12		43.12		37.23		29.23		24.13	
40 times	43.23		39.26		36.71		31.15		20.09	
40 times	42.35▲	41.3	39.03▲	38.64	34.03▲	34.83	30.01▲	29.79	20.03▲	19.04
40 times	38.32		37.63		33.75		28.21		17.02	

▲, samples selected for microscopic analysis.
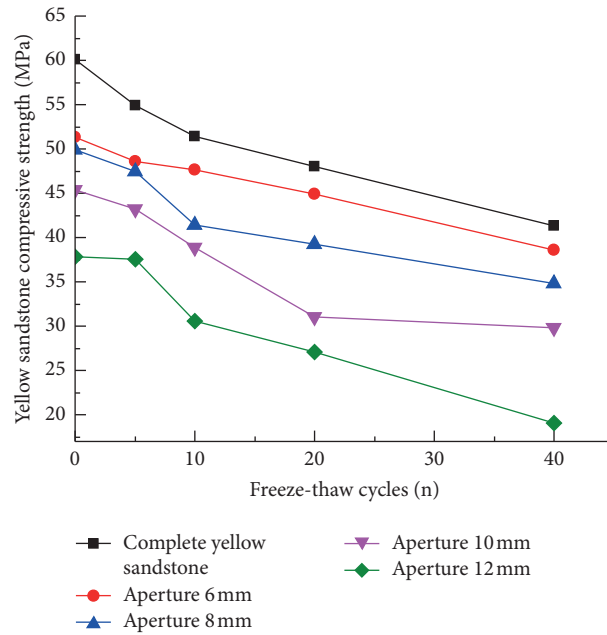
FIGURE 4: Compressive strength curve of yellow sandstone under freeze-thaw cycles.
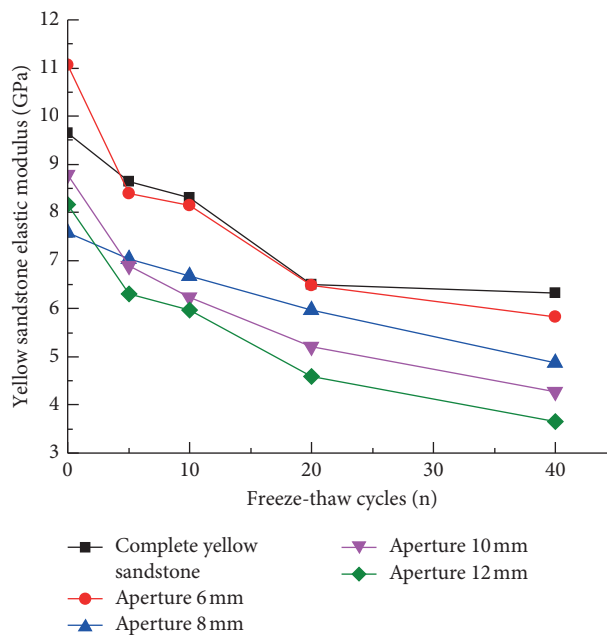
FIGURE 5: Elastic modulus curve of yellow sandstone under freeze-thaw cycles.

accompanied by pores. The phenomenon of the pass: ④ When the freeze-thaw cycle is 40 times, the main damage modes of the yellow sandstones in the A and B regions are pore expansion and accompanied by particle spalling, indicating that, under the cycle number, the high-order circulation freeze-thaw causes the rock sample to have larger pores. At the same time, micropores are continuously generated inside. On the other hand, due to serious damage, the pores inside the rock mass penetrate, resulting in larger pores in the A and B regions.

4.3. Microscopic Quantitative Study. In Figures 9 and 10, (a), (b) and (c) are the pore volume sizes of the A and B regions of the yellow sandstone containing pores measured by nitrogen adsorption, and from (d), (e), and (f) for the relative change of pore volume of different pore sizes (compared with the previous freeze-thaw cycle), the relative change amplitude is used to characterize the response of different types of microscopic pores to freeze-thaw.

As can be seen from (a), (b), and (c), that, as the number of freezing-thawing cycles increased, the pore volumes of
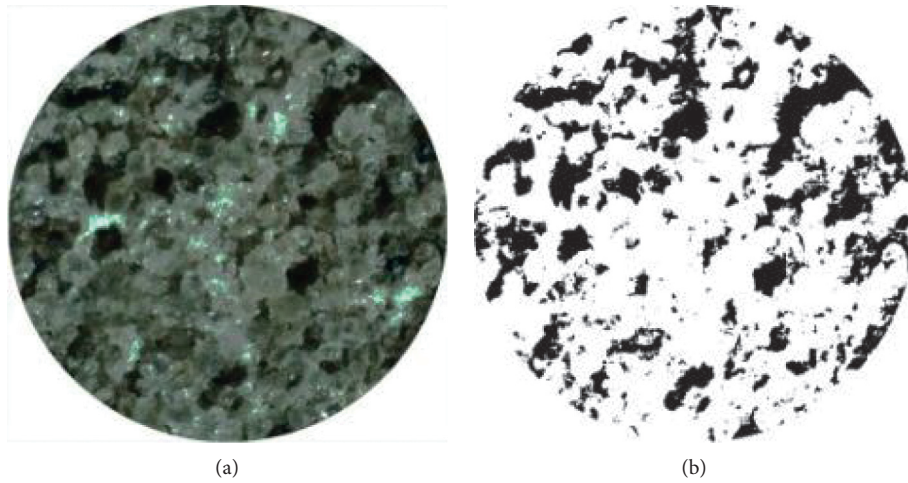
FIGURE 6: Pore extraction.
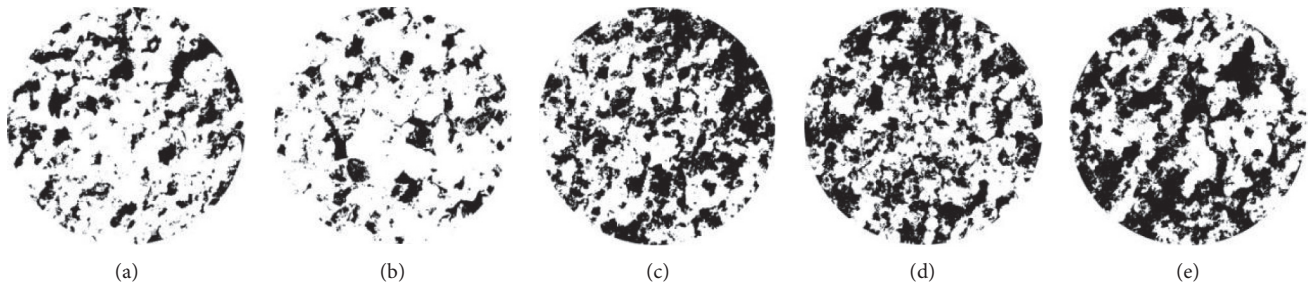
FIGURE 7: Microporosity change diagram of A zone in yellow sandstone under freeze-thaw cycles. (a) Freeze-thaw 0 times. (b) Freeze-thaw 5 times. (c) Freeze-thaw 10 times. (d) Freeze-thaw 20 times. (e) Freeze-thaw 40 times.
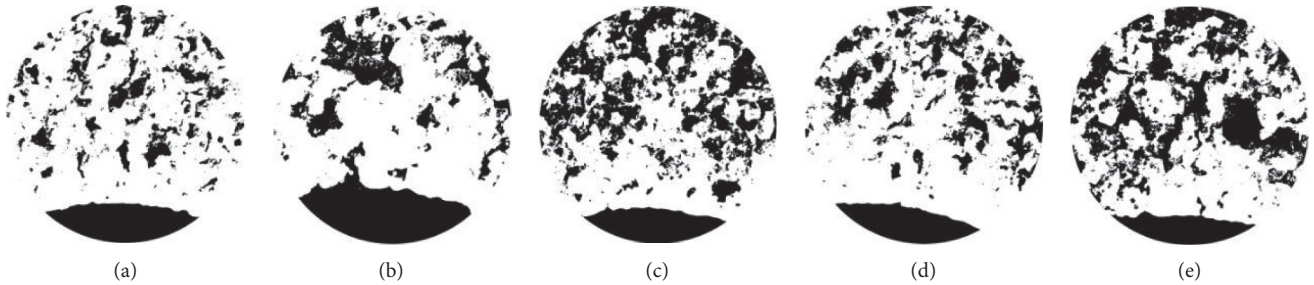
FIGURE 8: Microporosity change diagram of B zone in yellow sandstone under freeze-thaw cycles. (a) Freeze-thaw 0 times. (b) Freeze-thaw 5 times. (c) Freeze-thaw 10 times. (d) Freeze-thaw 20 times. (e) Freeze-thaw 40 times.

small holes, medium holes, and large holes in area A (0~2 nm is micropores, 2~50 nm is medium holes, and holes more than 50 nm are large holes according to the international IUPAC definition) increased on the whole. Only the mesopore volume decreased in the freeze-thaw cycle 5 times, and the volume of small, medium, and large pores in the B region increased overall. Analysis of (d), (e), and (f) combined with microscopic observations shows that the response of A and B regions of yellow sandstone to freezing and thawing is different. ① When the freezing and thawing cycle is 5 times, the pore volume in the A region has the following characteristics. The relative decrease is −36.67%, the relative volume of large pore volume is 0%, and the

relative increase of medium and large pore volume in B area is 83.3% and 41.18%, respectively. Under the cycle number, free mineral particles are produced on the surface of yellow sandstone. In the A region, the pore volume is reduced due to the shrinkage of the mesopores or by the filling of mineral particles. The expansion of the pores and the pores in the B region leads to an increase in the volume of the mesopores and macropores. ② When the freeze-thaw cycle is 10 times, the A region is small. The relative increases in volume of pores, mesopores, and macropores were 100%, 54.89%, and 16.67%, respectively. The relative volume increases of small, medium, and large pores in B region were 80%, 36.36%, and 4.17%. Under the number of times, the connection between
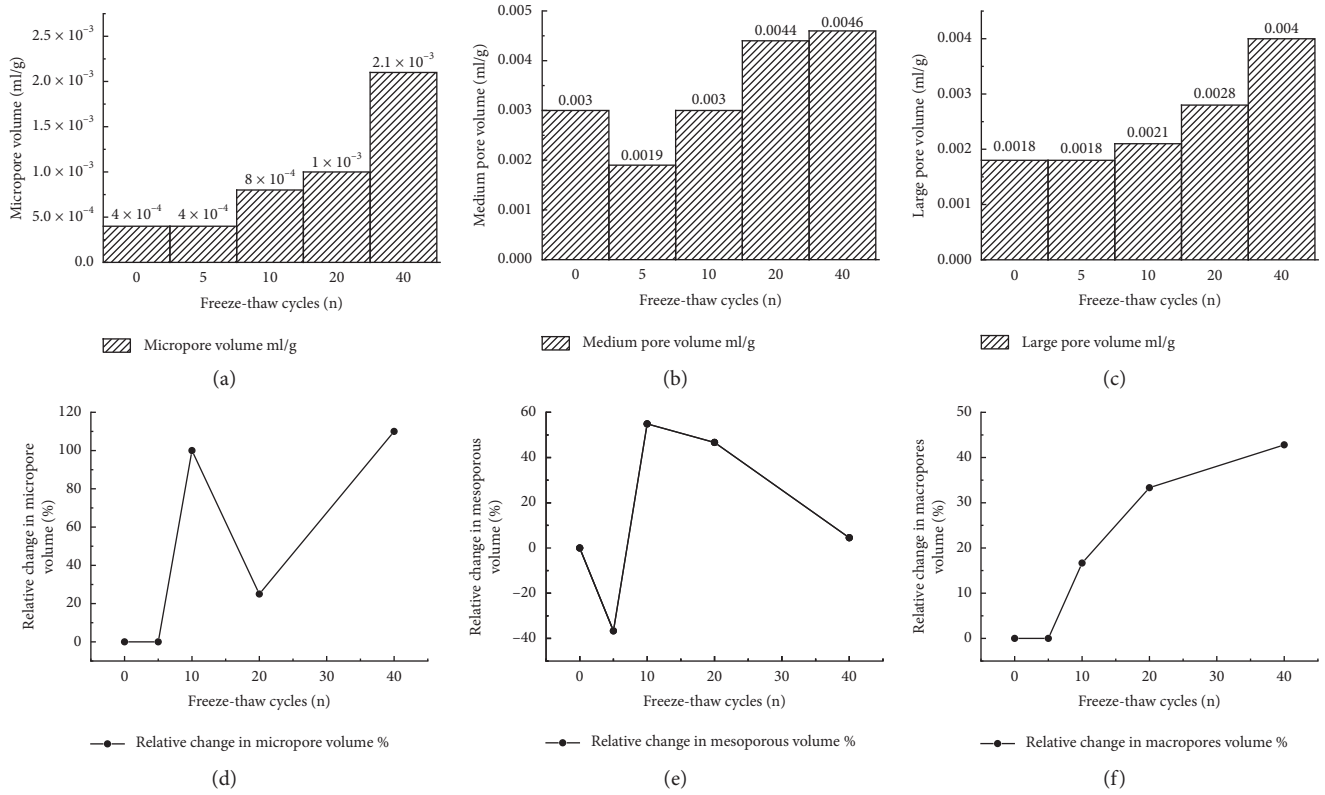
Figure 9: Pore volume and relative change amplitude of A in yellow sandstone under freeze-thaw cycles. (a) Micropore volume. (b) Mesoporous volume. (c) Macropores volume. (d) Relative change in micropore volume. (e) Relative change in mesoporous volume. (f) Relative change in macropores volume.
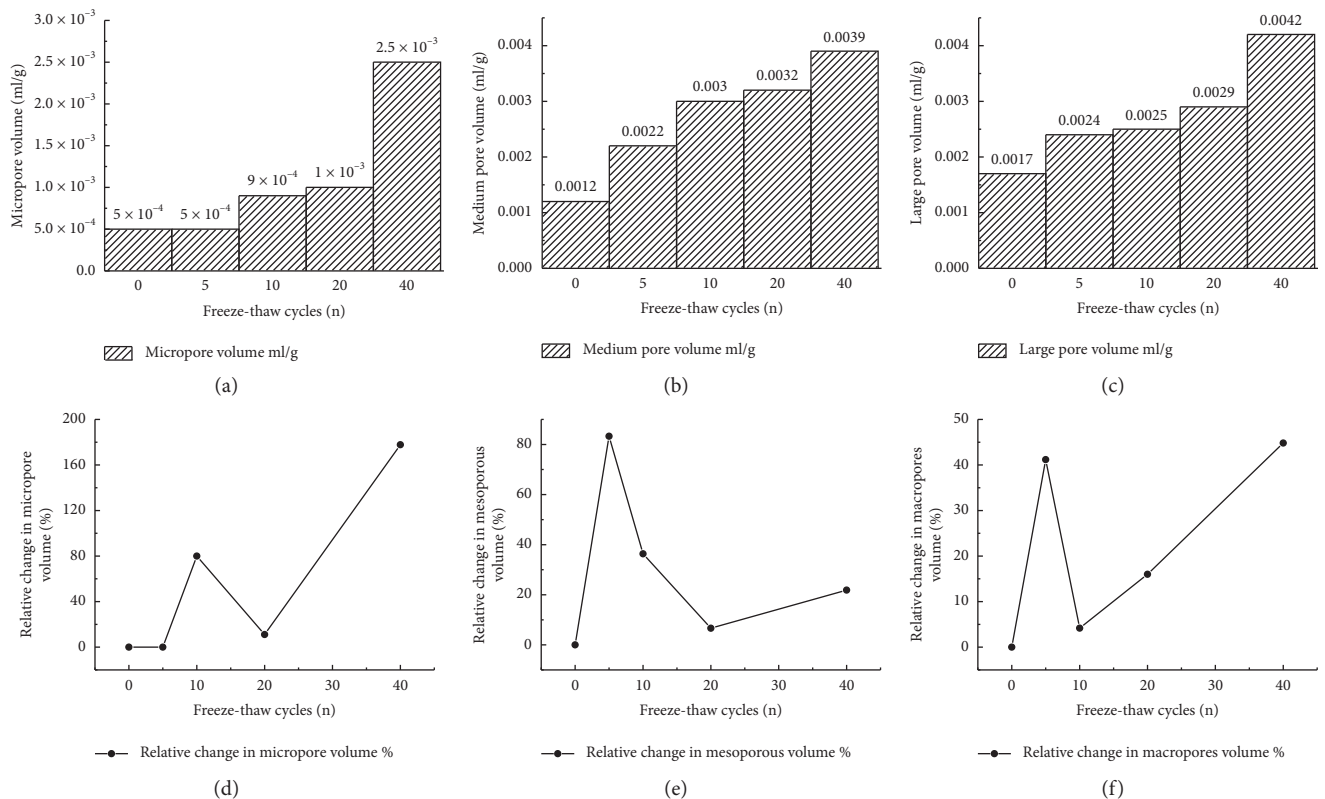
Figure 10: Pore volume and relative change amplitude of B in yellow sandstone under freeze-thaw cycles. (a) Micropore volume. (b) Mesoporous volume. (c) Macropores volume. (d) Relative change in micropore volume. (e) Relative change in mesoporous volume. (f) Relative change in macropores volume.

the aggregates of the yellow sandstone aggregates is loose, and the pores in the A region increase. At the same time, due to the spalling of the particles, the mesopores and macropores are continuously generated. The small pores in the B region increase, while the mesopores and macropores do not change significantly. ③ When the freeze-thaw cycle is 20 times, the pore volume in the A region has the following characteristics. The relative increase is 46.67%, the relative increase of macropore volume is 33.33%, the relative increase of pore volume in B region is 6.66%, and the relative increase of macropore volume is 16%. The volume of mesopores and macropores increases in A region due to pore expansion. Severely, the volume of pores communicating with mesopores and large pores increased slightly in the B region due to particle spalling. ④ When the freeze-thaw cycle was 40 times, the relative increases in the volume of small pores, mesopores, and macropores in the A region were 110%, 4.54%, and 42.8%, respectively. The relative increase of the volume of small holes, mesopores, and macropores in B area was 177.78%, 21.87%, and 44.82%. The A and B areas were seriously damaged by freezing and thawing, and the internal cracks were generated by new cracks. The decrease in force causes the particles to peel off continuously, and the volume of small holes, mesopores, and large pores increases.

In summary, the freezing and thawing cause the pores in the yellow sandstone to increase continuously, the cohesive force decreases, and the strength is continuously reduced, but the single hole also causes damage. In zone A, freezing and thawing 10 times are the threshold for the generation of small holes, mesopores, and macropores in yellow sandstone. In the B region, the freezing and thawing 5 times are the thresholds for the mesopores and macropores, and the freezing and thawing 10 times are the thresholds for the pores. Compared with the pores in the A and B regions, the mesopores and macropores in the B region are significantly better than the A regions. The production time is earlier and the quantity is more, which indicates that, under the action of freezing and thawing and pores, the freezing and thawing will damage the interior of the yellow sandstone, and the pores will further accelerate the degradation of the yellow sandstone, and then the mechanical properties will be accelerated.

5. Yellow Sandstone Damage Function under Freeze-Thaw Cycles

By studying the strength and microscopic properties of the yellow sandstone containing pores after freezing and thawing, it is known that both freezing and thawing and pore effects cause significant damage to the rock. Figure 11 shows the damage process of the yellow sandstone containing pores after freezing and thawing. The volume of the intact yellow sandstone is assumed to be $V1$. The effective volume of the yellow sandstone in the hole is $V1$. The effective volume of the yellow sandstone containing pores under the freezing and thawing is $V2$, so the damage value of the yellow sandstone in the hole is $D1$. The damage value of the frozen-thawed yellow sandstone is $D2$, and the damage value of the
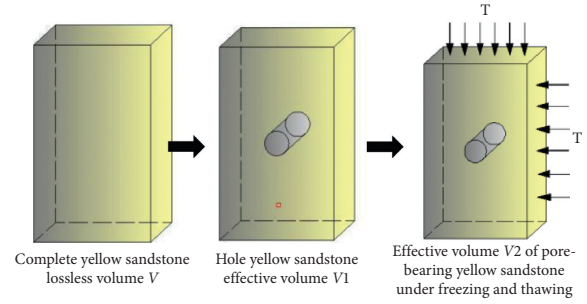
FIGURE 11: Damage process of yellow sandstone with pores under freezing and thawing.

frozen-thawed yellow sandstone is the Dt. The damage of the yellow sandstone in different states is characterized by the change of bulk density:

$$1 - D_1 = \frac{V_1}{V}$$

$$1 - D_2 = \frac{V_2}{V_1} \quad (1)$$

$$1 - D_t = \frac{V_2}{V}.$$

Among them,

$$V\alpha(e)$$
$$V_1\alpha(d, e_1) \quad (2)$$
$$V_2\alpha(d, e_2),$$

where e is the pore volume of the intact yellow sandstone, $e1$ is the pore volume of the yellow sandstone containing the pore, $e2$ is the pore volume of the yellow sandstone containing the pore after freezing and thawing, and d is the diameter of the pore of the yellow sandstone.

According to the above formula, the total damage formula of the yellow sandstone containing pores under freezing and thawing is

$$D_t = D_1 + D_2 - D_1 D_2. \quad (3)$$

The rate of change of compressive strength of the yellow sandstone containing pores after freezing and thawing is taken as the measure of the damage degree of the yellow sandstone, which is expressed as D. Then

$$D = \frac{\sigma_0 - \sigma_i}{\sigma_0}. \quad (4)$$

Among them, σ_0 and σ_i are the compressive strength of yellow sandstone in the initial state (freezing and thawing 0 times, hole diameter is 0 mm); the degree of damage D of the yellow sandstone containing pores after freezing and thawing is shown in Table 3.

The yellow sandstone with a pore size of 0 mm and the damage curve of the yellow sandstone with zero-degree freeze-thaw under the action of freezing and thawing alone were fitted, and the graphs shown in Figures 12 and 13 were obtained.

TABLE 3: Damage degree of yellow sandstone with pores under freezing and thawing.

Freezing and thawing times	Hole diameter (mm)				
	0	6	8	10	12
0	0.000	0.145	0.168	0.245	0.370
5	0.086	0.191	0.210	0.281	0.374
10	0.145	0.206	0.310	0.353	0.491
20	0.200	0.253	0.346	0.483	0.549
40	0.312	0.357	0.42	0.504	0.683
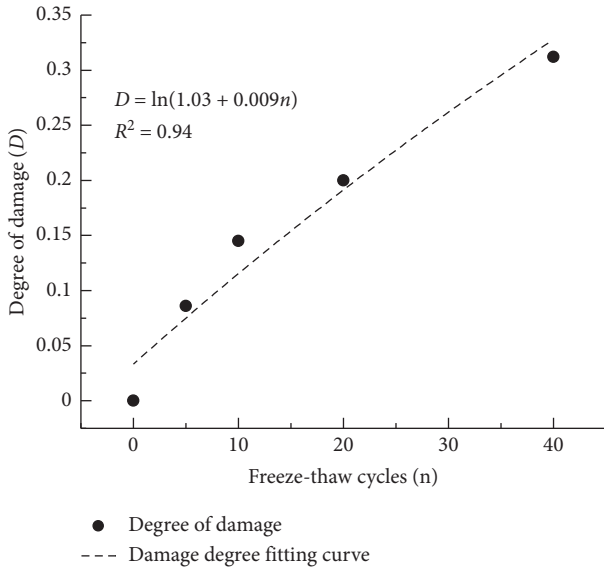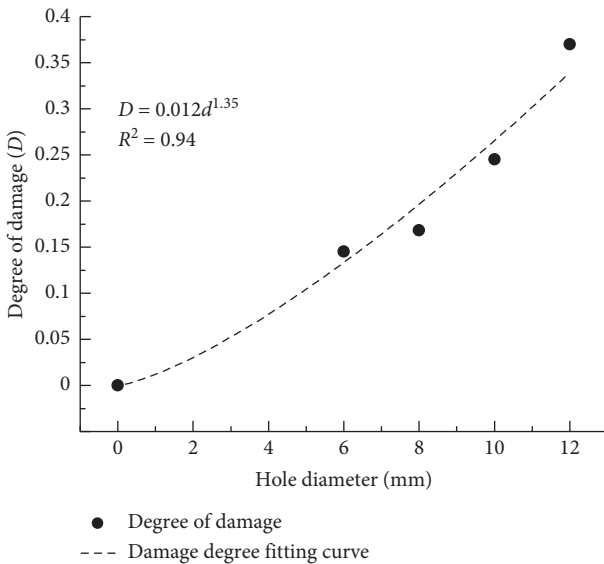
It can be seen from the figure that the damage law of the frozen-thawed yellow sandstone accords with the logistic function:

$$D_2 = \ln(1.03 + 0.009n), \tag{5}$$

where is the number of freeze-thaw cycles.

The damage of yellow sandstone with a pore diameter of 0 mm under the action of freezing and thawing is defined as $D2$, and the damage of yellow sandstone with zero freezing and thawing under the action of pore is defined as $D1$. It can be seen from the figure that the damage curve of frozen-thawed yellow sandstone accords with the logistic function. One has

$$D_1 = 0.012 \times d^{1.35}, \tag{6}$$

where d is the diameter of the hole.

Taking formulas (5) and (6) into (3), the nonlinear equation for the number of freeze-thaw cycles n and the diameter d of the hole is

$$D_t = a\left(0.012d^{1.35}\right) + b\ln(1.03 + 0.009n)$$
$$- c\left(0.012d^{1.35}\right) \times \ln(1.03 + 0.009n), \tag{7}$$

where a, b, and c are the influence factors, respectively.

The following is a fitting of the rock damage with pores under the freeze-thaw cycle. Figure 14 shows the damage curve of yellow sandstone under different freeze-thaw cycles when the aperture is 6 mm. Figure 15 shows the yellow sandstone under different pore sizes when the number of freeze-thaw cycles is 5. The damage curve and the fitting result are shown in Table 4. The damage value of the yellow sandstone containing pores under freezing and thawing is represented by the equation. The fitting curve returns the scattered points into a function with certain physical meaning and has good correlation.

Through the analysis of the fitting curve, it is found that the effects of freezing and thawing and pores have obvious effects on the yellow sandstone. This equation can better reflect the damage degree of the yellow sandstone under the freezing and thawing.

Li et al. [22] and Yuan et al. [23] studied the rock under the combined action of freezing-thawing and crack (joint) and showed that the total damage of rock sample increased under the combined action of freezing-thawing times and crack. The damage is related to freezing-thawing times, crack length, and inclination angle. The macroscopic damage and its coupling effect determine the obvious anisotropy of the joint to the macroscopic damage of rock. With the increase of the number of freeze-thaw cycles, the macroscopic anisotropy of the jointed rock samples is weakened, and the degree of weakening is related to the joint properties and freeze-thaw degree. The anisotropy of rock samples aggravated was verified.

According to the results of hole and freezing-thawing test, this paper shows that, after 5 cycles of freezing-thawing, large hole and middle hole begin to appear around the hole, but far away from the hole area, it has not yet occurred (or the production is few and cannot be monitored). After 10

FIGURE 12: Yellow sandstone damage curve under freezing and thawing.

FIGURE 13: Yellow sandstone damage curve under the action of holes.
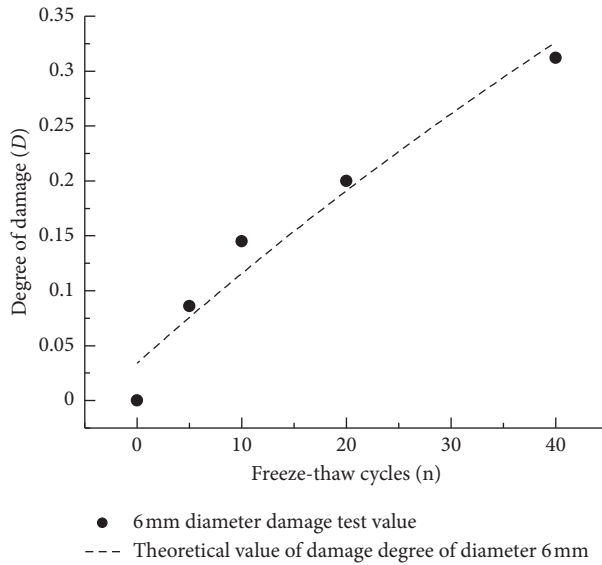
FIGURE 14: Yellow sandstone damage curve of different freeze-thaw cycles (aperture 6 mm).
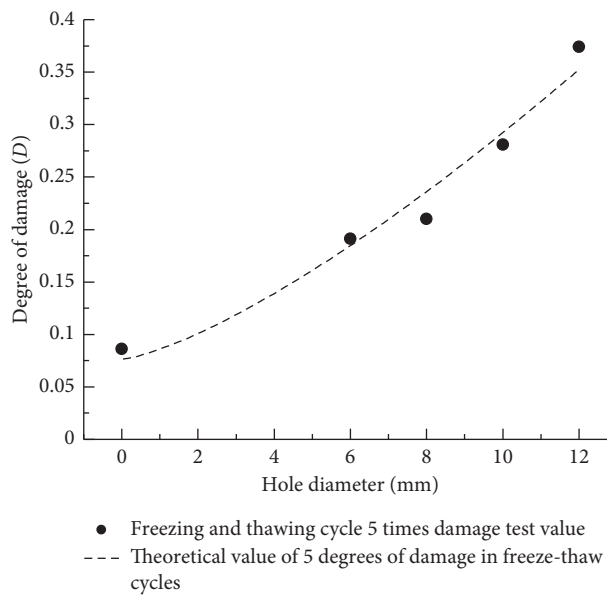
FIGURE 15: Damage curves of different diameter yellow sandstones (5 freeze-thaw cycles).

TABLE 4: Fitting curve related parameters.

Test piece condition	Combined function $D_t = a(0.012d^{1.35}) + b\ln(1.03 + 0.009n) - c(0.012d^{1.35}) \times \ln(1.03 + 0.009n)$			
	a	b	c	R^2
Hole diameter $d = 6$ mm	0.038	1.05	0.59	0.91
Hole diameter $d = 8$ mm	0.85	1.01	0.94	0.8
Hole diameter $d = 10$ mm	0.88	1.09	0.65	0.73
Hole diameter $d = 12$ mm	0.98	1.2	0.37	0.92
Freezing and thawing times $n = 5$	0.94	1.06	1.86	0.94
Freezing and thawing times $n = 10$	1.05	1.01	0.55	0.87
Freezing and thawing times $n = 20$	1.13	0.84	0.28	0.85
Freezing and thawing times $n = 40$	1.18	0.79	0.45	0.71

cycles of freezing-thawing, small holes begin to form around the hole, and then large holes, middle holes, and small holes begin to form when they are far away from the hole area. Therefore, the macroscopic anisotropy of rock samples changed by pore action can be divided into two stages: when the number of freezing-thawing cycles is 0–10 times, the pore patterns around the hole and away from the hole area are different, and the change law is opposite. The macroscopic anisotropy of the sample was enhanced by pore action. When the freezing-thawing cycle was repeated for 10–40 times, the pore patterns around the hole and far away from the hole area were the same, the variation law was the same, and the macroscopic anisotropy of the sample gradually weakened.

6. Conclusion

(1) With the increase of freezing and thawing times and pore size, the compressive strength and elastic modulus of yellow sandstone gradually decrease.

(2) The rock sample with pores after freezing and thawing is divided into two damage areas: the periphery of the hole and the distance from the hole; five kinds of microdamage modes of the yellow sandstone after freezing and thawing are as follows: (1) particle peeling, (2) pores filled by particles, (3) holes extended, (4) pore shrinkage, and (5) pore communication.

(3) As the number of freeze-thaw cycles increases, the damage pattern at the farther hole is different from the damage pattern around the hole. The damage mode at the far hole is filled by pores and the pores are filled with particles (5 times), particle peeling (10 times), pore expansion (20 times), and pore expansion and particle spalling transition (40 times); damage pattern around the hole by pore expansion (5 times), particle spalling (10 times), pore connectivity (20 times), and pore expansion and particles peeling transition (40 times), and the mesopores and macropores around the pore are farther than the pores. The time of occurrence is earlier and the damage is more serious, indicating that the freezing and thawing damage the yellow sandstone, and the hole promotes the damage of the yellow sandstone.

(4) Under the combined action of hole and freeze-thaw, the sample anisotropy caused by hole is divided into two stages: freezing-thawing cycle 0–10 times, the macroscopic anisotropy of the sample was enhanced by pore action; freezing and thawing times 10–40 times, the sample macroscopic anisotropy gradually weakened.

(5) Under the same freezing and thawing frequency, the total damage of rock sample increases with the increase of hole diameter. With the same hole diameter, the total damage of rock sample increases with the increase of freezing-thawing times. The damage

degree of yellow sandstone is closely related to the number of freezing-thawing cycles and the pore size. The damage equation of the yellow sandstone with pores under freezing and thawing is nonlinear. The equation can better reflect the damage of rock with pores under freezing and thawing and provide reference for the long-term stability of damaged rock.

Data Availability

The data used to support the findings of this study are included within the article.

Conflicts of Interest

The authors declare that they have no conflicts of interest.

Acknowledgments

References

[1] K. Hall, "A laboratory simulation of rock breakdown due to freeze-thaw in a maritime Antarctic environment," *Earth Surface Processes and Landforms*, vol. 13, no. 4, pp. 369–382, 1998.

[2] N. Matsuoka, "Microgelivation versus macrogelivation: towards bridging the gap between laboratory and field frost weathering," *Permafrost and Periglacial Processes*, vol. 12, no. 3, pp. 299–313, 2001.

[3] T. Yamabe and K. M. Neaupane, "Determination of some thermo-mechanical properties of Sirahama sandstone under subzero temperature condition," *International Journal of Rock Mechanics and Mining Sciences*, vol. 38, no. 7, pp. 1029–1034, 2001.

[4] X. Tan, W. Chen, J. Yang, and J. Cao, "Laboratory investigations on the mechanical properties degradation of granite under freeze-thaw cycles," *Cold Regions Science and Technology*, vol. 68, no. 3, pp. 130–138, 2011.

[5] B. Fatih, "Predicting mechanical strength loss of natural stones after freeze-thaw in cold regions," *Cold Regions Science and Technology*, vol. 83-84, pp. 98–102, 2012.

[6] G. Yang, Q. Zhang, and Y. Pu, "Study on the influence of freezing temperature on microscopic damage expansion characteristics of rock," *Rock and Soil Mechanics*, vol. 25, no. 9, pp. 1409–1412, 2004.

[7] G. Yang, Q. Zhang, J. Ren et al., "Study on the variation of CT number of Tongchuan sandstone damage caused by freezing speed," *Chinese Journal of Rock Mechanics and Engineering*, vol. 23, no. 24, pp. 4099–4014, 2004.

[8] L. M. Del Roa, F. Lopez, F. J. Esteban et al., "Ultrasonic study of alteration processes in granites caused by freezing and thawing," in *Proceedings of the IEEE Ultrasonics Symposium, 2005*, Rotterdam, The Netherlands, September 2005.

[9] L. Wang and C. H. Yang, "Study on the difference of freezing and thawing damage of red sandstone in different initial

saturated states," *Rock and Soil Mechanics*, vol. 27, no. 10, pp. 1772–1776, 2006.

[10] L. Lang, H. Jia, and Y. Guo, "Study on the mechanism of freeze-thaw damage and mechanical properties of freeze-thaw in sandstone," *International Journal Hydroelectric Energy*, vol. 30, no. 11, pp. 118–121, 2012.

[11] J. Park, C.-U. Hyun, and H.-D. Park, "Changes in microstructure and physical properties of rocks caused by artificial freeze-thaw action," *Bulletin of Engineering Geology and the Environment*, vol. 74, no. 2, pp. 555–565, 2015.

[12] H. Zhang and G. Yang, "Experimental and damage propagation characteristics of rock freeze-thaw," *Journal of China University of Mining & Technology*, vol. 40, no. 1, pp. 140–145, 2011.

[13] H.-M. Zhang and G.-S. Yang, "Experimental study on damage and mechanical properties of freeze-thawed rock," *Journal of China Coal Society*, vol. 38, no. 10, pp. 1756–1762, 2013.

[14] H. Zhang and G. Yang, "Effects of water and freeze-thaw cycles on physical and mechanical properties of red sandstone," *Journal of Experimental Mechanics*, vol. 28, no. 5, pp. 635–641, 2013.

[15] H. Zhang and G. Yang, "Mechanical properties test and damage analysis of red sandstone under freezing and thawing environment," *Mechanics and Engineering*, vol. 35, no. 3, pp. 57–61, 2013.

[16] H. Zhang, M. Zhang, X. Xie et al., "Experimental study on physical and mechanical properties of red sandstone under freeze-thaw cycles," *Journal of Taiyuan University of Technology*, vol. 46, no. 1, pp. 69–74, 2015.

[17] H. Zhang, H. Xia, G. Yang et al., "Experimental study on the effects of freeze-thaw cycles and confining pressure on physical and mechanical properties of rocks," *Journal of China CoalSociety*, vol. 43, no. 2, pp. 441–448, 2018.

[18] Y. Huseyin, "Effect of freeze-thaw and thermal shock weathering on the physical and mechanical properties of an andesite stone," *Bulletin of Engineering Geology and the Environment*, vol. 70, no. 2, pp. 187–192, 2011.

[19] X. Li, Y. Lu, and Y. Wang, "Study on damage model of single-fractured rock mass under the coupling of freeze-thaw load," *Chinese Journal of Rock Mechanics and Engineering*, vol. 32, no. 11, pp. 2307–2315, 2013.

[20] K.-P. Zhou, B. Li, J.-L. Li, H.-W. Deng, and F. Bin, "Microscopic damage and dynamic mechanical properties of rock under freeze-thaw environment," *Transactions of Nonferrous Metals Society of China*, vol. 25, no. 4, pp. 1254–1261, 2015.

[21] Y. Tian and S. Xu, "Correlation analysis of rock physical and mechanical indexes under freeze-thaw cycles," *Mining Safety & Environmental Protection*, vol. 44, no. 4, pp. 24–27, 2017.

[22] X. Li, Y. Lu, and Y. Weng, "Research on damage model of single jointed rock masses under coupling action of freeze-thaw and loading," *Chinese Joural of Rock Mechanics and Engineering*, vol. 32, no. 11, pp. 2307–2315, 2013.

[23] X. Yuan, H. Liu, and J. Liu, "A damaging model of jointed rock under coupled action of freezing and thawing," *Chinese Joural of Rock Mechanics and Engineering*, vol. 34, no. 8, pp. 1602–1611, 2015.

Research Article

Development of an Ensemble Intelligent Model for Assessing the Strength of Cemented Paste Backfill

Yuantian Sun,[1] Guichen Li [iD],[1] Junfei Zhang,[2] Junbo Sun,[2] and Jiahui Xu[1]

[1]*School of Mines, Key Laboratory of Deep Coal Resource Mining, Ministry of Education of China,*
 China University of Mining and Technology, Xuzhou 221116, China
[2]*Department of Civil, Environmental and Mining Engineering, The University of Western Australia, Perth 6009, Australia*

Correspondence should be addressed to Guichen Li; liguichen@cumt.edu.cn and Qiusong Chen

Cemented paste backfill (CPB) is an eco-friendly composite containing mine waste or tailings and has been widely used as construction materials in underground stopes. In the field, the uniaxial compressive strength (UCS) of CPB is critical as it is closely related to the stability of stopes. Predicting the UCS of CPB using traditional mathematical models is far from being satisfactory due to the highly nonlinear relationships between the UCS and a large number of influencing variables. To solve this problem, this study uses a support vector machine (SVM) to predict the UCS of CPB. The hyperparameters of the SVM model are tuned using the beetle antennae search (BAS) algorithm; then, the model is called BSVM. The BSVM is then trained on a dataset collected from the experimental results. To explain the importance of each input variable on the UCS of CPB, the variable importance is obtained using a sensitivity study with the BSVM as the objective function. The results show that the proposed BSVM has high prediction accuracy on the test set with a high correlation coefficient (0.97) and low root-mean-square error (0.27 MPa). The proposed model can guide the design of CPB during mining.

1. Introduction

Cemented paste backfill (CPB) is widely used for mining operations in underground metal mines, in which tailings are normally used as main aggregates and they are mixed with cementitious material and water [1]. CPB is normally filled into the underground stope, and thus, it plays a critical role in supporting the roof and surrounding rock mass after a certain period of dehydration and consolidation [2–5]. Compared with other backfill materials, CPB is an eco-friendly and economic mine composite due to the maximum utilization of mine waste, which attracts much attention these years [6–11].

Filling strength is the most important mechanical parameter that affects filling quality, and unconfined compressive strength (UCS) is the most basic and key parameter to evaluate the filling strength of CPB [12]. Generally, the UCS of CPB is obtained in the laboratory, similar to the strength evaluation of the concrete. However, when multiple parameters are related to UCS of CPB, experimental

measurement is a tedious, time-consuming, and expensive method [13, 14]. Many scholars have put forward many methods to predict the strength of CPB such as empirical formula estimation, numerical simulation, and elastic mechanics analysis [15, 16]. It should be pointed out that the CPB is a multiphase composite and the mentioned methods normally cannot obtain accurate prediction results. To accurately predict the UCS of CPB, it is necessary to put forward simple and reliable methods.

Recently, machine learning methods have been widely used for predicting the mechanical properties of construction materials [12, 17–23]. The assessment of the strength of CPB by artificial intelligence methods has also been presented. For instance, artificial neural network (ANN) considering influencing variables of CPB has been used to model the relationship between inputs and outputs [24, 25]. Furthermore, the evolutionary ANN method, namely, ANN-based methods, was proposed for estimating the UCS of CPB, by which the hyperparameters such as the number of

neurons and the structure of ANN are optimized by some global optimization algorithms, i.e., particle swarm optimization (PSO) and firefly algorithm (FA). Similarly, other normally used machine learning methods such as the random forest algorithm (RF) and RF-based models reported in the literature are also used for predicting the UCS of CPB [26]. Although the above artificial intelligence methods (ANN, ANN-based, RF, and RF-based) were applied in strength prediction of CPB, they are limited in calculating efficiency and uncertain structures. Besides, there is no intelligent model for the prediction of UCS of CPB considering the overall effect of cement-coarse tailings ratio, solids-water ratio, fine tailings percentage, and curing time.

Therefore, in this paper, the machine learning algorithms, support vector machine (SVM) that has the perfect ability in regression and classification, and an excellent global optimization algorithm, beetle antennae search algorithm (BAS) that is used for selecting hyperparameters of SVM, were combined. Therefore, an evolutionary support vector machine model (BSVM) is proposed. Several contributions to the literature can be concluded as follows:

(1) The support vector machine (SVM) and beetle antennae search (BAS) algorithms were combined to establish the evolutionary support vector machine model;

(2) The strength properties of CPB was analyzed by conducting the experiments considering the key influencing variables, i.e., cement-coarse tailings ratio, solids-water ratio, fine tailings percentage, and curing time

(3) The UCS of CPB was directly estimated by considering the combined effect of four key influencing variables

(4) The sensitive analysis of the mentioned influencing variables of CBP was first analyzed and discussed

2. Materials and Methods

2.1. Mechanical Tests.
To prepare the CPB specimen, the grain size distribution of tailings and the mineralogical composition are necessary to determine. Thus, a laser diffraction analyzer was utilized for determining the size distribution of coarse tailings and fine tailings. As we can see from Figure 1, there are two different tailings of various sizes. To analyze the influence of fine tailing on the strength of CPB is critical. The Portland cement P.O 32.5R was applied as a binder. The water obtained in this mine was used as the mixing water. According to the field trial tests, coarse tailings-cement ratio (T/C) was set as 4, 6, 8, and 10, and the solids-water ratio (S/W) was set as 0.68, 0.70, and 0.72. The fine tailings are as an admixture, and its percentage (FTP) was set as 0%, 10%, 15%, and 20%. The blinder and aggregates were mixed by using a mixer (UJZ-15) for 5 min. Then, the prepared mixture was poured into the molds (70.1 mm × 70.1 mm × 70.1 mm). The curing time in this study was set as 7, 28, and 60 days. The detailed statistics of variables of CPB are given in Table 1. A total of 435 specimens were completed, and they were used for obtaining the
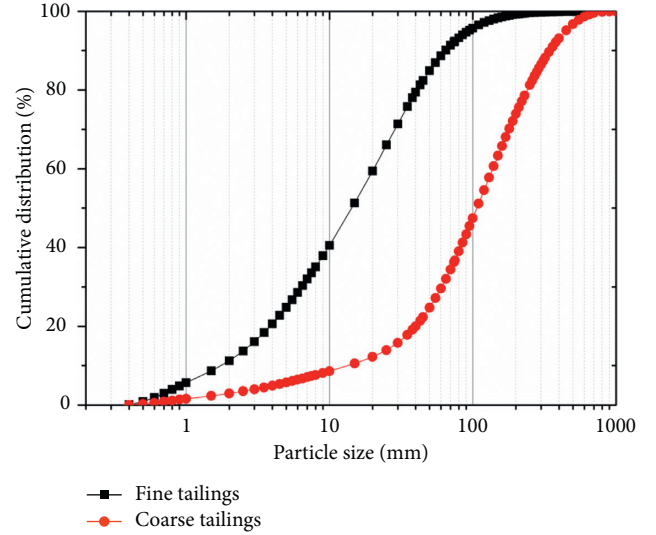
FIGURE 1: Grain size distribution of coarse and fine tailings.

UCS values by conducting unconfined compressive tests according to ASTM C 39.

2.2. Model of Evolutionary Support Vector Machine (BSVM)

2.2.1. Support Vector Machine (SVM).
SVM is normally applied for classifying the samples by the hyperplanes [26]. When the hyperplane can make a large margin in two classes, the vectors corresponding to the hyperplanes are support vectors. The schematic diagram of the SVM is depicted in Figure 2.

Generally, the hyperplane equation is as follows:

$$f(\mathbf{x}) = \mathbf{w}^T g(\mathbf{x}) + b, \tag{1}$$

where $\mathbf{w}$ means an m-dimensional vector; b denotes the bias term; and when $\mathbf{w}$ and b are obtained, the x can be classified by the sign of $f(x)$.

For linear separable data, the following equation can be concluded as follows:

$$y_i\left(\mathbf{w}^T g(\mathbf{x}) + b\right) - 1 \geq 0. \tag{2}$$

The support vectors are on the hyperplane:

$$y_i\left(\mathbf{w}^T g(\mathbf{x}) + b\right) = 1. \tag{3}$$

To minimize the $\|\mathbf{w}\|^2$, the hyperplane can be found ($\|\mathbf{w}\|$ is the Euclidean norm of w).

2.2.2. Beetle Antennae Search (BAS).
BAS is a very famous metaheuristic algorithm, which is proposed recently [20]. It can be used for global optimization problems. Nowadays, BAS has been widely utilized in obtaining hyperparameters in machine learning algorithms [20, 21]. In this algorithm, it simulated the beetles' behavior, and the objective of its antennae is to find the odor with high concentration. A typical flow chart of BAS is shown in Figure 3.

In this study, the hyperparameters of SVM (C, penalty coefficient and γ, kernel parameter) were tuned by BAS instead of trial-and-error methods.

TABLE 1: Statistics of influencing variables.

Variable	Min	Max	Mean	Standard deviation
Coarse tailings-cement ratio (T/C)	4	10	7	2.2
Solids-water ratio (S/W)	0.68	0.72	0.7	0.02
Fine tailings percentage (FTP)	0	0.2	0.11	0.07
Curing time	7	60	31.6	21.8
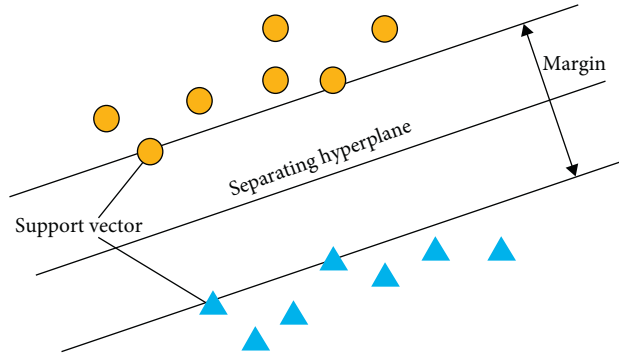
FIGURE 2: Diagram of SVM.
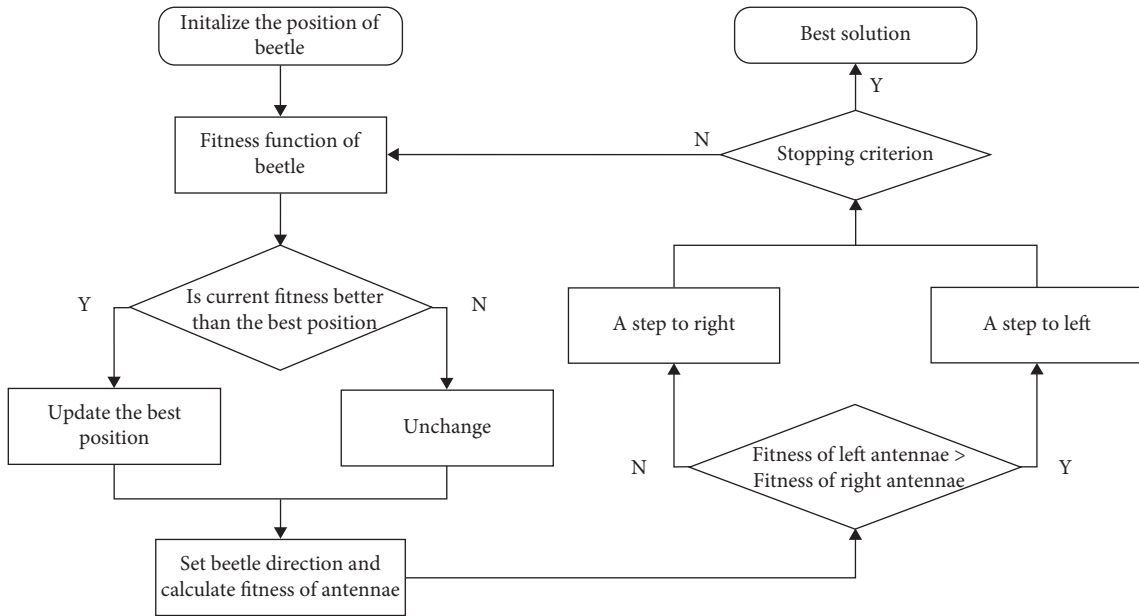
FIGURE 3: Flow chart of BAS.

2.3. Performance Evaluation. According to the suggestion in previous studies, the training dataset and testing dataset are split into 70% dataset and 30% dataset, respectively. A 10-fold cross-validation method was applied. The correlation coefficient (R) and root-mean-square error (RMSE) for evaluating the performance of the established model are defined as follows:

$$R = \frac{\sum_{i=1}^{N}(y_i^* - \overline{y^*})(y_i - \overline{y})}{\sqrt{\sum_{i=1}^{N}(y_i^* - \overline{y^*}^2)}\sqrt{\sum_{i=1}^{N}(y^i - \overline{y}^2)}},$$

$$\text{RMSE} = \sqrt{\frac{1}{N}\sum_{i=1}^{N}(y_i^* - y_i)^2},$$

(4)

(a)

(b)

(c)
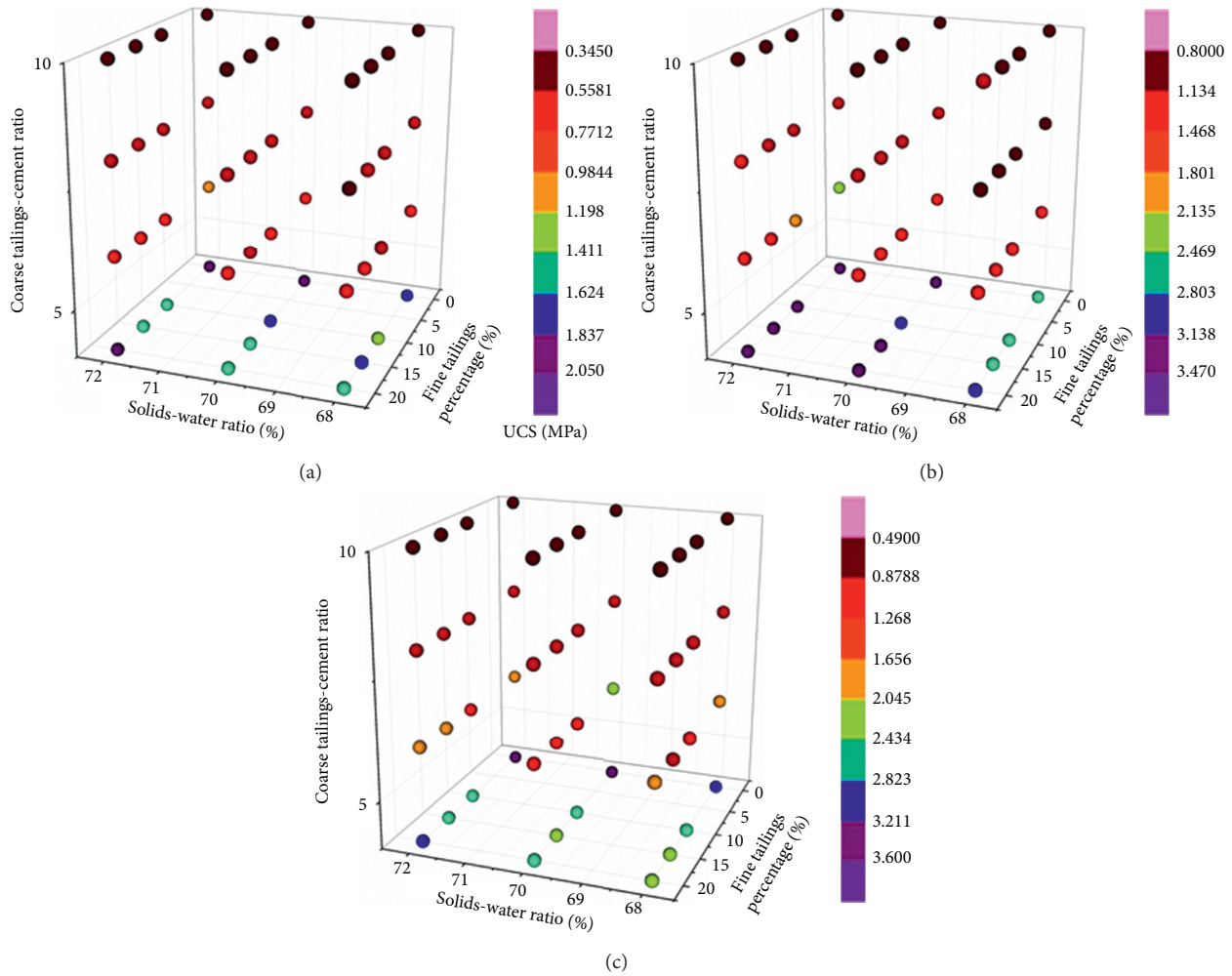
FIGURE 4: UCS test results of CPB in 4D: (a) 7 days; (b) 28 days; (c) 60 days.

where N means the numbers in the dataset; y_i^* and y_i are the expected values and real values, respectively; and $\overline{y}$ and $\overline{y^*}$ indicate the mean predicted values and mean actual values, respectively.

3. Results and Discussion

3.1. Results of UCS of CPB. Figure 4 shows the UCS of CPB combined with different variables under different curing times. It can be seen that the coarse tailings-cement ratio is the main index for determining the strength of CPB. With the increase of coarse tailings-cement ratio, the UCS of CPB increased obviously. Similarly, the UCS of CPB improved with the increase of the solids-water ratio. However, in terms of the effect of fine tailing percentage on CPB strength, it depends on the solids-water ratio. Specifically, when the solids-water ratio is between 68% and 70%, with the increase of the fine tailing percentage, the UCS of CPB increased to the peak values and then declined. When the solids-water ratio is 72%, the UCS of CPB decreased slightly with the increase of fine tailing percentage. The curing time played a positive effect on the increase in the strength of CPB, which is consistent with the previous studies.

3.2. Results of Hyperparameter Tuning. In this study, BAS is applied to tune hyperparameters of SVM on the training set. RMSE is selected as the objective function. Figure 5 shows the RMSE versus iteration curve. It can be seen that RMSE decreases significantly and is stable after 15 iterations, indicating that the BAS is efficient in tuning hyperparameters. The final hyperparameters of SVM are tabulated in Table 2.

3.3. Assessment of the Established Model. Figure 6 shows the correlation between predicted UCS values and actual UCS values on the training and test sets. A nearly linear relationship is observed with R values of 0.9701 and 0.973 on the training and test sets, respectively, indicating that the proposed SVM model can establish the relationship between the UCS of CPB and its influencing variables successfully. Besides, the low and similar RMSE values on the training (0.1798) and test (0.2674) sets suggest that no underfitting or overfitting phenomena are produced.

3.4. Analysis of the Variable Importance. The relative importance of the input variables is calculated using global sensitivity study, as shown in Figure 7. It can be observed
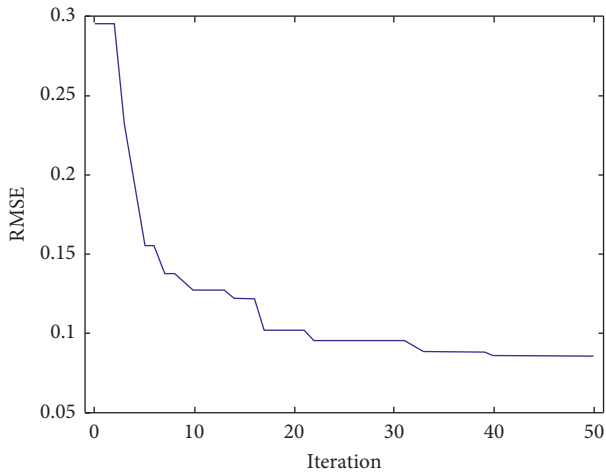
Figure 5: RMSE versus iterations.

Table 2: The obtained hyperparameters of RF.

Parameters	Empirical scope	Initial	Results
C	[0.1, 1000]	14	65
Γ	[0.001, 100]	14	1.01

(a)

(b)
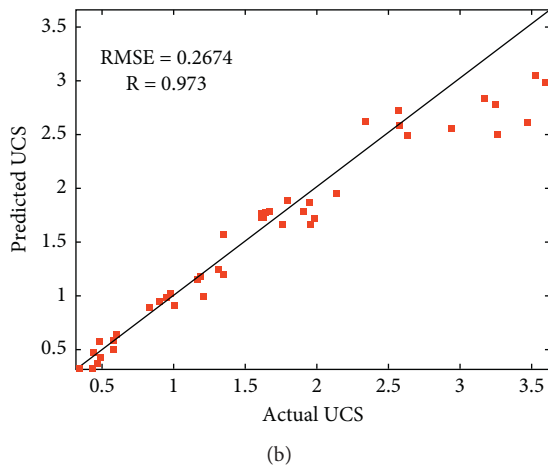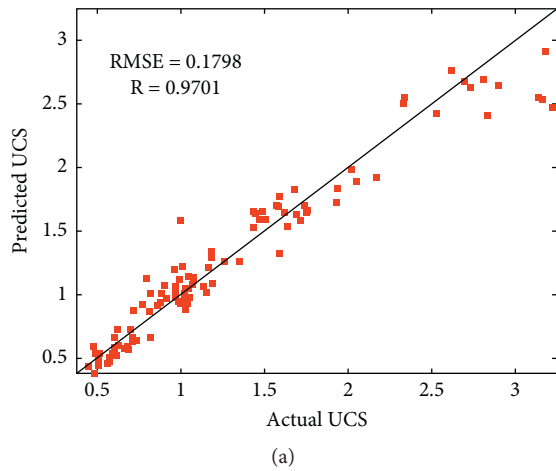
Figure 6: Comparison of UCS values. (a) Training dataset. (b) Testing dataset.
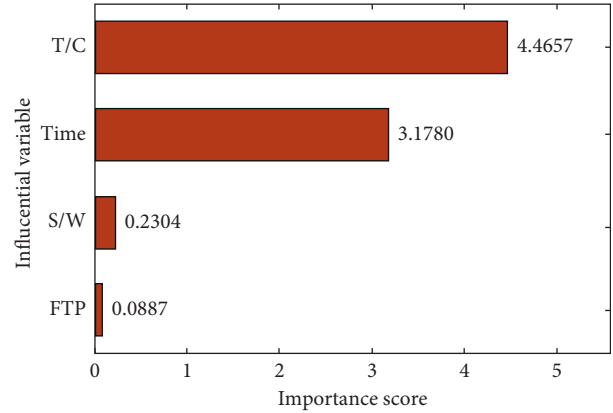
Figure 7: Variable importance of CPB based on the BSVM.

that the coarse tailings-cement ratio has the most significant influence on the UCS of CPB with an influencing score of 4.46, followed by curing time (3.178) and solids-water ratio (0.23), while fine tailings percentage is the least sensitive variable with an influence score of 0.088. This result agrees well with the previous study. It should be noted that the importance score is obtained by the dataset used in this paper. More accurate results can be obtained if more data samples are included in the dataset in the future.

4. Conclusions

This study uses the BSVM for predicting the UCS of CPB. The hyperparameters of SVM are tuned by BAS. The BSVM can establish the relationship between the UCS of CPB and its influencing variables successfully, indicated by high correlation coefficients on the training (0.97) and test (0.973) sets. Also, the calculated variable importance by sensitivity analysis shows the coarse tailings-cement ratio is the most important variable to UCS.

In future work, the dataset will be enlarged by including more influencing variables and samples to improve the generalizability of the proposed model. Also, a graphical user interface will be implemented to facilitate the use of the model in designing CPB mixtures.

Data Availability

The Microsoft Excel Worksheet data used to support the findings of this study are available from the corresponding author (liguichen@cumt.edu.cn) upon request.

Conflicts of Interest

The authors declare that there are no conflicts of interest.

Acknowledgments

References

[1] C. Qi and A. Fourie, "Cemented paste backfill for mineral tailings management: review and future perspectives," *Minerals Engineering*, vol. 144, p. 106025, 2019.

[2] Y. Sun, G. Li, and J. Zhang, "Investigation on jet grouting support strategy for controlling time-dependent deformation in the roadway," *Energy Science & Engineering*, vol. 8, no. 4, pp. 1–8, 2020.

[3] Y. Sun, G. Li, J. Zhang, and D. Qian, "Experimental and numerical investigation on a novel support system for controlling roadway deformation in underground coal mines," *Energy Science & Engineering*, vol. 8, no. 2, pp. 490–500, 2020.

[4] Y. Sun, G. Li, J. Zhang, and D. Qian, "Stability control for the rheological roadway by a novel high-efficiency jet grouting technique in deep underground coal mines," *Sustainability*, vol. 11, no. 22, p. 6494, 2019.

[5] H. Basarir, Y. Sun, and G. Li, "Gateway stability analysis by global-local modeling approach," *International Journal of Rock Mechanics and Mining Sciences*, vol. 113, pp. 31–40, 2019.

[6] Y. Sun, G. Li, and J. Zhang, "Developing hybrid machine learning models for estimating the unconfined compressive strength of jet grouting composite: a comparative study," *Applied Sciences*, vol. 10, no. 5, p. 1612, 2020.

[7] Q. Chen, Q. Zhang, C. Qi, A. Fourie, and C. Xiao, "Recycling phosphogypsum and construction demolition waste for cemented paste backfill and its environmental impact," *Journal of Cleaner Production*, vol. 186, pp. 418–429, 2018.

[8] Q. Chen, Q. Zhang, A. Fourie, and C. Xin, "Utilization of phosphogypsum and phosphate tailings for cemented paste backfill," *Journal of Environmental Management*, vol. 201, pp. 19–27, 2017.

[9] Q.-S. Chen, Q.-L. Zhang, A. Fourie, X. Chen, and C.-C. Qi, "Experimental investigation on the strength characteristics of cement paste backfill in a similar stope model and its mechanism," *Construction and Building Materials*, vol. 154, pp. 34–43, 2017.

[10] C.-c. Qi, "Big data management in the mining industry," *International Journal of Minerals, Metallurgy and Materials*, vol. 27, no. 2, pp. 131–139, 2020.

[11] D. Wang, Q. Zhang, Q. Chen, C. Qi, Y. Feng, and C. Xiao, "Temperature variation characteristics in flocculation settlement of tailings and its mechanism," *International Journal of Minerals, Metallurgy and Materials*, 2020.

[12] C. Qi, A. Fourie, Q. Chen, and Q. Zhang, "A strength prediction model using artificial intelligence for recycling waste tailings as cemented paste backfill," *Journal of Cleaner Production*, vol. 183, pp. 566–578, 2018.

[13] Z. Zhang, E. Wang, and N. Li, "Fractal characteristics of acoustic emission events based on single-link cluster method during uniaxial loading of rock," *Chaos, Solitons & Fractals*, vol. 104, pp. 298–306, 2017.

[14] Z. Zhang, E. Wang, Y. Zhang et al., "Analysis on the time-frequency characteristics of ultrasonic waveform of coal under uniaxial loading," *Fractals*, vol. 27, no. 06, pp. 1950100–1950123, 2019.

[15] S. Xu, F. T. Suorineni, K. Li, and Y. Li, "Evaluation of the strength and ultrasonic properties of foam-cemented paste backfill," *International Journal of Mining, Reclamation and Environment*, vol. 31, no. 8, pp. 544–557, 2017.

[16] W. Xu, X. Tian, and P. Cao, "Assessment of hydration process and mechanical properties of cemented paste backfill by electrical resistivity measurement," *Nondestructive Testing and Evaluation*, vol. 33, no. 2, pp. 198–212, 2018.

[17] J. Zhang, G. Ma, Y. Huang, J. sun, F. Aslani, and B. Nener, "Modelling uniaxial compressive strength of lightweight self-compacting concrete using random forest regression," *Construction and Building Materials*, vol. 210, pp. 713–719, 2019.

[18] C. Qi, A. Fourie, and Q. Chen, "Neural network and particle swarm optimization for predicting the unconfined compressive strength of cemented paste backfill," *Construction and Building Materials*, vol. 159, pp. 473–478, 2018.

[19] J. Sun, J. Zhang, Y. Gu, Y. Huang, Y. Sun, and G. Ma, "Prediction of permeability and unconfined compressive strength of pervious concrete using evolved support vector regression," *Construction and Building Materials*, vol. 207, pp. 440–449, 2019.

[20] Y. Sun, J. Zhang, G. Li, Y. Wang, J. Sun, and C. Jiang, "Optimized neural network using beetle antennae search for predicting the unconfined compressive strength of jet grouting coalcretes," *International Journal for Numerical and Analytical Methods in Geomechanics*, vol. 43, no. 4, pp. 801–813, 2019.

[21] Y. Sun, J. Zhang, G. Li et al., "Determination of Young's modulus of jet grouted coalcretes using an intelligent model," *Engineering Geology*, vol. 252, pp. 43–53, 2019.

[22] J. Zhang, D. Li, and Y. Wang, "Toward intelligent construction: prediction of mechanical properties of manufactured-sand concrete using tree-based models," *Journal of Cleaner Production*, vol. 258, Article ID 120665, 2020.

[23] Y. Sun, G. Li, J. Zhang, and D. Qian, "Prediction of the strength of rubberized concrete by an evolved random forest model," *Advances in Civil Engineering*, vol. 2019, Article ID 5198583, 7 pages, 2019.

[24] L. Orejarena and M. Fall, "The use of artificial neural networks to predict the effect of sulphate attack on the strength of cemented paste backfill," *Bulletin of Engineering Geology and the Environment*, vol. 69, no. 4, pp. 659–670, 2010.

[25] L. Orejarena and M. Fall, "Artificial neural network based modeling of the coupled effect of sulphate and temperature on the strength of cemented paste backfill," *Canadian Journal of Civil Engineering*, vol. 38, no. 1, pp. 100–109, 2011.

[26] C. Qi, Q. Chen, A. Fourie, and Q. Zhang, "An intelligent modelling framework for mechanical properties of cemented paste backfill," *Minerals Engineering*, vol. 123, pp. 16–27, 2018.

Research Article

Mapping BIM Uses for Risk Mitigation in International Construction Projects

Tsenguun Ganbat,[1] **Heap-Yih Chong** ⓘ**,**[2] **and Pin-Chao Liao** ⓘ[1]

[1]*Department of Construction Management, School of Civil Engineering, Tsinghua University, Beijing 100084, China*
[2]*Department of Construction Management, School of Built Environment, Curtin University, GPO Box U1987, Perth,
WA 6845, Australia*

Correspondence should be addressed to Pin-Chao Liao; pinchao@tsinghua.edu.cn

International construction projects (ICPs) have become more popular in the current wave of globalization. The Building Information Model (BIM) has been adopted in ICPs. However, the utility of the BIM in ICPs for effective risk control remains unclear. This paper maps the relationship between ICP risks and BIM use to improve the adoption and selection of the BIM. The results show that the BIM can effectively facilitate communication management, mitigating risks engendered by language barriers among stakeholders, for instance, design errors. The BIM can also effectively mitigate risks caused by particular and temporal differences during the construction process. This research highlights internal/technical ICP risks that can be effectively mitigated by certain applications of the BIM; however, in contrast, external risks of ICPs cannot be mitigated by the BIM. However, some risks need to be addressed by new BIM functions. For example, regarding legal risks, laws and regulations of various countries can be included in the BIM information integration model to facilitate timely acquisition of legal provisions by project participants. This study complements prior risk-management research, which typically focused on the BIM as an advanced tool by which to manage project risk, such as design errors, quality, and budget. Practically, the contractor and owner can select suitable BIM applications for different project objectives and risks in the pre-project phase.

1. Introduction

The rapid adoption and development of the Building Information Model (BIM) has brought tremendous advantages to construction enterprises. However, new risks exist due to the characteristics of international construction, such as cross-cultural differences, multiple stakeholders, and legal and standards differences [1]. Although many BIMs have the capability to address complex construction problems, BIMs are still in the development stage, and new uses of BIMs are constantly emerging [2, 3]. Previous studies have reviewed various applications of BIMs, from 4D scheduling aspects [4], 5D cost aspects [2, 5], facility management [6], sustainability [7, 8], safety aspects [9], and general BIM tools for construction management [10]. These important studies provide useful references for end-users in selecting suitable

BIM applications for their projects. Most risk-management research based on BIMs focused on the BIM as an advanced tool by which to manage project risk, such as design errors, quality, budget, and visual perspective, but did not typically address ICPs' risk management explicitly [9]; however, most ICP risks related to proposed contract conflict and design error are caused by language differences. However, very little information is available as to select language barrier based from the perspective of ICP risks. Furthermore, reviews of BIM use in international construction risk management are few in number. Therefore, BIM cannot currently be effectively promoted and used in ICP management.

Hence, this study maps the relationship between ICP risk and BIM application to improve the adoption and selection of the BIM. The linkage between BIM application and ICP risks helps provide effective control or prevention of risks

and thereby improve project performance. This study involved two main research tasks. First, a critical review was conducted to compile a list of ICP risks and BIM applications in construction projects. Subsequently, a panel discussion method was used to analyze the BIM applications in association with ICP risks. Second, a meta-network method was adopted to analyze which BIM applications would be of utility in ICPs to help achieve project objectives in terms of cost, time, quality, safety, and environment. This paper is organized into five sections. Section 1 explains the study's theoretical background. Section 2 describes the critical review and research design. Section 3 explains the results of the meta-network analysis. Section 4 discusses the study's research contributions. Section 5 summarizes the study's research findings, highlights its limitations, and presents suggestions for future studies.

In recent years, the risks associated with ICPs have gradually increased, due to the increased complexity and requirements of these projects. There is a wide range of risks associated with ICPs, such as structural risks, construction risks, health and safety risks, financial risks, and environmental risks. Risk management is critical to the success of any construction project. Several studies [11, 12] have shown that current risk management approaches largely depend on experience and multidisciplinary knowledge.

Moreover, there is a lack of interaction among types of risk information in current risk management approaches [9]. This may lead to information that is not effectively shared, recorded, and updated during the development of a project. Large amounts of risk information may be lost if they are not properly recorded and communicated to other project participants.

In recent years, information models have become increasingly popular. These models offer the potential for collaboration and communication, increased productivity and quality, and reduced project costs and implementation time [13]. Data-based collaboration and communication environments help identify and mitigate risks early [14, 15]. BIMs have become a systematic approach and process that have changed the presentation of projects [16], design [17], and communication [18]. Many studies have proposed BIMs as a tool for managing project risks, involving design errors, occupational safety, quality, and budget, but they often do not directly reference the concept of risk management. Risk management will play a more important role as project participants begin to use these latest technologies as part of their daily work.

Since BIM technology can integrate information in an nD model [19], future BIM applications could process risk-management data [20]. In the construction industry, BIMs are continuing to develop; in practice, companies want to advance implementation theory and make full use of BIM-based tools to improve project performance and risk management [10]. However, in the current construction industry, the sharing and communication of risk information are often incomplete and inconsistent; it is necessary to integrate and visualize this information through BIMs. However, there is little BIM-related research that has focused on international construction project risk management.

Related studies of BIMs in international construction risk management have illustrated that the 4D system can visually simulate a proposed construction sequence, via which planners could easily identify potential risks [21]. Additionally, 3D visualization has been deployed to review and understand the degree and location of damaged components of a building when assessing potential hazards [22]. The 5D automated cost estimating model has been used to provide more accurate cash flow forecasts [23], and decision-making for workspace analysis [24]. However, these studies have yet to address ICP's critical risks, such as those related to language barriers, cultural barrier, and natural disaster. Furthermore, the studies to date only independently discussed BIM applications for specific risks; however, in construction projects, risks are often interrelated. Therefore, BIM applications should be considered holistically with respect to ICP risks.

2. Materials and Methods

The main research framework and research process of this study are shown in Figure 1. A detailed description of each step and method is provided below.

2.1. Critical Review of ICP Risks and BIM Applications.
First, an in-depth literature review was conducted to determine the research trends in this field and the major research omissions, including the following aspects: (1) selecting classic literature on risk definition and risk management in ICPs; (2) assessing the development and application of BIMs in the construction industry, new BIM software, and other relevant literature to analyze international construction risk management and BIMs. Details of the ICP risks are shown in Table 1.

To compile the list of BIM applications in construction projects, more than one hundred peer-reviewed academic publications and twenty-five (25) BIM guidelines were selected and reviewed. PMBOK (2013) was also selected as a main reference. The details of BIM applications are shown in Table 2.

2.2. Panel Discussion of BIM Applications from the Perspective of ICP Risks.
The panel discussion assessed BIM applications with respect to international construction risks. Twenty-four core project managers discussed a scenario simulation, based on grounded theory. This enabled generation of an international construction project risk-correlation matrix. This component of the study consisted of preliminary analysis, in-depth interviews, the establishment of an initial indicator set, and panel discussions of BIM application with respect to risk factors. The profile of the respondents is shown in Table 3.

The panel discussions commenced with an introduction of the discussion topic. The purpose of the discussions was to identify the role of BIM application in risk management of international engineering projects. Each panelist first assessed the identified BIM applications and verified
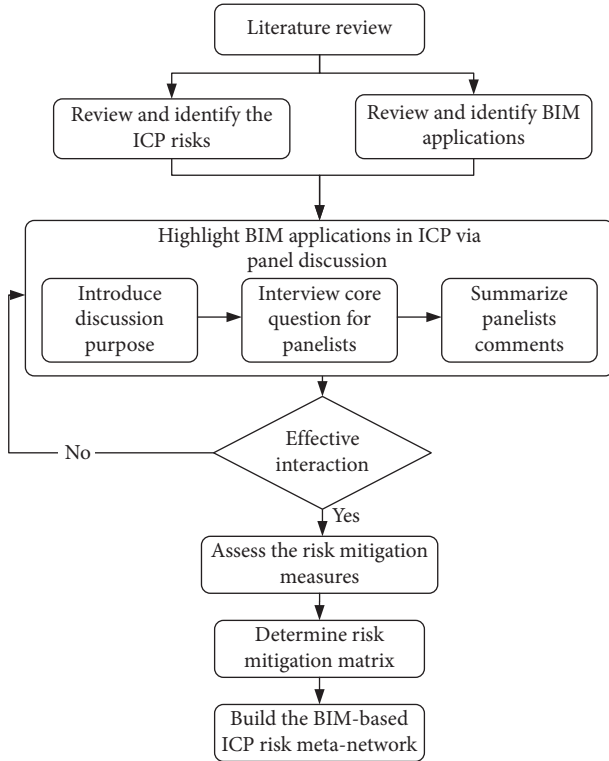
Figure 1: Research map.

whether the main uses of BIMs were represented. Second, the utility and benefits of these BIM applications were considered. Then, the particular role of these applications in risk management of international construction projects was discussed. Finally, the panelists' comments were summarized; panel discussion process is shown in Figure 2.

The project managers then evaluated the correlation between risks and BIM application, via a risk matrix. Respondents were asked to directly score the matrix according to the influence of BIM aspect X on risk Y. The respondent was asked to consider all possible relationships and their directions. To quantify the relationships, respondents used a scale from 1 to 5 to represent the impact of the influence as well as the probability that this influence occurs [67]. If the respondent considered that there was no relationship between two risks, a value of 0 was assigned.

To obtain the degree of interaction between different risks and risk factors, a risk-structure matrix was used to evaluate the relationship between risks, risk impact on project objectives, and risk factors. To reflect the effect of the two directions, risk A on risk B and vice versa, but this needs to be stated explicitly for each type of bidirectional relationship, a numerical matrix corresponding to the two directions was aggregated, using geometric averages. The risk management intensity matrix was then obtained as $R^*_{ij} = (r_{ij})n * n$, among $R_{jj} = \sqrt{R^e_{ij} \times R^c_{ij}}$. According to Yang and Zou's method of measuring the degree of association of each risk node, R_j, S_j expressed the degree of association of each risk node R_j, which was equal to the sum of all the elements of the row vector in the risk matrix and all the elements of the vector in the risk column.

$$S_j = \sum_{j=1}^{n} r_{ij} + \sum_{i=1}^{n} r_{ij}, \quad i = 1, 2, \ldots, n; \ j = 1, 2, \ldots, n. \quad (1)$$

Based on the panel discussion, the links between risks and BIM for risks were assessed. First, matrices for different network relationships were established, namely, the matrix representing the impact of risk on project objectives, that representing the interaction between risks, and that representing the impact of risk factors on risk. A total of 24 panelists' comments were collected from the on-site panel discussion with project managers.

2.3. Meta-Network Analysis. Finally, the assessment structures were inputted to a meta-network analysis tool (ORA-NetScences), to establish a network of risk interactions in the implementation phase of ICPs. From a network perspective, important risks and risk factors that influence project objectives were identified and analyzed.

Meta-network theory describes the commitment of resources, assignment, networks, and skills (PCANS), according to a model developed by Krackhardt and Carley [68]. These elements constitute a set of nodes, and relationships among these elements constitute a set of relationships. The meta-network provides a promising way by which to understand and visualize the complex interactions in a project's organizational network [69, 70]. The meta-network is multilayer, multilevel, and multimodal and can reveal the complex network systems in a project and identify the relationships between networks [69]. Recent network analysis approaches only address "who" is in the network, but the meta-network can simulate and analyze "who, when, where, what, and why" [69]. In a project's meta-network, changes in one network cascade into changes in other networks, thereby influencing the overall performance of the project [71].

The analysis was based on different types of nodes and links. In particular, there were four types of nodes: project objective (cost, time, quality, safety, and environment), 16 risk nodes (R1-R16, shown in Table 1), risk factors nodes (F1–F84, shown in Table 1), and 25 BIM application nodes (BC1-BC25, shown in Table 2). The types of networks among the different nodes were as follows: risk factor network (risks × factors), risk event network (risks × risks), risk mitigation network (BIM × risks), and risk influence network (risks × objectives). The links in the different networks have different weights that reflect the degree of influence transfer. The purpose of this study was to determine the overall risk network of the project and changes in the overall risk network of the project given risk control measures, by understanding the relationships between different risk factors and the impact of different risk factors.

To reflect the overall effect of the two directions, the numerical matrix corresponding to the two directions was aggregated using a geometric average, and the risk-management intensity matrix obtained. The network connections in the meta-network were expressed by two directional influence matrices. All numerical matrices corresponded to the panel discussion results explained in Section 3.1. The

TABLE 1: International construction project risks and risk factors.

Code	Risks	Codes/risk factors	References
R1	Wars and civil unrest among local population	F1 local political/social instability F2 local government change F3 cultural and religious conflicts F4 exchange rate changes F5 poor availability of local foreign exchange	KarimiAzari et al. [25] Zayed et al. [26]
R2	Increasing costs of fuel, material, equipment, and labour	F6 local currency changes F7 local market price changes/inflation F8 lack of funding F9 supply deficiencies (transport/delivery of materials, equipment, and labour) F10 increase in bank interest rate	Xiaopeng and pheng [27] Liu et al. [28] Zhao et al. [29]
R3	Exchange rate change	F11 local and national tax increase (payment, evasion, implementation) F12 new local government regulations (taxation, labour, safety, waste, environment, etc.)	Creedy et al. [30] Santoso and soeng [31] Yildiz et al. [32]
R4	Project fund shortage	F13 no fund management system F14 incorrect cash management/foreign exchange management F15 excess monetary investment in early project stages	
R5	The local public objected to the project	F64 communication conflicts between project employees and residents (language barriers, use of translators, translation accuracy, etc.) F65 malicious attacks on individuals by project employees F66 construction has considerable impact on residents' lives	Zayed et al. [26]; yildiz et al. [32] Dikmen and Birgonul [33] Liu et al. [28]
R6	Changes in laws and regulations	F61 contracts with local governments are mandatory F62 local government departments/services are inefficient, slow to respond, and bureaucratic F63 strict/different local business practices (business culture, systems, geography, personality, assimilation requirements, etc.)	Han et al. [34] Hakami [35] Tran and molenaar [36] Mathew et al. [37]
R7	Environmental damage caused by construction	F80 construction pollution F81 emission of hazardous chemicals and gases from construction F82 improper disposal of construction waste F83 hazardous construction sites and materials F35 no substitute supplier/subcontractor in case of failure or failure to deliver F36 aboriginal land rights and owners F37 restrictions of local laws and regulations (including customs/export/import restrictions, etc.) F38 poor land conditions (mining activities, public facilities, historic sites, pollutants, etc.) F39 transport difficulties (poor local traffic conditions, traffic restrictions by relevant departments) F40 local government interference	Han et al. [34] Xiaopeng and pheng [27] Han et al. [34]
R8	Regional disparity and climate impacts	F41 imperfect supervision/control system (quality, cost, time) F46 employees refused to sign up F47 employee diseases (plague F48 project labour absence/potential occupational liability/laziness F49 insufficient work experience of project employees in using materials/technologies/equipment (problems with the use of special materials and new materials) F50 lack of safety knowledge, skills, and training for employees F51 poor accessibility of local materials/technologies/equipment (raw materials and semi-finished products are unavailable) F52 improper material/technology/equipment procurement plan F19 poor quality of goods and services from suppliers/subcontractors F41 imperfect supervision/control system (quality, cost, time)	Xiaopeng and pheng [27] Liu et al. [28] Liu et al. [28]

TABLE 1: Continued.

Code	Risks	Codes/risk factors	References
R9	Quality defects in construction materials	F42 poor attitudes of field staff toward quality, cost, environment, safety, trust, and opportunity	El-sayegh and mansour [38]
		F43 lack of sampling inspection/product contamination leading to quality defects	Zhao et al. [29]
		F44 low quality, competence, reliability, and productivity of project employees	Lee et al. [39]
		F45 insufficient identification of safety, quality, etc.	
		F30 insufficient technical resources, skills and knowledge of suppliers/subcontractors	
		F53 errors in installation of construction equipment	
R10	Damage to labour, materials, equipment, and building	F54 equipment reliability/safety/low productivity	Hakami [35]
		F55 local natural disasters (heatwave, wind, rain, cold, damp, fire, tsunami, volcano, earthquake, flood, storm, tornado, landslide, lightning, etc.)	Liu et al. [28] Santoso and soeng [31]
		F57 insufficient safety material and equipment	Yildiz et al. [32]
		F58 low accessibility/high maintenance cost for key components and accessories	
		F60 construction equipment type mismatch	
		F36 aboriginal land rights and owners	
		F67 local government approval/intervention	
		F68 government expropriation, government nationalization restrictions on business operations	
		F69 the scale of the project does not conform to the scale required	
		F70 innovation and development needs (standardization level, technology/details/materials, etc.)	Liu et al. [28]
R11	The design changes of the project	F71 unclear expectations/requirements of owner/user/operator	El-sayegh and mansour [38]
		F72 owners' overdependence on consultants/construction interventions	
		F74 design error	
		F75 imperfect databases, outdated information, late information, inaccurate information, unusable information, incomprehensible information	
		F76 design code conflicts with local code	
		F77 engineers' corruption/unreasonable decisions	
		F78 engineer's uncertainty about changes in the scope of work, specifications, costs, duration, etc.	
		F39 transport difficulties (poor local traffic conditions, traffic restrictions of relevant departments)	
		F42 poor attitudes of field staff toward quality, cost, environment, safety, trust, and opportunity	
		F43 lack of sampling inspection/product contamination leading to quality defects	
		F45 insufficient identification of safety, quality, etc.	
		F50 lack of safety knowledge, skills, and training for employees	Hakami [35]
		F53 error in installation of construction equipment	Liu et al. [28]

TABLE 1: Continued.

Code	Risks	Codes/risk factors	References
R12	Accident occurrence	F54 equipment reliability/safety/low productivity	Santoso and soeng [31]
		F55 local natural disasters (heatwave, wind, rain, cold, damp, fire, tsunami, volcano, earthquake, flood, storm, tornado, landslide, lightning, etc.)	Yildiz et al. [32]
		F56 insufficient safety education tips on project construction site	
		F57 insufficient safety of material and equipment used	
		F58 low accessibility/high maintenance cost for key components and accessories	
		F59 crisis preparedness—inadequate contingency planning	
		F60 construction equipment credit type mismatch	
		R9 quality defects in construction materials	
		F16 lack of communication among project participants	
		F17 unfair provisions in overseas contracts	
		F18 conflict in industrial relations	
		F19 poor quality of goods and services from suppliers/subcontractors	
		F20 supplier/subcontractor increased costs and delayed costs for goods and services	
		F21 supplier/subcontractor goods without warranty service	
		F22 owner's cash flow/arrears	
		F23 errors or omissions in quantities invoiced, inconsistent information in practice, inaccurate budgets, etc.	Hanna et al. [40]
R13	Contract disputes/termination of contract	F24 project partner's credit insufficiency	Creedy et al. [30]
		F25 owner's requirement for technology/rights is too stringent	Liu et al. [28]
		F26 issues with contract terms (date of completion is not clear, etc.)	Yildiz et al. [32]
		F27 lack of guarantee or insufficient guarantee	Mathew et al. [37]
		F28 wrong expression of contract definition	
		F29 claim management is unclear	
		F30 insufficient technical resources, skills and knowledge of suppliers/subcontractors	
		F31 potential litigation issues; complexity of contracts and documents	
		F33 owner's attitude towards scope, norm, cost, duration, etc. is not clear	
		F34 owners' requirements for environmental protection, safety, quality, and time are too demanding	
		F35 no substitute supplier/subcontractor in case of failure or failure to deliver	
		F19 poor quality of goods and services from suppliers/subcontractors	
		F20 supplier/subcontractor increased costs and delayed costs for goods and services	
		F21 supplier/subcontractor goods without warranty service	
		F24 project partner's credit insufficiency	Santoso and Soeng [31] Liu et al. [28]
R14	Subcontractor breach	F26 issues with of contract terms (date of completion is not clear, etc.)	
		F28 wrong expression of contract definition	
		F30 insufficient technical resources, skills and knowledge of suppliers/subcontractors	
		F51 poor accessibility of local materials/technologies/equipment (raw materials and semi-finished products are unavailable)	
		F22 owner's cash flow/arrears	
		F24 project partner's credit insufficiency	
		F26 issues with contract terms (date of completion is not clear, etc.)	
R15	Client defaults on project	F28 wrong expression of contract definition	Xiaopeng and pheng [27] Yildiz et al. [32]
		F31 potential litigation issues; complexity of contracts and documents	
		F33 owner's attitude towards scope, norm, cost, duration, etc. is not clear	
		F34 owners' requirements for environmental protection, safety, quality, and time are too demanding	
R16	Disease and health problems	F47 employee diseases (plague)	Yildiz et al. [32]
		F84 unhygienic project site or staff dormitory, congenital diseases	Thweatt and long [41]

Table 2: BIM applications.

Code	BIM functions/ guidelines	AGC [42]	BCA [43]	CFM [44]	COD [45]	COSA [46]	CRC [47]	DOA, DSF [48]	FMS [49]	GSFIC [50]	GTFM [51]	HARVARD [52]	HKCIC [53]	IU [54]	LACCD [55]	MPA [56]	NATSPEC [57]	NRC [58]	NYCSCA [59]	NYCDDC [60]	OFCC [61]	PSU [62]	SDCCD [63]	STATSBYGG [64]	TPA [65]	USACE [66]
BC1	Modeling existing conditions	✓	✓		✓	✓	✓	✓	✓	✓		✓	✓	✓	✓	✓	✓	✓	✓	✓	✓	✓	✓	✓	✓	✓
BC2	Site analysis	✓	✓	✓	✓	✓	✓	✓	✓	✓			✓	✓	✓		✓	✓	✓	✓	✓	✓	✓		✓	✓
BC3	Cost estimation (5D)	✓	✓	✓	✓	✓	✓	✓			✓		✓	✓	✓	✓	✓	✓	✓		✓	✓	✓	✓	✓	✓
BC4	Planning and scheduling (4D)	✓	✓	✓	✓	✓	✓	✓	✓	✓	✓	✓	✓	✓	✓	✓		✓	✓	✓		✓	✓	✓	✓	✓
BC5	Program area and space validation		✓	✓	✓	✓	✓	✓	✓	✓	✓	✓	✓	✓	✓	✓	✓	✓	✓	✓	✓	✓	✓	✓	✓	✓
BC6	Design authoring			✓	✓	✓	✓		✓			✓	✓	✓	✓	✓		✓		✓	✓	✓	✓	✓	✓	✓
BC7	Design and constructability reviews	✓	✓	✓	✓	✓		✓	✓	✓	✓	✓	✓	✓	✓	✓	✓	✓	✓	✓	✓	✓	✓	✓	✓	✓
BC8	Modeling	✓	✓	✓	✓	✓	✓			✓	✓	✓	✓	✓		✓	✓	✓	✓	✓	✓	✓	✓	✓	✓	
BC9	Design and engineering analysis	✓	✓	✓	✓	✓	✓	✓		✓	✓	✓	✓	✓	✓	✓	✓	✓	✓	✓	✓	✓	✓	✓	✓	✓
BC10	Design coordination	✓	✓	✓	✓	✓	✓	✓	✓	✓	✓	✓	✓	✓	✓	✓	✓	✓		✓	✓	✓	✓	✓	✓	✓
BC11	Design documents		✓	✓			✓					✓			✓							✓	✓			
BC12	Digital fabrication	✓	✓	✓	✓	✓	✓	✓			✓		✓	✓	✓	✓	✓	✓		✓	✓	✓	✓		✓	✓
BC13	Trade coordination	✓		✓	✓														✓							
BC14	Site utilization planning	✓			✓							✓	✓			✓	✓	✓							✓	✓
BC15	In-field construction layout	✓			✓							✓	✓			✓		✓		✓		✓				
BC16	Safety planning and review									✓		✓				✓		✓							✓	
BC17	Construction system design				✓												✓			✓		✓	✓		✓	✓
BC18	Field and management tracking	✓										✓				✓		✓			✓	✓		✓		✓
BC19	Field supplements	✓										✓			✓	✓							✓	✓		
BC20	Record model/ as-built model	✓	✓		✓	✓					✓			✓	✓	✓	✓	✓			✓	✓		✓	✓	✓
BC21	COBie/ commissioning			✓		✓			✓					✓	✓	✓		✓				✓		✓	✓	✓
BC22	Asset management		✓		✓		✓					✓	✓			✓	✓	✓	✓		✓			✓	✓	✓
BC23	Operations and maintenance scheduling		✓		✓	✓								✓		✓	✓	✓				✓		✓	✓	✓
BC24	Space and management tracking	✓	✓		✓		✓	✓	✓			✓	✓		✓	✓	✓	✓					✓	✓	✓	✓
BC25	Disaster planning				✓		✓				✓	✓						✓				✓			✓	✓

TABLE 3: Basic information of the participants.

Characteristic	Category	Proportion of respondents (%)
Age (years)	≤25	18 (39%)
	26–30	17 (37%)
	31–35	6 (15%)
	≥36	4 (9%)
Experience of international construction projects (years)	1-2	27 (60%)
	3-4	12 (27%)
	5-6	5 (10%)
	≥7	1 (3%)
Education	Bachelor's degree	23 (51%)
	Master's degree	10 (22%)
	High school degree and associates degree	2 (4%)
	Other	10 (22%)
Job position	Administration office	3 (6%)
	Materials and equipment department	2 (4%)
	HSE management department	2 (4%)
	Senior project leader (chief)	3 (6%)
	Design department	3 (6%)
	Contract department	3 (6%)
	Engineering management department	29 (66%)
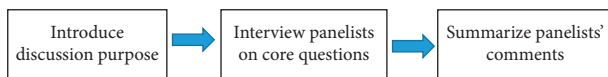
FIGURE 2: Panel discussion process.

outcome was a weighted graph $G = (N, K)$, where N represents the total number of nodes (risks) and K the total number of weighted links (relationships). The stakeholder category associated with each node is distinguished by color in the figures shown here. The thickness of each link represents its weight [72]. The meta-network analysis visualizes changes in the network, in network density, in the number of links (link count), and in the number of nodes.

3. Results

3.1. BIM Application to ICP Risk Meta-Network. Figure 3 shows the BIM-based ICP risk network, including the risk factor network (risks × factors), risk event network (risks × risks), risk mitigation network (BIM × risks), and risk influence network (risks × objectives); the network statistics and network link count statistics are shown in Tables 4 and 5. The central network shows the most used BIM applications (green nodes). In the middle network, yellow nodes represent risk factors with a direct relationship between BIM types and risk factors. Also shown are the five project objectives, such as cost, time, quality, HS-health and safety, and E-environment. The whole circle of the network shows the risks, five project objectives, risk factors, and BIM uses.

The main BIM application that affects risk displayed in the meta-network center is 3D visualization and design. 3D visualization and design: after establishing a 3D design model with attribute information (e.g., for equipment, pipeline, civil engineering) permitting full collision inspection, 3D audit, and 3D check, a BIM can directly generate or extract 3D design drawings and bills of materials,
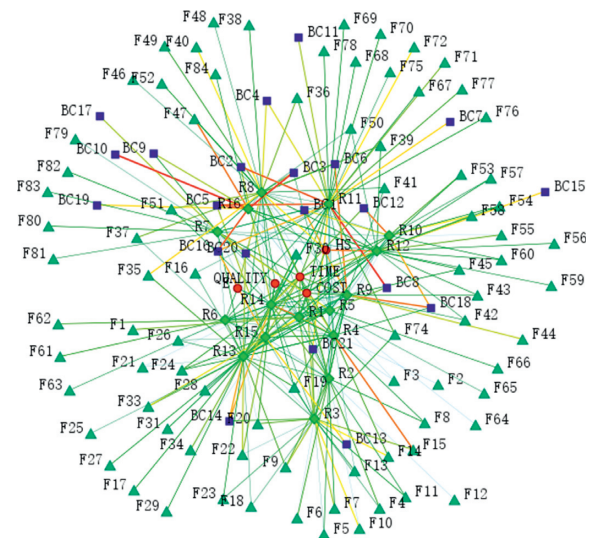
FIGURE 3: BIM-based ICP risk network.

TABLE 4: Network statistics.

Statistic	Minimum	Maximum	Average	Standard deviation
Number of nodes	1	128	8.385	8.537
Number of links	0	510	26.469	53.356
Density	0	0.14	0.887	0.268

thereby preventing design errors, risk of material accounting errors, and so forth.

Effective communication with the owner: due to the language barriers associated with international engineering, the contractor and foreign owner often cannot communicate fully and effectively. Here, BIM technology may be used to integrate the professional design content into a visual 3D model. Regular review by the project manager and the owner will not only facilitate the owner's understanding of the real-

TABLE 5: Network link count statistics.

Network	Minimum	Maximum	Average	Standard deviation
Risk × risk	0	120	21.233	43.768
Risk × factors	1	45	4	7.203
Risk × objectives	4	44	23.714	13.292
Risk factors × BIM	1	33	4.184	5.185

time progress of the design but also facilitate communication and agreement between the owner and contractor in a visual environment, effectively reducing the amount of rework on-site (e.g., preventing design changes, communication disputes, engineering disputes, rework, etc.).

Simulation and optimization of construction scheme: in complicated projects, the difficulties and key points of the construction can be found in advance, and the construction scheme can be further optimized.

BIM visualization model and roaming use: textual technical content can be expressed in a visual model, so that construction personnel can more intuitively and deeply understand technical content. This may improve professional collaborative communication efficiency, avoid unnecessary material and labor waste, and reduce the workload associated with reading materials.

Construction progress auxiliary management: visual management of the advance schedule of the construction project can facilitate reasonable arrangement of construction procedures, installation progress, reduction of waste, and improving efficiency.

Composition and material control: statistical engineering, based on a 3D model and construction organization, can improve quota design, subproject quantity statistics, real-time multicount comparison, and facilitating cost control.

The model can obtain information on all materials, physical quantities, and quotas to release materials, thereby saving material usage and reducing costs. After the project is completed, the actual material usage and planned material usage will be automatically counted and analyzed, which provides a reliable reference when costing similar projects in future.

In the network analysis, the most influential BIM was the 5D model (Figure 4). The BIM 5D cost estimate is centrally located in the network and influences project costs and schedule targets, especially for project contract risks, security risks, and subcontractor risks. This information can be used to display virtual project builds for other stakeholders and thereby discover project-relevant information. Additionally, the model simplifies the concept of the project; misunderstandings among stakeholders are reduced because they can see the final design before the project starts. Any changes that occur during the build process, such architectural alterations, are automatically transferred to the model, and everyone can access the new information. The greatest benefit is that anyone involved in the project has access to
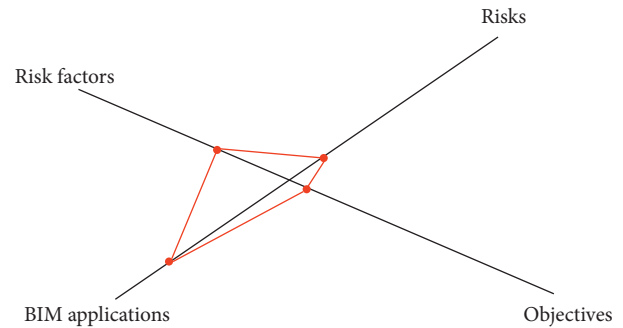
FIGURE 4: Node cross-analysis.

geometry, required resources, time, and cost, which enables all stakeholders to make quick decisions and reduces any misunderstandings that may occur.

The meta-network also can show the different networks relations. The direct relationships between the four meta-networks were demonstrated by node cross-analysis, shown in Figure 4. BIM types (in the network node named "Resources") have the most nodes and connections throughout the network, indicating that BIMs play a major role in the risk-management network. Moreover, of all relationships, that between BIM and risk factors was the strongest.

Figure 5 shows the network simulation result based on maximum likelihood estimation. Greater likelihood represents a greater chance that the event will occur under different conditions when the result is known. The results show that the central-hub assumptions in the network differed from other probability assumptions.

After applying BIMs, the density of the entire risk network was reduced by 69%. The 5D BIM network contained 164 links, which reduced risk by approximately 56%, with nodes reducing in number by 36% (reasonable cost planning, cost control). The 3D BIM network contained 232 links, which reduced risk by c. 23%, with the number of nodes reducing by 25%. The disaster plan network contained 251 links, reducing risk by c. 17% (reduced risk of personnel safety accidents), and nodes by 19%. The communication platform network contained 235 links, reducing risk by c. 22%, and nodes by 23% by promoting early risk identification and risk communication.

The best potential risk management paths were identified by determining the shortest paths that could control links. For example, for the 5D BIM to COST, the shortest path length was 5, and the number of shortest paths was 1. For the path Owner's requirements unclear (F71) $\longrightarrow$ Technical and design changes (R11) $\longrightarrow$ Cost (6.16) affected value; in the initial contract, the owner's requirements are not clear or the owner does not document requirements, which will lead to technical and design changes during project implementation, which will increase workload and/or increase costs due to the need
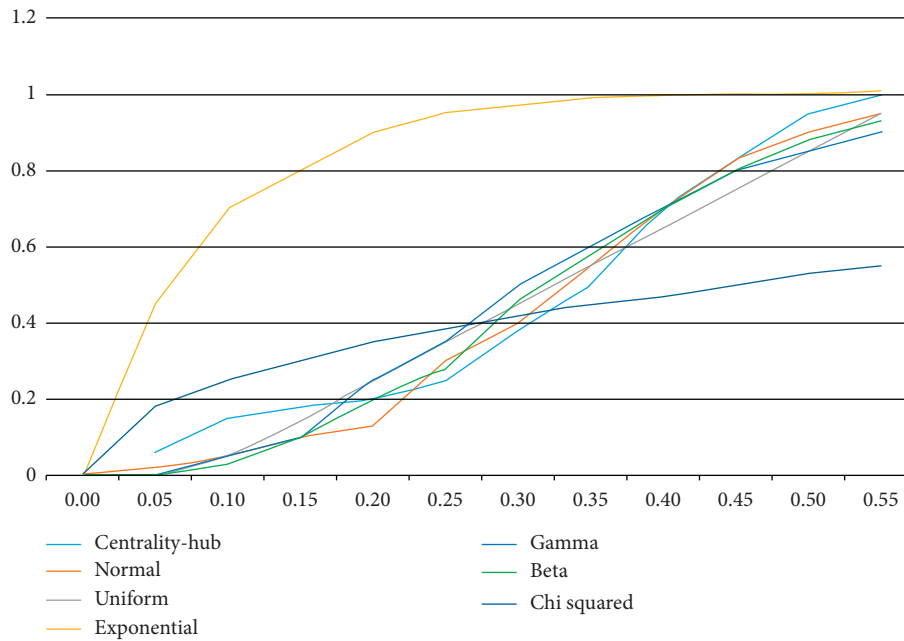
FIGURE 5: Network simulation results.

for new designs. The path Design errors (F74) ⟶ Technology and design changes (R11) ⟶ Cost (5.86) signifies that design errors are also a primary factor in design changes and continue to affect project costs.

4. Discussion

4.1. Theoretical Contribution. The meta-network revealed that BIMs can control internal risks and technical risks in ICPs, but they cannot control the external risks of ICPs. Political risk can be reduced by reviewing the country risk index (world political risk report). Social and cultural risks can be reduced by purchasing insurance (MIGA/AIG/ KLIN). Legal risks can be addressed by including the laws and regulations of various countries in the BIM information-integration model to facilitate the timely acquisition of relevant legal provisions. Economic risk can be addressed by including exchange rates between countries and interest rate changes in a 5D BIM at regular intervals; project financial managers or owners and contractors can regularly check the relevant information and adjust the project cost plan and construction plan according to economic changes. Health risk can be ameliorated using a safety management model to train staff on personal hygiene, and utilizing health screenings for timely detection of physical illness among staff. Environmental risk can be addressed via the platform or model of management of the environment to be developed, with its associated environmental management procedures and system management.

Advantages of BIMs have been studied thoroughly, and the rapidly available benefits contractors have obtained have been categorized in detail [73]. The process of facilitating BIM adoption and the latent challenges are being reciprocally studied [74, 75]. In practice, enterprises

need to advance implementation theories to fully use BIM-based tools and thereby improve project functionality [10]. While some features of BIMs can help address project risk, it is not possible to conduct comprehensive risk management.

Most risk-management research based on BIMs has focused on the BIM as an advanced tool by which to manage project risk, such as design errors, quality, and budget, from a visual perspective, but has rarely explicitly referenced ICP risk management [9]. Most ICP risks related to the proposed contract and design errors are caused by language differences; BIMs may help ameliorate the consequence of the risks.

4.2. Practical Implications. The practical implications of this research can be discussed from three perspectives, namely, shortage of talents, software issues, and government policy. From the perspective of the shortage of talents, the lack of individuals familiar with BIMs is the main problem underlying the application of BIM technology in enterprises. This includes a lack of professionals qualified to implement BIMs and a lack of systematic BIM technical training. BIM talent is the primary issue that needs to be addressed before BIM technology can be applied widely. Different national stakeholders have different perceptions and knowledge of BIMs. Therefore, it will take time for BIMs to be applied in ICPs.

Regarding technology issues, each country has developed different software, and compatibility and usability of packages differ. Therefore, before implementing a project, all parties should determine the software that will be used and the necessary standards. From an economic perspective, the benefits of deep application of BIM technology for enterprises are uncertain. The unclear long-term return on

investment and high input costs have hindered the wide application of BIM technology.

From the perspective of government policy, there is currently no relevant BIM standard in the industry; each country has different BIM standards. Thus, legal liability discrepancies are unknown, which hinders the use of BIM software and the deep application of BIM technology. At present, the development of BIM technology needs further research and improvement, and potentially even changes in standards, processes, software, and policies because different owners and contractors have different understanding of BIM in different countries. As well as the aforementioned software compatibility issues, there exist difficulties in model management as data security differs among networks, as do network speeds; these issues incur the risk of data loss. The unclear legal liability associated with the BIM system, intellectual property issues, model ownership issues, and ownership of data mean that BIM has a high short-term cost. Further, many participants in international engineering projects attach great importance to their interests and image, and data input that intentionally conceals real data may occur, reducing data reliability.

Finally, the main practical contribution of this research is its suggestion of appropriate BIM applications to various stakeholders, contractors, and project owners, according to their own project objectives and major risks in the early stage of the project.

5. Conclusion

This study mapped the relationship between ICP risks and BIM applications. A BIM project risk-mitigation network was constructed. From the perspective of the ICP risk network, the BIM has a notable ability to prevent design errors and design change risks. BIM use has great potential to prevent risks, as evidenced by the risk network, which incorporated BIM architecture, management structure model, quality and safety management, site analysis, and collaborative management platform. BIMs can help users visualize risk information and understand the exact location of risk in the project, and help stakeholders understand risk and its impact on project duration. BIMs potentially eliminate the risks caused by language barriers in international engineering projects and improve risk communication and risk information management. BIMs can also eliminate time issues in information communication inherent to international engineering projects. By combining specific BIMs, stakeholders and contractors in different countries can view relevant content in real time and change incorrect or conflicting content in timely manner.

However, promoting the BIM use in international engineering projects presents some difficulties. From a technical point of view, the software developed in different countries lacks compatibility. Differences in data security levels and network speeds among networks pose a risk of data loss. In terms of management, difficulties may arise due to differences in professional models used among countries, owners, and contractors, who have different understandings of BIMs. Further, different BIM standards and BIM specifications will lead to information loss and affect cooperation. The legal liabilities associated with the BIM system are not clear concerning intellectual property rights, model ownership, data ownership, and so on. These problems should be addressed in the contract, to avoid later conflicts.

Certain limitations need to be considered when interpreting the research findings. First, the results of the risk assessment might only apply to Chinese international project contractors. Other types of projects or contractors in other countries may face different situations regarding risk management of ICPs. Nevertheless, the meta-network approach itself is generalizable and can be used in other similar risk management studies in different countries. Second, this study did not consider the role of BIMs in international project management from the perspective of BIM technology and software development. The study only assessed and interpreted the role of BIMs in ICP risk management from a management perspective. Future research is needed to combine management and technical aspects, which might require the design and development of related BIM software. Finally, the integrated management of the final risk mitigation strategy needs to be verified in an actual project.

Data Availability

The data used to support the findings of this study are available from the corresponding author upon request.

Conflicts of Interest

The authors declare that they have no financial and personal relationships with anyone or any entity whose interests could be positively or negatively influenced by the content of this paper.

Acknowledgments

References

[1] F. K. Adams, "Risk perception and Bayesian analysis of international construction contract risks: the case of payment delays in a developing economy," *International Journal of Project Management*, vol. 26, no. 2, pp. 138–148, 2008.

[2] M. A. Vigneault, C. Boton, H. Y. Chong, and B. Cooper-Cooke, "An innovative framework of 5D BIM solutions for construction cost management: a systematic review," *Archives of Computational Methods in Engineering*, pp. 1–18, 2019.

[3] X. Wang and H.-Y. Chong, "Setting new trends of integrated Building Information Modelling (BIM) for construction industry," *Construction Innovation*, vol. 15, no. 1, pp. 2–6, 2015.

[4] R. Lopez, H.-Y. Chong, X. Wang, and J. Graham, "Technical review: analysis and appraisal of four-dimensional building information modeling usability in construction and engineering projects," *Journal of Construction Engineering and Management*, vol. 142, no. 5, Article ID 06015005, 2016.

[5] Ž Turk, S. Wu, G. Wood, K. Ginige, and S. W. Jong, "A technical review of bim based cost estimating in UK quantity surveying practice, standards and tools," *Journal of Information Technology in Construction*, vol. 19, pp. 535–563, 2014.

[6] E. A. Pärn, D. J. Edwards, and M. C. P. Sing, "The building information modelling trajectory in facilities management: a review," *Automation in Construction*, vol. 75, pp. 45–55, 2017.

[7] H.-Y. Chong, C.-Y. Lee, and X. Wang, "A mixed review of the adoption of Building Information Modelling (BIM) for sustainability," *Journal of Cleaner Production*, vol. 142, pp. 4114–4126, 2017.

[8] J. K. W. Wong and J. Zhou, "Enhancing environmental sustainability over building life cycles through green BIM: a review," *Automation in Construction*, vol. 57, pp. 156–165, 2015.

[9] Y. Zou, A. Kiviniemi, and S. W. Jones, "A review of risk management through BIM and BIM-related technologies," *Safety Science*, vol. 97, pp. 88–98, 2017.

[10] T. Hartmann, H. van Meerveld, N. Vossebeld, and A. Adriaanse, "Aligning building information model tools and construction management methods," *Automation in Construction*, vol. 22, pp. 605–613, 2012.

[11] C.-S. Shim, K.-M. Lee, L. S. Kang, J. Hwang, and Y. Kim, "Three-dimensional information model-based bridge engineering in Korea," *Structural Engineering International*, vol. 22, no. 1, pp. 8–13, 2012.

[12] L. Zhang, X. Wu, M. J. Skibniewski, J. Zhong, and Y. Lu, "Bayesian-network-based safety risk analysis in construction projects," *Reliability Engineering & System Safety*, vol. 131, pp. 29–39, 2014.

[13] S. Azhar, "Building information modeling (BIM): trends, benefits, risks, and challenges for the AEC industry," *Leadership and Management in Engineering*, vol. 11, no. 3, pp. 241–252, 2011.

[14] C. S. Dossick and G. Neff, "Messy talk and clean technology: communication, problem-solving and collaboration using building information modelling," *Engineering Project Organization Journal*, vol. 1, no. 2, pp. 83–93, 2011.

[15] A. Grilo and R. Jardim-Goncalves, "Value proposition on interoperability of BIM and collaborative working environments," *Automation in Construction*, vol. 19, no. 5, pp. 522–530, 2010.

[16] A. Porwal and K. N. Hewage, "Building information modeling (BIM) partnering framework for public construction projects," *Automation in Construction*, vol. 31, pp. 204–214, 2013.

[17] W. Liu, H. Guo, H. Li, and Y. Li, "Using BIM to improve the design and construction of bridge projects: a case study of a long-span steel-box arch bridge project," *International Journal of Advanced Robotic Systems*, vol. 11, no. 8, p. 125, 2014.

[18] B. Hardin, *BIM and Construction Management: Proven Tools, Methods, and Workflows*, Wiley, Indianapolis, IN, USA, 2011.

[19] D. Migilinskas, V. Popov, V. Juocevicius, and L. Ustinovichius, "The benefits, obstacles and problems of practical bim implementation," *Procedia Engineering*, vol. 57, no. 1, pp. 767–774, 2013.

[20] N. H. Philipp, "Building information modeling (BIM) and the consultant: managing roles and risk in an evolving design and construction process," in *Proceedings of Meetings on Acoustics Acoustical Society of America*, San Francisco, CA, USA, December 2013.

[21] Y. Zhou, L. Ding, X. Wang, M. Truijens, and H. Luo, "Applicability of 4D modeling for resource allocation in mega liquefied natural gas plant construction," *Automation in Construction*, vol. 50, pp. 50–63, 2015.

[22] S. Amirebrahimi, A. Rajabifard, P. Mendis, and T. Ngo, "A framework for a microscale flood damage assessment and visualization for a building using BIM–GIS integration," *International Journal of Digital Earth*, vol. 9, no. 4, pp. 363–386, 2016.

[23] Q. Lu, J. Won, and J. C. P. Cheng, "A financial decision making framework for construction projects based on 5D Building Information Modeling (BIM)," *International Journal of Project Management*, vol. 34, no. 1, pp. 3–21, 2016.

[24] H. Moon, H. Kim, C. Kim, and L. Kang, "Development of a schedule-workspace interference management system simultaneously considering the overlap level of parallel schedules and workspaces," *Automation in Construction*, vol. 39, pp. 93–105, 2014.

[25] A. KarimiAzari, N. Mousavi, S. F. Mousavi, and S. Hosseini, "Risk assessment model selection in construction industry," *Expert Systems with Applications*, vol. 38, no. 8, pp. 9105–9111, 2011.

[26] T. Zayed, M. Amer, and J. Pan, "Assessing risk and uncertainty inherent in Chinese highway projects using AHP," *International Journal of Project Management*, vol. 26, no. 4, pp. 408–419, 2008.

[27] D. Xiaopeng and L. S. Pheng, "Understanding the critical variables affecting the level of political risks in international construction projects," *KSCE Journal of Civil Engineering*, vol. 17, no. 5, pp. 895–907, 2013.

[28] J. Liu, X. Zhao, and P. Yan, "Risk paths in international construction projects: case study from Chinese contractors," *Journal of Construction Engineering and Management*, vol. 142, no. 6, Article ID 05016002, 2016.

[29] X. Zhao, B.-G. Hwang, and G. S. Yu, "Identifying the critical risks in underground rail international construction joint ventures: case study of Singapore," *International Journal of Project Management*, vol. 31, no. 4, pp. 554–566, 2013.

[30] G. D. Creedy, M. Skitmore, and J. K. W. Wong, "Evaluation of risk factors leading to cost overrun in delivery of highway construction projects," *Journal of Construction Engineering and Management*, vol. 136, no. 5, pp. 528–537, 2010.

[31] D. S. Santoso and S. Soeng, "Analyzing delays of road construction projects in Cambodia: causes and effects," *Journal of Management in Engineering*, vol. 32, no. 6, Article ID 05016020, 2016.

[32] A. E. Yildiz, I. Dikmen, M. T. Birgonul, K. Ercoskun, and S. Alten, "A knowledge-based risk mapping tool for cost estimation of international construction projects," *Automation in Construction*, vol. 43, pp. 144–155, 2014.

[33] I. Dikmen and M. T. Birgonul, "An analytic hierarchy process based model for risk and opportunity assessment of international construction projects," *Canadian Journal of Civil Engineering*, vol. 33, no. 1, pp. 58–68, 2006.

[34] S. H. Han, J. E. Diekmann, Y. Lee, and J. H. Ock, "Multicriteria financial portfolio risk management for international projects," *Journal of Construction Engineering and Management*, vol. 130, no. 3, pp. 346–356, 2004.

[35] W. G. M. Hakami, "The critical factors of project life cycle in Sudanese construction projects," *International Journal of Engineering Sciences & Research Technology*, vol. 4, no. 3, pp. 518–532, 2015.

[36] D. Q. Tran and K. R. Molenaar, "Impact of risk on design-build selection for highway design and construction projects," *Journal of Management in Engineering*, vol. 30, no. 2, pp. 153–162, 2014.

[37] S. Mathew, D. Tran, and L. D. Nguyen, "Examining impact of risk on cost growth in design-build projects using structural equation modeling," in *Proceedings of the Construction Research Congress 2018: Construction Project Management—Selected Papers from the Construction Research Congress 2018*, American Society of Civil Engineers, Reston, VA, USA, pp. 659–669, April 2018.

[38] S. M. El-Sayegh and M. H. Mansour, "Risk assessment and allocation in highway construction projects in the UAE," *Journal of Management in Engineering*, vol. 31, no. 6, Article ID 04015004, 2015.

[39] J. K. Lee, S. H. Han, W. Jang, and W. Jung, ""Win-win strategy" for sustainable relationship between general contractors and subcontractors in international construction projects," *KSCE Journal of Civil Engineering*, vol. 22, no. 2, pp. 428–439, 2018.

[40] A. S. Hanna, K. Blasier, and D. G. Aoun, "Risk misallocation on highway construction projects," *Journal of Legal Affairs and Dispute Resolution in Engineering and Construction*, vol. 7, no. 4, Article ID 04515002, 2015.

[41] W. T. Thweatt and R. J. Long, "EPC contract risk analysis associated with onshore projects in developing countries," *Long International*, vol. 303, pp. 1–31, 2017.

[42] AGC, *The Contractor's Guide to BIM*, Associated General Contractors of America, Richmond, VA, USA, 2009.

[43] BCA, *Singapore BIM Guide*, Building and Construction Authority, Singapore, 2013.

[44] CFM, *The VA BIM Guide*, Department of veterans affairs. Construction & Facilities Management, Washington, DC, USA, 2010.

[45] COD, *BIM Guide*, College of the Desert, Palm Desert, CA, USA, 2011.

[46] COSA, *Building Information Modeling (BIM) Development Criteria and Standards for Design & Construction Projects*, COSA BIM Standards, San Antonio, TX, USA, 2011.

[47] CRC, *National Guidelines for Digital Modeling*, CRC for Construction Innovation, Brisbane, Australia, 2009.

[48] D. S. F. DOA, *BIM Guidelines & Standards for Architects and Engineers*, Department of Administration. Division of State Facilities, Madison, WI, USA, 2012.

[49] FMS, *BIM Guidelines*, University of Southern California Facilities Management Services, Los Angeles, CA, USA, 2012.

[50] GSFIC, *BIM Guide. Georgia State Financing and Investment Commission*, GSFIC, Tbilisi, GA, USA, 2013.

[51] GTFM, *Georgia Tech BIM Requirements & Guidelines for Architects. Engineers and Contractors, Georgia Tech Facilities Management*, GTFM, Tbilisi, GA, USA, 2016.

[52] Adriaanse, *BIM Uses Guide*, Harvard University Construction Management Council, Cambridge, UK, 2016.

[53] HKCIC, *CIC Building Information Modelling Standards (Phase One)*, Construction Industry Council, Wanchai, China, 2015.

[54] IU, *BIM Guidelines & Standards for Architects, Engineers, and Contractors*, Indiana University, Indianapolis, IN, USA, 2015.

[55] LACCD, *BIM Standard*, Los Angeles Community College District, , Los Angeles, CA, USA, 2016.

[56] MPA, *Appendix A: MPA BIM Guidelines*, Massachusetts Port Authority, Boston, MA, USA, 2015.

[57] NATSPEC, *NATSPEC National BIM Guide*, NATSPEC Construction Information, Sydney, Australia, 2016.

[58] NRC, *National BIM Guidelines and Case Studies for Infrastructure*, Sustainable Built Environment National Research Centre, Perth, Australia, 2014.

[59] NYCSCA, *BIM Guidelines and Standards for Architects and Engineers*, New York City School Construction Authority, New York, NY, USA, 2014.

[60] NYCDDC, *BIM Guidelines*, Department Design and Construction, New York, NY, USA, 2012.

[61] OFCC, *BIM Protocol*, State of Ohio Facilities Construction Commission, Columbus, OH, USA, 2012.

[62] PSU, *BIM Execution Planing: BIM Uses*, Penn State University, University Park, Harrisburg, PA, USA, 2011.

[63] SDCCD, *BIM Standards for Architects*, Engineers & Contractors, San Diego Community College District, San Diego, CA, USA, 2012.

[64] Statsbygg, *Statsbygg BIM Manual*, Statsbygg, Oslo, Norway, 2013.

[65] TPA, "E/A design division BIM standard," The Port Authority of NY & NJ Engineering Department, New York, NY, USA, 2016.

[66] USACE, *Roadmap for Life-Cycle BIM*, United States Army Corps of Engineers, Washington, DC, USA, 2012.

[67] Y. Li and X. Wang, "Risk assessment for public–private partnership projects: using a fuzzy analytic hierarchical process method and expert opinion in China," *Journal of Risk Research*, vol. 21, no. 8, pp. 952–973, 2016.

[68] D. Krackhardt and K. M. Carley, "PCANS model of structure in organizations," *Research report series/Carnegie Mellon University Institute for Complex Engineered Systems*, Carnegie Mellon University, Pittsburgh, PA, USA, 1998.

[69] K. Carley, J. Diesner, J. Reminga, and M. Tsvetovat, "Toward an interoperable dynamic network analysis toolkit," *Decision Support Systems*, vol. 43, no. 4, pp. 1324–1347, 2007.

[70] J. Zhu and A. Mostafavi, "Dynamic meta-network modeling for an integrated project performance assessment under uncertainty," in *Proceedings of the Construction Research Congress 2016*, pp. 2340–2350, San Juan, Puerto Rico, May-June 2016.

[71] K. Carley, P. Pattison, and R. L. Breiger, *Dynamic Social Network Modeling and Analysis: Workshop Summary and Papers*, National Academic Press, Washington, DC, USA, 2003.

[72] R. J. Yang and P. X. W. Zou, "Stakeholder-associated risks and their interactions in complex green building projects: A social network model,," *Building and Environment*, vol. 53, pp. 208–222, 2014.

[73] L. L. Foster, "Legal issues and risks associated with building information modeling technology," University of Kansas, Lawrence, Kansas, Doctoral dissertation, 2008.

[74] N. Gu and K. London, "Understanding and facilitating BIM adoption in the AEC industry," *Automation in Construction*, vol. 19, no. 8, pp. 988–999, 2010.

[75] F. Khosrowshahi and Y. Arayici, "Roadmap for implementation of BIM in the UK construction industry," *Engineering, Construction and Architectural Management*, vol. 19, no. 6, pp. 610–635, 2012.

Research Article

Bridge Seismic Damage Assessment Model Applying Artificial Neural Networks and the Random Forest Algorithm

Hanxi Jia [iD],[1,2] **Junqi Lin** [iD],[1,2] **and Jinlong Liu**[1,2]

[1]*Institute of Engineering Mechanics, China Earthquake Administration, Harbin 150080, China*
[2]*Key Laboratory of Earthquake Engineering and Engineering Vibration, China Earthquake Administration, Harbin 150080, China*

Correspondence should be addressed to Junqi Lin; linjunqi@iem.net.cn

Earthquakes cause significant damage to bridges, which have a very strategic location in transportation services. The destruction of a bridge will seriously hinder emergency rescue. Rapid assessment of bridge seismic damage can help relevant departments to make judgments quickly after earthquakes and save rescue time. This paper proposed a rapid assessment method for bridge seismic damage based on the random forest algorithm (RF) and artificial neural networks (ANN). This method evaluated the relative importance of each uncertain influencing factor of the seismic damage to the girder bridges and arch bridges, respectively. The input variables of the ANN model were the factors with higher importance value, and the output variables were damage states. The data of the Wenchuan earthquake were used as a testing set and a training set, and the data of the Tangshan earthquake were used as a validation set. The bridges under serious and complete damage states are not accessible after earthquakes and should be overhauled and reinforced before earthquakes. The results demonstrate that the proposed approach has good performance for assessing the damage states of the two bridges. It is robust enough to extend and improve emergency decisions, to save time for rescue work, and to help with bridge construction.

1. Introduction

Seismic events cause tremendous damage to humans and socioeconomic impacts [1–4]. In order to reduce the loss, it is necessary to formulate a postearthquake rescue plan in a timely and scientific manner [5]. However, developing a rescue plan requires an understanding of the traffic situation around the disaster area [6]. The small amount of information obtained from the postearthquake field survey cannot guide the rescue work alone. At the same time, lifeline systems have been of growing concern, especially the vulnerability to risk-induced damage [7]. The transportation infrastructure is one of the most vital lifeline systems of society [8]. If the earthquake damage assessment of the bridge can be carried out before the disaster, the traffic capacity can be quickly judged after the earthquake [9]. This can help the government and save valuable rescue time [6]. Moreover, accurate preearthquake assessments can also identify areas of earthquake resistance in the region for prevention and reinforcement, thereby reducing the potential damage caused by the earthquake. Hence, how to carry out accurate seismic damage assessment has become an important practical issue.

Although there are many factors that affect the damage of bridges, not each one has a vital role. Hence, it is vital to choose an appropriate technique to assess the importance of different factors. Linear methods are often applied to evaluate factor importance [10]. Mangalathu et al. have established the correlation between bridge fragility and factors applying the linear technique [11]. However, because of the ambiguity of each correlation feature [12], ensemble models of machine learning are raised by some studies and used for factor correlation evaluation problems [13–15] for increasing the precise and generalized performance of the empirical methods [16]. It has been proven that the results of the ensemble models are better than the empirical methods

[10]. A recent study has given the relative importance of each uncertain input parameter on the fragility curves of skewed bridges based on three-layer neural networks [11]. However, no studies have used ensemble methods to assess the feature importance in the seismic risk area. One of the most widely used ensemble learning techniques is the RF method, which has the best overall performance compared to other algorithms, such as AdaBoost, logistic regression, and Classification and Regression Tree (CART) [17].

Different methodologies have been proposed to assess the fragility [18] or the damage of a bridge. Some of the previous studies have evaluated individual bridges in detail by using different methods, such as multipoint acceleration measurement and ANNs [19], assessing the relative risks of the failure modes of a bridge and the limitations of risk priority numbers (RPNs) associated with individual failure modes [20], as well as the Bayesian method [21]. Some studies present the assessment methods of bridge components [22]. However, emergency work needs a great deal of evaluation results of bridges to be obtained in a short period of time. Most studies used linear models or some evaluation systems, for example, Risk Priority Numbers (RPNs) [20], Hazards United States Multi-Hazard (HAZUS) [23], and the Failure Mode and Effect Analysis (FMEA) system [24]. These evaluation systems can give a risk assessment of a single bridge and give specific forms of damage, such as the ineffective angle, ineffective position, and ineffective number of structures. The evaluation procedure of the seismic performance of a highway bridge is divided into three branches: topological analysis, vulnerability analysis, and traffic flow analysis [6]. The study can serve as a tool for the decision-making of postemergency response management and seismic retrofit of the highway bridge. Nevertheless, statistical models often proposed linear techniques that were assessed by establishing functions [25], which may be difficult to formulate for structures subjected to large inelastic deformations [26]. These disadvantages can be overcome by ANNs. ANNs have a good predictability even if all the attributes are mixed together to estimate demand models [11].

Owing to their accuracy, versatility, and robustness, ANNs have been applied to a variety of problems including pattern recognition, data mining, and image processing [19]. With the rapid development of artificial intelligence, many studies estimating fragility based on the ANN method have begun to emerge [27]. It was used to assess the fragility of some different bridges [11]. The multiparameter fragility methodology helps to generate fragility curves for a specific skew angle and a set of bridge parameters. However, the fragility curves are obtained in a complex manner and cannot be obtained in a few minutes [11]. The steps are as follows: (1) estimating the demand based on the ANN, (2) using the Latin Hypercube Sampling (LHS) method to estimate the capacity, and (3) using logistic regression to get fragility curves. Hence, although the estimation can help the bridge inspection workers to prioritize their recovery methods following an earthquake, it cannot help the emergency rescue work.

This study presents an approach for the damage assessment of girder bridges and arch bridges considering the different importance of the features of seismic bridge damage. Unlike previous studies on the application of ANN for single or several bridges or bridge components assessment [11], this research explores the use of ANN for estimation of the damage state of most of the bridges in the entire disaster area. Also, unlike previous studies on the application of linear regression for bridge seismic assessment [5], this research uses the machine learning techniques to select features and propose the new model, which can avoid making assumptions and using empirical formulas and even can avoid the subjective impact of expert experience.

The main contribution of this paper includes the following: (1) considering the importance of features and applying the RF algorithms as the calculation model, which provides a different viewpoint for selecting the features as the input variables; (2) the fact that the damage states of a large quantity of bridges are obtained through improved ANN models of several deep learning algorithms. It provides an alternative method for developing the traditional pre-earthquake maintenance of bridges and decision-making for postearthquake emergency rescue.

This study evaluates the importance of the features by applying the RF model and using the data from the Wenchuan earthquake in 2008. Then, the ANN damage evaluation model is processed according to the results of the previous work on a girder bridge and the arch bridge, respectively. To examine the accuracy and applicability of the assessment model, this research selects the linear regression model [5] and 40 bridges in the Tangshan earthquake in 1976. Finally, the future extensions and limitations of the proposed method are discussed.

2. Data

The 12 May, 2008, Mw7.9 Wenchuan earthquake, with wide and significant influence, had great destructive power and the aftershocks lasted for a long time. After the earthquake, the China Earthquake Administration dispatched experts to conduct on-site investigations and set up 4,150 investigation sites with an investigation area of 500,000 square kilometers [5]. The survey data are comprehensive, standardized, detailed, and complete in comparing the data of the Tangshan earthquake and the Haicheng earthquake. Therefore, they are suitable for statistical analysis, and this study used the bridge data of the Wenchuan earthquake.

The investigation scope of the Wenchuan earthquake was based on the nationally identified severely affected areas, the national trunk highways in extremely severe disaster areas, and all the bridges on some county and township roads. It covers 10 counties and cities in Sichuan, Shanxi, and Gansu provinces: Wenchuan County, Beichuan County, Mianzhu City, Shifang City, Qingchuan County, Mao County, Anxian County, Dujiangyan City, Pingwu County, and Pengzhou City, making a total of 47 highways and national highways. The survey area covers the intensity as the VI–XI degree area. The seismic precautionary intensity of the bridges in most of the hardest and most severe areas before the earthquake is VII. A total of 2,154 bridges were

surveyed: 746 in the VI degree area, 287 in the VII area, 175 in the IX degree area, and 168 in the X and XI areas. Among them, 1,525 were girder bridges and 590 were arch bridges, and the remaining bridges were cable-stayed bridges and suspension bridges. Hence, this paper chose the girder bridges and arch bridges.

The investigation is divided into three stages. (1) The emergency rushing stage was from 12 May, 2008, to 27 May, 2008. The characteristic was that it enters the disaster area for the first time after the earthquake. The seismic damage data obtained could best reflect the earthquake damage of the highway bridge after the earthquake, and the timeliness was strong. The scope of investigation was limited to the life passage leading to the most severely affected areas. Basically, no equipment was used. Experts assessed the capacity of the bridge through earthquake damage to meet emergency traffic demand. (2) The ensured bridge capacity stage was from 23 May, 2008, to the end of July 2008. The competent transportation department coordinated and arranged this, and the investigation was extensive and comprehensive, including all highways and national and provincial trunk highway bridges in the disaster area. In the investigation, the instrument was used for comprehensive testing, and the system's postearthquake bridge test report was formed. (3) The supplementary investigation stage was from August 2008 to May 2009. On the basis of the survey data and data of the first two stages of the verification, a supplementary investigation was conducted on some bridges in the first two stages, where the earthquake damage investigation was insufficient and the inaccessible areas were not included. At this stage, some roads, bridges, and municipal bridges in counties and townships were also investigated. At the same time, the bridge design data, bridge coordinates, and bridge axis directions were collected.

Table 1 shows the investigation of the main seismic damage to the girder bridges and arch bridges. Figure 1 shows the damage pictures of a typical bridge in Wenchuan County: the Caopo 3rd bridge. The first picture is before the earthquake, and the others are after the damage. The second picture in the first row presents the seventh span of the bridge moving 32 cm to the left; the first picture in the second row shows the rupture of the joint between the left block and the coping of the pier coping girder. The crack developed from the top to the left (the root is cut and penetrated). The crack is about 0.7–1.2 m, and the width is about 0.15–0.35 m. The last picture shows that the cone slopes on both sides of the abutment have local cracking, some joints fell off, the cone slope sinks as a whole, and the settlement height is 0.1–0.4 m.

3. Features

3.1. Select Features. A crucial problem in seismic damage estimation projects is whether or not the features are indeed helpful for the evaluation. There are many features influencing the damage of bridges [28–30], for example, the intensity of seismic activity, the parameters of the bridge, and the environment around the bridge. Nevertheless, some features lack sufficient data. This study selected some factors

as follows: structural types, bridge pier types, foundation types, bearing types, bridge linear, bridge scales, the type of site, soil, seismic precautionary intensity, and the practical intensity of earthquakes. Table 2 presents the sorts of features.

(I) Different structural types have different reasonable spans, methods of force transmission, and principles of bearing load. Girder bridges are classified as the simply supported girder bridge, steel girder bridge (continuous girder bridge), and cantilever girder bridge in this study. A simply supported girder bridge has the following characteristics: (1) the force manners are simple and the method of force transmission is clear; (2) the deformation of the bridge cannot produce redistributed stress; and (3) the bridges are mostly used for small spans. A continuous girder bridge is suitable for larger spans and the deformability is poor with negative moment segments. Arch bridges are classified according to the material of the arch rings

(II) A bridge pier with larger stiffness is not conducive to absorbing vibration energy, and diagonal cracks will occur under seismic conditions [18], while a bridge pier with smaller stiffness is more easily deformed than the standard and becomes unstable. Therefore, the bridge pier, an important component that transmits the load from the superstructure to the foundation, has a very important influence on the bridge damage. The piers of the girder bridge are classified as five types: no pier, masonry solid pier, bent pier, rectangular thin-wall pier, and single column pier

(III) The influence of the foundation on the bridge's seismic damage is mainly due to the transmission of force [31]. Compared with the spread foundation, the open caisson foundation, and the multirow piles foundation, the bent pile foundation and tall platform pile foundation are prone to broken piles and pile detachment under the action of horizontal load. In addition, if the girder falls, it is also possible for it to break the pier or cover the pile cap. Therefore, the foundation is vital to the bridge damage

(IV) The bearings, important devices for transmitting force from the main beam to the pier, are classified as rubber bearing, steel bearing, concrete bearing, and tetrafluoroethylene bearing according to the material. The deformation capacity of the bearing has a certain influence on the bridge damage, and it is also an important component in the local seismic scheme [32–34]. For a bridge with bearing, the shock absorption support is usually used to reduce the impact of the earthquake on the bridge. The shock absorption bearing provides shock absorbers and uses the damping force generated by the viscosity of the medium or the elasticity of the rubber. Rubber

TABLE 1: Investigation of main seismic damage to the girder bridges and arch bridges.

Girder bridge	Superstructure and bearing	Plane displacement of the girder body, with or without girder falling, with or without potential risk of girder falling
		Impact damage of joint bridges at expansion joints
		Cracking of girder body, diaphragm, bridge deck, and hinge joint
		Bearing damage, deformation, displacement, hanging in the air, and failure of seismic anchors
		Damage of bridge deck pavement and displacement damage of expansion joint
	Substructure	Damage and crack to coping, padstone blocks, etc.
		Shearing, crushing, cracking, and tilting of the pier column
		Impact damage, cracking of the platform, and destruction of the truncated cone slope of the abutment
		Foundation displacement of piers and abutments
	Accessory structure	
Arch bridge	Superstructure	Whether the main and spandrel arch rings collapse, crack, dislocate, etc.
		Whether the vertical and horizontal connection of each arch box and the transverse connection of the arch ribs are cracked
		Whether the deck (girder) support of the girder type abdominal arch bridge is hanging in the air, displaced, and destroyed
		Whether the bridge deck is levelling and whether there is settlement on the arch fill
		Whether the side wall is cracked, extraversed, and displaced
		Whether the spandrel arch and the cross wall collapse or crack
	Substructure	Whether cracks, overturning, collapse, and settlement occur in piers, skewback, and abutments
		Cracking of the front wall and side wall of the abutment, and whether the abutment body is deformed by the earthquake force
		Whether the foundation has displacement
	Accessory structure	

(a)

(b)

(c)

(d)

FIGURE 1: The damage pictures of the Caopo 3rd bridge (seriously damaged; the bridge length is 225 meters).

bearing with a strong deformation ability is better than a concrete bearing with poor deformation ability. Therefore, the bearing type was also considered a factor

(V) The bridge linearity refers to the geometry of the main beam and the type of intersection angle with the riverbank. The internal force distribution of a skew bridge under external

Table 2: Features table of the girder bridge and the arch bridge (L is the length of the bridge [35]).

Features	Classification	
	Girder bridge	Arch bridge
Structural types	Simply supported girder bridge Continuous girder bridge (girder bridge of steel construction) Cantilever girder bridge	Masonry arch bridge Steel arch bridge Combined arch bridge
Bridge pier types	No pier Masonry solid pier Bent pier Rectangular thin-wall pier Single column pier Other types of piers	Masonry solid pier Other types of piers No pier
Foundation types	Shallow foundation Deep foundation	
Bearing types	Laminated rubber bearings Basin rubber bearings Tetrafluoroethylene bearings Other types of bearing No bearing	
Bridge linear	Linear orthogonal bridge (curve bridge with large curve radius) Curve orthogonal bridge Skew bridge	
Bridge scales	Small bridge ($8 \leq L \leq 30$) Medium bridge ($30 < L < 100$) Large bridge ($100 \leq L \leq 100$) Super large bridges ($L > 1000$)	
The type of site soil	I II III IV	
Seismic precautionary intensity (degree)	VI VII VIII IX VI VII VIII	
Practical intensity (degree)	IX X XI	

force is very complicated, and there are large reactions and negative moments in the obtuse angle region. There are large differences and uncoordinated internal forces between the obtuse and acute angle regions under dynamic loading in deformation and internal force. This can easily cause damage to the bridge deck. Therefore, the seismic performance of a skew bridge is much worse than that of an orthogonal bridge

(VI) Due to the large mass, a bridge with a larger span has greater inertia force under the action of seismic acceleration. The lateral load is larger, and lateral slip occurs more easily. In addition, the mid-span deflection of a bridge with a larger span is also large under the vertical load, which makes it easy for the main beam to crack or even break. Hence, the bridge scale is vital to seismic damage [11]

(VII) Site soil refers to the soil layer where the bridge is located. It can be classified as four categories. Site soil affects the bearing capacity of the foundation and the foundation failure. The failure from the class I site soil to the class IV site soil gradually increased under the same seismic intensity. Additionally, the foundation failure means that the load from the superstructure is difficult to bear on the foundation, which often causes serious damage to the bridge. Therefore, the type of site soil is also an important factor affecting the earthquake damage of the bridge

(VIII) The intensity scale consists of a series of certain key responses such as people awakening, the movement of furniture, damage to chimneys, and finally total destruction. The precautionary intensity refers to the highest intensity of earthquakes in a

certain area for many years and is the main indicator for earthquake resistance in bridge construction. Seismic precautionary intensity is an indicator that comprehensively reflects the level of bridge construction and seismic performance. It involves the effects of seismic factors such as seismic checking, layout, and local seismic components. These factors cannot be divided in detail, but they have a certain degree of influence on the seismic performance of the bridge

(IX) The practical seismic intensity is an important factor affecting the degree of bridge damage. This means the designed seismic intensity and is not associated with the design ground acceleration or peak ground acceleration (PGA) of an earthquake. Obviously, from the overall trend, the higher the seismic intensity under other conditions, the more serious the damage of the bridge. Although the results also include other factors, the degree of intensity and damage is positively correlated to the overall trend. In addition, the earthquake damage assessment must give the intensity. Therefore, the seismic intensity should be used as a factor

3.2. Default Processing.

There is default value in the data set. This study chose the K-Nearest Neighbor (KNN) algorithm to treat the default value. KNN, a simple machine learning algorithm, is mainly used to solve classification problems. In the process of assuming a default value, it is necessary to calculate the Euclidean distance (equation (1)) of all the data sets for each predicted object. The Euclidean distance can describe the true distance (physical distance) of two points in n-dimensional space. There are two n-dimensional vectors $x = (x_1, x_2, x_3, \ldots, x_n)$ and $y = (y_1, y_2, y_3, \ldots, y_n)$, where x is the default value and y is the data with complete features. The Euclidean distances of x and y are expressed as

$$d(x, y) = \sqrt{\sum_{i=1}^{n} (x_i - y_i)^2}. \tag{1}$$

The results are sorted, and the K points closest to the predicted data are selected to form the decision set C. S is the default value set. We fill in the default value by averaging

$$x = \frac{1}{K} \left(\sum_{k=1}^{K} \sum_{S} C \right). \tag{2}$$

3.3. Importance of Factors.

The damage states were divided into five states as per previous studies [6, 36] (Table 3): no damage, slightly damaged, moderately damaged, seriously damaged, and completely damaged. There are many seismic damage state assessment methods; for example, expert-based/judgmental, empirical, experimental, analytical, and hybrid methods. The expert-based and empirical methods do not need the demand/capacity ratio and ductility

deformation ratio. The damage states of this study are based on the in situ inspections and can obtain much information about bridges quickly. The RF algorithm was proposed by Breiman [37] and had been proven to achieve suitable results in the application of feature selection [38]. The RF algorithm was chosen as the classifier to assess the importance of nine features, and the Classification and Regression Tree (CART) algorithm was applied to classify the data [14]. CART is a technique that is used in supervised learning for solving classification and regression tasks; a CART model learns simple decision rules that are inferred from the features by using a tree-like graph to demonstrate the course of actions. Each branch of a decision tree represents a possible decision, occurrence, or reaction in terms of statistical probability. The Gini index (GI_m) based feature selection can achieve both dimension reduction and the elimination of noise from the classification task [39]. The RF model was processed along with the Gini index in the Spyder module, which is a scientific Python development environment. The number of trees was classified to be 82 according to the running tests. The steps of the RF model are as follows: find the contribution of each feature on each tree in the RF, take an average, and finally compare the contribution between the features. The contribution indicates the importance of a factor. This algorithm uses VIM to represent the variable importance measures and GI to represent the Gini index. Suppose there are m features $X_1, X_2, X_3, \ldots, X_c$. Then, each feature X_j is calculated. The Gini index score is $VIM_{jm}^{(\text{Gini})}$, which is the average change of the j-th feature's node splitting impurity in all RF decision trees. GI_m is expressed as

$$GI_m = \sum_{k=1}^{|K|} \sum_{k_I \neq k} P_{mk} P_{mk}' = 1 - \sum_{k=1}^{|K|} P^2 mk, \tag{3}$$

where m is the number of the features (nodes), K is the number of classifiers, and pmk is the proportion of k in m. The change in GI_m before and after m is expressed as

$$VIM_{jm}^{(\text{Gini})} = GI_m - GI_l - GI_r, \tag{4}$$

where $VIM_{jm}^{(\text{Gini})}$ is the change in GI_m and GI_l and GI_r indicate the Gini index of the two new nodes after the branch, respectively. If the node where the feature j appears in the decision tree is in the set M, then the importance $VIM_{ij}^{(\text{Gini})}$ of the feature j at the ith number is

$$VIM_{ij}^{(\text{Gini})} = \sum_{m \in M} VIM_{ij}^{(\text{Gini})}. \tag{5}$$

If there are n trees of the RF model, the importance value of the feature j, $VIM_j^{(\text{Gini})}$, is expressed as

$$VIM_j^{(\text{Gini})} = \sum_{i=1}^{n} VIM_{ij}^{(\text{Gini})}. \tag{6}$$

Finally, all the importance scores normalized are obtained:

$$VIM_j = \frac{VIM_j}{\sum_{i=1}^{c} VIM_i}. \tag{7}$$

TABLE 3: The characteristics of five damage states.

Damage degrees	Characteristics
No damage	Load-bearing and non-load-bearing components are intact, or individual load-bearing components are slightly damaged and can be used without repair
Slightly damaged	Visible cracks appear in individual load-bearing components; non-load-bearing components have obvious cracks; can be used without repair or repair
Moderately damaged	Most load-bearing members have slight cracks; some have obvious cracks; some nonbearing members are seriously damaged; can be used after general repair
Seriously damaged	Most of the load-bearing members are seriously damaged; nonbearing members are partially collapsed; the repair is difficult
Completely damaged	Most of the load-bearing components are severely damaged; the structure tends to collapse or have collapsed; no repair is possible, and there is a need for reconstruction

The average accuracy (mean scores) of the classification of the random forest algorithm is 0.8304, and the standard deviation of random forest classifier is 0.0124. This accuracy is greatly improved compared with the classification accuracy of the logistic regression model, 0.7879, with the same parameters. The importance of different factors in girder bridge and arch bridge seismic damage assessment is presented in Figure 2. The range is between 0.0 (min) and 1.0 (max) for the two types of bridges. This is normalized and the sum of all features equals 1.0. During the entire RF model experiments, three experiments were selected randomly. The order of the features of the three experiments is the same, and it can be seen that the results of each time are almost the same. Figure 2 also shows the results of three experiments. The I–IX values on the abscissa represent nine features, and the ordinate is the importance value of the features. This proves that the RF algorithm can obtain a suitable evaluation of the problem of feature correlation [15].

4. Assessment Model

Seven features were selected as the variables of the girder bridge and arch bridge assessment models, respectively (Table 4). The choice of the input parameters depended on the importance of the priority, preferring more important parameters. The importances of structural types and bridge linearity were 0.014 and 0.027 of the girder bridge model. The importances of the foundation types and bridge liners were 0.004 and 0.031 for the arch bridge. The features mentioned above were not selected because of their low importance.

The Wenchuan earthquake had several characteristics that were higher than other huge earthquakes: intensity, scope of impact, and level of data collection. Therefore, there were 1525 girder bridges and 590 arch bridges of the Wenchuan earthquake in 2008 selected as the data set. The samples were preprocessed by the openpyxl function of the Anaconda Navigator environment. In the girder bridges model, there were 1300 bridges as the training set and 225 bridges as the testing set. In the arch bridges model, there were 400 bridges as the training set and 190 bridges as the testing set.

The ANN consists of an input layer, multiple hidden layers, and an output layer. Once the input data are given to the ANN, the output values are computed sequentially along the layers of the network. At each layer, the input vector comprising the output values of each unit in the layer below is multiplied by the weight vector for each unit in the current layer to produce the weighted sum. Then, a nonlinear function, such as a sigmoid, hyperbolic tangent, or rectified linear unit (ReLU), is applied to the weighted sum to compute the output values of the layer. The computation in each layer transforms the representations in the layer below into slightly more abstract representations. Based on the types of layers used in ANN and the corresponding learning method, ANN can be classified into multilayer perceptrons, which are based on the feed-forward neural network (FFNN), Stacked AutoEncoders (SAEs), or deep belief networks. For an intricate problem, the method can solve the problem well when it has 5 to 20 layers [40]. A five-layer ANN was decided due to the data set of the Wenchuan earthquake. The number of neurons in the middle layers was selected to obtain suitable and satisfactory results [41]. In order to obtain these, the running process started from 10, 3, and 2, respectively. The processes were repeated for more neurons. Through training, it was finally decided to take 40, 20, and 5 neurons as the number of neurons in the middle layers for decreasing the difficulty and training time of the method. There are several ways of controlling the training of ANN to prevent overfitting in the training phase. The most common form of regularization, L2 regularization, was chosen. Using the gradient descent parameter update, L2 regularization signifies that every weight will be decayed linearly towards zero. The hyperparameters were acquired as presented in Table 5.

The moving average model, adaptive moment estimation (Adam), and small batch gradient descent were selected as the optimization algorithms of the ANN model. The Adam method addressed problems in large data sets and high-dimensional parameter spaces [42]. It could overcome the shortcomings of random gradient descent and maintain a single learning rate to update ownership, and the learning rate did not change during the training process. It designed an independent adaptive learning rate for the parameters. The mini-batch gradient descent can overcome the short-comings of batch gradient descent and random gradient descent [43] by dividing the data into some training pools and update the parameters according to the pool. Therefore, choosing the appropriate training pool size can achieve the
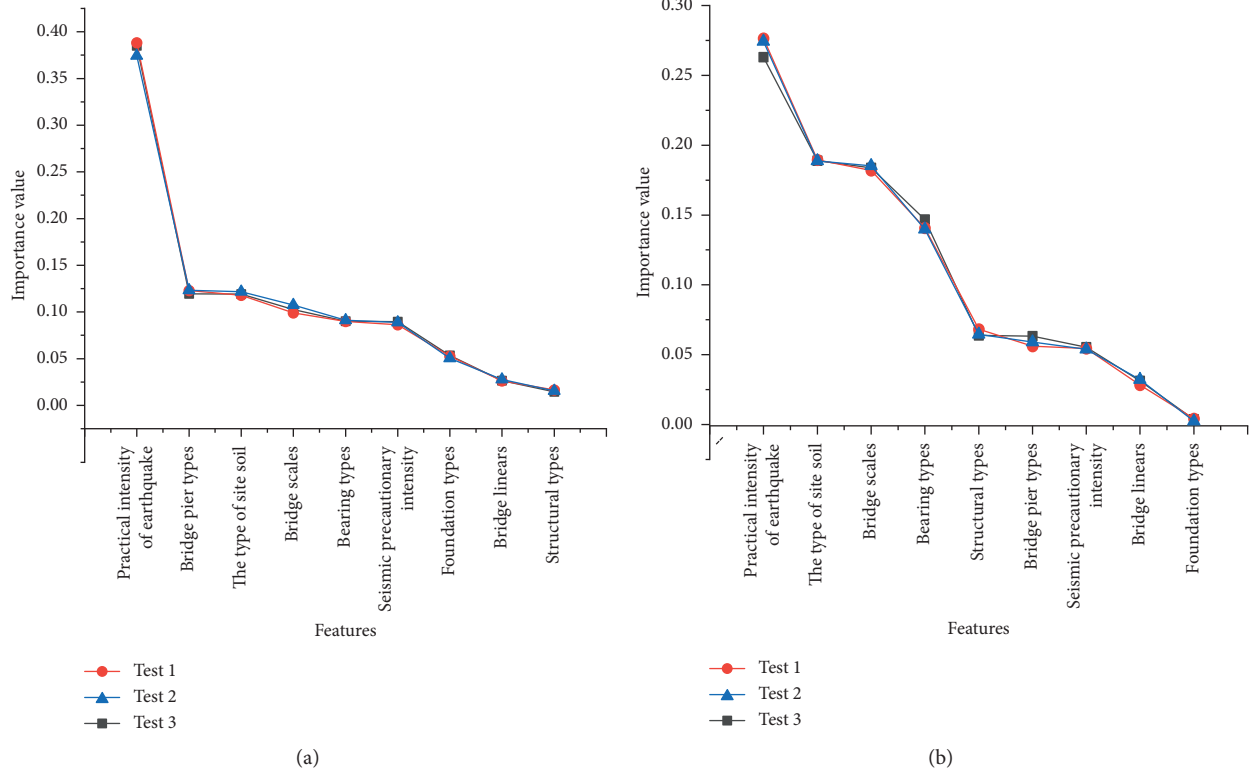
(a)

(b)

FIGURE 2: Processing of the girder bridge and arch bridge in random forest models: (a) girder bridge; (b) arch bridge.

TABLE 4: Selected features of the girder bridge and arch bridge.

Girder bridge	Arch bridge
Practical intensity of earthquakes	Practical intensity of earthquakes
Seismic precautionary intensity	Seismic precautionary intensity
The type of site soil	The type of site soil
Bridge pier types	Bridge pier types
Bridge scales	Bridge scales
Bearing types	Bearing types
Foundation types	Structural types

TABLE 5: Hyperparameters of the girder bridge and arch bridge models.

Hyper parameters	Mini-batch	Basic learning rate	Decay rate of the learning rate	L2	Decay rate of the moving average
Number	16	0.8	0.98	0.0001	0.99

purpose of algorithm optimization, less computation, faster calculation, improved proficiency, and accelerated convergence [44] and cannot effectively control the data of turbulence and gradient descent. The number of samples of this study was no more than 2000. Therefore, 16 bridges were decided upon for the experimental pool. The moving average model is designed to avoid mutations as the process of parameters updating [45]. This can improve the accuracy of

the ANN model on the test set to a certain extent. This is achieved by the exponential moving average function in the TensorFlow framework [46], which maintains a shadow variable for each variable. The initial value of the shadow variable is the initial value of the corresponding variable, and the values of the shadow variables (w and b) are updated. The decay rate determines the update speed of the model. The greater the attenuation, the greater the proportion of shadow variables.

The TensorFlow framework [46] was used for the model. The forward propagation, structure of the network, and initial weights were decided. The normal distribution and the ReLU function [40] were chosen as the weight generating function and the activation function, respectively. The ReLU function was applied in the second and third layers. It is slightly faster to compute than other activation functions, and gradient descent does not get stuck on plateaus as much when compared to the logistic function or the hyperbolic tangent function that usually saturates at 1. The fourth layer and the fifth layer were processed as the linear regression. The Adam technique was chosen as the back-propagation method. The mean square error loss function was chosen because of the function usually being applied with the ReLU activation function.

5. Results

The results of the model were compared with those of the linear regression model based on the Wenchuan

earthquake in 2008, and equation (8) presents the re- gression equation (5):

$$\ln Y = \ln\left(c \prod_{i,j=1}^{n} a_{ij}^{X_{ij}} \right) = \ln c + \sum_{i,j=1}^{n} X_{ij} \ln a_{ij}, \qquad (8)$$

where Y is the damage index of the bridges, corresponding to five damage levels, separately. The indexes are as follows from no damage to completely damaged: $0.00 \leq Y < 0.10$, $0.10 \leq Y < 0.30$, $0.30 \leq Y < 0.55$, $0.55 \leq Y < 0.85$, and $0.85 \leq Y < 1.00$; c is the constant coefficient; and a_{ij} are the regression coefficients in the j-th subclass of the i-th class in the identified classification via Statistical Product and Service Solutions software (SPSS). Because of the collinearity problem between the independent variables, Yu selected one of each feature to set an initial coefficient and then sub- tracted the coefficient from the dependent variable [5]; x_{ij} is the value of the parameter of the j-th subclass in the i-th class of the bridge, the bridge meets the set parameter value of 1, and the nonconformity is 0. Table 6 presents the comparative results of the girder bridges and arch bridges between the ANN model and the linear regression model. In actual emergency rescue, it is acceptable to have a difference be- tween the actual value and the predicted value (one level). However, if the predicted result differs from the actual value by two levels or even more than two levels, it will affect the decision of the relevant government institution. The results of the study show that the optimization algorithms have good performance in terms of improving running time. The precision of the ANN models (92.3% and 88.5%) is far greater than those in the linear regression models (71.9% and 71.5%) of an equal level. Similarly, the proportion of one level difference (5.6% and 8.2%) is much smaller than the linear model (26.4% and 27.6%). The prediction precision of the girder bridge is higher than the arch bridge for the ANN models, and the results of the two types of bridges of the linear regression model are similar.

There were 40 bridges including girder bridges and arch bridges in the Tangshan earthquake in 1976 which were chosen as the validation set. The type of site soil was deleted for the occurrence of sand liquefaction phenomena. Since this earthquake happened more than 40 years ago, the specification has been updated for generations. Therefore, the seismic precautionary intensity and the bridge scale are deleted because they are not applicable. Table 7 shows the data of 40 bridges and the prediction results. Among them, the results of a total of nine bridges are different from the true value. However, all exhibit one-level difference. The result of the four bridges is that they were seriously damaged, but the true values were moderately damaged; the other five bridges resulted to be slightly damaged, with the true value of the four bridges being moderately damaged and the other being no damage. The probability that the damage of the simply supported girder bridge is different from the true value is 5/19 (23.3%), that of the continuous girder bridge is 2/5 (40.0%), and the arch bridge is 2/16 (12.5%).

TABLE 6: The comparison between the ANN models and the linear regression models of the girder bridges and arch bridges (%). The results demonstrate the difference between the prediction value and the actual value of level zero, level one, and the other levels.

Differences	ANN model		Linear regression model	
	Girder bridges	Arch bridges	Girder bridges	Arch bridges
Equal	92.3	88.5	71.9	71.5
One level	5.6	8.2	26.4	27.6
≥two levels	2.1	3.3	1.7	0.9

6. Discussions

6.1. Importance of Different Features. In this study, the bridge data of the Wenchuan earthquake were used to detect the importance of different influencing factors of the two bridges applying the random forest algorithm. When ana- lyzing a single bridge or its components, it is possible to analyze the importance of the influencing factors and take all factors into account to get better results [19]. The main purpose of this study is to analyze a large number of bridges in a certain area, so it is meaningful to conduct feature importance analysis. This fully proved the importance of the practical intensity of earthquakes, seismic precautionary intensity, the type of site soil, bridge pier types, bridge scales, and bearing types of the girder bridges and arch bridges. The importance of the six factors is more than 90% for the two bridges. Therefore, the six features mentioned above were first as the input variables. Then, the seventh feature for each of the two bridges will be discussed. The orders of impor- tance of the characteristics of the two bridges are similar. This is because, even though the type and construction process of the bridge are different, the design principles of the bridge are the same, the components are similar, and the earthquake is the same, so the results are similar.

The foundation type is ranked seventh for the girder bridge and is ranked ninth for the arch bridge. The foun- dation type was used for the girder bridge model but not for the arch bridge model because the feature importance is 5% in the former and 0.4% in the latter. Besides, the results accord with the experience of some researchers. Arch structures are very sensitive to the deformations and the strength of foundations, especially in the case of earthquake (horizontal direction) load. The foundation type is vital to the seismic damage of an arch bridge. However, the result of the RF model shows that this is not important, which is the shortcoming of the model. There are many reasons for this phenomenon: (1) the more classes are distinguished by a feature, the more significant the feature is [15]. There are only two types of foundation; (2) the RF model is a black box, and the results might be different from the experience of experts, which is one of the biggest flaws of the model; (3) the results obtained by this model are of relative importance value and are the result of several feature comparisons and not the importance of independence. The structural type is

TABLE 7: The data of the 40 bridges and the comparison of the true value and prediction results by the ANN model for the Tangshan earthquake in 1976 (the arch bridges are specially marked and the girder bridges are not marked. "Intensity" means the practical intensity).

	Structural type	Bridge pier	Foundation	Bearing	Intensity	ANN	True value
1	Simply supported	Bent	Deep	Other	X	Seriously	Moderately
2	Simply supported	Masonary solid	Deep	Other	X	Seriously	Moderately
3	Simply supported	Masonary solid	Deep	Other	X	Seriously	Moderately
4	Simply supported	Thin-wall	Deep	Other	X	Seriously	Seriously
5	Continuous	Bent	Deep	Other	IX	Seriously	Moderately
6	Simply supported	Masonary solid	Deep	Other	IX	Moderately	Moderately
7	Simply supported	Bent	Deep	Other	IX	Moderately	Moderately
8	Continuous	Bent	Deep	Other	IX	Moderately	Moderately
9	Continuous	Bent	Deep	Other	VIII	Moderately	Moderately
10	Continuous	Bent	Deep	Other	VIII	Seriously	Seriously
11	Continuous	Bent	Deep	Other	VIII	Moderately	Moderately
12	Continuous	Bent	Deep	Other	VIII	Moderately	Moderately
13	Continuous	Bent	Deep	Other	VIII	Moderately	Moderately
14	Simply supported	Bent	Deep	Other	VIII	Moderately	Moderately
15	Simply supported	Bent	Deep	Other	VIII	Moderately	Moderately
16	Continuous	Bent	Deep	Other	VIII	Moderately	Moderately
17	Continuous	Bent	Deep	Other	VIII	Moderately	Moderately
18	Continuous	Bent	Deep	Other	VIII	Seriously	Seriously
19	Continuous	Masonary solid	Deep	Other	VIII	Moderately	Moderately
20	Simply supported	Masonary solid	Deep	Other	VIII	Moderately	Moderately
21	Simply supported	Masonary solid	Deep	Other	VIII	Moderately	Moderately
22	Continuous	Bent	Deep	Other	VIII	Slightly	Slightly
23	Simply supported	Bent	Deep	Other	VII	Slightly	Moderately
24	Simply supported	Bent	Deep	Other	VII	Slightly	No
25	Simply supported	Bent	Deep	Other	VII	Slightly	No
26	Simply supported	Bent	Deep	Other	VII	Moderately	Moderately
27	Simply supported	Bent	Deep	Other	VII	Moderately	Moderately
28	Simply supported	Bent	Deep	Other	VII	Slightly	Slightly
29	Continuous	Bent	Deep	Other	VII	Slightly	Slightly
30	Simply supported	Bent	Deep	Other	VII	Slightly	Slightly
31	Continuous	Bent	Deep	Other	VII	Slightly	Slightly
32	Simply supported	Bent	Deep	Other	VII	Slightly	Moderately
33	Continuous	Bent	Deep	Other	VII	Slightly	Slightly
34	Simply supported	Bent	Deep	Other	VII	No	No
35	Continuous	Bent	Deep	Other	VII	Slightly	No
36	Deck type (arch)	No	Deep	No	VIII	Slightly	Slightly
37	Deck type (arch)	No	Deep	No	VIII	Slightly	Moderately
38	Deck type (arch)	Bent	Deep	No	VIII	Slightly	Slightly
39	Deck type (arch)	No	Deep	No	VIII	Slightly	Moderately
40	Deck type (arch)	No	Deep	No	VIII	Slightly	Slightly

ranked ninth for the girder bridge (1%) and is ranked fifth for the arch bridge (6%). Therefore, the structural type was the factor for the arch bridge model but not for the girder bridge model. In summary, the features selected by the RF experiments are consistent with those used by other scholars to study the earthquake damage of bridges [11]. There were seven features for the two types of bridges, respectively. It can also be seen from these results that it is still meaningful to do this work. If the importance of these factors is not analyzed, less important factors are taken into account. This will greatly affect the emergency rescue time, thus increasing economic losses and casualties. At the same time, this study only removed two factors that have less impact on the two bridges. In practical applications, if a bridge in an earthquake has some factors that cannot be obtained due to some reasons, such as age, data loss, and other human factors, the corresponding influencing factors can be deleted and the model can be modified in a short time.

The RF model performs better than the other ensemble algorithms [17]. The reason for this may be that it works better with categorical features than the other methods. Also, since it uses implicit feature selection, overfitting was reduced significantly. Using logistic regression is a convenient probability score for observations. However, it does not perform well when the feature space is large, and it does not handle a large number of categorical features well. It also solely relies on transformations for nonlinear features. Using a Support Vector Machine (SVM) model, we would be able to handle a large feature space with nonlinear feature interactions without relying on the entire dataset. However, this is not very good for a large number of observations. Nevertheless, it can sometimes be difficult to find an appropriate kernel.

6.2. Assessment Model of Bridge Damage. This paper developed a bridge seismic damage state evaluation method based on previous work. The accuracy is the sum of the predicted values, and the true values differ by one or the same probability. The accuracy of the Wenchuan earthquake test is as high as 97.9%, while the accuracy of the Tangshan earthquake test is slightly reduced at 95%. The data in the training set come from the Wenchuan earthquake, so the expression on the Wenchuan earthquake test set is better. In general, this model can be used in the assessment of bridge damage in other areas, and the accuracy is acceptable. The training effect on the arch bridge is not as good as that of the girder bridge because the training set of the arch bridge is less than the girder bridge. When the predicted value is inconsistent with the true value, there is more chance of moderate damage because it occurs most frequently in the entire training set. The results of the assessment of the IX and X degrees of the practical intensity of earthquakes are always lower than the actual damage. An earthquake with a practical intensity greater than the VIII degree has a greater destructive power, and the factors affecting bridge damage are more complicated, such as earthquake secondary disasters, the bridge being been damaged before the earthquake, geological impact, and scouring effect [5]. Even if these factors have a certain impact on the bridge damage, the model does not consider these factors. This is because these factors are very complicated. Secondary disasters are difficult to obtain in the few minutes after the earthquake, and the current technology cannot accurately predict this in advance. Bridges may be eroded before the earthquake, such as by construction defects, or they are sometimes not repaired after damage from natural disasters. These conditions can only rely on daily monitoring and relevant departments should monitor the status of important bridges in time. Geological factors cannot be obtained in a short period of time, and some of them may even need to be investigated after the earthquake. The scouring effect is not considered in this study, which is one of the reasons leading to the reduction of the accuracy of the model. Erosion may cause reinforcement corrosion, spalling of concrete, and damage to foundations and platforms. However, not all the samples selected in this study were affected by scouring, so they were not considered. Hence, these factors were neglected.

The accuracy of the two bridges in the prediction of the equal level of failure and phase difference is much higher than that of the linear model [5]. The accuracy of being two levels greater or equal level is slightly lower than the linear model, but both are between 0% and 4%, which is within the acceptable range in emergency work [5]. In summary, the performance of the ANN model is better than the linear model. The reason for the small difference in accuracy between the two bridges of the linear model is that the regression technique initially has some assumptions that increase the accuracy. The ANN model does not require any assumptions throughout the process of establishment [47]. The results of the linear model must be fully calculated before they can be obtained. The ANN model can improve the training speed by setting the training rounds and steps according to the accuracy and the requirements of the specific situation, because it is more convenient and faster than the linear model.

In the practical application of the whole method, there are still some problems and challenges. (1) Since it is a rapid assessment, in addition to the speed of the model calculation, it is necessary to collect data faster. This is very difficult in practice and requires extensive experience from experts, scholars, and engineers. (2) When a bridge is less damaged, this method needs to be combined with experts and experienced decision-makers in order to improve the performance of the ANN model. (3) In practice, it is necessary to combine this method with the road to conducting an overall assessment of the road network to obtain an optimal rescue path.

6.3. Main Contributions and Significance. The method has some significance in engineering and science. The main contributions and significance of this study are as follows:

(1) The proposed method selects suitable and easily available input features based on the RF ensemble model rather than choosing features directly according to expert experiences [5] or statistical methods [11].

(2) This study uses some optimization algorithms to improve the performance of the ANN model, and the accuracy, rationality, and speed are better than the traditional back-propagation neural network [40].

(3) This study shows that an estimation of the damage states of many bridges in a few minutes can be achieved, while previous studies usually evaluate the performance of one bridge [21, 22] or some components [19].

(4) This method can be used under both preearthquake and postearthquake conditions. When it is used before an earthquake, the practical intensity of earthquakes can be obtained according to the historical maximum earthquake or seismological predictions. When the government conducts disaster prevention and mitigation planning, the formulation of relevant laws and regulations, bridge seismic damage assessment can be carried out. This can help the organization to judge the damage of bridges in the whole region on a macroscopic basis, to plan and establish the lifeline facilities in advance, and to prevent the traffic capacity of the traffic network from being affected by the damage of the bridge after the earthquake. When evaluating after the earthquake, it is possible to quickly assess the damage of the bridge in the entire earthquake zone and select the optimal path for rescue to save valuable rescue time due to the impassibility of the bridge.

7. Conclusions

The intention of this research is to propose a new model using the RF algorithm and ANN method for the evaluation of bridge

damage states. The features of girder bridges and arch bridges are assessed using the RF algorithm. The practical intensity of earthquakes, seismic precautionary intensity, type of site, soil, bridge pier type, and bridge scales are very important to the damage of the two bridges. The bearing types contribute more than the foundation types of the girder bridge, and the opposite is presented for the arch bridge. The different features are selected as the input variables in the ANN model through the results of the assessment of the feature importance. The output variables are the five damage states.

The results show that the RF model has good stability and accuracy, the accuracy and calculation speed of the ANN model are better than the linear model, and the model still performs well for other earthquakes. The proposed method of this study can serve as a tool for disaster prevention and mitigation planning, daily bridge maintenance inspections, and decision-making for postearthquake emergency response projects.

The limitations and future works of the method are as follows. (1) There are only two types of bridges in the study: girder bridges and arch bridges. Other bridges should be further investigated to make the method more applicable, such as suspension bridges and cable-stayed bridges. (2) Some features are neglected for different reasons, which will affect the applicability and accuracy of the method. The features ought to be further expanded upon to meet engineering needs. (3) The data come only from Wenchuan earthquake and Tangshan earthquake. The existing bridges in the two earthquakes were used for many years, and the performance deterioration of the materials due to corrosion and fatigue would decrease the load-bearing capacity and the ductility of the structures, consequently reducing the seismic performance and affecting the damage analysis results of the bridges. This issue should also be investigated in the future to expand the available data. (4) The RF model is a black box operation and will be influenced by the data, which might reduce the accuracy of the importance value. This issue also can be overcome by expanding the data set in the future. The model also can be improved by acting on hyperparameters or changing its architecture. For a more comprehensive analysis, additional study is needed to extend the earthquake data and determine suitable features of bridge damage.

Data Availability

The data used to support the findings of this study belong to the Ministry of Transport of the People's Republic of China and Department of Transportation of Sichuan Province. The data can be made available from the first author upon request.

Conflicts of Interest

The authors declare that there are no conflicts of interest regarding the publication of this paper.

Acknowledgments

References

[1] T. J. Carey, H. B. Mason, A. R. Barbosa, and M. H. Scott, "Multihazard earthquake and tsunami effects on soil–foundation–bridge systems," *Journal of Bridge Engineering*, vol. 24, no. 4, Article ID 04019004, 2019.

[2] E. Isik, M. F. Isik, and M. A. Bulbul, "Web based evaluation of earthquake damages for reinforced concrete buildings," *Earthquakes and Structures*, vol. 13, no. 4, pp. 387–396, 2017.

[3] T. K. Šipoš and M. Hadzima-Nyarko, "Rapid seismic risk assessment," *International Journal of Disaster Risk Reduction*, vol. 24, pp. 348–360, 2017.

[4] E. Isik, "Consistency of the rapid assessment method for reinforced concrete buildings," *Earthquakes and Structures*, vol. 11, no. 5, pp. 873–885, 2016.

[5] F. Yu, *Methodology for Bridge Seismic Damage Estimation Based on Wenchuan Earthquake*, Institute of Engineering Mechanics, China Earthquake Administration, Harbin, China, 2018.

[6] A. Guo, Z. Liu, S. Li, and H. Li, "Seismic performance assessment of highway bridge networks considering post-disaster traffic demand of a transportation system in emergency conditions," *Structure and Infrastructure Engineering*, vol. 13, no. 12, pp. 1523–1537, 2017.

[7] R. Twumasi-Boakye and J. O. Sobanjo, "Resilience of regional transportation networks subjected to hazard-induced bridge damages," *Journal of Transportation Engineering, Part A: Systems*, vol. 144, no. 10, Article ID 04018062, 2018.

[8] Y. Dong, D. M. Frangopol, and D. Saydam, "Sustainability of highway bridge networks under seismic hazard," *Journal of Earthquake Engineering*, vol. 18, no. 1, pp. 41–66, 2014.

[9] Z. Peng, Q. Guojin, and W. Yihuan, "Risk assessment system for oil and gas pipelines," *Energies*, vol. 12, pp. 1–21, 2019.

[10] W. Chen, Z. Sun, and J. Han, "Landslide susceptibility modeling using integrated ensemble weights of evidence with logistic regression and random forest models," *Applied Sciences*, vol. 9, no. 1, p. 171, 2019.

[11] S. Mangalathu, G. Heo, and J.-S. Jeon, "Artificial neural network based multi-dimensional fragility development of skewed concrete bridge classes," *Engineering Structures*, vol. 162, pp. 166–176, 2018.

[12] W. Chen, A. Shirzadi, H. Shahabi et al., "A novel hybrid artificial intelligence approach based on the rotation forest ensemble and naïve Bayes tree classifiers for a landslide susceptibility assessment in Langao County, China," *Geomatics, Natural Hazards and Risk*, vol. 8, no. 2, pp. 1955–1977, 2017.

[13] H.-Y. Hu, Y.-C. Lee, T.-M. Yen, and C.-H. Tsai, "Using BPNN and DEMATEL to modify importance-performance analysis model—a study of the computer industry," *Expert Systems with Applications*, vol. 36, no. 6, pp. 9969–9979, 2009.

[14] S. Park and J. Kim, "Landslide susceptibility mapping based on random forest and boosted regression tree models, and a comparison of their performance," *Applied Sciences*, vol. 9, no. 5, p. 942, 2019.

[15] F. Provost, C. Hibert, and J.-P. Malet, "Automatic classification of endogenous landslide seismicity using the Random

Forest supervised classifier," *Geophysical Research Letters*, vol. 44, no. 1, pp. 113–120, 2017.

[16] A. Altmann, L. Toloşi, O. Sander, and T. Lengauer, "Permutation importance: a corrected feature importance measure," *Bioinformatics*, vol. 26, no. 10, pp. 1340–1347, 2010.

[17] H. Jia, J. Lin, and J. Liu, "An earthquake fatalities assessment method based on feature importance with deep learning and random forest models," *Sustainability*, vol. 11, no. 10, p. 2727, 2019.

[18] S. P. Stefanidou and A. J. Kappos, "Methodology for the development of bridge-specific fragility curves," *Earthquake Engineering & Structural Dynamics*, vol. 46, no. 1, pp. 73–93, 2017.

[19] P.-j. Chun, H. Yamashita, and S. Furukawa, "Bridge damage severity quantification using multipoint acceleration measurement and artificial neural networks," *Shock and Vibration*, vol. 2015, Article ID 789384, 11 pages, 2015.

[20] F. U. Ashraf and P. A. Johnson, "Assessing relative risk for the failure modes of a bridge scour countermeasure," *Journal of Bridge Engineering*, vol. 21, no. 5, Article ID 04016010, 2016.

[21] S. Mustafa and Y. Matsumoto, "Bayesian model updating and its limitations for detecting local damage of an existing Truss bridge," *Journal of Bridge Engineering*, vol. 22, no. 7, Article ID 04017019, 2017.

[22] B. Zakeri and F. Zareian, "Bridge design framework for target seismic loss," *Journal of Bridge Engineering*, vol. 22, no. 10, Article ID 04017061, 2017.

[23] S. Mangalathu, F. Soleimani, and J.-S. Jeon, "Bridge classes for regional seismic risk assessment: improving HAZUS models," *Engineering Structures*, vol. 148, pp. 755–766, 2017.

[24] F. Franceschini and M. Galetto, "A new approach for evaluation of risk priorities of failure modes in FMEA," *International Journal of Production Research*, vol. 39, no. 13, pp. 2991–3002, 2001.

[25] L. I. N. Qingli, L. I. N. Junqi, and L. I. U. Jinlong, "A study on the fragility of highway bridges in the Wenchuan earthquake," *Journal of Vibration and Shock*, vol. 36, no. 4, pp. 110–126, 2017.

[26] N. D. Lagaros and M. Fragiadakis, "Fragility assessment of steel frames using neural networks," *Earthquake Spectra*, vol. 23, no. 4, pp. 735–752, 2007.

[27] C. C. Mitropoulou and M. Papadrakakis, "Developing fragility curves based on neural network IDA predictions," *Engineering Structures*, vol. 33, no. 12, pp. 3409–3421, 2011.

[28] K. Peng, Z. Liu, Q. Zou, Q. Wu, and J. Zhou, "Mechanical property of granite from different buried depths under uniaxial compression and dynamic impact: an energy-based investigation," *Powder Technology*, vol. 362, pp. 729–744, 2020.

[29] K. Peng, J. Zhou, Q. Zou, and X. Song, "Effect of loading frequency on the deformation behaviours of sandstones subjected to cyclic loads and its underlying mechanism," *International Journal of Fatigue*, vol. 131, Article ID 105349, 2020.

[30] K. Peng, J. Zhou, Q. Zou, and F. Yan, "Deformation characteristics of sandstones during cyclic loading and unloading with varying lower limits of stress under different confining pressures," *International Journal of Fatigue*, vol. 127, pp. 82–100, 2019.

[31] S. Soltanieh, M. M. Memarpour, and F. Kilanehei, "Performance assessment of bridge-soil-foundation system with irregular configuration considering ground motion directionality effects," *Soil Dynamics and Earthquake Engineering*, vol. 118, pp. 19–34, 2019.

[32] K. Peng, J. Zhou, Q. Zou, J. Zhang, and F. Wu, "Effects of stress lower limit during cyclic loading and unloading on deformation characteristics of sandstones," *Construction and Building Materials*, vol. 217, pp. 202–215, 2019.

[33] K. Peng, Y. Wang, Q. Zou, Z. Liu, and J. Mou, "Effect of crack angles on energy characteristics of sandstones under a complex stress path," *Engineering Fracture Mechanics*, vol. 218, Article ID 106577, 2019.

[34] P. Kang, L. Zhaopeng, Z. Quanle, Z. Zhenyu, and Z. Jiaqi, "Static and dynamic mechanical properties of granite from various burial depths," *Rock Mechanics and Rock Engineering*, vol. 52, no. 10, pp. 3545–3566, 2019.

[35] Ministry of Transport of the People's Republic of China, *General Specifications for Design of Highway Bridges and Culverts*, Ministry of Transport of the People's Republic of China, Beijing, China, 2015.

[36] J. M. Andrić and D. G. Lu, "Fuzzy methods for prediction of seismic resilience of bridges," *International Journal of Disaster Risk Reduction*, vol. 22, pp. 458–468, 2017.

[37] L. Breiman, "Random forests," *Machine Learning*, vol. 45, no. 1, pp. 5–32, 2001.

[38] G. O. Gutiérrez-Esparza, M. Vallejo-Allende, and J. Hernández-Torruco, "Classification of cyber-aggression cases applying machine learning," *Applied Sciences*, vol. 9, no. 9, Article ID 1828, 2019.

[39] B. H. Menze, B. M. Kelm, R. Masuch et al., "A comparison of random forest and its Gini importance with standard chemometric methods for the feature selection and classification of spectral data," *BMC Bioinformatics*, vol. 10, pp. 1–16, 2009.

[40] Y. Lecun, Y. Bengio, and G. Hinton, "Deep learning," *Nature*, vol. 521, no. 7553, pp. 436–444, 2015.

[41] H. Aghamohammadi, M. S. Mesgari, A. Mansourian, and D. Molaei, "Seismic human loss estimation for an earthquake disaster using neural network," *International Journal of Environmental Science and Technology*, vol. 10, no. 5, pp. 931–939, 2013.

[42] D. P. Kingma and J. lei Ba, "Adam: a method for stochastic optimization," in *Proceedings of the ICLR*, pp. 1–15, San Diego, CA, USA, May 2015.

[43] K. Gimpel, D. Das, and N. a. Smith, "Distributed asynchronous online learning for natural language processing," in *Proceedings of the Conference on Computational Natural Language Learning (CoNLL)*, pp. 213–222, Uppsala, Sweden, July 2010.

[44] G. Danner and M. Jelasity, "Fully distributed privacy preserving mini-batch gradient descent learning," in *Proceedings of the IFIP WG 61 International Conference on Distributed Applications & Interoperable Systems*, vol. 9038, pp. 30–44, France, July 2015.

[45] S. E. Said and D. A. Dickey, "Testing for unit roots in autoregressive-moving average models of unknown order," *Biometrika*, vol. 71, no. 3, pp. 599–607, 1984.

[46] M. Abadi, P. Barham, J. Chen et al., "TensorFlow: a system for large-scale machine learning," in *Proceedings of the 12th USENIX Symposium on Operating Systems Design and Implementation*, Savannah, GA, USA, November 2016.

[47] A. Ferreira, L. Bondi, L. Baroffio et al., "Data-driven feature characterization techniques for laser printer attribution," *IEEE Transactions on Information Forensics and Security*, vol. 12, no. 8, pp. 1860–1873, 2017.

Research Article

Prediction of the Strength of Rubberized Concrete by an Evolved Random Forest Model

Yuantian Sun (ID),[1] **Guichen Li** (ID),[1] **Junfei Zhang** (ID),[2] **and Deyu Qian** (ID)[1]

[1]*School of Mines, Key Laboratory of Deep Coal Resource Mining, Ministry of Education of China,*
 China University of Mining and Technology, Xuzhou 221116, China
[2]*Department of Civil, Environmental and Mining Engineering, The University of Western Australia, Perth 6009, Australia*

Correspondence should be addressed to Guichen Li; liguichen@cumt.edu.cn and Junfei Zhang;
junfeizhang2010@163.com

Rubberized concrete (RC) has attracted more attention these years as it is an economical and environmental-friendly construction material. Normally, the uniaxial compressive strength (UCS) of RC needs to be evaluated before application. In this study, an evolutionary random forest model (BRF) combining random forest (RF) and beetle antennae search (BAS) algorithms was proposed, which can be used for establishing the relationship between UCS of RC and its key variables. A total number of 138 cases were collected from the literature to develop and validate the BRF model. The results showed that the BAS can tune the RF effectively, and therefore, the hyperparameters of RF were obtained. The proposed BRF model can accurately predict the UCS of RC with a high correlation coefficient (0.96). Furthermore, the variable importance was determined, and the results showed that the age of RC is the most significant variable, followed by water-cement ratio, fine rubber aggregate, coarse rubber aggregate, and coarse aggregate. This study provides a new method to access the strength of RC and can efficiently guide the design of RC in practice.

1. Introduction

Concrete has been the most widely used construction material in civil engineering, and its demand still increases quickly due to the rapid growth in urbanization and industrialization. Reducing costs and maximizing the strength and durability of concrete are quite challenging issues [1]. Hence, recycled aggregate concrete (RAC) containing some recycling materials, such as plastic materials [2, 3], construction and demolition (C&D) wastes [4, 5], and waste tire rubber [6], has been a hot research area. Given the rapid growth of tire rubber waste and its harmful effect on the environment, using rubber as a substitute in concrete not only contributes to economic growth but also benefits the environment [7]. Considering its ductility and strain behavior, rubber is normally utilized as fine aggregates (FAs) and coarse aggregates (CAs) in concrete, and therefore, the new cementitious composites, namely, rubberized concrete (RC), can be applied in civil engineering.

RC has some special advantages such as reducing CO_2 emissions and decreasing construction costs, and therefore, it

attracts many concerns of scholars recently [8–11]. To evaluate the applicability of RC, some mechanical properties including compressive strength and elastic modulus have been studied [12–15]. Moreover, the uniaxial compressive strength (UCS) is the key indicator that has been commonly used for assessing the strength property of RC. Normally, with the increase in the content of rubber in RC, the compressive strength decreases. Some models considering the laboratory tests or compiled databases of previous studies have been proposed to predict the UCS of RC [16–18]. However, due to the limitations of input parameters and the small number of obtained results, these models are not generalizable and not convenient for application. Consequently, systematical investigations are necessary to evaluate the compressive strength of RC by more economic and efficient techniques as per a compressive database including various input parameters.

Nowadays, machine learning methods are considerably used for the prediction of the mechanical properties of cementitious materials [19–21]. The estimation of the mechanical strength of RAC has also been considered. For

example, the multilinear and nonlinear regression models were proposed and used for evaluating the UCS of RAC [22]. The artificial neural network (ANN) methods were applied to assess the strength of RAC [23–25]. Genetic programming (GA) methods were also introduced for nonlinear regression in predicting mechanical properties of RAC [26, 27]. However, to the authors' knowledge, there were no reports of the prediction of RC by artificial intelligence approaches. In addition, though the mentioned machine learning algorithms (ANN, GA, etc.) were used for prediction in concrete, they still had some limitations such as lower efficiency, time-consuming, and indefinite structures. Therefore, more robust and simple machine learning models need to be proposed and utilized in predicting the compressive strength of RC. Nowadays, the random forest (RF) approach has been employed in predicting the mechanical parameters of concrete due to its excellent performance on nonlinear regression and classification [28, 29]. However, no relative studies to date used RF to predict the strength of RC. It should be pointed out that some hyperparameters still need to be optimized to reach its best predictive ability. In this paper, a high-efficiency global optimization algorithm called the beetle antennae search (BAS) algorithm was applied to obtain the best parameters of RF [30].

Therefore, a robust machine learning technique (evolved random forest, namely, BRF) was proposed for the evaluation of the UCS of RC. Several contributions to the literature are as follows:

(1) The random forest (RF) and beetle antennae search (BAS) algorithms were combined to form the BRF model

(2) The strength of rubberized concrete (RC) was, for the first time, predicted and analyzed considering 9 key influencing variables

(3) The variable importance that affected the UCS of RC was first revealed

The proposed method can be a fast tool for estimating the strength of RC and efficiently guide the design and application of RC in practice.

2. Materials and Methods

2.1. Model of Evolved Random Forest (BRF).
As mentioned above, the BRF is the combination of RF and BAS, in which the RF was applied to obtain the nonlinear relationship in datasets, while the BAS was used for hyperparameter tuning of RF. In this part, the RF and BAS were introduced as follows.

2.1.1. Random Forest (RF).
Random forest is a classification algorithm that employs an ensemble of classification trees, each of which is established by applying a bootstrap sample of the data [31]. For tree building, the variables are selected randomly as the candidate set of variables at each split. The other way is to use bagging which can combine unstable learners successfully. The random forest has outstanding performance in classification tasks such as strong robustness in terms of large feature sets, incorporation of interactions

among predictor variables, and high quality and free implementations [32]. The diagram of the structure of RF is shown in Figure 1. This method has been widely used for dealing with the questions of classification and regression in civil engineering.

2.1.2. Beetle Antennae Search (BAS).
BAS algorithm is proposed recently, which can be efficiently used for optimizing the global problems and has been used for selecting the optimum parameters of algorithms such as BPNN and SVM [33, 34]. It simulates the behavior of beetles that utilize two antennae to explore nearby areas randomly and turn to a higher concentration of odor. The flowchart of beetle antennae search algorithms is depicted in Figure 2.

2.2. Performance Validation and Evaluation Methods.
In this paper, the proposed model was trained and validated on the 70% dataset and tested on the other 30% dataset [21]. During the training and testing processes, all data were split randomly. In addition, the predictive effect on the dataset was assessed by the correlation coefficient (R) and root-mean-square error (RMSE), which were widely used in the previous literature. The relevant equations are as follows:

$$R = \frac{\sum_{i=1}^{N} \left(y_i^* - \overline{y^*}\right)\left(y_i - \overline{y}\right)}{\sqrt{\sum_{i=1}^{N} \left(y_i^* - \overline{y^*}\right)^2} \sqrt{\sum_{i=1}^{N} \left(y^i - \overline{y}\right)^2}},$$

$$\text{RMSE} = \sqrt{\frac{1}{N} \sum_{i=1}^{N} \left(y_i^* - y_i\right)^2}, \quad (1)$$

where N denotes the numbers in the collected dataset; y_i^* and y_i are the expected values and real values, respectively; and $\overline{y}$ and $\overline{y^*}$ indicate the mean predicted values and mean actual values, respectively.

Furthermore, to minimize the bias, a 10-fold cross-validation method was introduced [35]. Specifically, the samples in the training dataset were divided into 10 subsets. Then one of the 10 subsets was selected for validating the overall performance of the proposed model, while the other 9 subsets were applied to train. This process would be repeated for 10 times.

2.3. Procedures of Hyperparameter Tuning.
To obtain the best structure of RF, the hyperparameter tuning is necessary. In this paper, two key parameters (i.e., the number of the trees (tree_num) and the minimum required samples at a leaf node (min_sample_leaf) in RF) were tuned by BAS. By the described 10-folder cross-validation method, the 9 subsets as training sets were used for searching the ideal hyperparameters of RF by BAS for 50 times. The smallest RMSE in terms of the validation set can be chosen after 50 iterations, which represents the best RF model in this fold. Therefore, the best RF model and its corresponding optimum hyperparameters (tree_num and min_sample_leaf) were chosen after 10-folds. The performance of the RF model should be verified by evaluating the test set due to the possibility of
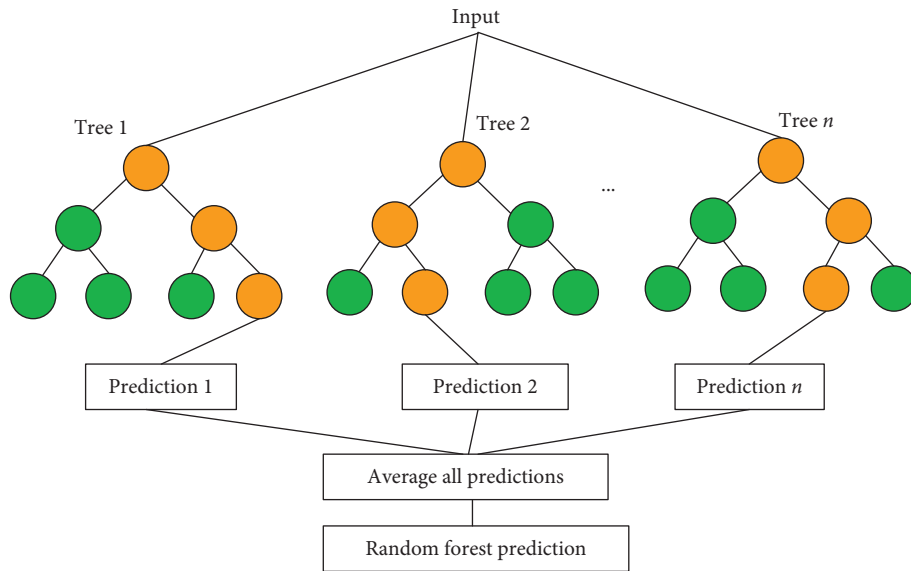
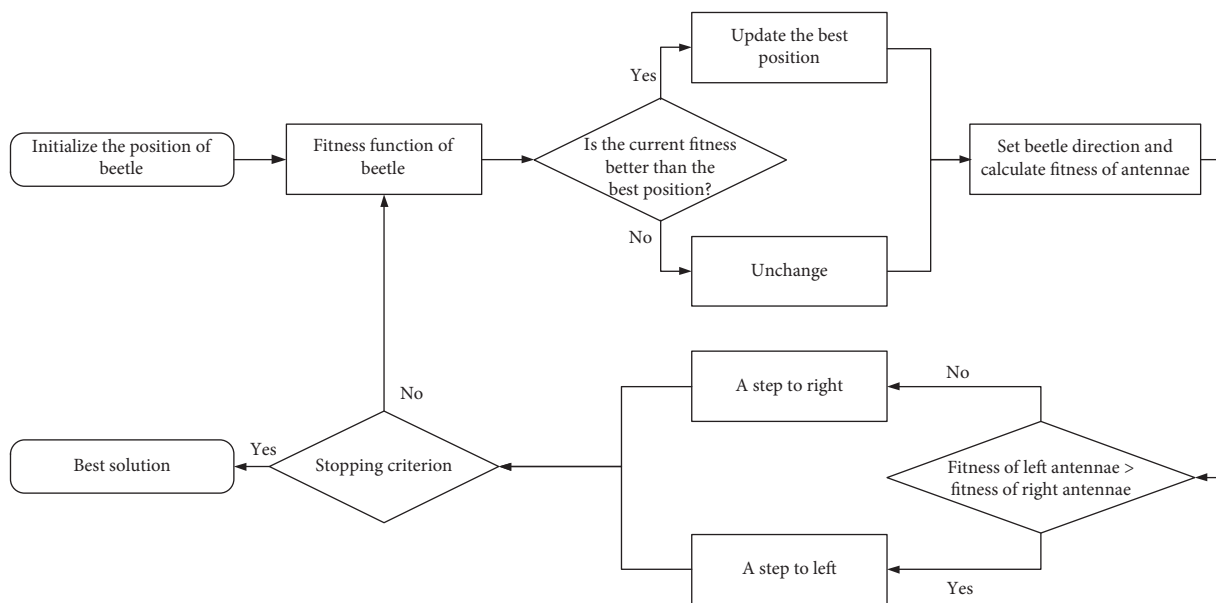FIGURE 1: General structure of the RF model.

FIGURE 2: The flowchart of beetle antennae search algorithm.

overfitting problems. The flowchart of hyperparameter tuning of RF by BAS in training and testing is shown in Figure 3.

2.4. Dataset Description. The dataset of RC was collected from the literature [13, 15, 18, 36–38], which was used for establishing and validating the BRF model for strength prediction. A total number of 138 valid samples with 9 key influencing variables were assembled in this study. Generally, depending on the different sizes of rubber, the crumb rubber is used for replacing the fine aggregate (FA) in concrete, while the tire chips are used for replacing

coarse aggregate (CA). The compressive strength normally decreased with different rates by replacing various contents of rubber and different rubber types. Therefore, it is necessary to distinguish the rubber into two types in RC, i.e., fine rubber aggregate (FRA) and coarse rubber aggregate (CRA). Moreover, the influencing variables and their description in statistics are given in Table 1. The main objectives are to predict the UCS of RC that is determined by its influencing variables. The relative importance of variables is to be further analyzed. To improve the efficiency of the model, the collected data were normalized into [0, 1]. According to the percentage split of the dataset, 97 samples were randomly chosen as the
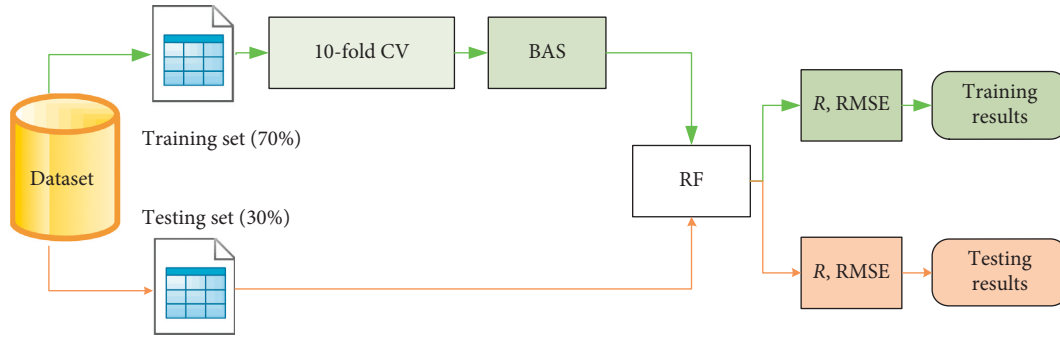
FIGURE 3: The flowchart of hyperparameter tuning of RF by BAS.

TABLE 1: The input influencing variables in the BRF model.

No.	Influencing variables	Min	Max	Average	Standard deviation
1	Cement (kg/m^3)	131	550	368.1	73.9
2	Water (kg/m^3)	150	225	187.6	24.3
3	[a]SCMs (kg/m^3)	0	357.5	71.0	125.3
4	Superplasticizer (%)	0	7.8	1.76	2.9
5	[b]CA (kg/m^3)	0	1202.8	999.8	238.3
6	[c]CRA (kg/m^3)	0	1160	63.1	186.7
7	[d]FA (kg/m^3)	0	942	619.4	165.1
8	[e]FRA (kg/m^3)	0	630	49.9	98.3
9	Ages (d)	1	91	26.6	25.7

[a]Supplementary cementitious materials; [b]coarse aggregate; [c]fine aggregate; [d]coarse rubber aggregate; [e]fine rubber aggregate.

training set and the remaining 41 samples were set as the test set.

3. Results and Discussion

3.1. Results of Hyperparameter Tuning. In this study, according to the RMSE obtained from 10-fold cross-validation, the hyperparameters were tuned on the testing set. The RMSE versus iterations during BAS tuning is shown Figure 4. As can be seen, the RMSE decreased considerably, revealing that the BAS can tune the RF effectively. Then, the RMSE became stable at 15 iterations. Here, only 20 iterations were shown. The final hyperparameters of RF are given in Table 2.

3.2. Assessment of the Established Model. The comparison of the predicted UCS of RC by the BRF model and actual UCS of RC in datasets is depicted in Figure 5. As can be seen, the predicted UCS values of RC were rather close to the actual UCS, indicating that the BRF can establish the nonlinear relationship between UCS of RC and input variables successfully, and therefore, the model can predict the strength accurately. In addition, the high R values for the training set and test set were 0.985 and 0.959, respectively. The low RMSE values of 2.24 in the training set and 3.90 in the testing set were observed. Overall, the above results showed that there is no underfitting or overfitting phenomena by the proposed BRF model.
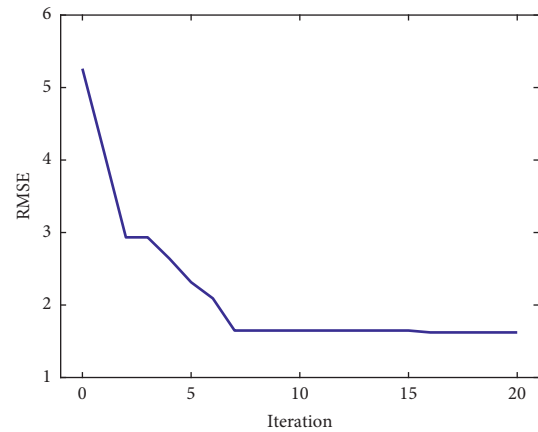

FIGURE 4: RMSE versus iterations.

TABLE 2: The obtained hyperparameters of RF.

Parameters	Empirical scope	Initial	Results
tree_num	[1, 10]	6	8
min_sample_leaf	[1, 10]	6	1

3.3. Variable Importance of RC. Furthermore, the relative importance of the input variables is shown in Figure 6. As can be seen, the age of RC was the most important variable with an important score of 1.42, and this result was consistent with the strength development of cementitious materials reported in the previous studies [12, 39]. The water-cement ratio also played a crucial role in the strength of RC, and the superposition effect of water and cement in this study was similar to the age. This agrees well with some studies that the water-cement ratio affects the strength considerably [40, 41]. As can be seen, the FA ranked third with an importance score of 1.23, which was more sensitive than CA (importance score of 0.49) in RC. Correspondingly, the FRA had a relatively larger influence on the UCS of RC than CRA. It should be pointed out that both the FRA and CRA affect the strength of RC obviously, and therefore, more attention should be paid when adding rubber materials to RC in practice. The admixture of SP and SCMs had the least influence on the strength of RC with the importance score of 0.27 and 0.24, respectively. The obtained results can guide the design of RC effectively and select the proper parameters
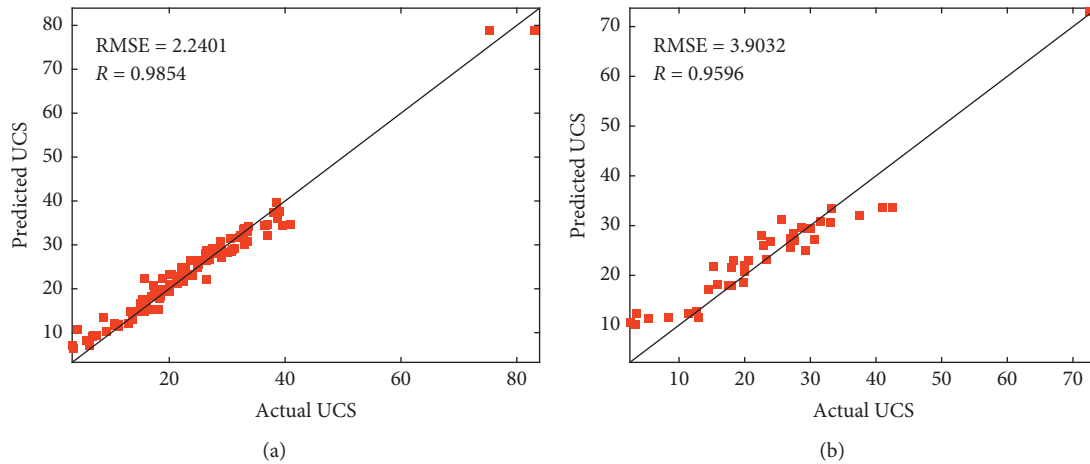
(a)

(b)

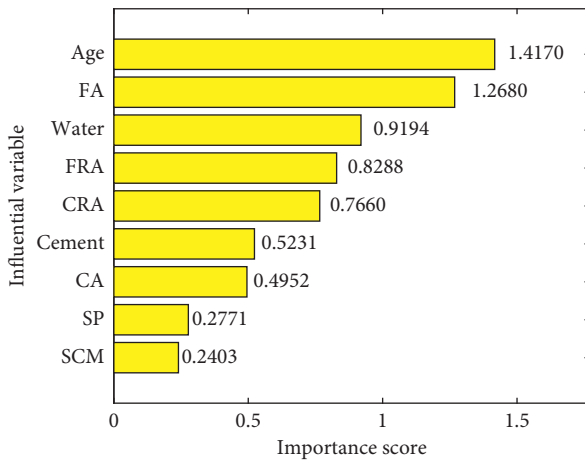FIGURE 5: Comparison of UCS values. (a) Training dataset. (b) Testing dataset.

FIGURE 6: Variable importance of RC based on the BRF.

for optimizing RC. The results can guide the accurate design of RC and boost the application of RC.

4. Conclusions

This paper presented an evolved random forest algorithm, namely, BRF, for evaluating the UCS of RC. Based on the 138 samples collected from the previous literature and 9 key influencing variables, the compressive strength of RC can be determined by the independent variables by BRF. The hyperparameters of RF were tuned by using the BAS algorithm and validated by 10-fold cross-validation. In addition, the performance of optimized BRF was examined by R and RMSE. The variable importance was first revealed and discussed. The main results are as follows: BAS can efficiently tune the hyperparameters of RF and can be used in evolved RF to establish the BRF prediction model; the proposed BRF model can accurately predict the strength of RC, which can guide the design of RC; on the testing set, R and RMSE were 0.96 and 3.9, respectively, meaning that the proposed BRF model has a good prediction on the collected RC data; the age of RC is the most significant variable for the strength,

followed by the cement ratio, FRA, CRA, and CA; the SP and SCMs have the least influence on the strength of RC.

It should be pointed out that the results were limited by the amount of the samples. If the larger dataset was obtained, the more accurate results would be derived. In the future, we would collect more samples and design a bigger dataset for analysis by machine learning methods, which can significantly promote the application of RC in the field.

Data Availability

The Microsoft Excel Worksheet data used to support the findings of this study are available from the corresponding author upon request.

Conflicts of Interest

The authors declare that there are no conflicts of interest.

Acknowledgments

References

[1] T. Xie, A. Gholampour, and T. Ozbakkaloglu, "Toward the development of sustainable concretes with recycled concrete aggregates: comprehensive review of studies on mechanical properties," *Journal of Materials in Civil Engineering*, vol. 30, no. 9, Article ID 04018211, 2018.

[2] R. Siddique, J. Khatib, and I. Kaur, "Use of recycled plastic in concrete: a review," *Waste Management*, vol. 28, no. 10, pp. 1835–1852, 2008.

[3] Z. Z. Ismail and E. A. Al-Hashmi, "Use of waste plastic in concrete mixture as aggregate replacement," *Waste Management*, vol. 28, no. 11, pp. 2041–2047, 2008.

[4] G. Dimitriou, P. Savva, and M. F. Petrou, "Enhancing mechanical and durability properties of recycled aggregate concrete," *Construction and Building Materials*, vol. 158, pp. 228–235, 2018.

[5] S.-C. Kou, C.-S. Poon, and H.-W. Wan, "Properties of concrete prepared with low-grade recycled aggregates," *Construction and Building Materials*, vol. 36, pp. 881–889, 2012.

[6] F. Azevedo, F. Pacheco-Torgal, C. Jesus, J. L. Barroso de Aguiar, and A. F. Camões, "Properties and durability of HPC with tyre rubber wastes," *Construction and Building Materials*, vol. 34, pp. 186–191, 2012.

[7] Z. Zhang, H. Ma, and S. Qian, "Investigation on properties of ECC incorporating crumb rubber of different sizes," *Journal of Advanced Concrete Technology*, vol. 13, no. 5, pp. 241–251, 2015.

[8] A. S. Hameed and A. P. Shashikala, "Suitability of rubber concrete for railway sleepers," *Perspectives in Science*, vol. 8, pp. 32–35, 2016.

[9] R. Pacheco-Torres, E. Cerro-Prada, F. Escolano, and F. Varela, "Fatigue performance of waste rubber concrete for rigid road pavements," *Construction and Building Materials*, vol. 176, pp. 539–548, 2018.

[10] P. Asutkar, S. B. Shinde, and R. Patel, "Study on the behaviour of rubber aggregates concrete beams using analytical approach," *Engineering Science and Technology, an International Journal*, vol. 20, no. 1, pp. 151–159, 2017.

[11] A. Grinys, H. Sivilevičius, and M. Daukšys, "Tyre rubber additive effect on concrete mixture strength," *Journal of Civil Engineering and Management*, vol. 18, no. 3, pp. 393–401, 2012.

[12] I. B. Topçu, "The properties of rubberized concretes," *Cement and Concrete Research*, vol. 25, no. 2, pp. 304–310, 1995.

[13] B. S. Thomas, R. C. Gupta, P. Kalla, and L. Cseteneyi, "Strength, abrasion and permeation characteristics of cement concrete containing discarded rubber fine aggregates," *Construction and Building Materials*, vol. 59, pp. 204–212, 2014.

[14] Z. K. Khatib and F. M. Bayomy, "Rubberized portland cement concrete," *Journal of Materials in Civil Engineering*, vol. 11, no. 3, pp. 206–213, 1999.

[15] L. Zheng, X. S. Huo, and Y. Yuan, "Strength, modulus of elasticity, and brittleness index of rubberized concrete," *Journal of Materials in Civil Engineering*, vol. 20, no. 11, pp. 692–699, 2008.

[16] F. Aslani, "Mechanical properties of waste tire rubber concrete," *Journal of Materials in Civil Engineering*, vol. 28, no. 3, Article ID 4015152, 2015.

[17] T.-C. Ling, "Prediction of density and compressive strength for rubberized concrete blocks," *Construction and Building Materials*, vol. 25, no. 11, pp. 4303–4306, 2011.

[18] W. H. Yung, L. C. Yung, and L. H. Hua, "A study of the durability properties of waste tire rubber applied to self-compacting concrete," *Construction and Building Materials*, vol. 41, pp. 665–672, 2013.

[19] C. Qi, A. Fourie, Q. Chen, and Q. Zhang, "A strength prediction model using artificial intelligence for recycling waste tailings as cemented paste backfill," *Journal of Cleaner Production*, vol. 183, pp. 566–578, 2018.

[20] C. Qi, A. Fourie, and Q. Chen, "Neural network and particle swarm optimization for predicting the unconfined compressive strength of cemented paste backfill," *Construction and Building Materials*, vol. 159, pp. 473–478, 2018.

[21] J. Zhang, G. Ma, Y. Huang, J. Sun, F. Aslani, and B. Nener, "Modelling uniaxial compressive strength of lightweight self-compacting concrete using random forest regression," *Construction and Building Materials*, vol. 210, pp. 713–719, 2019.

[22] K. H. Younis and K. Pilakoutas, "Strength prediction model and methods for improving recycled aggregate concrete," *Construction and Building Materials*, vol. 49, pp. 688–701, 2013.

[23] Z. H. Duan, S. C. Kou, and C. S. Poon, "Prediction of compressive strength of recycled aggregate concrete using artificial neural networks," *Construction and Building Materials*, vol. 40, pp. 1200–1206, 2013.

[24] N. Deshpande, S. Londhe, and S. Kulkarni, "Modeling compressive strength of recycled aggregate concrete by artificial neural network, model tree and non-linear regression," *International Journal of Sustainable Built Environment*, vol. 3, no. 2, pp. 187–198, 2014.

[25] K. Sahoo, P. Sarkar, and P. Robin Davis, "Artificial Neural Networks for Prediction of Compressive Strength of Recycled Aggregate Concrete," *International Journal of Research in Chemical, Metallurgical and Civil Engineering*, vol. 3, no. 1, 2016.

[26] I. González-Taboada, B. González-Fonteboa, F. Martínez-Abella, and J. L. Pérez-Ordóñez, "Prediction of the mechanical properties of structural recycled concrete using multivariable regression and genetic programming," *Construction and Building Materials*, vol. 106, pp. 480–499, 2016.

[27] A. Gholampour, A. H. Gandomi, and T. Ozbakkaloglu, "New formulations for mechanical properties of recycled aggregate concrete using gene expression programming," *Construction and Building Materials*, vol. 130, pp. 122–145, 2017.

[28] L. Breiman, "Random forests," *Machine Learning*, vol. 45, no. 1, pp. 5–32, 2001.

[29] E. Scornet, "On the asymptotics of random forests," *Journal of Multivariate Analysis*, vol. 146, pp. 72–83, 2016.

[30] X. Jiang and S. Li, "BAS: beetle antennae search algorithm for optimization problems," *International Journal of Robotics and Control*, vol. 1, no. 1, pp. 1–3, 2018.

[31] A. Liaw and M. Wiener, "Classification and regression by random forest," *R News*, vol. 2, no. 3, pp. 18–22, 2002.

[32] S. Janitza, G. Tutz, and A.-L. Boulesteix, "Random forest for ordinal responses: prediction and variable selection," *Computational Statistics & Data Analysis*, vol. 96, pp. 57–73, 2016.

[33] Y. Sun, J. Zhang, G. Li, Y. Wang, J. Sun, and C. Jiang, "Optimized neural network using beetle antennae search for predicting the unconfined compressive strength of jet grouting coalcretes," *International Journal for Numerical and Analytical Methods in Geomechanics*, vol. 43, no. 4, pp. 801–813, 2019.

[34] Y. Sun, J. Zhang, G. Li et al., "Determination of Young's modulus of jet grouted coalcretes using an intelligent model," *Engineering Geology*, vol. 252, pp. 43–53, 2019.

[35] J. Sun, J. Zhang, Y. Gu, Y. Huang, Y. Sun, and G. Ma, "Prediction of permeability and unconfined compressive strength of pervious concrete using evolved support vector regression," *Construction and Building Materials*, vol. 207, pp. 440–449, 2019.

[36] M. M. Reda Taha, A. S. El-Dieb, M. A. Abd El-Wahab, and M. E. Abdel-Hameed, "Mechanical, fracture, and microstructural investigations of rubber concrete," *Journal of Materials in Civil Engineering*, vol. 20, no. 10, pp. 640–649, 2008.

[37] S.-F. Wong and S.-K. Ting, "Use of recycled rubber tires in normal-and high-strength concretes," *ACI Materials Journal*, vol. 106, no. 4, p. 325, 2009.

[38] Q. Dong, B. Huang, and X. Shu, "Rubber modified concrete improved by chemically active coating and silane coupling agent," *Construction and Building Materials*, vol. 48, pp. 116–123, 2013.

[39] F. Valadares, M. Bravo, and J. de Brito, "Concrete with used tire rubber aggregates: mechanical performance," *ACI Materials Journal*, vol. 109, no. 3, p. 283, 2012.

[40] Z. Chen, Y. Zhang, J. Chen, and J. Fan, "Sensitivity factors analysis on the compressive strength and flexural strength of recycled aggregate infill wall materials," *Applied Sciences*, vol. 8, no. 7, p. 1090, 2018.

[41] J. Tinoco, A. Gomes Correia, and P. Cortez, "Application of data mining techniques in the estimation of the uniaxial compressive strength of jet grouting columns over time," *Construction and Building Materials*, vol. 25, no. 3, pp. 1257–1262, 2011.